High temperature resistant geopolymers: composition, microstructure and performance

Kinga Małgorzata Klima

Bouwstenen 346

High-temperature resistant geopolymers: composition, microstructure and performance

Kinga Małgorzata Klima

This work originates as part of the research programme of the Foundation for Fundamental Research on Matter (FOM), and falls as of April 1, 2017 under the responsibility of Foundation for Nederlandse Wetenschappelijk Onderzoek Instituten (NWO-I), which is part of the Dutch Research Council (NWO). Fire safety of innovative geopolymer-based building materials (Project No. 16347)

This research was carried out under project number S17013a in the framework of the Partnership Program of the Materials innovation institute M2i (www.m2i.nl)

CIP-DATA LIBRARY TECHNISCHE UNIVERSITEIT EINDHOVEN

High-temperature resistant geopolymers: composition, microstructure and performance / by Kinga Klima

A catalogue record is available from the Eindhoven University of Technology Library

ISBN: 978-90-386-5653-3

Bouwstenen 346

NUR 955

Cover design: Kinga Klima, Photo by Pim Verkoelen

Ph.D. thesis, Eindhoven University of Technology, the Netherlands

High-temperature resistant geopolymers: composition, microstructure and performance

PROEFSCHRIFT

ter verkrijging van de graad van doctor
aan de Technische Universiteit Eindhoven,
op gezag van de rector magnificus prof.dr.ir. F.P.T. Baaijens,
voor een commissie aangewezen door het College voor Promoties,
in het openbaar te verdedigen op donderdag 19 Januari 2023 om 16:00 uur

door

Kinga Małgorzata Klima

geboren te Limanowa, Polen

Dit proefschrift is goedgekeurd door de promotoren en de samenstelling van de promotiecommissie is als volgt:

Voorzitter:	prof. dr. ir. T.A.M.Salet
1e Promotor:	prof. dr. ir. H.J.H. Brouwers
2e Promotor:	prof. dr. ir. Q.L. Yu (Wuhan University)
Promotiecommissieleden:	prof.dr. M.C. Bignozzi (Universita di Bologna)
	prof.dr. K.E. Zarębska (AGH University of Technology)
	prof.dr. J. Provis (University of Sheffield)
	prof.dr. H. Justnes (Norwegian University of Science and Technology)
	prof.dr.ir. D.M.J. Smeulders
	prof.dr.S.R. van der Laan

Het onderzoek of ontwerp dat in dit proefschrift wordt beschreven is uitgevoerd in overeenstemming met de TU/e Gedragscode Wetenschapsbeoefening.

Dedicated to my beloved parents

PREFACE

My four-year adventure known as the PhD is difficult for me to accurately describe or define. Several factors have certainly led me to where I am now, including the pursuit of dreams, determination, ambitions, a hunger for knowledge, and self-development. In October 2018, I began my adventure in the Netherlands at the prestigious Technical University in Eindhoven, where I had the privilege of working on an exciting project that combined several of my scientific interests, namely the development of alternative, more sustainable fire-resistant geopolymer-based materials. The project was carried out in the framework of the program of the Materials innovation institute M2i and the Technology Foundation TTW, which is part of the Netherlands Organization for Scientific Research (NWO).

First and foremost, I would like to thank my promotors, without whom none of this would be possible, Professor Jos Brouwers who gave me a chance and entrusted me with a PhD position in this project. Jos, thank you very much for all the valuable advice you gave me, as well as the great freedom in the direction in which I wanted to develop this project. Your support on both research and my career has been invaluable. I would like to thank my second supervisor, professor Qingliang Yu, on whom I could always rely due to his extensive experience and knowledge and who was able to guide me to the correct research path. Thank you for countless meetings, discussions, revisions/proofreading of my articles and much valuable advice concerning both my career and everyday life. Also, words of thanks go to Katrin Schollbach, for her scientific contribution, and cooperation and for answering my countless questions. At this point, I would like to thank the partners of my project, in particular, Paul van Dooren and Ricardo Weewer (VRBZO), Sieger van der Laan (TATA Steel), Louis Cleef (Rockwool) and Sigrin Drost (now Deerns Nederland, formerly Nieman) for a warm welcome and very pleasant cooperation. I sincerely thank the entire promotion committee, prof. Katarzyna Zarębska, who agreed to add a Polish accent to my PhD defence, as well as other members who, through their feedback and suggestions, significantly improved the quality of my doctoral dissertation, namely prof. dr. Maria Bignozzi, prof.dr Harald Justnes, prof. dr. John Provis, prof. dr.ir David Smeulders and prof. dr. Sieger van der Laan.

None of my lab tests would have been possible without an incredible team of technicians and employees who assisted me and for whom my cheerful visit always meant more tasks per day than was planned. This group includes Anneke Delsing, Harrie Smulders, Geer-Jan Maas, and two Tata Steel employees, Paul van den Idsert and Jaap Koster, who assisted me with the high-temperature measurements.

In addition to my scientific work, these four years allowed me to build new friendships. I would like to take this opportunity to thank Jawad, with whom I was fortunate enough to begin my PhD studies. I had no idea that Pakistan's culture and people were so similar to those of Poland. I would also like to mention Yan, the person with whom the friendship, which began with a shared doctoral project, grew into a friendship on many levels. I can thank them both for their encouragement, assistance, and tears of laughter. Charles, Iris, Winnie, and Jonathan, my joy at meeting wonderful people do not stop there. Your unique sense of

humour and approach to life completely caught my heart, so please do not lose this positivity at any point in your doctoral studies or future life. It is time to recognise three wonderful, wise Polish girls Ania, Agata and Ewa, who brought warmth and a family atmosphere to the workplace. You have no idea how much your presence brightened my daily life. I would like to express my deepest appreciation to Ania, who paved the way for me to become a PhD student in a foreign country and supported me with her kindness and great knowledge, which she shared with me at any time and any place. I would like to thank you individually, Alex, for your excellent scientific cooperation. With your extensive knowledge and experience, you have significantly improved the quality of my research.

I want to thank my big group of very smart and amazing people who created a good atmosphere, namely Florent, Marc, Hoss, Kate, Marina, Felix, Naomi, Zhihan, Xuan, Daoru, Tao, Leila, Samuel, Ricardo, Helong, Yanjie, Zixiao, Fan, Samantha, Jia, Zixing, Beatrice and our former colleagues whom I had a chance to meet Perry, Veronica, Qadeer, Yuri, Gang, Peipeng, Cao, Xiaoxiao, Zhengyao, Yuxuan and Shaohua. I want to keep in mind every memory, meeting, and conversation I have had with you. They brought me a great deal of joy. During my doctoral studies, I had the opportunity to supervise two master's students, Nora Kuiper and Sanne van Diemen. Thank you for your fruitful collaboration. I had a lot of fun working with you, and I was very proud of your progress and accomplishments.

I was lucky to also make new friends on the sixth floor outside of the building materials group, so my space team: Julien, Oindrila (Cindy) and Waqas. Our awkward, introverted-extroverted concoctions are far to look for. I would like to refer to the above-mentioned Polish accent again because they are my friends Lidia, Daria, Ela and Anastazja, who, regardless of the distance, stayed with me and support me in the best possible way. Last but not least, I would like to thank Kars for sticking by me through all of my struggles and hard times. You provided me with care and support, took the time to assist me in resolving my problems, and had a strong belief in my work. All of this cannot be forgotten.

And going back to the roots, the time has come for my lovely family and, in the first place, for my parents, Wiesława and Piotr, who did not try to influence my career decisions but consistently supported, comforted and believed in me. My two wonderful sisters Kasia and Ania, their husbands Grzegorz, Jan and my beloved nieces Lena, Gabriela and Olga. It is a great fortune to have such a family with me. Dziękuje, że bez względu na odległość, która nas dzieli, otrzymywałam od was wsparcie i pocieszenie którego tak bardzo potrzebowałam.

My PhD scientific journey is presented in this thesis, but I hope that in the few words above, I also highlighted how incredible this chapter of my life has been for me. Finding myself in a new country, environment, language, and scientific world was only made possible by the people who played a larger or smaller role in this unforgettable time of my life.

CONTENT

LIST OF ABBREVIATIONS

AA	Artificial aggregates
AAM	Alkali activated materials
AIC	Aerogel-incorporated concrete
BD	Bulk density
BET	Brunauer-Emmett-Teller
BFA	Biocoal fly ash
CMC	Critical micelles concentration
CS	Compressive strength
CSH	Calcium silicate hydrate
CTAB	Cetyltrimethylammonium Bromide
DSC	Differential scanning calorimetry
DTG	Derivative Thermogravimetry
EDX	Energy-dispersive X-ray spectroscopy
EOR	Enhanced oil recovery
FA	Siliceous Fly ash
FSEU	Fire Safe Europe
FT-IR	Fourier-transform infrared spectroscopy
GFC	Geopolymer foam concrete
GGBFS	Ground granulated blast furnace slag
HLB	Hydrophilic-lipophilic balance
ICP-OES	Inductively coupled plasma-optical emission spectrometry
ICSD	Inorganic Crystal Structure Database
ITZ	Interfacial transition zone
l/b	Liquid/binder ratio
l/s	Liquid/solid ratio
LCA	Life cycle assessment
L-D-H	Layered double hydroxide
LOI	Loss on ignition
MIP	Mercury intrusion porosimetry
M-S-H	Magnesium silicate hydrate
MWW	Mineral wool waste
N-A-S-H	Sodium aluminosilicate hydrate
NS	Nanosilica
OPC	Ordinary Portland Cement

PSD	Particle size distribution
QXRD	Quantitative X-ray Diffraction
RH	Relative humidity
RUL	Refractoriness under load
SDS	Sodium dodecyl sulphate
SEM	Scanning Electron Microscopy
SF	Silica fume
SLS	Sodium laurate sulphate
SSA	Specific surface area
T60	Tween 60
TEC	Thermal expansion coefficient
TG	Thermogravimetric analysis
T100	Triton X-100
UHPC	Ultra High-Performance Concrete
VOI	Volume of interest
w/b	Water/binder
XRD	X-ray powder diffraction
XRF	X-ray fluorescence
η	Water uptake
λ	Thermal conductivity
μCT	Micro-computed tomography
φ	Porosity

CHAPTER 1 INTRODUCTION

1.1 Background and motivation

There is currently an alarming trend concerning fires and their causes. Unfortunately, due to more and more applications of synthetic materials, fires in buildings are much larger, more hazardous, and difficult to control. Furthermore, the lack of uniformity in legal requirements regulating fire prevention in the European Union exacerbates this issue [1]. It is recognized that, especially in high-rise buildings, it is important to minimize the rate at which the fire spreads through the use of non-combustible cladding and thermal insulation materials. Fortunately, there is a growing interest in fire protection and the development of new technologies to reduce the impact on people's lives, health and the environment. As shown by statistical data in 2020, about 80 % of all injuries caused by fire in European Union occurred in buildings, including as much as 60.6 % in residential buildings [2]. Therefore, in the following years, an increase in expenditure on investments related to passive fire protection in buildings is expected **(Fig. 1.1b)** [3]. Concrete, gypsum, bricks, asbestos cement, stone, and glass are examples of fire protection materials. Coatings, mortar, sealants and fillers, sheets or boards, spray, prefabricated materials, and others are the most common forms of fire protection materials used in construction [3]. Moreover, in favour of the development of the fire-resistant materials sector, we observe a tightening of the policy and legal regulations regarding the approval of materials for use, also taking into account fire safety.

In order to develop better fire protection materials that can survive fire for a sufficiently long time and produce less smoke when burnt, several materials-related companies are focused on technological solutions, aiming at producing materials capable of withstanding high temperatures and reducing toxic emissions gases in contact with high-temperature decomposition.

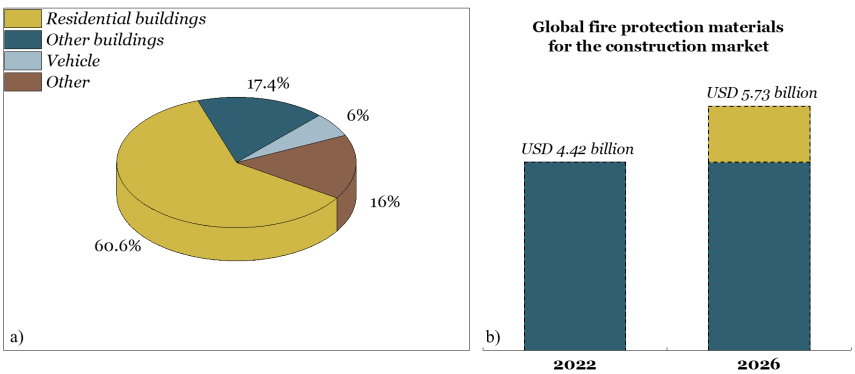

Fig. 1.1 a) Distribution of fire injuries by types in the 48 countries representing 1/6 of all countries in the world (2020) [2] b) Fire protection materials market growth forecast [3].

An inorganic material with limited heat resistance is Portland Cement (OPC) concrete structures which unfortunately show mechanical strength loss at high temperatures, which can impede rescue and evacuation actions. High temperature causes concrete degradation at the micro and meso scale, what is more, the possibility of thermal spalling is a threat to the structure of the building as well as may pose a threat to the life and health of people staying nearby [4].

Geopolymer-based materials

In the 1950s, Glukhovsky [5] established a reaction model of solid aluminosilicate precursors activated by alkali hydroxide and/or silicate solutions, which served as the theoretical foundation for the development of alkali cements. While in 1972 Davidovits [6] defined "geopolymers" as three-dimensional alumino-silicates produced by inorganic polycondensation. Geopolymeric binder, as an alternative to traditional Portland cement, possesses many interesting properties including high sustainability and intrinsically excellent thermal resistance property [7]. They also exhibit strong acid resistance [8] and heavy metal immobilisation [9] from waste materials utilised as a solid precursor for geopolymer synthesis. The capacity of geopolymers to maintain their strength even after being exposed to high temperatures is their principal feature. Additionally, because geopolymer technology can potentially have between 70% to 90% lower CO_2 emissions than OPC [10], using them as non-combustible building materials will benefit the environment. Geopolymers are formed by reacting an alkaline source with inorganic precursors that comprise alumina and silica. The process of bonding SiO_4 and AlO_4 tetrahedra units to create a three-dimensional skeletal structure is known as geopolymerization [11].

The great temperature endurance is demonstrated by the spatial structure, and more especially by the inorganic 3D framework. Due to its inorganic nature, it does not emit combustible vapours, hazardous gases or smoke when exposed to high temperatures. It should be noted, however, that while geopolymers do perform better than OPC-based materials when exposed to high temperatures, several factors need to be under control to achieve a good thermal response. These factors include the type of raw material, its chemical and mineralogical composition, an alkali cation, the silica modulus, and the source of the silica. Additionally tailoring the properties such as porosity, and aggregates/fillers-paste thermal compatibility is of great importance [12].

Fly ash is a common solid precursor used in geopolymer manufacturing due to its high content of silica, and alumina and low content of calcium. Furthermore, geopolymers based on fly ash have a low water demand and a high porosity, allowing for a reduction in the negative impacts of water evaporation under high-temperature conditions [13]. In addition, the continuous thermally-induced fly ash particles fusion and sintering further increases the materials' strength [14]. However, there are still unknowns about the link between material properties for room temperature and increased temperature behaviour which affects further material design optimization.

Foamed composites

Open porosity, which allows water to pass through the material structure during heating, is one of the above-mentioned material qualities that influence thermal responsiveness. Moreover, due to the presence of air voids, porous materials provide additional functionality, namely superior thermal insulation capabilities [15]. This feature is critical for the energy efficiency in heating of buildings, which accounts for up to 40% of total energy consumption in the European Union [16]. Hence, porous geopolymers can be a green alternative for organic materials [17] while also providing sufficient thermal comfort. Thermal conductivity for porous geopolymer foams ranges from 0.083 to 0.766 (W/m·K) [18] depending on the base material and aeration method.

Foamed geopolymers have the potential to be used for not only thermal insulation but also hygrothermal [19] and acoustic applications [20]–[22]. There are several methods for designing the pore structure, including direct foaming, sacrificial filler methods, and replica methods, with direct foaming being the most commonly applied (**Fig. 1.2**) [23]. There are numerous foaming agents available today, including aluminium powder [24], metallic Si [25], silica fume [26], silicon carbide [27], or hydrogen peroxide (H_2O_2) [28].

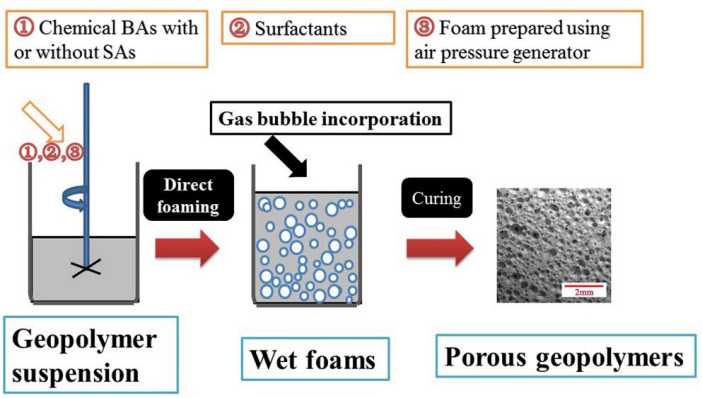

Fig. 1.2 Schematic diagram of direct foamed geopolymer [23]. Note: BA: blowing agent; SA: surfactant.

In practice, foam stabilisers are also commonly used to reduce surface tension, bubble rupture, and coalescence [18], [29]. As a result, the system's stability is improved, allowing for greater control over porosity and pore size distribution. Amphiphilic compounds with hydrophilic heads and hydrophobic tails are surfactants. Based on the composition of the head, they are classified as nonionic, anionic, cationic, or amphoteric. Surfactants can also be categorised based on their origins, such as natural surfactants like egg white [30] or olive oil [31], or commercial detergents [32]. The most prominent group, however, are synthetic surfactants, which are popular due to their good stabilising properties. However, still many challenges remain for foam geopolymers design [18], including scaling up effects, long-term durability, and composite interacting with other materials used in assemblies.

Waste material utilization – mineral wool waste

The concern of waste generation and according re-utilization has been known for many years and is still the subject of numerous scientific studies. The amount of waste produced globally is expected to reach 2.2 billion tonnes by 2025 [33]. Mineral wool waste (MWW) is one of the waste streams that is gaining ground among researchers and has been extensively studied in the last few years [34]–[40]. Mineral wool has been used as a material for the thermal insulation of buildings or pipes since the early twentieth century [41], and it now accounts for more than half of all insulation materials available on the market [42], [43]. As a result, the expected amount of MWW from building renovation and demolition is expected to be 2.82 million tonnes by 2030 [43], thus it is of great importance to find and optimize the solutions for MWW utilization.

Mineral wool waste contaminates the environment during storage, and the costs of landfilling rise year after year [44]. Moreover, another negative aspect of MWW storage is the large landfill capacity required due to the low bulk density of MWW. Currently, several application areas can be distinguished, such as solid precursors for the production of alkali-activated materials [45], wood-fibre composites [46], gypsum boards [47], substitute for coarse and fine aggregates in the production of cement-based composites [48], a precursor for foam glass synthesis [38] or as an adsorbent [49], [50]. Unfortunately, MWW reutilization remains low due to its fibrous character and the heterogeneity of the phase composition depending on the production method. One of the major problems, for instance, of an alkali activation approach is the large amount of alkali-activator required, which leads to a large impact on the environment. Furthermore, the existence of organic resins in MWW, such as phenolic resin, polyesters, and melamine-urea-formaldehyde, may result in harmful volatile compounds if the reuse includes chemical pre-treatment [34]. Yap et al.[43], on the other hand, believe that the advances made in the field of mineral wool waste disposal are consistent and promising and that in the near future the research should be expanded beyond the currently known range.

1.2 Scope and objectives

Intending to design a geopolymer for high-temperature applications, the focus is on three main aspects. The first step is to establish the crucial factors that determine thermal characteristics and propose a potential solution for increasing the thermal properties of fly ash-based geopolymer. The focus of the second section is on widely studied porosity and how it affects the performance of foamed composites in both ambient- and high-temperature conditions. Finally, the utilisation of waste materials is the main topic, with a particular emphasis on the design of artificial aggregates and their potential use in geopolymers for high-temperature applications. These objectives are covered by the following topics:

Siliceous fly ash-based geopolymer for high-temperature application

A large number of experimental studies have identified fly ash-based geopolymers as a possible alternative to Portland Cement with improved thermal properties. However, the wide variation in the results and inconsistency in the characterization of the solid precursor and geopolymers prompted the development of a guideline for fly ash-based geopolymers for high-temperature applications. This study gives a detailed assessment of current research developments in the field of mix design. In addition, research is being conducted on the high-temperature behaviour of zeolite-geopolymer composites based on fly ash. Sodalite is synthesized from siliceous fly ash (according to EN 197-1) and the sodalite-enriched geopolymer has been investigated in terms of mineralogical and microstructure variations from plain geopolymer. Additionally, the role of the crystalline additive in improving geopolymer behaviour at high temperatures is studied. Sodalite was synthesised from the same base material (siliceous fly ash), which was then evaluated in terms of the role of the structure enhancer during heating to 1000 ^{o}C.

Foam composites- hygrothermal and high-temperature performance

Surfactant use in foamed composites is a common approach, but critical is the amount of surfactant required to maintain adequate foam stability. As a result of the increased material prices, environmental impact and insufficient control over the generated pore structure, a co-surfactant mixing system is proposed. Given that the mixed surfactant system has lower surface tension and interfacial tension than single surfactants on the same substrate, the combination of two different types of surfactants is thought to demonstrate synergism or cooperative effects that can alter microstructures. The two-surfactant component system improves the foaming efficiency and stability of geopolymer pastes. The effect of the binary system on total porosity, pore size distribution, and open pore volume, as well as room temperature characteristics, such as thermal, hygrothermal, and mechanical insulation, is evaluated. With the aim to further improve room temperature properties, the addition of silica aerogel and its effect on hygrothermal and acoustic performance is investigated. Finally, the potential of porous geopolymer application at high temperatures (1100 ^{o}C) is examined during one-side thermal exposure to reveal the role of open porosity and the feasibility of the proposed material design as a high-temperature protective material in the form of panels.

Mineral wool waste-based aggregates for high-temperature application

Implementing high-temperature stable aggregates improves geopolymer-mortar thermal stability. However, the majority of aggregates that are fairly popular owing to environmental concerns have not been sufficiently or commonly characterized in terms of thermal properties, such as thermal expansion or the maximum application temperature. These parameters are important for high-temperature applications since they allow to predict the nature of the interaction between geopolymer paste and aggregates, which results

in the preservation of the composite during high-temperature exposure, as well as post-firing / heating properties like density, shrinkage, crack formation, compressive and flexural strength. As the aforementioned environmental aspects are specifically related to artificial aggregates, which are often based on industrial byproducts or waste materials, this research assessed alkali-activated artificial aggregates based on mineral wool waste. The preparation parameters, as well as the selected room and high-temperature properties, are established. Moreover, the aggregates are tested on a small scale in a fly ash-based geopolymer, and their mortar behaviour is compared to sand aggregates and further discussed.

1.3 Outline of the thesis

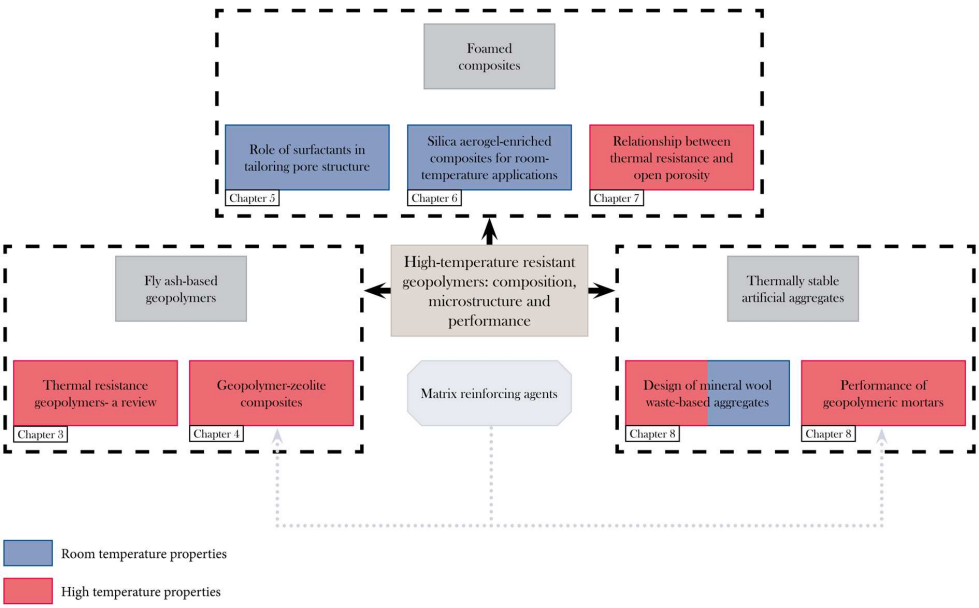

Fig. 1.3 Outline of the thesis.

Figure 1.3 depicts the outline of this thesis.In **Chapter 2** the methods used for analysing and characterising materials are described. The guidelines for fly ash-based geopolymer synthesis to improve high-temperature resistance are presented in **Chapter 3**. The synthesis of crystalline sodalite is presented in **Chapter 4** and the influence of sodalite-enriched fly ash-based geopolymer on high-temperature properties is discussed. At high temperatures, the role of the crystalline phase as a reinforcing agent/backbone is investigated further. Geopolymer foamed composites based on biocoal fly ash are designed and evaluated in the following three chapters. The role of cosurfactant mix in tailoring porosity, forming open-pore systems, and influencing pore size distribution is discussed in **Chapter 5**. Furthermore, room temperature properties that are strongly influenced by pore architecture, such as hygrothermal

performance of mechanical strength, are elaborated. The steady-state and dynamic evaluation of hygrothermal performance allowed for the evaluation of material behaviour in comparison to market materials. **Chapter 6** is a continuation of previous research in which the best performance mix is chosen based on the proportion of open pores vs. total porosity. Two solid precursors are used, namely siliceous fly ash and biocoal fly ash, and the composites are enriched with silica aerogel in amounts of 10% and 20%, respectively. The primary goal is to assess the effect of raw material and volume substitution on the pore architecture and thermal and sound insulation properties of porous composites. In the following chapter (**Chapter 7**), two mixes created in **Chapter 5** are used to perform a one-side high-temperature test. The composites with similar total porosity but different open pore contents are subjected to increased temperature of up to 1100 ° C, and the discussion focuses on the impact of temperature profile depth-related changes in porosity and mineralogical composition. **Chapter 8** discusses the possibility of using mineral wool waste to create artificial aggregates for high-temperature applications. The effect of the curing regime and alkali cation on the room and thermal properties is investigated. Furthermore, two selected samples are used in a siliceous fly ash-based geopolymer and exposed to 1000 °C to provide insight into the role of thermally stable aggregates as matrix reinforcing agents to minimise the negative effect of thermal shrinkage. Finally, in **Chapter 9**, the most important conclusions from the presented research are summarised, as well as proposals for the future research direction and continuation presented.

CHAPTER 2 ANALYTICAL AND CHARACTERIZATION METHODS

This chapter provides an overview of the methods used to characterize raw materials, such as siliceous fly ash, biocoal fly ash, and mineral wool waste, as well as the end products, geopolymer composites and artificial aggregates. To provide comprehensive material characterization, several groups of properties are distinguished, namely physical, chemical, microstructural, thermal, acoustic and mechanical analysis. Furthermore, under controlled laboratory conditions, this work investigates hygrothermal properties and thermal stability by exposing geopolymers to high temperatures and a wide range of relative humidity. These procedures are also mentioned and described in this chapter. Finally, the additional techniques used to characterize the granular materials (aggregates) are briefly described.

2.1 Physical properties

Bulk density and total pore volume fraction

The bulk density is calculated by dividing the mass of the sample, by the geometric volume measured using an electronic height gauge. For each mix, minimum six measurements are conducted to provide reliable results. The total pore volume fraction is calculated from

$$V_{total} = 1 - \frac{\varrho_{bulk}}{\varrho_{porefree}} \tag{2.1}$$

where $\varrho_{porefree}$ is the specific density on the crushed/powder material obtained via helium pycnometer (Accupyc 1330, Micromeritics, Norcross, GA).

Particle size distribution

Malvern Mastersizer 2000 is used to determine the particle size distribution of the powder precursors, which is then computed using Mie theory [51]. The analysis is possible by assuming that the particles are homogeneous and knowing the optical properties of the examined material and dispersant (2-propanol and/or demineralized water). While the sample is being dosed, ultrasound is used to de-agglomerate the particles, and the suspension is stirred for 1 minute to eliminate possible air bubbles.

Darcian gas permeability

The gas permeability test is conducted on the cylindrical samples with the size 30 x 50 mm^3 cut from the core of the specimens. The prism-shaped specimen is secured by employing a rubber gasket and a gasket holder in an inflatable sleeve to avoid a gas (air) bypass between the sample and the gasket. By applying the air pressure on one side of the test specimen and measuring the gas flow rate on the other side, the permeability of the samples can be determined by applying Darcy's law.

$$\Delta P = \frac{\eta \cdot L}{\mu \cdot A} Q \tag{2.2}$$

Where ΔP is the pressure drop measured using a manometer (Pa), η is the dynamic viscosity of a fluid (air $1.85 \cdot 10^{-5}$ (kg/(m·s)) at 20 °C), A and L represent the area of cross-section ($7.07 \cdot 10^{-4}$ m^2) and length of the sample (0.05 m), Q is a flow (m^3/s) and μ is measured Darcy's permeability.

2.2 Microstructure evaluation methods

Micro-computed tomography (μCT)

Using X-ray tomography, properties including closed pores, distribution of pore size are determined, and 3D reconstruction can be made. The measurements are performed with a μCT scanner (μCT 100, Scanco Medical, Switzerland). The core part of the two samples per mix in the shape of prism size 20 x 20 x 50 mm^3 are used. Each prism is analysed at three different heights to provide representative results. A voltage of 70 kV and a current of 200 mA and a wavelength of 14 W are used for the structure analysis. An aluminium filter of 0.5 mm is applied, and the 3D projection images are created by combining 705 slices which resulted in a 3.52 mm thickness of the composite. Voxel size is determined as 5 μm and the integration time was 220 ms giving the max resolution of the reconstructed image matrix (2048 px/cm). Using a dedicated Scanco Medical Evaluation program v6.6 the distance transformation is performed and the data are gathered in a 3D model of the sample [52]. The above-mentioned transformation, which consists of filling the empty spaces of the solid component and separating it from the matrix, is applied after the initial identification and separation of the pores from the denser geopolymer matrix and contrast optimization. The threshold is chosen visually in the middle of the histogram peaks. For research with similar samples, a fixed threshold is used. As a result, the pores and their volume in the VOI (volume of interest) constrained by the specified contour are determined after the identification of all pores on the surface and inside the prescribed contour [53]. To offer a quantitative examination of pore size distribution, the resulting pore size data are recorded as a histogram. The open porosity and its visualization are calculated from μCT after the separation of the pores. Identified pores are examined for connection to the outer contour and between each pore, as well as their volume. To provide 3D visualization, the disconnected pores are separated from the linked pores and displayed in the matrix contour.

Mercury intrusion porosimetry (MIP)

Specimens in size of 27 mm^3 are extracted from the sampled, immersed in isopropanol and subsequently dried in a desiccator. The measurements are conducted using an AutoPore IV Series Porosimeter. The applied contact angle of mercury was 130° and the surface tension was 0.485 N/m [54].

Scanning electron microscopy (SEM-EDX)

SEM analyses are performed by using a Phenom ProX scanning electron microscope with a BSE detector. Micrographs are recorded at 10.00 kV, while the EDX analysis is at 15 kV. The specimens are placed on carbon tape and sputtered with gold (Emitech K550X sputter coater current 60 mA, coating time 30 s).

2.3 Elemental and mineral composition of material

X-ray fluorescence spectroscopy (XRF)

The chemical composition is determined by using the Omnian approach to quantify the XRF spectra. The samples are prepared using the fused beads procedure, which involves combining the powder sample with the borate flux and non-wetting agent to create a glass disc of 4 cm diameter. The sample is further heated at 1065 °C for 24 minutes. Prior to the glassy disc preparation, the loss on ignition (LOI) is determined on the powder sample by heating it up to 1000 °C. The decomposition of organic compounds, carbonates, and salts is responsible for the mass change throughout the heating process. The LOI value is then utilised to recalculate the data acquired by XRF.

Phase assemblage (X-Ray Diffraction (XRD))

The phase analyses of samples both at room temperature and after exposure to certain elevated temperatures (up to 1100 °C) are performed using XRD measurements. Powder samples are backloaded in the sample holders and measured with a Bruker D4 equipped with a LynxEye detector. The range of 10–80 ° (2θ) is measured with a 0.02 ° step size using a Co-Tube. Qualitative analysis is carried out with X'Pert HighScorePlus 2.2 (PANalytical), while quantitative X-ray diffraction analysis (QXDA) with Rietveld refinement is conducted by the software Topas Academic v5.1. Silicon powder is used as an internal standard. The crystal structures with ICSD numbers are provided individually in each chapter.

High-temperature In-situ XRD

The powders are milled in XRD-Mill McCrone (RETSCH) and applied as a thin layer on a platinum strip. The strip function as the sample heater by applying a voltage and temperature is monitored and controlled with a type-S thermocouple welded at the back of the strip. High-temperature in-situ XRD is

used to determine the mineralogical transformation at high temperatures up to 1000 °C. The in-situ XRD method is performed by using an X'Pert Pro PANalytical diffractometer Co X-ray tube in theta-theta geometry equipped with an Anton-Paar HTK2000 heating stage. Corundum is used as an external standard. Samples were measured within the range 10-70° 2θ using a step size of 0.039° 2θ and a time per step of 40.9 s.

Inductively coupled plasma – Optical emission spectrometry (ICP-OES)

The content of reactive Si and Al of biocoal fly ash is quantified with ICP-OES (Spectroblue ICP-OES Sysmex). The obtained solutions are filtered with a 0.2 μm PTFE filter and acidified with ultrapure HNO_3.

2.4 Thermal analysis

Thermal conductivity

The thermal conductivity is measured with a heat transfer analyser (ISOMET model 2104), according to the standards ASTM D 5930. The analyzer applies a dynamic measurement method to determine simultaneously the volumetric heat capacity (J/(m^3·K)) and the thermal conductivity (W/(m·K)) of materials with a measurement time of about 8–16 min. The measurement is based on the analysis of the temperature response of the tested sample to heat flow impulses, while the heat flow is induced by electrical heating of a resistor heater inserted into the probe which is in direct contact with the test sample. The instrument is equipped with three probes with different thermal conductivity measurement ranges of 0.04–0.3, 0.3–2.0 and 2.0–6.0 W/(m·K) with an accuracy of 5 % of reading plus 0.001 W/(m·K). The temperature during the testing is constant at around 20 °C. The average thermal conductivity of three test specimens is calculated as the final thermal conductivity of the composite.

Thermogravimetric analysis

The thermal behaviour of specimens is evaluated using an STA F1 Jupiter analyzer (Netzsch Instruments). The measurement is carried out from 40 to 1000 °C at a heating rate of 10 °C/min in a nitrogen atmosphere with a flow of 20 ml/min. For the DSC analysis, additional measurements are included with a variety of heating rates from 5 to 20 °C/min in order to confirm the glass transition temperatures. The alumina crucibles are used and the average sample mass is 20 mg.

Isothermal Calorimetry

The isothermal calorimetry analysis is carried out using an isothermal calorimeter (TAM Air, Thermometric 3-channel) using ampoules with 125 mL volume. The heat release during the first 7 days of

hydration is monitored at a constant temperature of 20 °C. Water to binder (w/b) ratio of 0.23 was employed. A certain amount of solid ingredients is first mixed by hand with the alkali activator in the ampoule for 1 minute to create a homogeneous paste, which is then immediately loaded into the calorimeter.

Volume change

The volumetric changes are measured on the prisms before and after exposure to high temperature, expressed in percentage. The values are an average of three measurements per mix and temperature setting using a digital calliper to find the length, width, and height of each prism and calculate the total volume.

Medium pressure structural integrity- Refractoriness under load

The refractoriness under load test (RUL) is performed on two cylindrical specimens (diameter= 50 mm, height 50 mm) under the desired mechanical load (0.5 MPa). The furnace is heated at a constant rate in accordance with the testing standard EN ISO 1893:2008. D_{max} denotes the specimen's maximum expansion in the percentage of its initial length.

2.5 Acoustic properties

Acoustic absorption

The impedance tube method is used to conduct the sound absorption test, as illustrated in **Fig. 2.1**. The hardened cylinder composite samples with a dimension of a height of 50 mm and a diameter of 40 mm are tested. According to Li et al.[55], the minimum thickness of a porous material should normally be no less than 1/4 wavelength in order to absorb all incident sound (2000Hz, 0.172m). The measuring technique is that a loudspeaker on one side of the tube generates a plane wave, which spreads through the tube before being reflected by the material. The composite alters the reflected wave, and the sound absorption coefficient of the samples may be measured by collecting the resulting standing wave. The wave is recorded at six distinct points within the tube.

Fig. 2.1. Measurement of acoustic absorption of porous composites.

Also, the average values of the coefficient of absorption are calculated for each sample, which is defined as the area under the absorption curves normalized over the frequency range and determined as shown in the

equation below, where f_1 is the lower frequency at 100 Hz and f_2 is the upper frequency at 2500 Hz, according to ASTM C384-4[56]:

$$\alpha_{med} = \left[\frac{1}{f_2 - f_1}\right] \int_{f_1}^{f_2} \alpha(f) df \quad (2.4)$$

where a_{med} is the median value of the coefficient of absorption, and f is the frequency at a certain range.

2.6 Mechanical properties

Compressive and flexural strength

Following EN196-1 [57], samples of 40 × 40 × 160 mm^3 are used to determine flexural strength at 7, 28 days, and after high-temperature exposure. Although standard EN196-1 applies for testing mortars, the protocol is shown to provide reliable results when applied to the paste specimens, as stated in EN 197, therefore it is adopted without modification. To calculate the average strength, at least three specimens are tested at each age. To determine compressive strength, cubic samples of 40 × 40 × 40 mm^3 are used in accordance with EN196-1 [57]. The final strength of the composite is calculated as the average strength of six test specimens.

2.7 Fresh state properties

Setting time

The setting time is measured with a Vicat Needle apparatus according to European Standard NEN-EN 196-3 [58]. The test method is adjusted to the formulation of the investigated mix design. The test procedure considers periodically inserting a standard needle into a cementitious material and analysing its particular resistance to penetration to establish the initial and final setting time.

2.8 Material exposure to various conditions

Climate chamber conditioning- hygrothermal performance

The test procedure followed the guidelines stated in ISO 12571:2013E [59]. The measurement is carried out in a climate chamber with an accuracy temperature of 0.1 °C and an accuracy humidity of 0.5 %. The samples are dried at 105 °C in a drying oven until a constant mass (mass change < 0.1%). The climate chamber's specimens are originally preconditioned at the test range's lowest stated humidity level (25 %, 40 %, 50 %, 65 %, 80 %) at a constant temperature of 23 °C. The samples are consistently weighed until they are in equilibrium with their surroundings and the mass change between two measurements 24 h

apart is less than 0.1 %. The possible water uptake (η) at different humidity is calculated based on the weight difference between the mass of the sample dried at 105 °C (m_o) and the sample exposed to different humidity at 23 °C (m_1).

$$\eta = \frac{(m_1 - m_0)}{m_0} \times 100\% \tag{2.3}$$

High-temperature exposure

The samples are placed in a muffle furnace at room temperature and heated up to the temperatures 400, 600, 800 or 1000 °C respectively at a heating rate of 10 °C/min and exposed at specific temperatures for 1 hour. The samples are then removed from the furnace and cooled in the ait at 20 °C.

2.9 Characterization of aggregates

Basic properties of aggregates

By following the guidelines of ASTM C128-01 [60], three basic parameters of the artificial aggregates are evaluated, namely:

Water absorption is defined as the increase in aggregate mass caused by water accessing the pores of the particles during a certain time.

The particle density ϱ_p (kg/m^3) defines as the oven-dry mass of aggregate per unit volume of aggregate particles, including permeable and impermeable pores but excluding spaces between particles.

The apparent density ϱ_a (kg/m^3) is the mass per unit volume of the impermeable portion of the aggregate particles.

The volume fraction of the open porosity that is interconnected is calculated as follows [61]:

$$V_{open} = 1 - \frac{\varrho_p}{\varrho_a} \tag{2.5}$$

Where ϱ_p corresponds to the bulk density of the aggregate grain and ϱ_a refers to the apparent specific density which defines the mass of a volume of the impermeable portion of a material at a stated temperature.

Single crushing strength

According to [62], the single crushing strength of aggregates is performed using a crushing testing apparatus recording the failure load (P) and the diameter of the aggregate (x) and presented as an average value per batch and calculated as follows [63]:

$$\sigma = \frac{2.8*P}{\pi*x^2} \tag{2.6}$$

Grain shape analysis

The images of various aggregates fractions, are processed and analysed with the free image processing software ImageJ to evaluate the regularity of their shape by circularity factor. Circularity (C) is defined as

$$C = \frac{4\pi S}{P^2} \tag{2.7}$$

where S denotes grain area and P denotes grain perimeter [64], [65].

High-temperature stability of aggregates

Contour microscopy is used to determine the thermal expansion/shrinkage of aggregates during heating up to 1000 °C. The pictures are taken with the step 100 °C and analysed by using ImageJ. For both types of aggregates, 5 grains are analysed and per each 8 reference lines on the obtained photographs are selected to observe the changes.

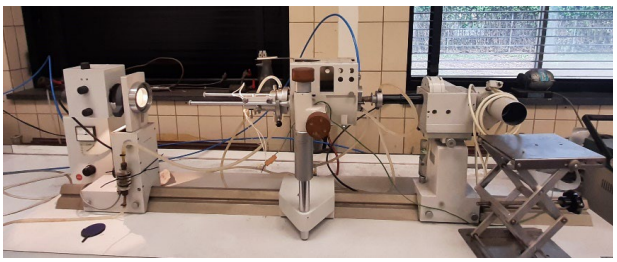

Fig. 2.2. Setup for high-temperature contour microscopy analysis.

CHAPTER 3 THERMAL AND FIRE RESISTANCE OF SILICEOUS FLY ASH-BASED GEOPOLYMERS

This chapter provides a comprehensive summary of the recent research progress concerning mix design, curing and their effects on the thermal and fire resistance of siliceous fly ash geopolymers. Due to the wide variety of characteristics, the performance of siliceous fly ash is recommended to be assessed in terms of its reactive phases. The influence of different alkali sources and their effects on thermal resistance are discussed, showing that potassium-based activators contribute to better performances. By applying Factsage calculations, the role of minor elements in controlling melting temperature and phase formation as well as the mechanisms behind the initial strength increase of fly ash-based geopolymers during heating are discussed. Moreover, the evolution of material properties during high-temperature exposure and the key parameter pore interconnectivity to avoid damage such as spalling are reviewed. Finally, recommendations for further investigations are provided.

The results presented in this chapter are published in the following article:

K.M. Klima, K. Schollbach, H.J.H. Brouwers, and Q.L. Yu, "Thermal and fire resistance of Class F fly ash based geopolymers–A review" Constr. Build. Mater., vol. 323, p. 126529, (2022).

3.1 Introduction

Increasing attention is being paid to the issue of fire resistance of building materials and the associated safety aspects, which are especially motivated by the numerous fires in residential buildings and public infrastructure. According to the platform FSEU (Fire Safe Europe), 2 million fires are reported in Europe each year and more importantly, 90% of them occur in buildings, partly attributed to the increased use of flammable materials. Ordinary Portland Cement (OPC) based concrete, with a worldwide production of 25 billion tons in 2018 [66], has great room-temperature performance, but its structure is weakened remarkably by the action of fire. Explosive spalling in dense concrete can be observed in the temperature range of 300 to 450 ^{o}C [67] and the loss of load-carrying capacity occurs if the temperature is higher than 400 ^{o}C due to the decomposition of portlandite [68], which causes irreversible structural changes.

Recent studies [69]–[71] demonstrated that geopolymers, an alternative to Portland cement, present better fire behaviour. Research on the aspect of fire resistance originates from Davidovits' work on modern fire-retardant materials [72], as a response to the catastrophic fires involving plastics in France in 1970-1973. A major advantage of geopolymers is their strength-retaining ability after high-temperature exposure. Moreover, applying geopolymers as a non-combustible construction material would have a positive impact on the environment because their CO_2 emissions are up to 80% lower than OPC [67]. Geopolymers, often described as anti-spalling materials [73], are produced from the reaction of an alkali source with inorganic precursors containing alumina and silica [74]. The reaction is called geopolymerization, a process by which SiO_4 and AlO_4 tetrahedra are combined to form a three-dimensional framework structure. The inorganic 3D framework provides geopolymers with excellent thermal stability that do not generate toxic fumes during a fire, enabling their high-temperature application such as fire-resistant coatings, thermal insulation layers and wall panels [68].

In recent years, geopolymers for high-temperature applications have been widely investigated owing to the growing awareness of the importance of passive fire protection of buildings and structures, as well as the demand for cost-effective and environmentally friendly construction materials [75]–[82]. Research shows that the performance of fly ash-based geopolymers is strongly affected by numerous factors, such as type of alkali reagent [83], curing conditions [83], silica modulus [84], porosity [85], phase composition [86], volumetric changes [87] and thermal compatibility of the components [80]. However, many results are considered conflicting and there is still no clear consensus about mix designs as well as influential factors concerning fire performance. Lahoti et al. [88] composed a comprehensive review on the fire performance of geopolymers but it primarily focused on the degradation of geopolymers under high temperatures at different scales from micro-, meso- to macro-, while the significance of influential factors mentioned above was not addressed in detail. Further, various solid precursors, as well as activators, were covered which makes it fairly difficult to derive trends or mechanisms for certain specific materials. Understanding how to alter geopolymer mixes with single fly ash is vital but there is a lack of comprehensive study which underlines the most critical aspects of the geopolymer mix design for high-temperature applications. It has

been investigated that not all fly ash-based geopolymer formulations have strong thermal stability. Rickard et al. [86], [89] investigated fly ash samples from different origins that provide varied high-temperature performance, implying that single system fly ash-based needs to be thoroughly investigated in terms of high-temperature resistance for designing good performing geopolymer based on locally available fly ash, both in a single or blended mixes. Therefore, a new comprehensive review with the focus on these items may help in understanding the interdependence of factors, the sensitivity of the geopolymer system to the action of high temperature and fire and provide insight on the mix design for such applications.

In this chapter, I review fly ash geopolymer-related works and summarize relationships between parameters that define the initial composition, optimal preparation conditions and the expected behaviour at elevated temperatures, to obtain a guideline for fly ash geopolymers in high-temperature applications. Apart from highlighting the unique properties of fly ash geopolymers for high-temperature applications, perspectives on features that could be enhanced, and areas of research still need to be explored are also provided.

3.2 Factors affecting geopolymer properties

3.2.1 *Fly ash reactivity*

The focus of this review is siliceous fly ash **(Fig. 3.1)** as the starting material of the geopolymers **(Table 3.1)**. Siliceous fly ash is primarily amorphous, but also contains some crystalline phases such as quartz, mullite, iron oxides, lime and periclase [90], [91].

Table 3.1: Summary of siliceous fly ash chemical composition ranges characterized worldwide (approximate values based on [92]).

% Chemical composition

SiO_2	Al_2O_3	Fe_2O_3	CaO	K_2O	MgO	SO_3	TiO_2	Na_2O	P_2O_5	MnO	LOI
30-70	15-50	1-30	<10.0	<4.0	<4.0	<2.00	<3.0	<2.0	<2.00	<0.5	< 20

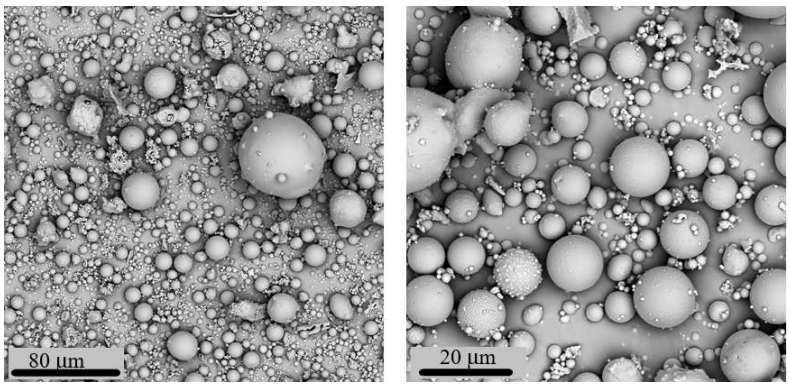

Fig. 3.1 Typical SEM of fly ash including fly ash precipitators and cenospheres.

Its reactivity in an alkaline environment is strongly related to the content of the vitreous (amorphous) phase and its composition. Higher content of the vitreous phase results in a faster activation and a higher degree of reactivity [93]. However, it should also be noted that the reactive phase is not entirely associated with the amorphous phase of ash. For instance, some refractory phases are not reactive but are also considered part of the fly ash amorphous phase. The crystalline components are typically non-reactive. A content of reactive silica between 40 to 50 % by mass is crucial [94], as is the amount of reactive Al_2O_3. However, this content can vary quite considerably, because the composition of fly ash itself is very variable and so is the ratio between amorphous and crystalline phases. This variability makes it difficult to compare results from different studies because the amount of reactive oxides is rarely determined. The chemical bulk composition (for example determined by XRF) that is often given contains no information about how the oxides are bound. This missing information is likely the reason for some conflicting results in the literature. There are existing methods which determine fly ash reactivity such as measuring the heat release and calcium hydroxide consumption in a high pH environment [95] or the method proposed by Pietersen [96] as the dissolution of fly ash in sodium hydroxide at different temperatures 20- 40 ^{o}C. It can be stated that chemical composition does not reflect reactivity. It is influenced by the aforementioned crystalline and refractory amorphous phase contribution in the overall composition, particle size and geometry (angularity) of the particles. Measuring the bulk chemical composition of fly ash before and after dissolution and combining it with the mass loss during dissolution would at least offer some consistent insight into the amount of reactive oxides present and the subsequent composition of reaction products. An alternative approach was proposed by Fernandez-Jimenez et al. [97], who stated that chemical analysis with hydrofluoric acid, Rietveld refinement and nuclear magnetic resonance can be combined to achieve a reasonably precise quantification of the vitreous phase materials in fly ash. Recent research [98] regarding the potential reactivity of fly ash for geopolymer designing showed that by combining fly ash dissolution in 10 M NaOH at 80 °C and treatment of the residue by HCl solution, the total amount of reactive Si/Al molar ratio can be reliably determined. This research underlined the main difference between Si/Al ratio for bulk fly ash obtained via XRF (1.63), amorphous based on XRD (3.75) and reactive via NaOH/HCl treatment (2.65-2.98). Observations revealed a substantial reliance of the results on the time of dissolution or solution alkalinity; moreover, refractory phases may exist among the amorphous component, which, despite their amorphous structures (XRD), are not reactive. In order to compare the findings obtained and use them for further study, we recommend that any research on fly-ash geopolymers should be focused on the reactive portion of the ash.

3.2.2 *Si/Al ratio*

The ratio of reactive silica and alumina plays one of the most important roles in geopolymerization reactions. For example, quartz and mullite increase the ratio of Si/Al in the bulk composition, however, they do not contribute in the context of alkali activation due to their crystalline character [11], as mentioned above. The Si/Al ratio determines the thermal expansion of geopolymers; lower thermal stability is

observed with an increased Si/Al due to the swelling of silica-rich secondary phases [86][99]. Further, the origin of silica and alumina plays an important role. For instance, research presented by Rickard et al. [86] showed that increasing the reactive Si/Al molar ratio from 1.15 and 1.87 to 2.0 and 3.0 respectively by adding extra silicate solution causes greater expansion and lower thermal stability of the samples and also the reduction of residual compressive strength after exposure to fire. A large portion of the excessive silicon added via solution does not react to form geopolymeric gel and the residual silicate is likely to swell at high temperatures that cause strength loss after firing [86]. Provis et al. [99] explained this phenomenon in high-silica activating solution by the low amount of silicate monomers, which causes slow dissolution of fly ash particles, leading to lower amounts of Al in the geopolymeric gel and therefore lower rates of geopolymerization. The low degree of geopolymeric gel cross-linking causes rapid thermal expansion. However, increasing the Si/Al ratio with more silica fume, which contains monomers, can improve compressive strength. Noteworthy, this contribution is not limited to chemical improvement; it also possesses the function of a microstructure refinement [100], by a small amount of well-distributed nanoparticles acting as a matrix compaction agent. Rodriguez et al. [101], who gave insight into the role of nanomaterial (nanosilica) in the formation of the microstructure of fly ash-based geopolymer, stated that when a commercially available silicate solution was replaced with nanosilica, a denser microstructure with reduced porosity and permeability was obtained, which is directly connected to lower water demand. By enriching one mixture with 8 wt.% silica fume it was possible to improve strength performance over the entire temperature range significantly (**Table 3.2**) [102]. Shaikh et al. [103] studied the impact of nanosilica (NS) and fine silica fume (SF) on geopolymer specimens at elevated temperatures. They reported that geopolymers containing 2% and 10% of NS and SF respectively, generated mullite which is considered a desirable high-temperature phase in refractory materials [104]. As a result, lower mass loss, volumetric shrinkage and greater residual strength were observed at high temperatures [103]. Moreover, as some latest studies found, an alternative and more eco-friendly source of silica, waste glass powder, shows desirable performances. It enhanced not only the fresh state characteristics and room temperature performance but also the high-temperature related to the melting of waste glass, which improves the geopolymer gel's integrity [105], [106].

Table 3.2 Compressive strength of cooled geopolymers based on fly ash after high-temperature exposures [102].

Mix detail	**Compressive Strength (MPa)**			
	80 °C	**600 °C**	**800 °C**	**1000 °C**
Fly ash + NaOH/Na_2SiO_3	36.7	41.8	12.8	8.3
Fly ash +8wt% SF+ NaOH/$(Na_2O)_x{\cdot}SiO_2$	67.6	70.1	34.2	31.3

It is noteworthy, that the Si/Al ratio also determines the initial temperature of the gel crystallization process during elevated temperature curing, the higher the SiO_2/Al_2O_3 ratio, the higher the temperature of crystallization. The process of crystal formation can be harmful to the stability of the material due to volumetric contraction associated with crystallisation [107]. It was also observed that a higher Si/Al ratio causes a lower water demand, higher density and lower porosity during the production of the geopolymer, which contributes to higher compressive strength and modulus of elasticity [108]–[110]. Krivenko and Kovalchuk [111] stated that a SiO_2/Al_2O_3 ratio in the geopolymer bulk composition between 2 and 4 provides the material with good mechanical performance and helps with the formation of more thermally stable crystalline phases (such as hydroxysodalite or zeolite R) in sodium-based geopolymer at high temperature, however, this can only serve as a general rule of thumb and the actual amounts of reactive alumina and silica should be considered, as mentioned in Section 2.1.

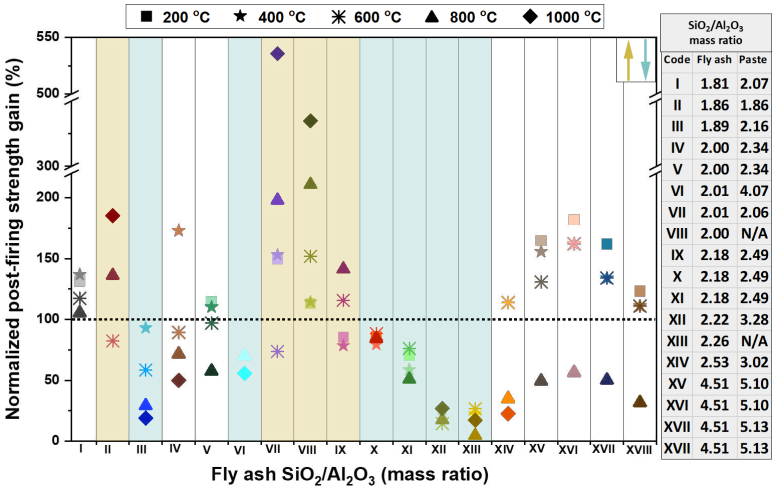

Fig. 3.2 Strength gain/loss in the temperature range 20 to 1000 °C measured at room temperature for different SiO_2/Al_2O_3 weight ratios based on XRF (fly ash) and with the addition of silicate from activator solution (paste) I [112]; II[113]; III [114]; IV [115]; V [103]; VI [116]; VII [87]; VIII [117]; IX-XI [118]; XII [119]; XIII [117]; XIV [102]; XV-XVIII [120].

Figure 3.2 shows examples of the bulk XRF SiO_2/Al_2O_3 of fly ash and paste together with the strength gain/loss at high temperatures. The yellow colour represents the ranges where, as the temperature rose, the strength increased in comparison to the strength measured at 20 °C, whereas the green colour represents the materials whose strength decreased after thermal exposure, which could be partially related to the percentage of added silica in the form of activator solution (see the SiO_2/Al_2O_3 in **Figure 3.2**). It is observed that silica from the solution does not exhibit a clear pattern or correlation when taking into consideration the percentage enrichment of the fly ashes. As a result, determining the reactive component of the ash is of significant interest as only this information can be useful to link future research to other authors' recommendations for geopolymeric paste design.

3.2.3 *Alkali reagent*

The alkaline modulus SiO_2/M_2O (M = K, Na) describes the ratio between the content of silica and alkalis added as a hydroxide (MOH) and silicate solutions ($(M_2O)_x{\cdot}SiO_2$). It was previously mentioned (Section 3.2.2) that an excessive silicate content hinders structure formation by inhibiting the geopolymerization reaction [121]. High concentrations of MOH can provide more hydroxyl groups to initiate geopolymerization reactions and promote gel formation [122]. Regarding the potassium-based activator, some discrepancies in values can be observed, for instance, the ratio SiO_2/K_2O of 1.88 (C_{KOH}= 8 M, ϱ = 1.33 g/cm^3) exhibited the highest residual strength at all ranges of elevated temperature treatment up to 800 °C, while Sindhunata et al. [123] stated that the best-performing specimens used the modulus ratio of 1.4. **Table 3.3** presents these inconsistencies. It displays the silica modulus as well as the alkali cation and the major observations at elevated temperatures. The investigations that compared the thermal reactions of geopolymers with different activators (K or Na) provided a qualitative examination of the function of the alkali cation in thermal efficiency by reducing the influence of variations in fly ash composition [124], [125]. Based on **Table 3.3**, it can be observed that when the potassium-based solution was used, there was a better high-temperature performance because there was less fracture development observed and thermal shrinkage. Furthermore, the massive discrepancy between silica modulus values (from 1.0 to 1.88) and comparable findings make it difficult to determine which value is the best. The objective, however, should be to determine the reactive component of the fly ash in order to calculate overall mix ratios, such as Si/Al, Al/M (M = Na, K) and H_2O/M_2O. Indeed, values obtained using comparable approaches can provide a broad picture of the best ratios for high-temperature applications.

Table 3.3: Literature on molar SiO_2/M_2O ratio for fly ash-based geopolymer for high-temperature response tests.

SiO_2/M_2O (molar ratio)*	Ref.	Activator	Type	T (°C)	Observations
1.00	[126]	Potassium	Concrete	700	A slight increase in the strength of geopolymer is seen at 300 °C, which is probably attributed to the sintering reaction of un-reacted fly ash particles in geopolymers. Higher splitting tensile strength of geopolymer than OPC in all temperature range from 25-700 °C
1.14	[71]	Sodium	Concrete	750	The main reason for substantial degradation is dehydration above 300 °C Recommendation: changing alkali type or optimizing mix design to reduce the influence of dehydration on the degradation propagation

SiO_2/M_2O (molar ratio)*	Ref.	Activator	Type	T (°C)	Observations
1.15	[127]	Sodium	Concrete	800	No cracking was observed at 800 °C. Geopolymer concrete gains strength beyond 600 °C due to densification
1.16	[114]	Sodium	Concrete	1000	Faster heat transfer in geopolymeric samples than in OPC was observed, as well as better resistance to cracking of geopolymer up to 1000°C.
1.20	[13]	Potassium-sodium	Paste	800	Fly ash-based geopolymer showed better performance than metakaolin-based with the same SiO_2/M_2O (no cracking occurs).
1.24	[115]	Sodium	Concrete	1000	Better performance of geopolymer than OPC both when air- and water-quenching applied.
1.26	[128]	Sodium	Mortar	800	The further geopolymerization and sintering of the matrix cause a strength increase. This effect counteracts another simultaneously occurring phenomenon, namely aggregates incompatibilities
1.30	[125]	Sodium Sodium/potassium potassium	Paste	800	The softening temperature of the geopolymer was determined only by the cation used and the higher was obtained for potassium K(800°C)> Na(610°C)> Na/K (570 °C)
1.42	[129]	Potassium-sodium	Concrete	800	Investigated molar ratio was 0.63 to 1.42 (Na_2SiO_3/KOH mass ratio 0.5 to 2.5) in which ratio equals 1.42 (2.5) performed the best.
1.43	[124]	Sodium	Composite	1100	Timber coating. Specimens exhibit good fire resistance, however, K-based exhibits fewer cracks after 1100°C than Na-based.
1.43	[130]	Sodium	Paste	800	Fly ash activated by Na-based solution. The investigated mass ratios Na_2SiO_3/NaOH were 2.0, 2.5, and 3.0. At room temperature, the better mechanical performance showed a sample with 2.5 (SiO_2/Na_2O = 1.35), but at high temperatures up to 800°C better results were obtained for the mass ratio 3.0 (SiO_2/Na_2O = 1.44)

SiO_2/M_2O (molar ratio)*	Ref.	Activator	Type	T (^oC)	Observations
1.44	[131]	Sodium	Paste	800	Blast furnace slag and fly ash blended in a weight ratio of 1:1 which cause the formation of C-(N)-A-S-H Strength development until 400 ^oC, crystallization of the gel at 600 ^oC causes strength decrease and shifting porosity towards big size pores
1.88	[124]	Potassium	Composite	1100	Lower shrinkage and thermal conductivity of potassium-based than Na-based;
1.88	[130]	Potassium	Paste	800	Paste with mass ratio K_2SiO_3/KOH 3.0 (SiO_2/K_2O = 1.88) shows the highest residual strength. Fewer cracks, lower volumetric shrinkage and mass loss than Na-based.

***Mass ratios MOH/M_2SiO_3 recalculated on the assumption that density equals:**
$D_{(NaOH\ 8M)}$=1.28 g/cm³; $D_{(NaOH\ 10M)}$ = 1.33 g/cm³ $D_{(NaOH\ 14M)}$ =1.5 g/cm³ $D_{(KOH\ 7M)}$=1.29 g/cm³ $D_{(KOH\ 8M)}$=1.33 g/cm³

Geopolymeric gel formation is dependent on the present cations [132], [133]. The initial strength of potassium-based geopolymers is lower than those activated by sodium [134] because potassium leads to the formation of more porous gels [134], however potassium-based geopolymer performance is compensated by better high-temperature behaviour. The use of potassium hydroxide also results in a longer setting time, however, it also leads to a higher rate of fly ash dissolution and aluminium incorporation in the gel matrix [133], [135]. This occurs because potassium is incorporated into the aluminosilicate framework faster than sodium due to lower charge density that is directly connected to the charge and atomic radius. Furthermore, sodium has a stronger interaction with its first hydration shell than potassium. Na^+ hydration sphere contains strongly bound 6 H_2O molecules, whereas for K^+ the number is ranging from 5 to 10 [136]. Water molecules formed during the condensation of aluminosilicates will be transferred into the hydration spheres of potassium/sodium ions. From the point of energetic contributions of each hydration shell, it is more favourable for Na ions to adsorb released water molecules and for K to be associated with oligomers [137]. The potassium-based geopolymers exhibit better thermomechanical properties, better thermal stability [138], lower mass loss and lower volumetric shrinkage [124] than their sodium counterparts at elevated temperatures [103]. Bakharev [139] reported that geopolymers prepared using a potassium activator had higher compressive strength after fire exposure at 800 ^oC compared to their initial strength, while the specimens based on Na-containing activator deteriorated rapidly above 800 ^oC which was related to the crystallisation of Na-feldspars and a significant increase in pore size. Potassium-based aluminosilicate gels have a higher temperature of decomposition than sodium ones, which explains that the K_2O/SiO_2 system is more suitable for fire resistance applications [11]. The decomposition at lower temperatures for a Na-based system is caused by the higher diffusion coefficient of sodium at high temperatures [139], [140]. Pan and Sanjayan [125] concluded that the softening temperature (T_s, temperature at which the reversible

transition in amorphous regions from a solid into a viscous state takes place) reached the highest value for K-based geopolymer (800 °C) and the lowest value for mixed cation type Na/K (570 °C), while it was 610 °C for Na. The authors suggested that the mechanism determining the behaviour is similar to the one that occurs in the T-O-T structure in glass and applies to both sole and mixed alkali cations. Sodium aluminosilicate glass has a lower softening temperature than potassium glass, and mixed alkali cations (Na-K) cause a further decrease in the softening temperature [141]. This specific effect can be explained by the smaller atomic radius of sodium compared to potassium. Therefore, sodium forms stronger bonds with oxygen, resulting in a stronger inductive effect in Na-O bonds when compared to K-O bonds, and the stronger inductive effect results in lower strength at high temperatures [125]. Furthermore, Barbosa and MacKenzie [142] stated that K-based geopolymers melt only at 1400 °C and their thermal stability is related to the partial recrystallization to feldspars. In aluminosilicate systems, the presence of sodium reduces the melting temperature of the entire system by the formation of crystalline phases such as $Na_2O{\cdot}2SiO_2$ ($T_{liquidus}$ = 874 °C), $Na_2O{\cdot}SiO_2$ ($T_{liquidus}$ = 1089 °C) or albite $Na_2O{\cdot}Al_2O_3{\cdot}6SiO_2$ ($T_{liquidus}$ = 1108 °C). Potassium activation in low alumina systems (< 10%) also reduces the melting temperature of the geopolymer due to the formation of high silica potassium silicates, such as $K_2O{\cdot}4SiO_2$ and $K_2O{\cdot}SiO_2$, with a melting temperature of 770 °C and 976 °C respectively. However, the content of alumina above 10% results in the formation of phases such as leucite $K_2O{\cdot}Al_2O_3{\cdot}4SiO_2$ ($T_{liquidus}$ = 1693 °C) with a higher melting point. Overall, the use of K-based activator is advantageous for fly-ash based geopolymers owing to its beneficial impact on high-temperature performance, including more stable phase formation, the strength evolution and reduced mass loss and shrinkage.

3.2.4 *Role of water*

The properties of geopolymers are strongly determined by the amount of water in the initial solution and the content and type of residual water, such as entrapped in the small framework pores [143]. Some researchers stated that the water content has more influence on the microstructure and strength development than the chemical composition of the geopolymer gel [143]–[145]. Water is the medium for OH^- anions that dissolve fly ash particles and hydrolyse Al^{3+} and Si^{4+} ions. High alkalinity is required to initiate raw material dissolution and geopolymeric gel formation which influences the reaction rate [146]. After the geopolymerization reaction, the water stays in the pores as physically bound water or gets incorporated into the geopolymer network as chemically bound water. The high H_2O content causes lower strength by creating larger pores [147] and increasing pore volume which also increases the shrinkage occurring at high temperatures [89]. However, water decreases the interaction of ions by enhancing dissociation, which enhances and accelerates their transport/movement. Furthermore, an increase in the concentration of ions in the solution can be seen when ions become more mobile [148]. Thus, when OH^- ions concentration in the system is high enough, more water can increase the rate of the dissolution and hydrolysis reactions through:

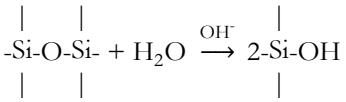

(3.1)

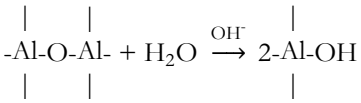

(3.2)

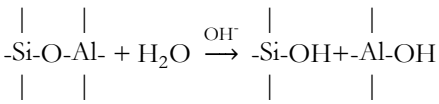

(3.3)

This is beneficial for improving geopolymerization reaction efficiency, but at the same time, the water hinders polycondensation kinetically [149]. Barbosa and Mackenzie [150] also observed that a higher water content increases the amount of unbound sodium that can migrate to the surface over time. It undergoes atmospheric carbonation, forming Na_2CO_3 that undergoes a melting process after reaching 1000 ^{o}C [137], forming a glaze.

3.2.5 *Curing regime*

Different curing regimes can be applied to obtain geopolymer with good performance at room and high temperatures. Heat-cured geopolymers in general are characterized by high compressive strength, low drying shrinkage and moderately low creep [114], because the higher temperatures increase the dissolution of the aluminosilicate source, thus increasing the polycondensation reaction and gel formation. Additionally, greater polycondensation shortens the setting time of the specimens.

The most typical temperature range for the initial hours (up to 24 hours) of curing is 50-80 ^{o}C, followed by room temperature curing. The initial 48 hours are crucial for geopolymerization reactions. Many investigations have reported that a curing temperature of 60-65°C [151]–[154] and a curing duration of 24 hours is optimal. The prolonged exposure or exposure to higher temperatures is unprofitable since there was no significant improvement in compressive strength at temperatures beyond 60 ^{o}C [155]. Sindhunata et al. [123] demonstrated that temperatures over 50 °C promote geopolymerization by raising the geopolymer's final Si / Al ratio and increasing the system reactivity (**Table 3.4**), suggesting that geopolymerization is first and foremost reliant on the curing temperature. Taking into consideration the costs associated with energy, increasing the heating duration from 24 to 40 hours results in only a 10 % gain in strength [156], while additional heating up to 72 hours results in a negligible improvement in strength, according to [151].

Table 3.4: Differences in final Si/Al ratios of the geopolymeric gel of FA-based material cured at elevated temperatures based on the same fly ash [123].

Curing time (h)	Curing temperature (°C)	Final Si/Al
24	50	1.66
48	50	1.64
24	75	1.75

Curing at lower temperature (~32 °C) conditions for up to 3 days before applying high-temperature curing has been shown to be particularly effective for achieving higher strengths than the specimens cured directly at 60 °C (**Table 3.5**) [155]. These results need further investigation; however, it seems an initially slow dissolution of aluminosilicate species during ambient temperature curing could be beneficial for further temperature-induced condensation. Nevertheless, it has to be mentioned that realistically the necessity of curing at elevated temperatures limits the possibility of wide industrial application of fly ash geopolymers as fire-resistant material to the precast geopolymer concrete.

Table 3.5. Geopolymer strength variations as low-temperature curing is used prior to exposure at 60 °C curing [155]. Sample A (NaOH molarity 14M), sample B (12M).

	Compressive strength variation (100% refers to the material directly cured at 60 °C)	
Low temperature curing	A (%)	B (%)
1 day	139	122
2 days	146	130
3 days	155	133
4 days	155	134
5 days	154	135

3.3 The influence of minor elements on the geopolymeric microstructure

3.3.1 *Calcium*

In siliceous fly ash (CaO < 10 wt. %, EN 197-1), calcium is present in the form of calcium silicate and aluminosilicate glasses [157]. It is believed that a small quantity of reactive calcium improves the early and late age properties of fly ash-based geopolymer cured at room temperature [158]–[160]. Calcium plays the role of a promotor of reaction and co-existing (C-S-H) phase formation in the geopolymer matrix [161], so adding reactive calcium to siliceous fly ash can be beneficial. Calcium provides nucleation points for dissolved species and improves strength. As a result of the presence of calcium, at high temperatures, small amounts of various Ca-bearing minerals are formed, such as gehlenite, anorthite, β- wollastonite [162].

Dombrowski et al. [113] studied the influence of calcium content on fly ash-based geopolymers. The fly ash initially contained 2.8 wt.% CaO and the samples were modified by the addition of 8 wt.% calcium hydroxide, which provided better material performance both at room and high temperature than non-modified samples. They had much higher strength after 28 days and the smallest shrinkage upon heating to 1050 °C. However, more than 8 wt.% of $Ca(OH)_2$ decreased the softening temperature which plays a crucial role in high-temperature behaviour [113]. In general, the addition of calcium hydroxide is more effective than the addition of free lime, which is related to the uncomplete hydration of CaO in the alkaline medium to form $Ca(OH)_2$ [163][164].

3.3.2 *Iron*

Originally, iron occurs in the fly ash as hematite and magnetite, partly as an iron oxide surrounded by a sintered glass phase. However, the dominant part of iron fraction occurs in the iron-bearing glass, as cenosphere and microspheres (**Figure 3.3**), in the form of ions Fe^{2+} and Fe^{3+} [165] and as particles of superparamagnetic spinel structure such as hercynite [166].

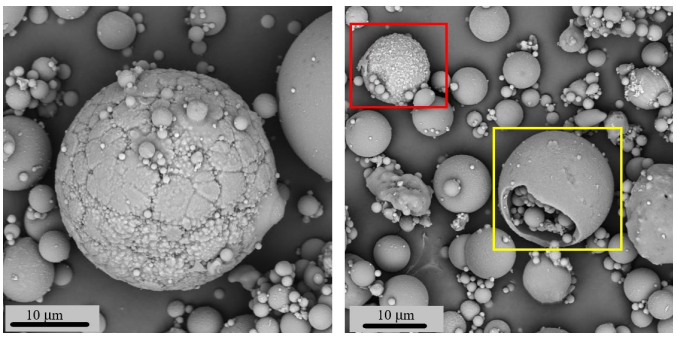

Fig. 3.3 Ferrospheres (red) present in the ash as well as ash particles trapped in the spherical structure (yellow).

It has been stated that the iron present in raw fly ash is mainly amorphous [167], [168] and the total iron content varies in a wide range from 1 to 28% (**Table 3.1**). A common phenomenon observed in fly ash-based geopolymers is colour change at high temperatures that is mainly related to the oxidation of iron from Fe^{2+} to Fe^{3+} [114], and in particular, a dark red colour appears due to the increased formation of hematite [166]. An interesting phenomenon occurs above 600 °C when the viscous sintering of aluminosilicates takes place, the high-ferrous glasses undergo melting and the amorphous iron, which can be captured in the ash spheres, can be exposed to the atmosphere and undergo oxidation reactions. Furthermore, the formation of crystalline phases occurs during the inversion of unstable maghemite (γFe_2O_3) to hematite (αFe_2O_3) [167], [170], and this new crystalline product tends to form agglomerates and causes expansion at high temperatures, resulting in strength loss.

3.3.3 *Magnesium*

Magnesium, like calcium, can form magnesium-containing silicate hydrates (M-S-H ($Mg_8Si_8O_{20}(OH)_8 \cdot (H_2O)_{12}$)) in alkali-activated materials. Its influence is generally low in fly ash-based geopolymers due to low concentrations (**Table 3.1**), but it needs to be considered when external MgO is added either directly or in the form of GGBFS. Typical GGBFS contains about 8 wt. % of magnesia and it leads to the formation of hydrotalcite-like phases ($Mg_4Al_2O_7{\cdot}10H_2O$). Concerning the effect of magnesium on the thermal stability of geopolymers, the research of Yang et al. [171] about high-magnesium nickel slag incorporation can be referred. Slag obtained from the pyrometallurgical process leads to the formation of N-A-(M)-S-H gel that mitigates the structure degradation effect after high-temperature exposure. N-A-(M)-S-H gel reduces the evaporation of free and physically bound water, additionally, the amount of water is significantly lower than that in N-A-S-H gel. The composition and structure modification by Mg cause an increase in the sintering temperature of the gel. The obtained magnesium-silicate phases improve the thermal volumetric stability as a result of reduced thermal shrinkage. Drying shrinkage was also reduced by high-magnesium nickel slag incorporation from 0.8% to 1.6% for a solution with modulus M_s=1.4. Nevertheless, as Jin et al. [172] emphasized, the impact on the material performance depends on the form in which magnesium occurs. However, there is still insufficient information related to the microstructure development of N-A-(M)-S-H gel behaviour at high temperatures. Due to this fact, this topic requires further investigation.

3.4 Zeolites

Zeolites, a new crystalline phase present in the geopolymer structure, were recognized as the secondary reaction products during the geopolymerization process in many scientific works [173]–[176]. The type and content of zeolite are conditional on the raw material composition, type of alkali activator and curing conditions [177]. From the mechanical point of view, the presence of zeolites is unfavourable for the geopolymer performance, because zeolites are crystalline aluminosilicates with a variable Si/Al ratio that form a highly porous framework structure. However, it is possible to obtain the geopolymer-supported zeolite material which possesses high compressive strength (e.g. 57 MPa [178]). This effect is driven mainly by slow zeolite nucleation that enhances the development of strong crystallization contacts between zeolites and the primary gel phases [177], [179], [180].

Thermally stable zeolites, both in-situ and ex-situ synthesized, can enhance high-temperature performance [169] and durability. Materials that include 2.5 to 10 wt.% of zeolite-like products showed good fire behaviour [111]. The thermodynamic stability of zeolites depends on the high strength of the Si-O and Al-O bonds and the stability is enhanced with a higher aluminium content [181]. The process of heating causes damage to the Si-O-Si bonds, especially in the pores and channels of zeolites. However, high-temperature exposure may also be advantageous, when Si, Al, and O atoms of the framework can approach the cations by bending and stretching. The electrostatic and van der Waals forces become more repellent as the distance

between the cations and the framework atoms decreases, partially offsetting the bonds' propensity to break under bending and stretching [182]. Another aspect is related to the volumetric stability of zeolites during heating. The thermal expansion coefficient of zeolites is reported to be remarkably negative, between $-3 \cdot 10^{-6}$ K^{-1} and $-26.1 \cdot 10^{-6}$ K^{-1} [183]. Moreover, zeolites have micropores and geopolymers are mainly mesoporous [184], indicating that combining them in a composite may favourably adjust the pore size distribution of the matrix [185]. Sturm et al. [186], by investigating a one-part geopolymer-zeolite composite, underlined its different behaviour at high temperatures. The rapid shrinkage of geopolymers without zeolites up to 400 °C is caused mainly by the evaporation of structural water (**Fig. 3.4**), while the performance of composites containing zeolite composite obviously differs. Up to 700 °C, the shrinkage is almost linear with a maximum value of ca. 2-3% in this temperature range. When compared to geopolymer without zeolites (**Fig. 3.5**), the difference in behaviour is due to the nature of water in composite, which has a more zeolitic character. Since the release of zeolitic water occurs at temperatures higher than the boiling point of water [187], less severe shrinkage is expected at the temperature range of 100-200 °C than in non-modified FA-geopolymer. However, extensive shrinkage occurring above 700 °C is caused by the structural breakdown of zeolite crystals. In the discussed case, the low- and medium-silica specimens underwent phase change, resulting in the formation of nepheline polymorphs and carnegieite-like phases [186].

3.5 Temperature-induced reactions: mechanism and products

3.5.1 *Temperature-controlled geopolymerization*

After mixing fly ash with the activator, a high rate of dissolution is observed due to the high concentration of alkali and silicates. This step is followed by the nucleation and gel growth process. Elevated temperature curing (as discussed in Section 3.2.5) increases the dissolution of aluminosilicate species and promotes the formation of geopolymeric gel due to polycondensation reactions. Once the alkalis get incorporated into the network structure the concentration of available alkaline ions decreases; thus, the reaction is slowed down. The dissolution and polycondensation still occur but at a lower rate until equilibrium is reached. After the geopolymer has set, the reaction speed is slowed down [123].

3.5.2 *High-temperature behaviour – reactions and performance*

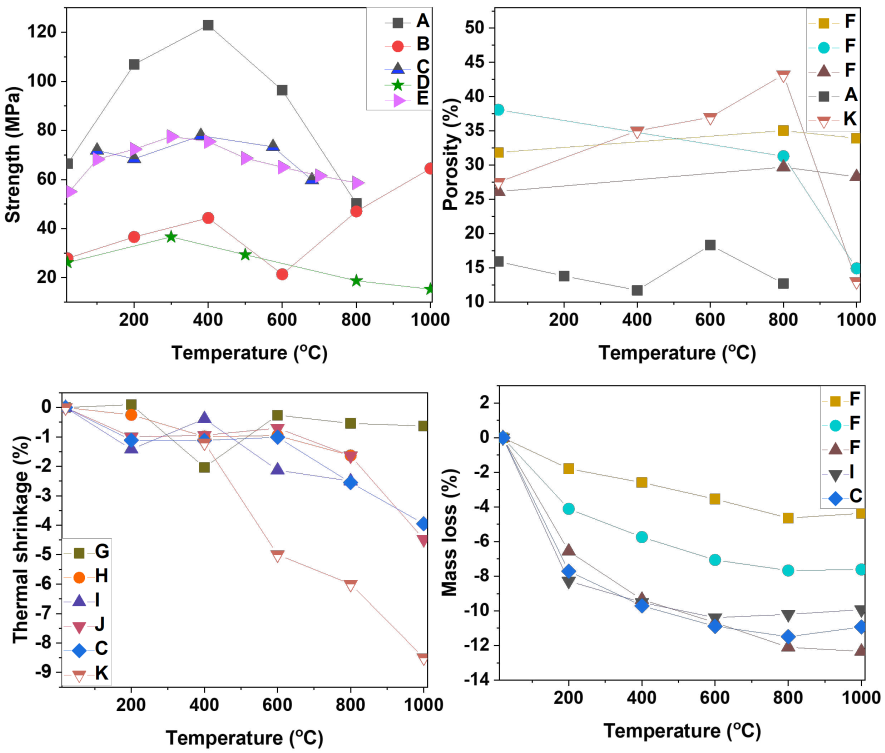

Fig. 3.4 Compressive strength, Porosity, Thermal deformation and mass loss of fly ash-based geopolymer based on literature after high-temperature exposure (cooled). A [131]; B [104]; C [87]; D [188]; E [116]; F [139]; G [113]; H [189]; I [167]; J [86], K [169].

Fig. 3.4 shows the properties of several different fly ash-based geopolymers depending on temperature. In comparison with OPC, fly ash-based geopolymers become stronger with increasing temperatures up to 400 °C, which is attributed to the densification (increased gel-to-space ratio). At temperatures above 400 °C, decomposition is detected, and the porosity starts to rise, suggesting that these phenomena are interrelated. The crucial temperature range for thermal shrinkage is placed above 600 °C due to the sintering which also affects the porosity of the composite. An increase in the porosity at high temperatures can be also observed due to thermal cracks formation. In order to make a clear view, the schematic diagram (**Fig. 3.5**) was created and divided into 5 sections where changes in the performance are visualized.

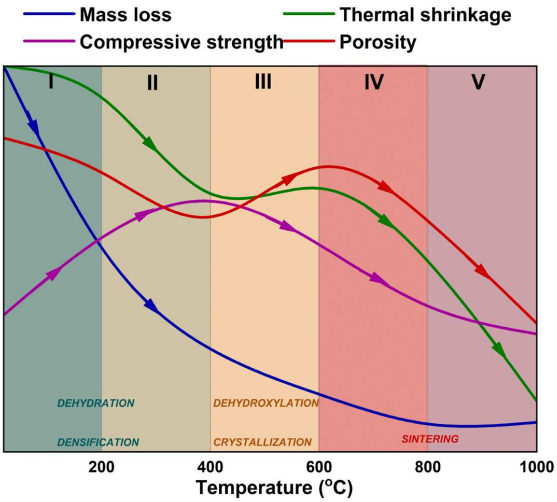

Fig. 3.5 Schematic diagram of fly ash-based geopolymer performance at high temperature. The arrows show the most significant temperature ranges for each parameter.

1st step below 200 °C: Evaporation of physically adsorbed water in the microporous structure [167]. Free water release causes mass loss and density to decrease. Mechanical performance is improved by temperature-induced densification (filling free space and voids).

2nd step 200 - 400 °C: high rate of contraction as a result of slow removal of chemically bound water, the shrinkage of the pores and partial pore collapse due to large capillary strain [167] and surface energy of the geopolymeric gel. Densification of the structure and fly ash particles fusion further contribute to strength development. As reported in [190], fly ash-based geopolymers can reach 158% of initial strength at 300 °C of the reference strength at room temperature. Moreover, porosity decreases due to the filling of voids and space by geopolymeric gel.

3rd step 400 - 600 °C: low rate of shrinkage due to slow dehydroxylation, for instance, dihydroxylation of amorphous iron hydroxides and formation of hematite [167], [191]

$$2FeOOH \rightarrow Fe_2O_3 + 2H_2O \quad (3.4)$$

4th step 600 – 800 °C: further increase of shrinkage due to the viscous sintering of the geopolymeric matrix [69]. Continuous oxidation of exposed iron oxides captured in unreacted fly ash spheres and recrystallization cause weakness of the structure. Porosity decreases due to the sintering process. Formation of macropores and thermal cracking takes place.

5th step 800 - 1000 °C: continuous viscous sintering that causes a more dramatic porosity decrease, thermal shrinkage and further homogenisation of the matrix. The process of gel crystallization takes place, causing

a strength decrease as a consequence of the nucleation of the new phases in the geopolymeric network and the formation of new pores.

3.5.3 *Thermally-induced phase formation: Feldspar and feldspathoid*

Commonly occurring felspars in geopolymers are alkali feldspars, characterized by various chemical compositions or solid solutions. Orthoclase and albite are two examples of such differentiation, since their structures may include varying amounts of sodium or potassium atoms due to their (Na and K) excessive replacement of each other. The majority of feldspars found in geopolymers are triclinic and have smaller cations (Na^+, K^+, Ca^{2+}) in the structure. Feldspars are known to undergo various order-disorder or displacive phase transitions [192]. The temperature of crystallization depends on the alkali content in the system and the composition of solid precursors [11]. During the heating of geopolymers, non-equilibrium melt will take place and new crystalline phases are formed. As the temperature rises, so does the rate of SiO_2 diffusion into the reaction zone. Subsequently, the thermal breakdown of the non-stable crystalline structure and sintering of the matrix, which is rich in SiO_2 and Al_2O_3 particles and metal ions from raw material and activator solution, begin the primary reaction pathway. Following the creation of feldspar, the system remains stable until the temperature reaches the melting point. According to Carabba et al. [108], the crystallization of thermo-stable nepheline ($(Na,K)AlSiO_4$) and plagioclase ($(Na,Ca)(Al,Si)_4O_8$) phase at 800 ^oC can positively influence the high-temperature performance by reducing the thermal conductivity of the geopolymer paste; plagioclase is a poor heat conductor [193] and the nepheline reduces the thermal diffusion of geopolymer due to the increased volume fraction [108], [194]. Furthermore, Alehyen et al. [195] stated that the presence of sodium-contained feldspar (albite) can help to maintain mechanical performance during high-temperature exposure and its formation in geopolymer matrix at 1000 ^oC was confirmed by another research [81]. Therefore, fully understanding the thermal properties of feldspars allows for further geopolymer modification, such as adding different feldspars to a fly ash-based geopolymer, which can be beneficial for high-temperature application and durability, as shown by Kumar and Mayengbam [196].

The production of feldspathoid (leucite) in potassium-rich geopolymer is most likely induced by the lack of SiO_2 in the reaction zone and by K_2O site saturation. For fly ash-based geopolymeric samples, temperatures between 550-650 ^oC are important when the change of the porosity and pore size distribution occurs. These changes are mostly related to the glass transition temperature and viscoelastic behaviour of the solids [86], [125], [188], meanwhile in sodium-activated system crystallization of the nepheline and plagioclase phases from amorphous gel takes place [108]. Thakur [197] and Duxson [145] observed that crystallization occurring during the heating improved the compressive strength of specimens. The suggested phase formation mechanism is suitable for both potassium and sodium-activated geopolymers. However, the temperature of the phase formations would be conditional on the used activator. Regarding the phase changes, it can be summarized:

- 600-900 °C: low silica crystals feldspathoid group (nepheline (Na-system), kaliophilite (K-system)).
- 900-1200 °C: high-silica feldspars (labradorite (Na-system), leucite (K-system)).
- Above 1300 °C: redistribution of phases based on thermodynamic stability (melting).

3.5.4 *The influences of the geopolymer mix composition on the onset melting temperature*

The main component in a geopolymer matrix is the geopolymeric gel together with the unreacted raw materials. The chemical composition of gels determines the melting temperature and therefore the thermal stability of the entire geopolymer at high temperatures. Thermodynamic calculations can be used to predict this behaviour, as the reactions during heating are complex and hard to determine in situ because most of the phases involved are amorphous. **Fig. 3.6** shows some calculations that were carried out with FactSage to illustrate the effect of the chemical composition on the melting temperature of a geopolymer. **Table 3.6** shows the starting composition that was used, which is based on Nazari et al. [115]. Only two oxides were varied at a time to achieve the elemental ratios shown, while the rest were kept fixed. The ratios were chosen to represent typical values found in geopolymers [21], [117], [139], [173], [198].

Table 3.6. The initial composition of the geopolymer used for the calculations shown in **Fig. 3.6** (based on Nazari et al. [115]).

Component	SiO_2	Al_2O_3	Fe_2O_3	CaO	Na_2O	K_2O
Composition (mass%)	53.93	23.04	11.25	3.87	7.28	0.63

The melting temperature is defined as the temperature when the last melt disappeared during cooling from a starting temperature of 1500 °C. It should be noted that volatiles were excluded from the calculation and that FactSage thermodynamic calculations [199] are based on phase equilibria. Geopolymer systems are not in equilibrium unless they are heated very slowly, which is usually not the case. The results in **Fig. 3.6** are therefore only meant as a qualitative overview of the influence of oxide composition on the melting temperature of geopolymers. When the influence of sodium and potassium activation is compared, it can be observed that potassium generally results in higher melting temperatures than sodium activation, which is consistent with other experimental results [125]. An interesting behaviour of the SiO_2/K_2O system is observed, namely up to a SiO_2/K_2O molar ratio of 11.6 for the same number of moles of SiO_2 (0.9 mol), the optimal value of K_2O is 0.12 mol; a further increase in K_2O causes a decrease in the initial value of the melting temperature. For the last two SiO_2/K_2O data points 13.8 and 15.9 mol, the amount of K_2O is kept (0.08 mol) and the amount of SiO_2 is increased from 0.9 to 1.23 mol, which is also disadvantageous for the initial melting temperature. In general, the type and amount of activator have the greatest influence on the resulting melting temperature and should be carefully adjusted when designing the mix. Variations in the SiO_2/CaO, SiO_2/Al_2O_3 and SiO_2/Fe_2O_3 ratios have much more limited effects.

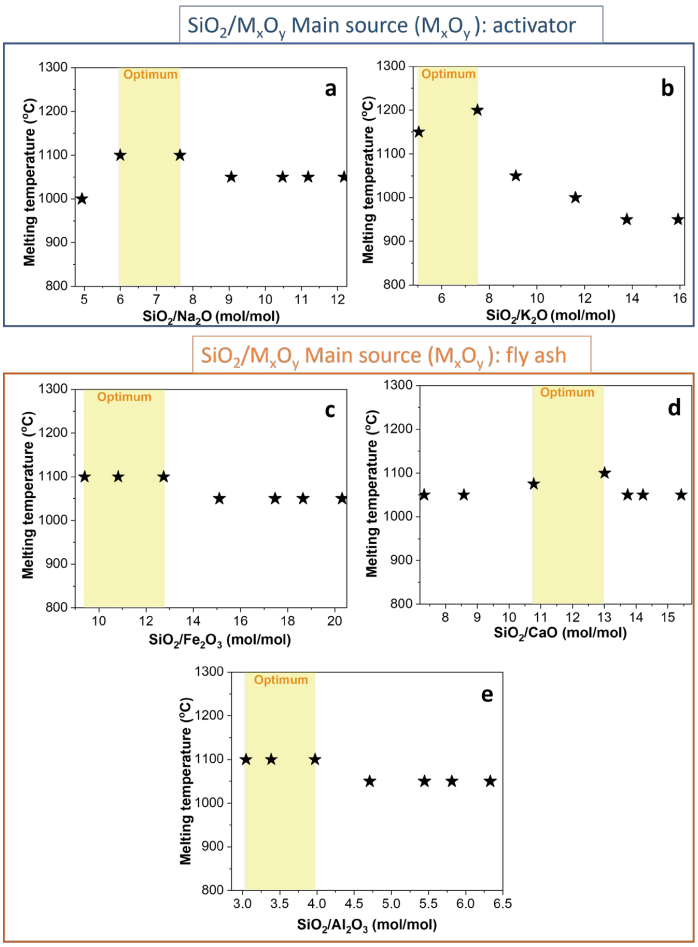

Fig. 3.6 The effect of molar ratio on the initial melting point of the geopolymer using FactSage thermodynamic calculations. Note: **Fig. 3.6b** based on K activator, while **3.6a, c, d, e** are based on Na. (Composition shown in **Table 3.5**).

3.6 Microstructure evolution under elevated temperature

3.6.1 *Pore structure*

The pore structure is formed during the gel formation and the heating leads to the evaporation of the water accumulated in the pores and channels (**Fig. 3.5**). The pores connectivity enables the water transport through the matrix and thus reduces spalling at high temperatures. In the other case, the high stress in the pore walls during the transfer of unbound water causes the pore to collapse and the development of shrinkage cracking. During the gel formation, the large pores are filled and the Si−O−Al-network (chains and branches) is formed, this porous structure has a mainly mesoporous character [123].

Wide pores that are not filled are macropores that can occur in the fly-ash-based geopolymers which are cured at medium temperature (~50 °C), while pores greater than 200 nm are found in geopolymers produced in a low-reactive system, for example, when geopolymer is cured at low (ambient) temperature. Fly ash-based geopolymers are characterized by a higher content of small-size pores when compared to metakaolin-based material (**Table 3.7**) [13].

Table 3.7. Comparison of the pore size percentage of the geopolymers based on metakaolin and fly ash at room temperature after 1 year [13].

IUPAC classification	Metakaolin geopolymer (%)	Fly ash geopolymer (%)
Micropores (<1.25 nm)	0.5	24.6
Mesopores (1.25 – 25 nm)	94.2	71.3
Macropores (25 – 5000 nm)	1.8	2.6
Air voids/cracks (5000 – 50 0000 nm)	3.5	1.5

During the formation of geopolymeric gel, the voids and space are filled, resulting in the generation of mesopores and the decrease of macropores. Pores larger than 200 nm are obtained when the curing temperature is too low (e.g. below 30 °C) or the activation is based only on hydroxide solution [123]. Sindhunata et al. [123] derived the relation between SiO_2/M_2O ratio of alkali solution and porosity. Increasing the SiO_2/M_2O ratio from 0.79 to 2.0 causes an increase in mesopore volume and surface area. More mesopores demonstrate a higher rate of geopolymer gel formation, for potassium-activated fly ash, 1.4 is considered the optimal ratio. Samples with a ratio lower than 1.4 contain larger particles of aluminosilicate gel, thus a higher porosity of the material is observed [123]. The pore volume (**Table 3.8**) and pore size distribution of geopolymers based on fly ash also differ based on the alkali cation. K-based material shows a wider range of pore diameter than the sodium counterpart due to a more significant structural disorder which results in the presence of larger silicate and aluminosilicate species in the matrix [200].

Table 3.8. Cumulative mercury intrusion volume of three types of geopolymer after various temperature exposures [83].

	Total mercury intrusion volume (ml/g)		
T (°C)	Na-based	Na/K-based	K-based
25	0.232	0.231	0.212
500	0.253	0.252	0.212
900	0.166	0.208	0.223

Sodium-based and mixed alkali systems revealed a total pore volume and pore size rise related to the development of cracks, while K-based remained stable. The cumulative number of pores found in samples was marginally decreased in the order of Na>NaK after exposure to 900 °C while cumulative pores in K-based were slightly increased. Regarding pore size, it was observed that at 900 °C both K- and Na-base geopolymer show pore size increase, mainly due to the cracks formations, however, the total pore volume is significantly reduced for sodium-based systems while it barely changes in the K-based system and those differences can be related to the sintering phase densification.

3.6.2 *Fire induced spalling*

The gel microstructure and pore morphology, as indicated in the previous subsection, affect the potential of high-temperature spalling [201], [202], which is the primary cause of thermally-induced material deterioration. Ozawa and Shaikh [75] confirmed the enhanced spalling resistance of the fly ash-based geopolymer compared to both the cement-based mix and the slag-enriched blends. When exposed to high temperatures, all of the specimens degraded severely, however, the FA-based system only showed micro-cracking. Furthermore, as compared to other mixtures, FA-based geopolymer mortar showed no abrupt increase and no following rapid fall in vapour pressure. The blends and single FA systems had maximum fracture depths of 40 mm and 0 mm, respectively. According to previous research, a blended system based on fly ash enriched with slag has a lower proportion of large and medium capillary pores in the matrix [203], which directly affects the likelihood of spalling, as this phenomenon occurs during excessive heating/contact with fire when the water vapour moves towards the cooler part of the material. Because of the lower temperature in the core sample, the water vapour condenses to create a layer, which limits further transit of water vapour, resulting in high vapour pressure. Thus, the increased water content trapped in the structure and the more packed structure indicated above are the main reasons why the blended system, despite the geopolymer structure, did not demonstrate superior spalling resistance.

Other investigations have corroborated the good stability of the FA-geopolymer structures [204], including Sarker and McBeath [205] and Colangelo et al. [206], who also validated both the structure's stability in heating cycles and the lack of spalling after exposure to a temperature around 1000 °C. As noted in the preceding section, porosity, and more specifically combined open porosity, plays a critical role in the enhanced spalling resistance of fly ash-containing composite [207] compared to OPC-based. However, there is still a lack of thorough understanding of the subject, which requires further assessment.

3.7 The evolution of physical and structural properties in terms of density

The quantitative analysis of the bulk density gives information regarding the thermally induced changes that take place during firing. The bulk density change during firing is associated with the mass loss and volumetric shrinkage of the sample as well as the porosity changes. The sample density variation is caused mainly by two effects [208]:

- Density reduction due to mass reduction (loss of free and chemically bound water and loosely packed matrix) (up to 400 °C).
- Density increase attributed to the sintering of aluminosilicates in the temperature range of 600 – 850 °C.

These density changes are also associated with changes in strength during and after contact with fire. However, when looking at the materials not in the direction of bulk density fluctuation, but the density of the skeleton, it is important to notice the positive influence of matrix densification at the temperature of 500 °C as a consequence of the continuity of geopolymerization reactions, which induces the improvement in structural strength. Then the geopolymer skeleton densification occurs as a result of the melting of the matrix, the melting process induces crack healing, which contributes to a better strength after exposure above 500 °C. Such variations can be more or less visible depending on the activator used, as shown by Lahoti et al. [83] that densification is noticeable according to the K <NaK <Na. That implies that K-geopolymer is less prone to densification than its sodium counterpart.

3.7.1 *Mass loss*

The mass loss of a geopolymer during heating causes the deterioration of the material, mitigation of the mass loss is therefore desirable. It occurs as a result of significant loss of free and pore water up to 250 °C [114], [209], and further up to 800 °C due to the polymerization reaction of free hydroxyl groups T-OH (T = Si, Al) (**eq. (3.9)**) [133]. Above 300 °C the decomposition of metal-OH groups compounds also takes place [210]:

- Acids: M-O−H+ (Si(IV), Ti(IV), Fe(III))
- Basics: M+HO− hydroxide (Na, Ca (II), K, Mg (II))
- Neutral: M-OH hydroxyl (Al (III), Mn (III))

The most crucial range regarding mass loss is between 20 and 300 °C, which is responsible for about 80% of total weight loss that is attributed to the loss of adsorbed water and water removed from geopolymeric gel [167], [191]. Further mass loss is related to the water release during gel condensation and its polymerization [69], [190]. Above 700 °C, condensation of silanol and aluminol groups on the geopolymeric gel and water removal occurs.

$$\equiv T\text{-}OH + HO\text{-}T\equiv \rightarrow \equiv T\text{-}O\text{-}T\equiv + H_2O \quad (3.5)$$

Kovárik et al. [211] showed that the temperature range from 800 to 1000 °C is characterized by a stable mass [212] and the decomposition of geopolymers at a temperature of about 1000 °C is caused mainly by

the melting process. Better results are obtained if the activator is based on potassium rather than that sodium [102]. Potassium-based geopolymer contains mainly pore water and water present as a hydration shell present in the structure cations which is released up to 200 °C [143].

3.7.2 *Thermal shrinkage*

Thermal shrinkage is a phenomenon in which a sample is subject to size/volume changes due to temperature exposure. Also, local temperature differences in the sample or differences between the temperature and the surroundings can cause cracks formation. The thermal shrinkage is determined by several parameters, for instance, raw material, type of activator and curing regime [89], [103], [114]. The crucial temperature range for thermal shrinkage is between 200 and 350 °C, in particular, due to the water evaporation and pores collapsing and above 600 °C when the sintering process occurs. Those volumetric instabilities cause cracks formation and shape deformations, the presence of which precludes the use of the material as the structural element for fire-resistance purposes. The first step in minimizing the occurrence of this negative phenomenon is to adjust the composition of the paste, both in terms of the chemical/mineralogical composition ensuring high-temperature stability (high melting temperature) as well as the pore structure allowing the non-explosive water evaporation during heating. From the chemical point of view, magnesium silicate [213] and bound calcium have the ability to reduce thermal contraction. Furthermore, the common treatment to minimize thermal contraction is the use of thermally stable fillers and the minimization of water contained in the geopolymeric structure. The selection of fillers and aggregates is driven by their properties such as moisture sorption, specific surface area, melting points and compatibility to the matrix thermal expansion coefficient. The proper selection of the filler can substantially reduce thermal shrinkage by up to 60% at 1000 °C as reported by Vickers et al. [87]. The phenomenon of shrinkage reduction by filler application can be explained by the hydrogen bond formation on the filler's surface that influences the content of water release [87] and the restraint effects.

3.8 Fillers, fibres and Aggregates

Fillers and aggregates are very important for fire performance. Their counterparts suitable for high-temperature applications should have high thermal stability themselves, higher or similar to the geopolymer paste. They may also undergo a thermal reaction that can positively influence the matrix by improving strength through sintering or bonding with the matrix. Furthermore, it is extremely important that their thermal expansion/shrinkage is similar to that of the geopolymer itself. Several examples of the use of various aggregates, along with the thermal reaction of concrete, are presented below (**Table 3.9**). It provides a picture of the negative and positive effects of aggregates and fillers at different exposure temperatures.

Table 3.9: Influences of aggregates on the high-temperature performance of geopolymer-based composites.

Ref.	Aggregates/ Fillers	Exposure Temp (°C)	Observations
[126]	Graded gravel and sand	700	The bond degradation above 300°C.
[71]	Quartz and expanded clay	750	Quartz: higher strength, poor thermal properties - high thermal expansion, greater strength loss. Expanded clay: low strength value at room temperature and low thermal expansion
[127]	Rubber tire fibres. Crushed basalt and river sand	800	The hairline cracks in rubberized geopolymer concrete above 600°C.
[128]	Sand	800	Strength determined by thermal incompatibility between matrix and aggregates.
[129]	Crushed basalt and slag aggregate	800	Used basalt or slag aggregates cause a reduction of strength after temperature exposure.
[114]	Crushed granite	1000	At 1000 °C the tension is generated by the differential expansion between the geopolymer matrix and the aggregates.
[115]	Sand and gravel	1000	Better performance of geopolymer than OPC both when air- and water-quenching applied. Cracking appearing in both OPC and geopolymer concrete at 1000 °C

3.8.1 *Fillers (maximum grain size of 125 μm) and fibres*

By applying fillers and fibres it is possible to reduce internal tension and the propagation of microcracks, which helps to improve the strength of the material. What is more, the incorporation of fibres can stabilize thermal expansion and promote the retention of mechanical strength at temperatures up to 1000 °C [107]. The key role of fillers and fibres plays to control the thermal expansion of geopolymer are their thermal expansion coefficient in the target temperature range [87]. Moreover, fillers lead to a shrinkage reduction and strength improvement during the curing of the geopolymer. The length of the fibre determines its reinforcement capacity [214]. For instance, Rahman and Radford [214] used nanofillers such as silicon carbon whiskers and stated that at high temperatures, longer nanofillers perform better than their shorter counterparts. The authors [214] suggested that the length of a nanofiller should be higher than at least twice the sum of particle size and inter-particle distance in a geopolymer network. Above 350 °C, the toughness of the geopolymer linearly depends on the length of the nanofillers. It was suggested that the sample failure is mainly caused by the tensile failure of nanofibres over the interfacial separation. Rahman and Radford [214] stated that the weak interface between filler and matrix is better for crack energy dissipation. Bernal et al. [107] proposed 15 vol. % of filler particles (milled refractory bricks average particle

size 203.2 μm) and 1.0 vol. % fibres (alumina-silica-zirconia fibre 3.5μm, length 20-35mm) to maintain the compressive strength at high temperature and reduce volumetric contraction. Furthermore, studies on the addition of 2% of nano- TiO_2 [215] have shown that the additive has favourable benefits, such as improving strength at room temperature by increasing the solubility of Si^{4+} and Al^{3+} from fly ash, as well as minimizing thermal degradation of geopolymer. Incorporation of 15 vol. % small size bricks particles, characterized by low thermal expansion, provides better performance both at room and high temperature than unreinforced or with 10 vol. % incorporation. Higher content of filler particles shows a higher degree of macrocracking in the geopolymer matrix after high-temperature exposure which influences the residual strength of the samples. Furthermore, it was observed that 10 vol. % of milled refractory bricks do not influence the ductility but increase its mechanical performance at high temperatures by creating a hurdle on the cracks propagation path [107]. Carbon and basalt fibres have also shown promising results [124]. However, carbon fibres perform better because of their greater thermal conductivity and higher heat diffusion which can facilitate heat transport. It is noteworthy that the application of wollastonite fibre ($TEC_{25\text{-}800°C} = 6.5\times 10^{-6}$ K^{-1}) in fly ash based geopolymer (10 vol. %) leads to both compressive and flexural strength improvement in comparison to the control sample, playing the role of the structure's backbone. Wollastonite reacts with the geopolymer matrix, promoting a dense microstructure and through that provides high compressive and flexural strength. The filler's surface reactions are possible due to surface defects and high surface energy. Wollastonite surface reaction influences also the performance after firing, as a result of which at 1000 °C the sample gains strength by 156% compared to the sample at room temperature. This significant change was accompanied with relatively low thermal shrinkage and mass loss [87].

3.8.2 *Aggregates (minimum grain size of 125 μm)*

The properties of geopolymers (e.g. residual compressive strength) are strongly related to the nature of the applied aggregates. The aggregates should be stable and non-reactive or alternatively, show positive reactivity at high temperatures. They need to possess a low volumetric expansion compatible with the paste and high strength at high temperatures. Rickard et al. [71] showed that quartz aggregates are not suitable for high-temperature application due to their rapid high thermal expansion at 573 °C, when the α-β phase transition takes place. Sarker [205] observed a decrease in strength of up to 65% attributed to the incompatibility between the thermal expansion between river sand aggregates (1.2-2.5%) and the geopolymer paste (1.6%).

Particles such as ceramic spheres have good thermal stability and can make geopolymeric material more stable during fire exposure. However, aggregates with a high angularity such as milled refractory brick are preferred, because they show a strong interaction between matrix and aggregate that results in good load transfer of the material [107].

Temperature-induced strength decrease in a geopolymer concrete in the temperature range between 400 °C and 600 °C is generally caused by the incompatibility of aggregates and matrix, dehydroxylation reaction

and dehydration. It can be concluded that the size, geometry and thermo-physical properties of aggregates greatly affect the concrete behaviour during the fire.

3.9 Future directions

Apart from the above-discussed topics, a number of new directions that have been developed in recent years require special consideration in the future.

Coupling effects of environmental and thermal loadings on geopolymer durability

The continuation of in-depth research on the effect of weathering on the properties of fire-resistant geopolymers on fly ash bases is highly recommended. This research allows for guiding the potential production and application of the composite (tunnel protection, building interior protection). For instance, there is no reliable information on the long-term properties of these materials, whether and how fly ash-based geopolymers lose their thermal and fire-resistant properties. Thus, more research should focus on the analysis of parameters of fire-resistant materials after longer periods than the standard 28 days. Besides, most of the current research suggests that FA-based geopolymers have favourable characteristics, although most studies focus on sole heat exposure. Thus, I believe that further research into whether material rehabilitation or replacement is necessary after long composite exposure cycles is also a worthwhile consideration. Furthermore, study of external factors, such as moisture content [207], atmospheric precipitation, or chemical attack cycles, such as hydrocarbon fluids [216] and their impact on high-temperature properties is of great need.

Blended systems

As mentioned in the introduction, this review focuses on pure fly ash-based systems, however, blended systems can offer an improvement of solely FA-based geopolymer pastes, especially considering the slow reaction rate of the latter under ambient conditions. However, when it comes to mixing, the resulting hybrid gel composition should be taken into account, as it may be helpful for room temperature performance but give poorer high-temperature performance compared to a pure FA-based mix. For instance, the thermal transition of the C-A-S-H and N-A-S-H gel mixture based on coal combustion fly ash should be thoroughly elaborated, and the resultant phases may be used to analyse their influence on geopolymer behaviour at high temperatures. Furthermore, the microstructure evolution of a geopolymeric gel supported by magnesium (N-A-M-S-H) has not been systematically presented to assess its impact on the high-temperature performance of geopolymers including Mg-rich precursor. Recent studies have shown that it is feasible to increase FA-based geopolymer high-temperature performance by blending it with other materials, such as dolomite [217] or metakaolin [122], to achieve this goal. Thus, further investigation and use of other industrial by-products and wastes in blends would be recommended, such as various slags (e.g. zinc or ferronickel slag), which can either improve material parameters at room temperature without

compromising temperature resistance or enhance high-temperature resistance by introducing new crystalline and amorphous phases.

Geopolymer foam concrete (GFC)

GFC is made by introducing large voids into geopolymer slurry by various foaming methods [79], [218], [219]. By decreasing thermo-mechanical stresses at high-temperature, they exhibit improved performance. Based on my knowledge and observations, this trend has emerged more prominently in the field of fire protection of geopolymers based on siliceous fly ash in recent years [15]. Owing to the very porous structure of GFC, they possess low thermal conductivity. Thus, thanks to the decreased heat flow, these composites can perform protective functions as passive fire protection/thermal barriers. Additional studies, such as on rheology and its alteration, will be required for the production of porous boards/panels or spray-applied materials. However, this topic suffers from lack of sufficient study of durability, lifetime assessment and research in relation to an upscaling process and application, as is the case for standard geopolymers. Additionally, more attention should be paid into the insulation capacity measurement via standard heating regimes, such as ISO 834, as well as shrinkage behaviour during thermal exposure.

Alternative applications

Fly ash geopolymers have good thermal characteristics, as demonstrated in this chapter. Besides serving as passive fire protection, the interesting use of the FA-based composite's features, such as high heat capacity and density, is creating a low-cost alternative to conventional molten salt 2-tank storage for high temperatures thermal energy storage [220]. This research presents the indirect use of superior thermal characteristics. Another alternative application is utilizing FA-based geopolymer as a superior alternative binder for OPC concrete in rigid airbase paves [216] for their good resistance to heat and chemical attack. Such considerations on the usage of fly ash-based geopolymer properties at elevated temperatures, according to the authors, may expand the field of application.

3.10 Concluding remarks

This chaper summarizes the comprehensive studies conducted during the last decades regarding siliceous fly ash geopolymers for high-temperature and fire- applications. The important factors such as phase-mineral composition, melting point, volume stability and zeolites dosage are summarized that would contribute toward the synergy of thermal stability and strength development. The following conclusions are drawn from this study:

- The phase composition of fly ash differs from other commonly used solid precursors, such as GGBFS or metakaolin by a higher crystalline content. The research on the suitability of FA-based geopolymer for high-temperature applications should be based on the reactive phases of fly ash. The phase composition of activated fly ash reveals that part of the amorphous phase and the crystalline phases behave inertly. Due to that, designing a rigorous evaluation of conducted research is difficult to perform due to discrepancies in the characteristics of fly ash and its reactivity. This analysis would influence the material on the design level by enriching the mixture with silica, alumina, and calcium source and calculating silica modulus and sufficient alkali content. Specifying the suitable SiO_2/M_2O ratio due to inconsistency in presented results is not currently possible.
- One factor affecting material stability is the initial melting temperature. Thermodynamic calculations of the sensitivity of the fly ash-based system reveal that the temperature of melting is mostly affected by the type and amount of alkali in the system. The influence of the variations of SiO_2/MO ratios (where, M = Al, Fe, Ca) on the initial melting temperature can be negligible. Nevertheless, the form (vitreous, crystalline) in which Si, Al and minor elements (Ca, Fe and Mg) occurs has a fundamental role in fly-ash reactivity and thermally induced phase transformations.
- The proposed diagram showing the behaviour of fly ash-geopolymer during temperature exposure differs from geopolymers based on other precursors and the observations can be made on the basis of this. The phenomenon of the strength increase of fly ash-based geopolymers at high temperatures in the first stage of heating (up to 400 ^{o}C) is attributed to thermally stimulated densification. Moreover, it is important to stabilize contraction and thermal cracks formation in the ranges 200-400 ^{o}C and 600-800 ^{o}C to provide high-temperature-stable fly ash geopolymer. Volumetric and strength stability at high temperatures can be improved by applying aggregates, and fibres, such as wollastonite or carbon fibres. In that case, the thermal stability and thermal expansion coefficient should be comparable with the matrix.
- Despite the range in which the zeolites improve the thermal properties of the composite (2.5 to 10 wt. %), it is believed that the influence of zeolite on fire resistivity of fly ash geopolymer cannot be unanimously evaluated due to the properties that vary among the zeolite group. The type of zeolite, the temperature of nucleation and structure breakdown determine its role as a high-temperature backbone of the composite.

- Further study is needed in several areas, including the durability and long-term performance of fly ash-based composites, as well as systematic research on the fire resistance of fly ash-based mixes with other wastes and by-products. It is also worth mentioning that changing the microstructure of foamed composites and exploiting their promising thermal response in a number of applications other than passive fire prevention may be accomplished.

CHAPTER 4 ENHANCING THE THERMAL PERFORMANCE OF SILICEOUS FLY ASH-BASED GEOPOLYMER BY SODALITE

In this chapter, the study of the effect of enriching the siliceous fly ash with synthetic sodalite phase to enhance the thermal properties of the formed geopolymer is performed. The morphological changes, compositional changes, alterations in porosity, high-temperature gel behaviour, and the effect of sodalite on the deformation of the material after thermal exposure up to 1000 °C are investigated by a multiple-analytical approach. Results indicate that adding 5 wt. % of the sodalite phase enhances considerably high-temperature performance by inducing phase formation, including anorthoclase, wollastonite, and leucite. Besides, the sodium-bearing sodalite phases lowered the glass transition temperature, owing to the formation of a mixed K-Na glass phase. Moreover, thermal shrinkage at high temperatures is substantially reduced by the addition of sodalite, suggesting its function as a skeletal reinforcement.

The results presented in this chapter are published in the following article:

K.M. Klima, K. Schollbach, H.J.H. Brouwers, and Q.L. Yu, "Enhancing the thermal performance of Class F fly ash-based geopolymer by sodalite" Constr. Build. Mater., vol. 314, p. 125574, (2022).

4.1 Introduction

The aluminosilicate gel contributes essentially towards the high-temperature performance. However, geopolymers also release physically and chemically bound water at elevated temperatures, which can destabilize the material structure and cause thermal shrinkage and crack formation [221]. Besides, the vapour pressure produced by both the physically and chemically absorbed water within the matrix will attempt to escape at elevated temperatures. Thus, the level of thermally-induced damage is highly dependent on the pore structure of the material. Moreover, the research conducted by Ozawa and Shaikh [75] showed that pure fly ash-based geopolymer did not exhibit the abrupt increase in vapour pressure reported in cement-based and fly ash/slag-based materials, causing spalling and cracks, which may also demonstrate the advantageous utilization of fly ash in the synthesis of geopolymer. Taking into account the enormous influence of the microstructure on geopolymer thermal degradation, the research focusing on the improvement of the matrix in order to address these issues is of great significance.

Currently, different approaches have been taken to minimize shrinkage by enriching geopolymer with different fillers [87], [107], [177], [214], [222], as well as, to change the microstructure by optimizing the pore structure. Direct foaming [24], [27], [219], [223] or sacrificial filler [27], [224], [225] are two methods for generating highly porous geopolymers. Those methods are effective; however, a substantial decrease in material strength is observed across the entire temperature range, as well as increased shrinkage induced by viscous flow at above 600 ^{o}C [23]. Several recent studies focus on hybrid geopolymers due to their unique room and high-temperature performance. This hybrid form of geopolymers can be produced by incorporating organic compounds, such as organic resin [226], or inorganic compounds, such as highly crystalline zeolites [177]. The latter approach provides an alternative path to alter the pore structure of geopolymer composite.

Zeolites have been reported for various applications such as the adsorption of heavy metals for disposal [177], [227], as a geopolymer precursor [228], [229] or as a filler to improve strength performance [230]. Zeolites are aluminosilicates with an open tetrahedral framework that results in considerable open micropores in the structure and allows ion exchange and reversible dehydration. These characteristics could provide geopolymers with defined pathways that make dehydration at elevated temperatures possible without causing structural damage.

Several zeolites are known to maintain their crystal structure at elevated temperatures, for example, those with a sodalite, analcime, or faujasite framework [231]. Among these zeolites, sodalite ($(M_8(AlSiO_4)_6X_2)$, where M is a cation (e.g., Na^+, Ca^{2+}) and X is an anion (e.g., Cl^-, I^-, OH^-)) is the most promising candidate, due to its high temperature [231], [232] and high alkaline stability [233]. Moreover, the synthesis proposed by Franus et al. [234] allows for the reproducible sodalite synthesis from siliceous fly ash, which can also serve as a solid precursor for geopolymers. However, there is little information about the high-temperature behaviour of the zeolites themselves. For instance, its path of transformations, the ability to undergo

amorphization, recrystallization, and dealumination during thermally-induced dehydroxylation [227], [235], and its large volumetric phase changes have not been systematically studied.

The main objective of this article is to evaluate whether ex-situ sodalite enrichment can influence the performance of fly ash-based geopolymer at high temperatures and the associated behaviour related to the phase composition and microstructure alteration. Firstly, I discussed the hydrothermal synthesis of sodalite from fly ash, as well as the identification of its structure and quantitative analysis of the resulting product using the Rietveld refinement method. The synthesized sodalite was then added to the geopolymer paste and the quantitative phase analysis was performed to investigate the evolution of the phase composition after high-temperature exposure, the stability of sodalite in the geopolymer matrix, and its influence on the formation of new phases. Besides, thermal analysis (TG-DSC) was employed to monitor the reactions as well as melting at elevated temperatures. Moreover, the effects of sodalite on the evolution of the strength, pore structure, as well as gel morphology under high-temperature conditions, were investigated. The investigation revealed that sodalite can play two roles in geopolymers, in both low (up to 600 °C) and high temperature (>600 °C) environments. At low temperatures, attributed to its porous structure, in combination with the pores in geopolymers, effective paths can be created for escaping water, which helps to reduce or avoid water vapour pressure-induced thermal spalling damages. In terms of high temperatures, above 600 °C, sodalite would act as a backbone for amorphous geopolymer gels, which would otherwise lose stability due to thermal shrinkage and melting.

4.2 Methodology

4.2.1 *Material and reagents*

In this study, siliceous fly ash siliceous is used as the solid precursor both for zeolite synthesis and geopolymer preparation. Sodium hydroxide pellets and sodium chloride solution (3 mol/l) are used (Sigma-Aldrich Chemie, analytical purity). The composition of fly ash is determined by X-ray fluorescence spectrometry (XRF; PANalytical Epsilon 3) on fused beads (**Table 4.1).**

Table 4.1. Oxide Composition of fly ash.

Component	SiO_2	Al_2O_3	Fe_2O_3	CaO	MgO	K_2O	P_2O_5	TiO_2	SO_3	SrO	Other oxides	LOI
Amount (%)	51.30	26.92	7.61	5.20	1.10	1.46	0.60	1.43	0.34	0.17	0.25	3.62

The Si/Al molar ratio based on XRF and XRD analysis reveals the potential reactivity of the analyzed system, an interesting phenomenon related to a similar value of Si/Al ratio between amorphous content

and XRF measurement. It is assumed in this study that an amorphous part is considered a reactive part of the raw material (**Table 4.2**).

Table 4.2. Fly ash reactivity based on amorphous Si/Al content.

	Moles of Si per 100 g of FA	Moles of Al per 100g of FA	Si/Al molar ratio
Total content (XRF)	0.85	0.53	1.60
Crystalline content (XRD)	0.20	0.13	1.60
Amorphous content	0.66	0.40	1.65

4.2.2 *Procedure of sodalite synthesis and its characterization*

The synthesis of sodalite is performed by mixing 60 g of fly ash with 0.8 l of sodium hydroxide solution (C_M= 5 mol/l) and 0.5 l of sodium chloride solution (C_M=3 mol/l). This methodology is based on Franus et al. [234], which, by the authors, is considered to be one of the most practical ways to obtain the sodalite phase from fly ash. The synthesis is carried out using a round bottom flask (volume 2 litres) with a reflux condenser to avoid evaporation and keep a constant liquid-to-solid ratio (L/S). The slurry is mixed constantly using a magnetic stirrer with temperature control. Heating is performed on the heating plate with an oil bath. The synthesis conditions include 22 hours of stirring at a temperature of 105 ^oC after which the solids are separated by filtration and dried at 60 ^oC for 3 days.

Table 4.3. Oxide Composition of the reaction product after solid-liquid separation.

Component	SiO_3	Al_2O_3	Na_2O	Fe_2O_3	CaO	Cl	MgO	TiO_2	SO_3	P_2O_5	K_2O	Others	LOI*
Amount (% by mass)	31.8	25.6	14.3	6.9	5.4	1.3	1.2	1.5	0.3	0.2	0.1	0.3	12.5

***LOI at 1000 ^oC**

Table 4.3 shows the composition of the oxides and a significant reduction of silica content is observed due to the partial dissolution of soluble Si in NaOH solution, which results in a lower SiO_2/Al_2O_3 ratio. Furthermore, the presence of sodium and chloride is associated with the reaction environment. **Fig 4.1** shows the reaction product where sodalite formed clusters and precipitated on the fly ash spherical particles, and the formation of these aggregates has been observed in the literature [236], [237]. To determine the crystallite size of sodalite, the TOPAS 5.2 Bruker software is used. TOPAS calculates crystallite size based on peak shape (Lorentz/Gaussian convolution-Voigt profile). The crystal is estimated to be 48 nm in size and the BET surface area is 24.15 m^2/g. The pore width with the range > 3.5 nm and the mean pore width

is established at 14.6 nm which defines sodalite-rich material as meso-macroporous with a significant contribution of pores size 4 nm as visible in **Fig. 4.2**. The broad pore size distribution between 4 and 100 nm is in agreement with previous studies regarding sodalite crystals synthesis [237]–[239].

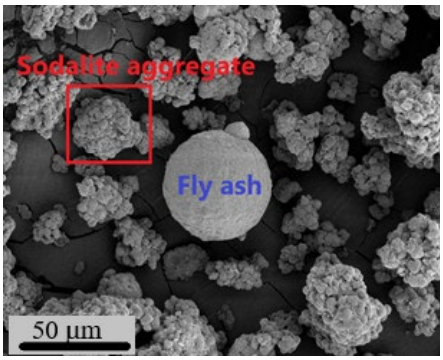

Fig. 4.1. SEM of a hydrothermal reaction product.

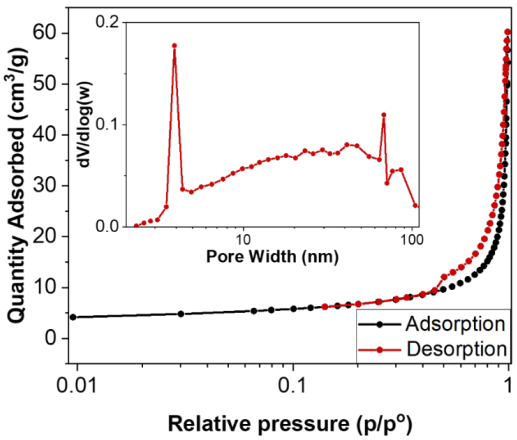

Fig. 4.2. SEM and BET analysis of sodalite crystals synthesized from fly ash.

Fig. 4.3 shows the XRD patterns of siliceous fly ash and sodalite-rich product. The phase composition of fly ash reveals a majority of amorphous phase (78.1 wt. %) and typical crystalline phases such as quartz, mullite, and iron oxides with a minor content of additional phases (see Table A.1 in Appendix A). The diffractogram of the sodalite-rich product shows that the synthesis was indeed successful and that sodalite is the main component (36.3 wt. %). Noteworthy, the ash has not undergone any additional treatments to remove impurities. The sodalite phase includes both chlorosodalite (30.5 wt. %) and hydroxysodalite (5.8 wt. %) which is a typical phenomenon of hydrothermal synthesis. It should be mentioned that the term

sodalite in this study describes a mixture of chloro- and hydroxy-sodalite. The crystal structures with ICSD numbers are listed in **Table 4.4**.

Table 4.4. List of XRD patterns used in qualitative and quantitative analysis with ICSD number.

Phase name		Formula	ICSD number
Quartz		SiO_2	27831
Mullite		$Al_{1.83}\ Si_{1.08}O_{4.85}$	43298
Magnetite		Fe_3O_4	31156
Hematite		Fe_2O_3	15840
Maghemite		γ-Fe_2O_3	87121
Sodalite group	**Sodalite**	$Na_8\ (Al_6Si_6)O_{24}Cl_2$	98807
	Hydroxysodalite	$Na_8(Si_6Al_6O_{24})(OH)_2(H_2O)_2$	412496
Leucite		$KAl_{0.96}\ Si_{2.04}O_6$	9826
Anorthoclase		$K_{0.333}Na_{0.667}\ Al\ Si_3O_8$	31180
Halite potassian		$K_{0.0997}Na_{0.9003}Cl$	28947
Anatase		TiO_2	63711
Periclase		MgO	26958
Wollastonite-1A		$CaSiO_3$	23567
Pyrrhotite		Fe_7S_8	42491
Calcite		$CaCO_3$	40107
Nepheline		$Na_3KAl_4Si_4O_{16}$	26007

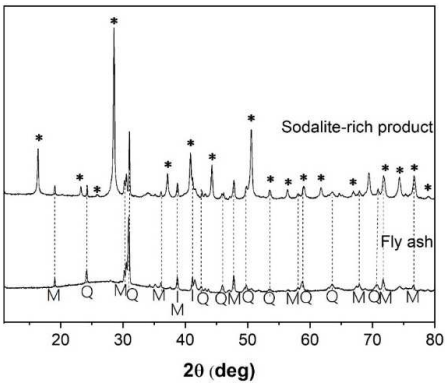

Fig. 4.3. XRD diffractograms of the fly ash and material after hydrothermal synthesis: sodalite-rich product. Legend: (* -Sodalite; Q – quartz; M – Mullite; I – Iron (III) oxide, *-Sodalite); (detailed phase analysis shown in Table A.1 (Appendix A)).

IR spectroscopy has been used to identify the structures of the synthesized sodalite. **Fig. 4.4** shows the FT-IR spectrum with the characteristic absorption bands highlighted, which allows the material to be classified as aluminosilicate sodalite based on the standard building structure units, confirming the formation of chlorosodalite [240].

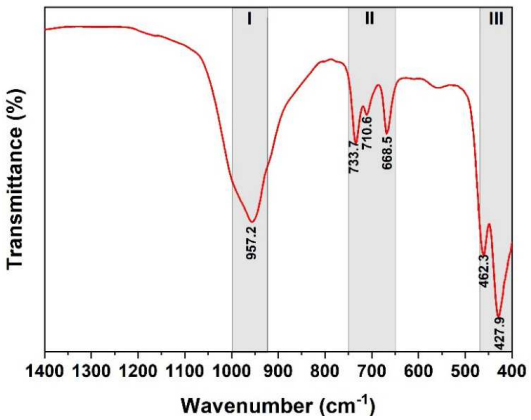

Fig. 4.4. FT-IR of sodalite-enriched material. Region I represent υ_{as} (Al-O-Si) ~ 957 cm^{-1}; region II υ_{s} (Al-O-Si) ~650-750 cm^{-1} and δ (O-T-O) ~ 460-400 cm^{-1}. (T= Si, Al).

4.2.3 *Mix design and sample preparation*

The alkaline solution for the geopolymer was prepared by mixing potassium hydroxide pellets (VWR Life Science, reagent grade) and potassium silicate solution (WHC, K_2O 8 %, SiO_2 20.8 %, 72.8 %

H_2O by mass) to obtain a SiO_2/K_2O ratio of 1.4. The selection of the silica modulus was based on previous research [123].

The sample composition is presented in **Table 4.5**. The amount of zeolite added, 3.5 wt. % and 5 wt. %, are based on work by Krivenko and Kovalchuk [111], who observed that the content of zeolite is between 2.5 and 10 wt. % performs well under high-temperature conditions. Prior to the application, the sodalite was pre-mixed with deionized water to avoid problems with workability due to the high-water adsorption [241].

Mixing the fly ash with a potassium-based activator for 3 minutes was preceded by a one-minute mixing of the dry fly ash for homogenization. Then zeolite slurry was added to the fresh paste. This blend was mixed for a further two minutes to obtain a homogeneous mixture with the evenly dispersed sodalite. The prepared pastes were cast into moulds with the dimensions of 40 mm × 40 mm × 160 mm. The samples were first sealed and cured at ambient temperature for 24 hours [242] and then cured at an elevated temperature of 60 °C for 24 hours in the climate chamber (80 % RH) to facilitate geopolymeric reaction [155]. Next, the samples were sealed in plastic foil and stored at room temperature until the testing time.

The high-temperature exposure was performed in the muffle furnace. The samples were placed in a room temperature oven and heated to the predetermined temperature in the range of 400-1000 °C at a heating rate of 10 °C/min for 1 hour. After then, the samples were taken out and cooled in air.

Table 4.5. The specific composition ratios of geopolymer pastes.

Sample	Fly ash wt. %	Sodalite-rich material		Water/Binder*	K_2O/Binder	SiO_2/K_2O
		In total	Pure sodalite			
G-FA	100	-	-	0.17	5.5	1.4
G-S1	90.4	9.6	3.5	0.23	5.5	1.4
G-S2	86.3	13.7	5.0	0.29	5.5	1.4

*includes water used for pre-treatment of sodalite-rich material

4.3 Results and discussion

4.3.1 *Phase characterization*

The phase analyses of both synthetic zeolites and geopolymer before and after high-temperature exposure were performed by XRD measurements. **Fig. 4.5** shows the diffractograms of the FA geopolymer containing 3.5 and 5.0 wt. % of sodalite in comparison with sodalite-free geopolymer before heating. All 3 samples were cured for 28 days. As can be seen, the addition of sodalite has very little influence on the crystalline structures. G-S2 paste is characterized by a lower content of the amorphous phase 76.7 wt. % compared to the reference paste G-FA 82.3 wt. %; however, the general composition stayed similar with the only exception of the presence of sodalite for samples G-S1 and G-S2.

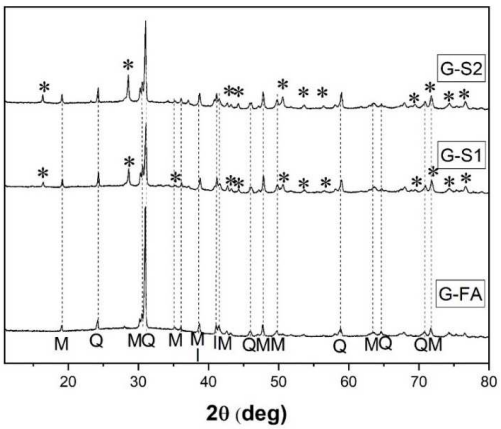

Fig. 4.5. XRD diffractograms of non-modified geopolymer paste (G-FA) and with sodalite-enrichment (G-S1 and G-S2) after 28 days, Legend: Q – quartz, M – Mullite, I – Iron (III) oxide, *-Sodalite; (detailed phase analysis shown in Appendix A).

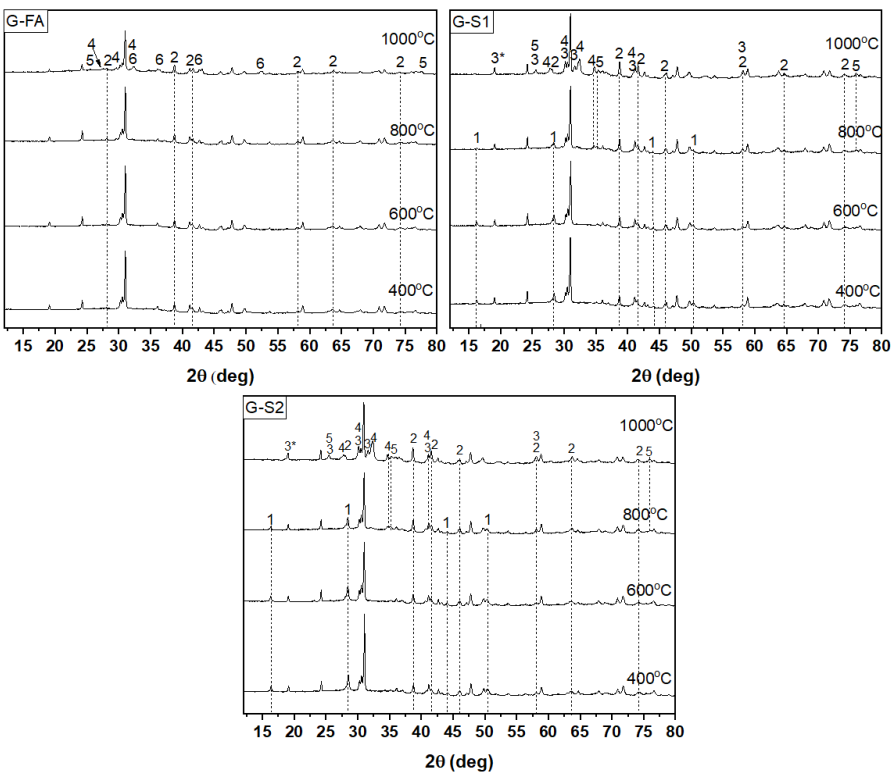

Fig. 4.6. XRD diffractograms of geopolymer pastes after high-temperature exposures with marked only new appeared phases and sodalite. Legend: 1.Sodalite; 2. Hematite; 3.Leucite; 3* overlapping peak of mullite and leucite; 4.Anorthoclase; 5.Wollastonite; 6.Nepheline.

To investigate the composition of pastes, the phases were identified and quantified by QXRD. At ambient temperature, mostly amorphous phases are formed, as a result of fly ash particle dissolution and geopolymer gel formation. It can be observed that the synthesized sodalite phase is relatively alkali-resistant [233]; the initial content of sodalite 3.5 and 5 wt. % is only slightly reduced to 2.6 and 3.9 wt. %, respectively. The maximum dissolved amount after 28 days is 25.7 %, obviously lower when compared to the results reported by Baykara et al. [243] who observed that the zeolite (mordenite) dissolution varied from 30 to 60 wt. %. The same curing method has been applied, namely curing at 60 °C for 24 hours. This confirms the relatively high stability of sodalite synthesized in this study in a high-alkaline environment.

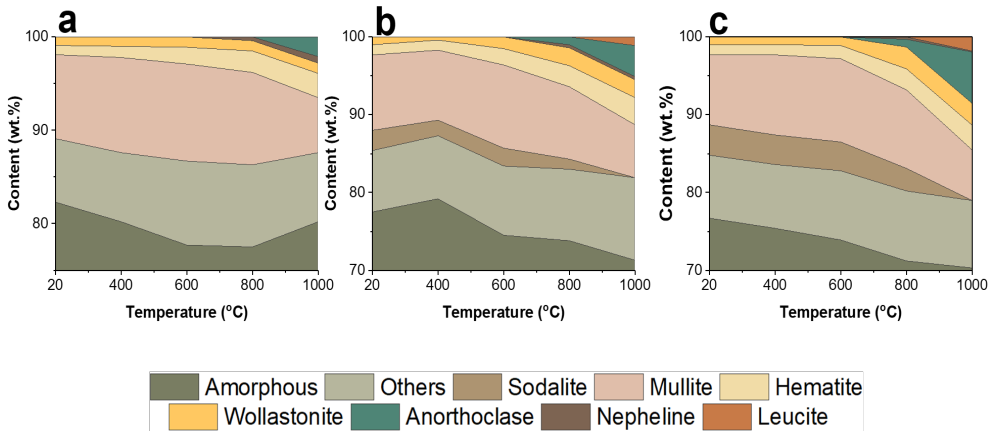

Fig. 4.7. XRD quantification of main phases in geopolymeric composites: a)G-FA; b)G-S1; c)G-S2**.**

To understand the evolution of crystalline phases, specimens of three geopolymer pastes were initially cured at 60 °C and finally stored at room temperature until the age of 28 days and heated at 400, 600, 800 and 1000 °C. **Fig. 4.6** depicts a qualitative analysis of the findings, whereas **Fig. 4.7** illustrates a quantitative explanation of the findings, including amorphous content variation. The analysis of three prepared specimens revealed that the addition of sodalite influences the phase formation in geopolymer at high-temperature. **Fig. 4.6** demonstrates the maximum temperature of the measurement in which sodalite is identified. Lastly, **Fig. 4.6** presents new thermally-induced crystalline phases, such as wollastonite, leucite, anorthoclase, nepheline or hematite. The maximum temperature where sodalite could still be identified is at 800 °C, which is similar to the findings of Bardez et al. [244]. This is due to the fact that changes in the range up to 900 °C are expected; however, the temperature measurement step (200 °C) does not allow for the precise determination of the temperature at which sodalite is no longer detected in XRD.

To better comprehend the nature of the aforementioned changes, a graphical depiction of the XRD Rietveld refinement was created **(Fig. 4.7).** In both G-S1 (**Fig. 4.7b**) and G-S2 (**Fig. 4.7c**), the amount of crystalline phase did increase, such as hematite, anorthoclase and leucite with the rise of the temperature, while G-FA undergoes amorphization at above 800 °C which can be related to the melting process that

lowers the stability of the matrix. In the sodalite-free sample, a decrease in the amorphous phase up to 800 °C (77.6 wt. % vs. 82.3 wt. %) is observed due to the crystallization of hematite and nepheline. At temperatures above 900 °C the amorphous content increases again (80.4 wt. %) and the mullite content decreases. The reduction of mullite content can be related to the reaction of mullite to form anorthoclase. In the sodalite samples, on the other hand, a continuous decrease in the amorphous phase is observed due to the crystallisation of wollastonite, anorthoclase, nepheline and leucite.

The crystalline phases that have been identified in the sodalite-enriched samples are wollastonite and two feldspars anorthoclase and leucite. During the hydrothermal reaction of fly ash with NaOH, calcium appears to have been released and enriched the binder phase [245]. No new calcium-bearing phases are identified in geopolymers but calcium-enriched gel in the presence of chlorides does enhance the wollastonite formation [246]. Wollastonite can be originally identified (<1.0 wt. %) in fly ash [247] and the analysed fly ash contains 0.6 wt. % of wollastonite phase. However, in the geopolymer composites, G-S1 and G-S2 wollastonite has formed after thermal exposure at above 600 °C, 2.3 wt. % and 2.8 wt. % respectively, which can be explained by the presence of chloride from sodalite decomposition that can influence wollastonite formation by lowering its crystallization temperature from 900 to 700 °C [245], [247]. Chloride ions can influence the interaction between silica and calcium present in the matrix and direct the formation of wollastonite. In this temperature range, the amorphous calcium silicates undergo melting, which makes the matrix more homogenous, thus the calcium ions are well-distributed in the matrix and could react with chloride providing the crystallization of wollastonite [248]. Along with the increase in the amount of sodalite from 3.5 to 5 wt. % in the initial composition, an increase in the amount of wollastonite at 800 °C, 2.3 and 2.8 wt. %, respectively is observed, while the reference shows the same wollastonite content (1.0 wt. %).

In the geopolymer sample of G-S1 and G-S2, the formation of anorthoclase ($(Na,K)AlSi_3O_8$) and a minor amount of leucite ($KAlSi_2O_6$) are driven by the sodalite decomposition. Anorthoclase is a potassium- and sodium-bearing feldspar whose presence is linked to both the potassium-based activator and the sodium-rich product of the hydrothermal reaction. Mouiya et al. [249] reported that potassium-containing minerals such as anorthoclase are easily embedded in molten silicate formed in the temperature range of 700-800 °C via dehydration and recrystallization. The quantified amount can be correlated to the initial amount of sodalite in the specimens. Leucite, the additional felspar, is formed as a result of sodalite decomposition by the reaction of K_2O with free SiO_2 coming from the sodalite. The amount of free silica and exposure temperature direct the content of leucite [250].

Furthermore, a small amount of halite is also formed due to the dissolution of sodalite and the presence of potassium ions in the glass phase. An interesting phenomenon is related to nepheline crystallization at above 800 °C. Based on previous research [251], [252], it is expected that the amount of nepheline would increase as a result of the sodalite decomposition, however, in this study sodalite promotes the formation of two thermally stable phases such as anorthoclase (6.6 wt. % G-S2) and wollastonite (2.8 wt. % G-S2). Moreover, the highest amount of nepheline at 1000 °C is detected in the reference (0.7 wt. %) while G-S1

and G-S2 possess 0.4 wt. % and 0.13 wt. % respectively. Noteworthy is the formation of the nepheline phase which is associated with a volume expansion as shown by Stjernberg et al. particularly in the range 650 to 750 °C, which can cause volumetric instability and formation of cracks[253], [254]. Thus, it can be assumed that sodalite improved the thermal stability of the paste by promoting the formation of more stable phases. Nepheline formation may result from the disintegration of mullite above 600 °C from 10.4 wt. % to 5.9 wt. % for the reference material, due to the reaction of this phase with the surrounding matrix [119]. In every sample irrespective of the sodalite enrichment the amount of quartz and anatase remained stable. Moreover, the increased content of iron oxide is explained by the dehydroxylation of amorphous iron oxides and the formation of hematite initiated above 400 °C [167], [191].

4.3.2 *Thermogravimetric analyses (TG-DSC)*

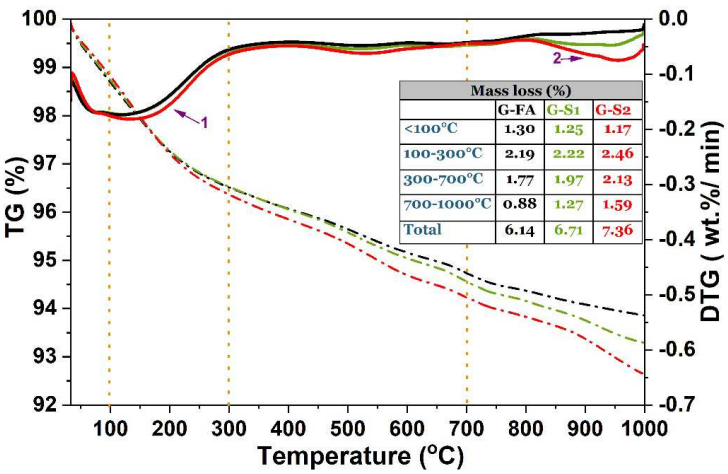

Fig. 4.8. TG curves of the composites after 28 days of curing. The table presents the mass loss in the specific temperature range (note: curve G-S1 and G-S2 overlaps) 1) *loss of chemically bound water* [255]*; 2) slow halite and chlorine decomposition and dehydroxylation associated with carbonate release from sodalite-rich material.*

The TG results (**Fig. 4.8**) shows that the geopolymer has a continuous mass loss at elevated temperature, and the cumulative mass loss at 1000 °C of G-FA, G-S1, and G-S2 is 6.14, 6.71, and 7.36 %, respectively. Each sample shows similar mass loss at temperatures ranging from 40 °C to 200 °C due to the loss of the water contained in the gel structure. Moreover, the initial dehydration of hydrated aluminosilicate species and polycondensation occurs above 100 °C [69]. Above 300 °C, the mass loss is attributed to the release of chemically bound water and the decomposition of metal-OH groups from sodalite [210]. The increase of the gradual weight loss between 300 °C and 700 °C (**Fig. 4.8**) is related to sodalite enrichment and is associated with dehydroxylation of the chemically bound group of silicon-hydroxyl and polymerization [256]. For sodalite-enriched pastes, the shift of the weight loss to a higher temperature range

(300-1000 °C) is associated with the dehydration of the sodalite structure and the transformation of sodalite to other aluminosilicates. Note that, hydrothermally synthesized chlorosodalite contains a small amount of hydroxysodalite, as indicated in XRD analysis, and this phase undergoes multiple-step dehydration and dehydroxylation [186]. Hydroxysodalite phase increases the mass loss up to 700 °C and increases with the increased sodalite addition. Above 700 °C the mass loss can be assigned to further dehydroxylation of sodalite structure and chlorine volatiles until complete decomposition of this crystalline phase.

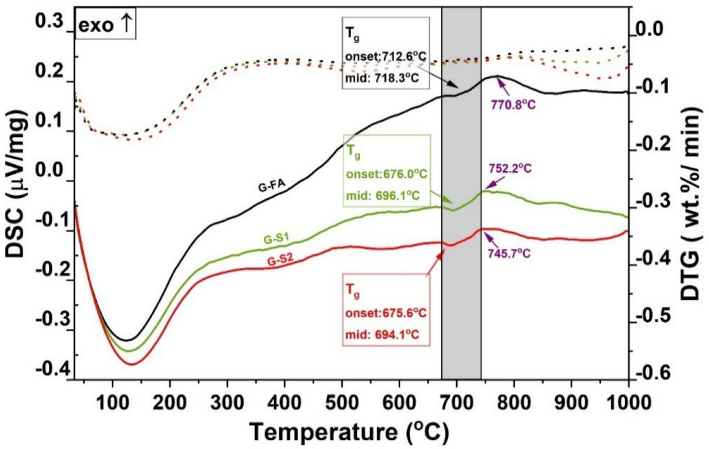

Fig. 4.9. DSC curves and glass transition determination of the samples combined with DTG curves (dotted-line). Grey area indicated the endothermic peak detected in each material.

DSC (**Fig. 4.9**) is applied to present the reactions that took place during the tested temperature range. The DSC curve provided information about the simultaneous (re)-crystallization and amorphization of the structures. The general observation of the DSC irrespective of the sodalite addition revealed a significant peak at around 150 °C, which is attributed to the gel decomposition. The observed peak shift between samples indicates the differences between water molecules binding with the matrix structures.

In the hump of glass transition (**Fig. 4.9** grey area), the peak for G-S1 and G-S2 is shifted slightly towards lower temperature which suggests the decomposition of sodalite that affects the glass transition temperature. As a decomposition product, the amorphous phase is enriched by chlorine and sodium present in the sodalite structure. The sodium oxide which is incorporated into the glass phase lowers the temperature of softening and further influences the formation of anorthoclase and the chloride determines wollastonite and halite formation, as discussed in the XRD analysis. It can be concluded that sodalite embedded in the matrix influences the glass composition and its melting temperature, mostly by the enriching system with sodium ions.

4.3.3 *Scanning electron microscopy and optical microscope*

The microscopic observations were carried out to further observe the effect of sodalite addition on the geopolymer composite. At room temperature, the geopolymer matrix appears similar; the additional spherical particles in **Fig. 4.10** G-S2 may be sourced from the post-reaction material from the hydrothermal process, as seen in **Fig. 4.1** The agglomerates formed by sodalite crystals (also see **Fig. 4.1**) would influence the composite porosity.

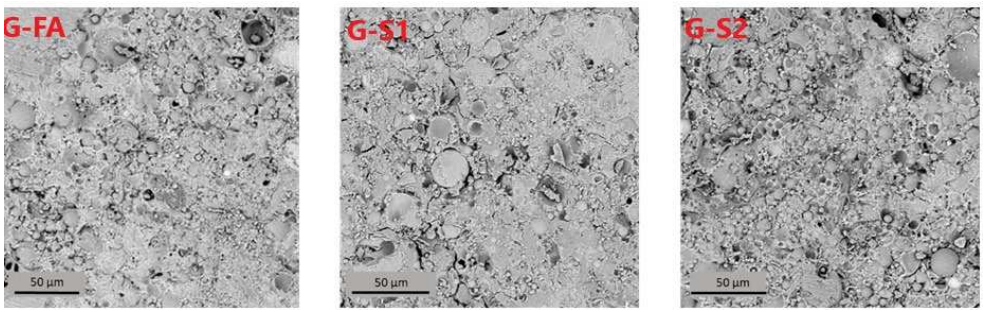

Fig. 4.10. SEM micrographs of geopolymer pastes at room temperature.

Further thermally-induced densification at 400 °C causes the phenomenon of decomposed sodalite embedding in a geopolymer gel, which could positively affect the homogenization of the matrix and increase the strength in this temperature range. [78], [128]. This possible phenomenon of coating the sodalite surface with geopolymer might additionally limit the access to the pores that distinguished the sodalite-enriched material. Furthermore, the stability of sodalite crystals in the matrix after high-temperature exposure at 800 °C is confirmed (**Fig. 4.11**). As mentioned in the various analyses, temperature above 700 °C defines the region of initiation of sodalite decomposition, but its durability can be defined in the range of 800-900 °C, allowing crystallites to be detected in both SEM and XRD analyses.

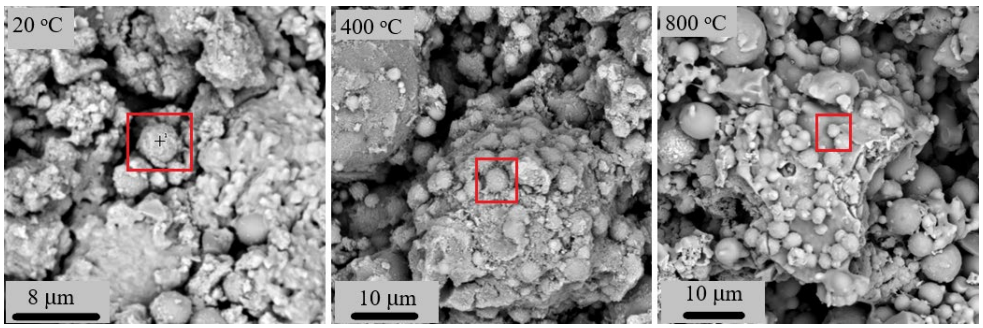

Fig. 4.11. Sample G-S2 at various temperatures. The red rectangle was marked with sodalite crystals (identification confirmed by EDS analysis).

After exposure to 1000 °C (**Fig. 4.12**), the geopolymer gel shows clear pores and channels and becomes more homogeneous and smoother due to viscous sintering. G-FA possesses a less porous structure with a predominance of closed pores, while in G-S1 and G-S2 it is possible to identify pores, voids, and channels. Furthermore, a clear difference in the colour of the reference sample's outer and inner parts is observed by the optical microscope. The observed reduced porosity of G-FA compared to G-S1 and G-S2, or the presence of closed pores, indicates intense melting and loss of material stability in the direction from the surface to the central part of the sample, resulting in limited oxidation processes in its interior and the characteristic blueish area suggested a reduction environment.

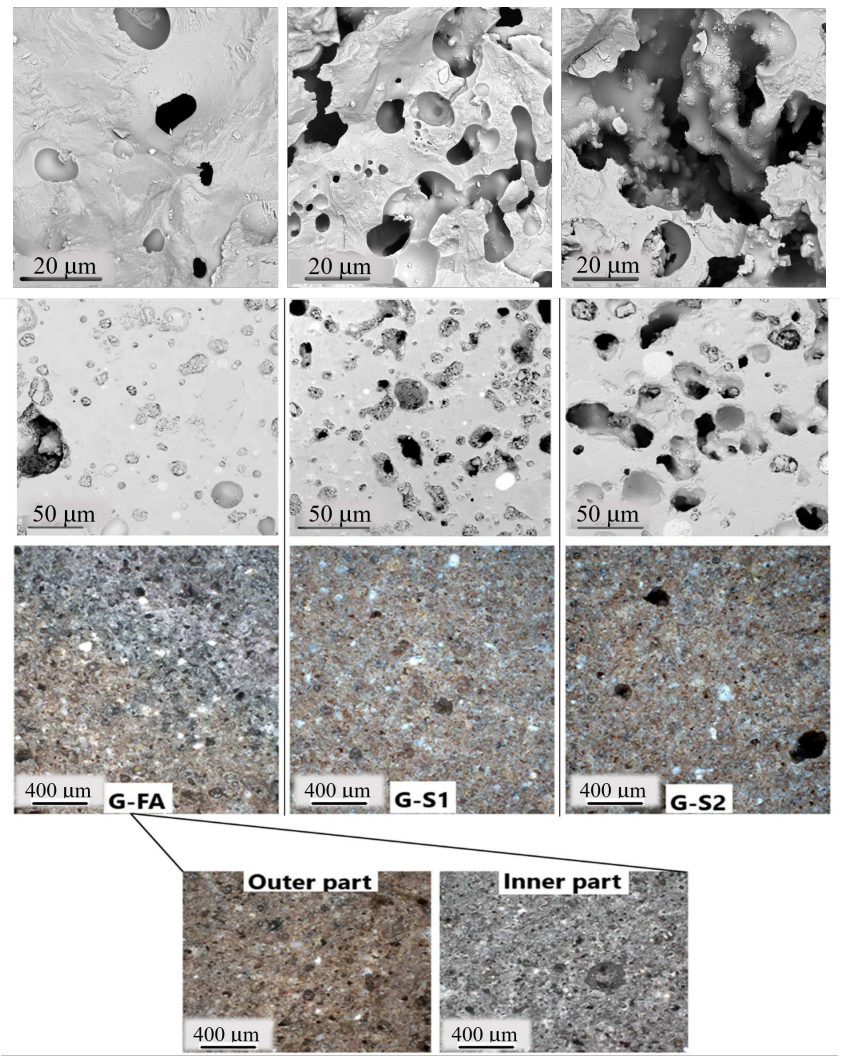

Fig. 4.12. SEM micrographs and optical microscope pictures of geopolymer pastes after exposure to 1000 °C.

4.3.4 *Mercury intrusion porosimetry*

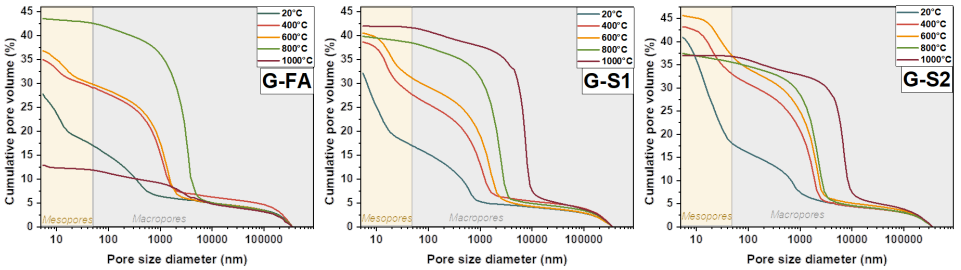

Fig. 4.13. Cumulative pore volume derived from Mercury Intrusion Porosimetry of the pastes after high temperature exposure.

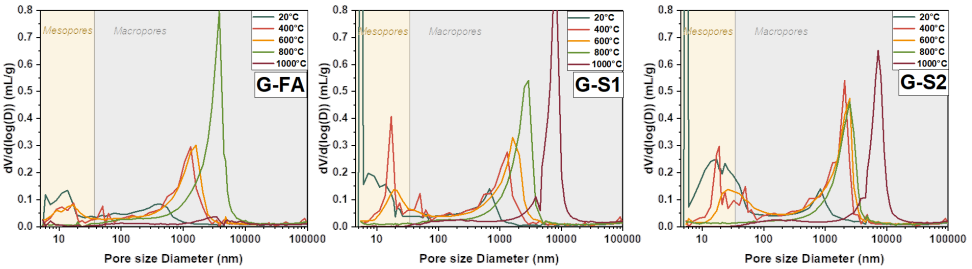

Fig. 4.14. Differential pore size distribution in the pastes after high-temperature exposure.

The cumulative porosity and pore size distribution results are presented in **Figs. 4.13** and **4.14**, respectively. The cumulative porosity confirms the hypothesis that the addition of sodalite leads to an increase in pore volume after high-temperature, which is associated with the meso-macroporous sodalite, as revealed by BET (**Fig. 4.2**), as well as the formation of sodalite agglomerates (**Fig. 4.11**) which additionally influences the pore volume [257]. In both samples G-S1 and G-S2 at 20 °C, the presence of sodalite is confirmed via an obvious peak shift towards a smaller pore size (~5.5 nm), which identifies mesopores coming from sodalite-rich material (**Fig. s4.2**). Besides, the higher peak for G-S2 agrees with the higher amount of sodalite addition. Furthermore, at 400 °C the peak around 19 nm is observed for samples G-S1 and G-S2 that was not observed in G-FA, which is in agreement with sodalite crystals with a dominant spectrum of porosity between 12 and 22 nm [234]. Moreover, the increase in pore throat size after exposure to 400 °C may be due to overlapping processes; the sodium-enriched system has a smaller pore size than the pure potassium-based system [83]. Besides, up to the temperature of 400 °C, fly ash particles react in a series of reactions, sticking to the sodalite crystals, and embedding them in an increasingly homogeneous geopolymer structure, as observed in SEM analysis. Simultaneously, an increase in the cumulative volume is observed which resulted from the formation of connections between pores and opening closed pores [83]. The pore size is characterized by a wider range of pores that corresponds to the potassium-based activation [139], whereas mesoporosity is primarily due to the voids in the geopolymeric

gel structure. Furthermore, the pore size (above 50 nm) could be related to the gaps between unreacted fly ash particles, regardless of the sample type. Moreover, a similar evolution of pore size distribution is also observed up to 600 °C due to the thermally-influenced processes, where the cumulative pore volume and the pore size increase via small size cracks, the opening of closed pores, improving the interconnectivity and pore throat [258]. Irrespective of the sodalite addition, more prominent changes at 800 °C are observed when the peak in a small region is flattened and the curve shifts towards large pores, which are the result of crystallization and thermally induced macropores formation. However, it should be emphasized that differences exist in the porous structure, despite the above-mentioned similarities. For sodalite-enriched pastes, the phase composition at high temperatures, and more specifically, the formation of anorthoclase, nepheline, and leucite might partially influence the reduction of the total porosity and the reduction of pore size. An additional role is played by the melting phenomenon, with the initiations determined by the DSC analysis. Although the sodalite-containing material is characterized by a lower glass transition temperature, which is also reflected in the reduced cumulative pore volume G-S2 and less significantly in G-S1 (**Fig. 4.13**), the sodalite-enhanced system does not suffer so much porosity degradation in the 800-1000 °C range. At 1000 °C, a distinct direction of microstructure transition between reference and G-S2 is visible.

Furthermore, between 800 and 1000 °C, sodalite-enriched specimens show continuous pore size increase with an insignificant change in small size pores up to 5 μm. Apart from that, the macropores peak is shifted towards larger pore size due to the conjoining of existing big-size pores. Above 800 °C, G-FA starts to lose thermal stability, which becomes the most prominent after exposure to 1000 °C. Dramatical structure densification at above 800 °C is due to the liquid formation, which indicates the loss of thermal stability of the geopolymer (porosity reduced from 44 to 13 %) [139], which is in agreement with the XRD quantification analysis, SEM, and optical microscope observations. This significant porosity decrease is not observed in sodalite-enriched samples, which supported the finding of improved performance of sodalite-geopolymer composite at high temperatures.

4.3.5 *Mechanical performance and volumetric deformation*

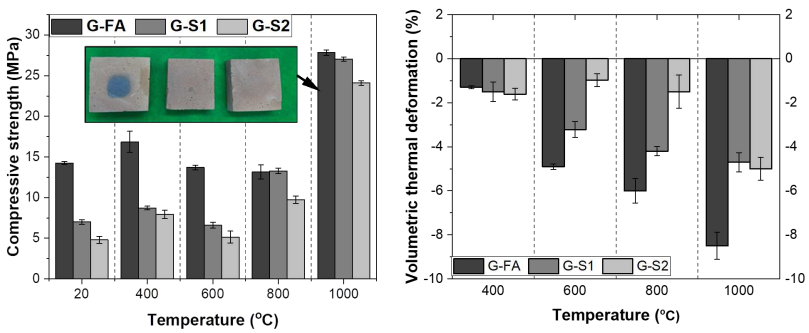

Fig. 4.15. Compressive strength evolution and volumetric deformation of the geopolymer specimens at different temperatures.

The compressive strength and volumetric change of the samples after different temperature exposures are shown in **Fig. 4.15**. It can be seen that the reference sample shows higher compressive strength as a result of lower porosity compared to sodalite-containing samples (**Fig. 4.13).** However, higher volumetric stability is shown in samples G-S1 and G-S2 thanks to the sodalite enrichment. In the temperature range from 20 to 600 °C, all the analyzed samples show a similar trend. The noticeable increase in strength after exposure to 400 °C is attributed to the matrix densification, which also results in comparable volumetric deformation because of condensation reactions of the hydroxyl groups [258], [259]. At 600 °C, strength reduction is observed as a result of two simultaneously coexisting phenomena, namely porosity increase and crystallization, which is in favour of the reduction of the amorphous part of the gel (**Fig. 4.7**). At 800 °C, a further strength increase is seen in G-S1 and G-S2, which is driven by the sodalite decomposition, pore volume maintained (G-S1) or decreased (G-S2), and formation of new crystalline products, such as anorthoclase and wollastonite. At the same time, as noted in the MIP and DSC analyses, a temperature of around 700 °C is the point at which glass transition is more significant in modified samples. The glass formation and cooling result in a porosity decrease at 800 °C and a strength increase by particle-binding effect. A minor influence can be also related to the formation of anorthoclase, whose small particles filled the small pores improving mechanical performance and wollastonite formation, which is confirmed as the promoter of mechanical strength by improving the tensile properties [260]. All geopolymer specimens show further shrinkage evolution due to the structure densification [89], [191], which however is more prominent in the non-enriched specimen. The considerable rise in shrinkage observed between 800 and 1000 °C in G-FA is due to the continued viscous sintering, which causes a more dramatic porosity decrease, thermal shrinkage, but also continuous homogenization of the matrix. Furthermore, G-S1 and G-S2 modified samples have a higher proportion of crystalline phases (**Fig. 4.7a**), which, as observed by Vickers et al. [86], act as 'intrinsic fillers' and may contribute to shrinkage reduction. At 1000 °C, G-FA has a large proportion of amorphous phase, making it more susceptible to melting events. Lin et al. [261] observed a dramatic shrinkage of a highly amorphous metakaolin-based geopolymer at elevated temperatures, implying that an amorphous geopolymer structure reinforced by thermally resistant crystals is beneficial for the volumetric thermal stability of the composite.

Viscous sintering at high temperatures affected the macropores formation, volumetric shrinkage, and strength increase. At 400 °C, regardless of the sodalite addition, all specimens are characterized by volumetric shrinkage in the range of 1.5 % that results from the degradation of the geopolymer gel. Afterwards, the shrinkage of G-FA in the range of 400 to 1000 °C tends to be linear. One of the reasons for this phenomenon is the melting process, which is also responsible for a significant decrease in porosity at 1000 °C. The overall sodalite-enriched materials show less shrinkage over the entire temperature range. However, attention should be paid to changes in individual temperature ranges and it can be noted that sodalite plays a special role up to a temperature of 800 °C, which is associated with its decomposition. Although the temperature at which the decomposition started is about 700 °C, taking into account the quantitative distribution, it is observed that between 600 and 800 °C the percentage of sodalite reduction

(0.8 wt. % for G-S2) is lower than that between 800 and 1000 °C (2.9 wt. % for G-S2). It has been therefore also possible to deduce a significant decrease in the volume of G-S2 between 800 and 1000 °C. This contraction is also affected by the change in the composition of the vitreous phase and its sodium enrichment. The noticeable lower shrinkage is due to the different compositions of the crystalline phases, the crystallization of which may reduce the negative effects of the melting. The lower degree of degradation may also confirm the different porosity of the composite after exposure to 1000 °C and, more precisely, the less noticeable reduction of the cumulative pore volume of G-S1 and G-S2 compared to G-FA.

In addition, after the compressive strength measurement, the resulting material residues were polished to show differences in the appearance of the cross-section (**Fig. 4.15**). It should be noted that the size of the polished specimens does not reflect the actual size of the composite due to the destructive nature of the strength test. The cross-sections show the difference in the colour of the central part of the G-FA, while the core parts of the G-S1, G-S2, and outer part of G-FA have a characteristic brown-orange colour. This colour is due to the presence of iron oxide that undergoes oxidation to hematite. The inner part of G-FA in black and grey indicates the lack of oxygen and the reduced conditions inside the material. As a result of the melting (**Fig.4.14**), the collapsing pores and the connections between them prevented air from entering the sample and causes thermal-induced transformations in the oxygen-deficient environment. Therefore, this observation confirms that enrichment with sodalite has a beneficial effect on the reduction of volumetric shrinkage, especially up to the temperature of 800 °C.

4.4 Conclusions

The present study investigates enriching geopolymer matrix with thermally- and alkaline- stable crystalline particles to improve its high-temperature properties. This research leads to a better understanding of the thermal behaviour of ex-situ synthesized zeolite in geopolymer matrix, its influence on phase composition, porosity evolution and volumetric changes. Based on the obtained results, the main conclusions are drawn as follows:

- Sodalite addition influences the gel composition and thus the high-temperature stability. Between the reference material and the sample with 5 % of sodalite addition, the temperature of the glass transition was lowered from 718.3 to 694.1 °C. This phenomenon was affected by the alkali ions which primarily define the liquefaction point, namely the melting point of potassium aluminosilicate glass is greater than that of potassium-sodium mixed glass.

- After being exposed to high temperatures, the sodalite-enriched paste's mineralogical phase composition differs from that of the plain geopolymer. Wollastonite, stable thermal anorthoclase and a small amount of leucite are all clearly seen to form, while nepheline is also seen to form in unmodified geopolymers. These differences are more significant in specimens with 5 wt. % sodalite

addition and are attributed to the slow disintegration of sodalite at 800 °C and the greater decomposition observed between 800 and 1000 °C.

- The mesoporous nature of the raw material rich in sodalite contributes to the increased content of mesopores of geopolymer paste which reduces the deteriorating structural impact of water evaporation that passes through the material during heating.

- The synthesized sodalite-enriched material plays the role of a skeleton that facilitates the transport of evaporable water and significantly counteracts the harmful effects of volumetric deterioration by up to 800 °C (e.g. from 6 wt. % for non-modified to 1.5 wt. % for specimen enriched by 5 wt. % of sodalite).

- The different strength evolution of geopolymer without and with sodalite results from a different path of porosity evolution between 400 and 800 °C and different phase compositions at high temperatures. The formation of new high-temperature stable crystalline from the sodalite-enriched matrix, such as anorthoclase and wollastonite which are embedded in the matrix at elevated temperatures positively influences the strength performance of cooled geopolymer after temperature exposure.

CHAPTER 5 SYNERGISTIC EFFECT OF SURFACTANTS IN POROUS GEOPOLYMER: TAILORING PORE SIZE AND PORE CONNECTIVITY

With the growing interest in foamed geopolymer manufacture, there is an increasing demand for tailoring these composites' pore structures. The binary system of two surfactants offers a possibility for enhancing foam formation efficiency and stability in geopolymer paste, however, their effects are not well understood. The influence of binary system blends on pore formation, size, and distribution in fly ash-based geopolymer matrix is investigated and their synergistic effects are evaluated. The results show that combining a nonionic surfactant with anionic Sodium Dodecyl Sulphate (SDS) increases open porosity, whereas cationic Cetyltrimethylammonium Bromide (CTAB) promotes the development of closed pores, improving thermal insulating, hygrothermal and mechanical performance. Moreover, a mechanism to describe the creation of pores in the presence of mixed micelles is proposed, as well as the benefit of employing mixed surfactant systems in customizing porous composites.

The results presented in this chapter are published in the following article:

K.M. Klima, C.H.A. Koh, H.J.H. Brouwers, and Q.L. Yu, "Synergistic effect of surfactants in porous geopolymer: Tailoring pore size and pore connectivity" Cem. Concr. Compos., vol. 134, p. 104774, (2022).

5.1 Introduction

Porosity is a significant parameter of materials characterized by low density and low thermal conductivity which are crucial for designing, for instance, protective materials for high-temperature applications. However, the distribution of pore size and the character of pores, i.e. the proportion of open pores, establish a material's suitability for particular applications. For fire-resistant composites exposed to high temperatures, it is advantageous to have an open pore structure that facilitates the transport of water vapour through the material, which significantly minimizes the risk of moisture clog, cracks formation, propagation and spalling [12]. Materials for thermal insulation applications have different requirements regarding the pore structure. The pores are desirably closed because increasing the open porosity increases gas permeability, including air, which is a heat transfer medium. Porous sound absorbents, as indicated by Cao et al. [262], should consist of a significant number of pores (such as cavities, channels, or interstices) with the proper size that are interconnected with each other to allow the sound wave to propagate inside the material. Furthermore, water has a great effect on thermo-physical properties, the amount of adsorbed water affects the deterioration process of the material and diminishes its superior insulating effectiveness. In light of the foregoing, it is clear that porous materials are used in a variety of industries, but their morphology has a considerable impact on their performance. Thus pore size and connectivity tailoring are of great importance for different applications.

Among various methods, the application of chemical foaming agents is widely utilized, however, controlling the pore morphology is critical when employing a chemical foaming method. As the previous research indicates, when utilizing foaming agents such as Al, Si, or H_2O_2, pore controlling and tailoring is difficult, both in terms of size and pore cavities formation [263]–[265]. It has been observed that adding surfactants can positively influence the performance of the created foam. Several types of surfactants have been applied in geopolymers, such as Tween 80 [263], Sika Lightcrete 02 [264], Sodium Dodecyl Sulfate (SDS) [266], Triton X-100 [267], Sodium Lauryl Sulphate (SLS) [268] or proteins [30], [269]. It is proven that by adding foaming agents and stabilizing agents to the geopolymer slurry, the porosity in the hardened geopolymer can be increased [265], [270], [271]. Further, it is revealed that by varying the surfactant and foaming agent concentration, the pore size and size distribution can be adjusted [263]. The samples foamed with hydrogen peroxide and surfactant showed more uniformity in the pore size distribution compared to the samples foamed by sole H_2O_2. An additional benefit is the optimized control of porosity when combining H_2O_2 and surfactant [264].

In terms of density reduction, SLS foam has been considered more cost-effective than protein-based foams [268]. Two non-ionic surfactants that are widely applied in geopolymers are Triton X-100 and Tween 80. Strozi Cilla et al. [267] discovered that an increase in the amount of surfactant (from 2 wt.% to 4 wt.%) to a metakaolin-based geopolymer leads to an increase in open porosity for both Tween 80 and Triton X-100. Tween 80 forms smaller pores in the geopolymer than Triton X-100, thus contributing to a higher compressive strength of the material. Bai et al. [263] researched the effect of H_2O_2 and Tween 80 on the

porosity and compressive strength of geopolymer foam. The positive interaction between H_2O_2 and Tween 80 was observed, which led to highly interconnected pores, good mechanical properties, low density and low thermal conductivity [263]. However, contradicting observations were noted by Petlitckaia and Poulesquen [272], who reported that both Triton X-100 and Tween 80 create heterogeneously distributed pores in the structure with low strength.

Noteworthy, non-ionic surfactant, such as Triton X-100 in combination with ionic surfactants shows better foamability [273]. Despite its remarkable foam-forming characteristics, the system based solely on the non-ionic Triton X-100 has issues regarding foam durability [274]. A similar problem with foam stability has been observed with the use of an ionic surfactant, an anionic Sodium Dodecyl Sulfate (SDS), which is a well-known surfactant applied in geopolymers. SDS can be used both as a stabilizing agent and a foaming agent [275], [276]. However, using solely SDS as a foaming agent results in an unstable foam, despite its strong foaming ability [275], [276]. Nevertheless, the use of cationic surfactants, such as Cetyltrimethylammonium Bromide (CTAB), in foams is known to generate low foamability but long-term stability [275], [276] even more than non-ionic surfactants [272]. Thus, the utilization of surfactants is potentially a promising technique employed in the manufacture of foamed geopolymers. Nevertheless, one problem is its insufficient foam formation efficiency or foam instability. Furthermore, another disadvantage is that a relatively large amount of surfactant has to be added to obtain highly porous material without providing good pore connectivity.

Considering the fact that the mixed surfactant system displays lower surface and interfacial tension on the same medium than individual surfactants, it is assumed that the combination of two different types of surfactant exhibits synergy [277] and can also tailor microstructures [273]. Sidim and Arda [278] emphasized the solution's unique features based on the blend of non-ionic and ionic surfactants. Different foamability, foam stability, surface tension, surface viscosity, contact angle, bubble size, and microemulsion stability may be observed when compared to the solution based on individual surfactants. Noteworthy, it is possible to combine surfactants to either obtain a set of desired features or reduce the amount of stabilizing substances used which would reduce the cost and environmental impact of the produced composite.

The above-mentioned properties of mixed surfactants have already been applied in several areas, such as Enhanced Oil Recovery (EOR) [279]. However, the beneficial effects of mixed surfactant systems on pore formation in geopolymers have not yet been investigated. Based on the evidence that mixing is beneficial in other fields and the use of a single surfactant system is utilized in foamed composites, it is hypothesized that mixing ionic with non-ionic surfactant can improve the performance both at room and high temperatures, with the focus on total pore volume, pore size distribution and pore connectivity. Furthermore, the hygrothermal and mechanical performance are elaborated in order to provide a recommendation towards surfactant mix determining pore structure and its potential application.

This research focuses on designing a biocoal fly ash-based geopolymer for room and high-temperature applications, with H_2O_2 as a foaming agent and different surfactant combinations as a stabilizing agent. Moreover, this study specifically aims to investigate the effect of binary surfactant systems on porosity and

pore connectivity. Two commonly used nonionic surfactants Triton X-100 and Tween 60, as well as ionic SDS and CTAB, are studied in this research, with the focus on pore morphology determined by microcomputed tomography, mercury intrusion porosimetry and gas permeability, as well as the mechanical, thermal and hygrothermal performance at a humidity-controlled environment coupled with the theoretical calculation of time-dependent heat and moisture transport.

5.2 Materials and methods

5.2.1 *Fly ash*

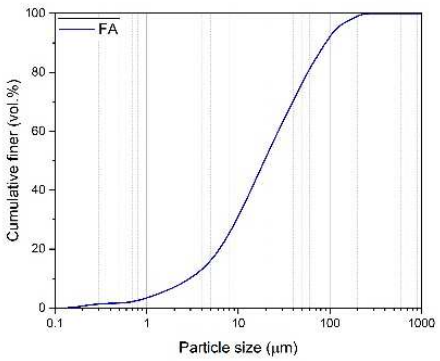

Fig. 5.1. Particle size distribution of the biocoal fly ash.

The raw material used in this research was biocoal fly ash (BFA), a by-product of power generation using coal and biomass (up to 40%) as fuel. Biocoal fly ash has a similar chemical composition as siliceous fly ash, nevertheless with a higher silica content and relatively lower aluminium content [92], moreover this material contains a higher amount of calcium (**Table 5.1**). A laser particle size analyzer (Mastersizer 2000, Malvern Instruments) was used to determine the particle size distribution of the biocoal fly ash, which is depicted in **Fig. 5.1.** The three-point specifications of particle size distribution is as follows: d_{10} = 2.89 μm, d_{50} = 19.68 μm and d_{90} 91.41 μm.

Table 5.1: Oxide composition of fly ash obtained via XRF measurement (in %).

SiO_2	Al_2O_3	CaO	Fe_2O_3	MgO	K_2O	SO_3	TiO_2	P_2O_5	MnO	Other	LOI
51.66	18.50	9.62	8.72	2.27	3.68	1.09	1.01	0.82	0.24	0.38	2.01

5.2.2 *Alkali activator, foaming agent and surfactants*

In this study, an alkaline solution was prepared with a silica modulus of molar SiO_2/K_2O 1.4 and 5.5 wt.% of K_2O on dry solid precursor by combining potassium hydroxide pellets (VWR Life Science,

reagent grade) and potassium silicate solution (WHC, K_2O 8%, SiO_2 20.8%, 72.8% H_2O by mass). Before being used for geopolymer synthesis, the solution obtained was kept unaffected for 24 h to reach equilibrium.

Table 5.2: Characteristics of the surfactants applied in this study (data taken from provider).

Name used	Chemical names and category	Linear formula and molecular weight	Trade name	HLB value*	CMC (mmol/L^{-1})**
SDS	Sodium Dodecyl Sulfate (anionic)	$CH_3(CH_2)_{11}OSO_3Na$ M.W. = 288.38	SDS	40.0	8.2
CTAB	Cetyltrimethylammonium Bromide (cationic)	$CH_3(CH_2)_{15}N(Br)(CH_3)_3$ M.W. = 364.48	CTAB	21.4	0.96
T60	Polyethylene Glycol Sorbitan Monostearate (non-ionic)	$C_{32}H_{62}O_{10}$ M.W. = 606.8	Tween 60	14.9	0.0167
T100	Octylphenol Ethylene Oxide Condensate (non-ionic)	$C_{14}H_{22}O(C_2M_2H_4O)_n$ M.W. = 625	Triton X-100	13.5	0.24

***The hydrophilic–lipophilic balance; ** Critical Micelles Concrentation**

As a foaming agent, hydrogen peroxide (30% Sigma-Aldrich, Germany) was used (**Table 5.2**). Furthermore, four various types of surfactants were used to study their foamability and foam stability in geopolymeric slurries, including anionic, cationic, and nonionic surfactants. Two nonionic surfactants, Tween 60 and Triton X-100 were purchased from VWR Chemicals. Sodium Dodecyl Sulfate (98% purity, Sigma-Aldrich, Germany) was selected as an anionic surfactant, while CTAB (98% Sigma-Aldrich, Germany) is a cationic surfactant. The properties of the used surfactants are presented in **Table 5.2**.

5.2.3 *Foamability and foam stability*

A fundamental test method was used to evaluate the effect of the mixed surfactant system on foamability and stability, with the details referred to Huang et al. [280] and Pedersen et al. [281]. Deionized water was combined with the surfactant at a mass ratio of 1:5 and was shaken for 1 minute using a laboratory shaker. The same weight ratios of nonionic to ionic surfactant were utilised to investigate surfactant interactions in both the aqueous solution and the paste, and they are presented in **Table 5.5**. The height of the formed foam was determined after 10 seconds and 15 minutes using a cylinder (250 ml). The above test was conducted twice for each mixture and the results are shown in **Table 5.3**. The results indicate that the mixed surfactant systems generate more foam with improved stability, which can be observed explicitly after 15 min. However, it should be emphasized that this test only provides insight into the synergy between two surfactants in an aqueous solution. When mixed with both Triton X-100 and Tween 60, the SDS system

has the highest value of foam height among the analysed systems, both after 10 seconds (22 cm and 23 cm) and after 15 minutes (14 cm and 15 cm). The interaction of these surfactants with one another affects foam formation and stability, either positively or negatively when interactions are synergistic or antagonistic, respectively. The synergy can be attributed to nonideal mixing effects in the aggregates, resulting in Critical Micelle Concentrations (CMC) and interfacial tensions that are significantly lower than theoretical values based on the characteristics of the unmixed surfactants alone. Parra et al. [282] ascribed this to the nonionic agent in those mixed surfactant monolayers that improved the flexibility of the liquid film, which prevented the fracture of the foams.

Table 5.3: Mass fraction of nonionic surfactant in total surfactant mix combined with the foam height of single surfactants and cosurfactant mixes measured after 10 seconds and 15 minutes.

	Single surfactant				**Cosurfactants**			
	Non-ionic		**Ionic**		**Mix**			
	Triton X-100	**Tween 60**	**SDS**	**CTAB**	**T100 +SDS**	**T100 +CTAB**	**T60 +SDS**	**T60 +CTAB**
$m_{nonionic}/m_{mix\text{-}surf}$	**-**	**-**	**-**	**-**	**0.51**	**0.61**	**0.45**	**0.43**
10s (cm)	20.0	16.0	21.0	10.1	22.0	17.0	23.0	12.0
15min (cm)	5.0	6.0	10.0	6.5	14.0	13.5	15.0	9.5

Noteworthy, the CMC of nonionic surfactants is usually two orders of magnitude lower (**Table 5.2**) than that of the corresponding anionic surfactant of the same alkyl chain length and the presence of nonionic surfactants in mixed monolayers enhances the stability of the foam film with certain synergy. The corresponding surfactant combinations in the mixtures and their interactions have been extensively studied [278], [283], [284]. El-Aila [285] showed that mixed systems with Triton X-100 both with SDS and CTAB show synergy in surface tension reduction efficiency and mixed micelle formation. Furthermore, Saiad et al. [286] showed that a low CTAB concentration with the dominance of T100 shows better foaming ability. Based on these findings, it can be assumed that the molecules of both surfactants in the mixture attract each other to produce mixed micelles with different characteristics than the micelle of a single surfactant. In addition, admixing an ionic surfactant with a non-ionic type results in a lower minimum concentration of ionic surfactants. In broader terms, this indicates that less material is required to trigger micelle creation. Referring to the results in **Table 5.3**, the blends can be ranked according to their highest foaming and stabilizing abilities in the following order: T60SDS> T100SDS> T100CTAB> T60CTAB. It is worth noting that the cosurfactant system considerably improves the foam's long-term stability, as shown after 15 minutes (**Table 5.3**). However, micelles behaviour in an aqueous solution may differ from geopolymer slurry. A geopolymer paste is considered a mix of different ions, salts, and solid particles which additionally

influence those surfactants interactions. For instance, salts tend to screen electrostatic repulsion between the hydrophilic group which makes the surfactant more hydrophobic and leads to the aggregation of monomers at lower concentrations, thus lowering the CMC of the system [287].

5.2.4 *Mix proportion and sample preparation*

Table 5.4: Mix proportion of geopolymers (normalized to 100 wt.%).

	BFA	**K_2SiO_3 solution**	**KOH**	**H_2O**	**H_2O_2**	**Triton X-100**	**Tween 60**	**CTAB**	**SDS**	**SiO_2/Al_2O_3 (mol/mol)**	**H_2O/FA (wt./wt.)**
T100SDS	72.3	17.1	3.1	6.6	0.5	0.2	-	-	0.2	5.1	0.27
T100CTAB	72.9	17.2	3.1	6.0	0.5	0.2	-	0.005	-	5.1	0.26
T60SDS	72.4	17.1	3.1	6.6	0.5	-	0.1	-	0.2	5.1	0.27
T60CTAB	73.0	17.2	3.1	6.0	0.5	-	0.1	0.005	-	5.1	0.26

Table 5.4 shows the mix composition of four geopolymers investigated in the current work. The amount of raw material, activator solution, and foaming agent was kept constant. The geopolymer pastes were prepared by mixing fly ash with the activator solution in a Hobart 5-litre mixer. The produced paste was then mixed with the foaming agent, and the resulting mixture was stirred at 150 rpm for 6 minutes, before casting into the moulds 40 x 40 x 160 mm^3, and 100 x 100 x 100 mm^3. After 24 hours, the samples were demolded, wrapped in plastic foil and heated at 65 ^oC for 4 hours before further curing at room temperature.

5.3 *Results*

5.3.1 *Raw material characterization and activation*

Table 5.5: Phase quantification via Rietveld refinement of BFA (error shows in the brackets) (%).

Amorphous	Quartz	Mullite	Hematite	Lime	Potassium carbonate	Magnetite	Periclase	Portlandite	Ammonium sulphate	Calcite	Anatase
ICSD	**83849**	**66451**	**22505**	**90486**	**662**	**85807**	**9863**	**15471**	**83025**	**40544**	**24276**
83.9	5.79	3.65	1.95	1.08	1.09	0.70	0.59	0.49	0.28	0.25	0.15
(0.32)	(0.09)	(0.15)	(0.11)	(0.05)	(0.11)	(0.08)	(0.08)	(0.06)	(0.09)	(0.06)	(0.04)

The XRD analysis **(Table 5.5)** reveals that the biocoal fly ash is highly amorphous (85%). Thus, the approach suggested by Sanalkumar et al. [98] was used to assess the reactive molar Si/Al ratio of the raw material. 200 ml of NaOH (10M) and 7.5g of biocoal fly ash were mixed and stirred at 80 °C for two hours. Subsequently, the inductively coupled plasma atomic emission spectroscopy (ICP-OES) analysis of the filtrate was performed. Additionally, the liquid filtrate was also examined by ICP-OES after the solid residue from NaOH treatment (2g) had been mixed with 500 ml of hydrochloric acid (32%) for three hours. The sum of the eluted silicon and aluminium obtained via ICP-OES was applied to determine the reactive Si/Al ratio. In **Table 5.6**, the comparison of the Si/Al ratio obtained by the various method applied in this study is presented. Based on the obtained results, the reactive Si/Al ratio is 2.93.

Table 5.6: Fly ash reactivity based on amorphous Si/Al content.

	Moles of Si per 100 g of FA	Moles of Al per 100g of FA	Si/Al molar ratio
Total content (XRF)	0.86	0.36	2.38
Crystalline content (XRD)	0.11	0.05	2.20
Amorphous content	0.75	0.31	2.42
Extraction	0.44	0.15	2.93

The setting time of alkali-activated material is highly related to the reaction temperature, a small increase in the temperature shortens the time significantly. The initial and final setting time measured for alkali-activated biocoal fly ash at room temperature was 16 min and 48 min, respectively. The alkali-activated BCFA shows a strongly exothermic reaction **(Fig. 5.2a)**, which in consequence reduces the setting time.

The observed exothermic peak corresponds to the wetting, dissolution-precipitation, which appeared within the first hour. Due to the relatively low reactivity of the ash sample at ambient temperature, after the dissolution peak, the line tends flatten to zero heat flow. The observed phenomenon might be owing to the slow rate of reaction. As found by Nath et al. [288], fly ash geopolymerization is a process in which the reaction proceeds for a longer duration with low heat evolution after precipitation (**Fig. 5.2b**).

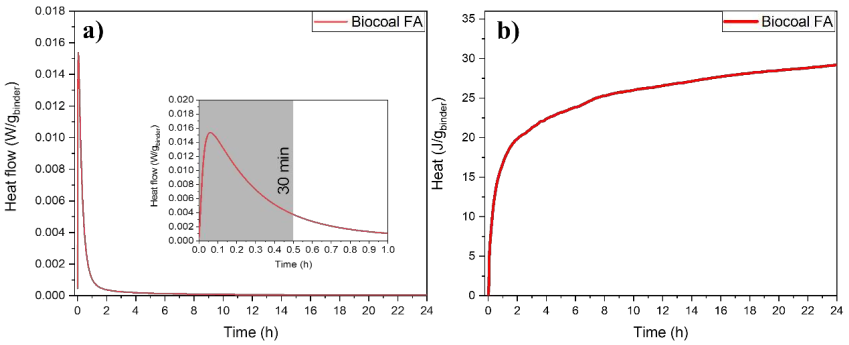

Fig. 5.2. Isothermal calorimetric response of biocoal fly ash geopolymer pastes at 20 °C a) normalized heat flow, and b) normalized cumulative heat.

Noteworthy, the evolution of a minor amount of $NH_{3(g)}$ has been observed through ion chromatography analysis. The gas released within the first 10 minutes was captured in an aqueous solution which was then analyzed for NH_4^+ ions. NH_3 can be found as molecules adsorbed on the surface of ash particles, forming chemical bonds at active sites, and also as an ammonium salt (mostly sulphates and bisulphates) that adheres to grain ash [289]. Moreover, the presence of free lime **(Table 5.5)** and the addition of alkali accelerates the NH_3 release. Furthermore, the production of K_2SO_4 is confirmed by XRD. **Fig. 5.3** presents the XRD results of raw material and reaction products after 30 minutes of activation (**Fig. 5.2a**). The primary finding is the consumption of calcium oxide and ammonium sulphate (shown by the arrows in **Fig. 5.3**) and the appearance of a new potassium sulphate phase, as a result of a highly alkaline activator solution that contains KOH. The above XRD analysis of geopolymer reaction products supports the findings of calorimetry and a potential explanation of the flash setting of the matrix.

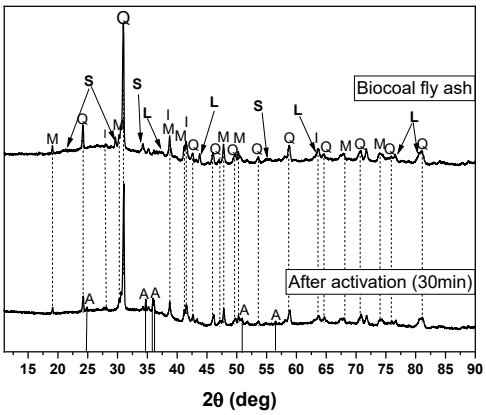

Fig. 5.3. XRD diffractograms of raw material and reaction product with marked only the most significant phases. Legend: **Q** Quartz; **M** Mullite; **I** Iron oxide; **L** Lime; **S** ammonium sulfate; **A** Arcanite.

Nevertheless, it should be highlighted that for the analysed porous matrix it is beneficial to have a short setting time, which provides less time for bubble collapse to occur and the influence of the setting time on the Ostwald ripening and pore collapse can be minimized. In many studies, the use of nucleating agents that accelerate the setting and reduce the extent of air bubble collapse is recommended [264].

5.3.2 *Density and total porosity*

The composites produced with a small quantity of a foaming and stabilising agent (**Table 5.4**) by the aeration process were characterised in terms of aeration efficiency. Thus, the overall porosity and bulk density of the collected porous geopolymers are depicted in **Fig. 5.4**. These values show that the three chosen blends have comparable porosity. T60CTAB, on the other hand, has a significantly lower porosity (e.g. 11.9% less than T100SDS). Comparing the foaming information in **Table 5.3** with the obtained porosity, it can be seen that the observed heights after 15 minutes, and more precisely the approximate values of the foam heights between T100SDS, T100CTAB, and T60SDS, as well as the significantly lower value for T60CTAB, are in agreement. One probable explanation for T60CTAB is that, due to the relatively high surface tensions of the cosurfactant, it is not feasible to increase the surface area to facilitate foam production, resulting in poor foamability [278], [284], [290], [291].

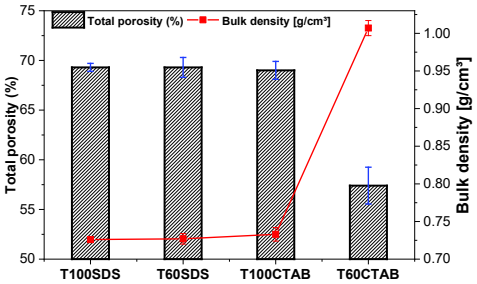

Fig. 5.4. Total porosity and bulk density of porous geopolymer pastes.

It can be observed that both non-ionic surfactants (T100 and Tween 60) combined with anionic surfactant SDS produce a more porous structure characterized by a low bulk density ~ 0.7 g/cm^3, thus SDS shows good foamability properties. Korat et al. [271] investigated fly ash-based geopolymer in which one type had similar content of hydrogen peroxide (0.5%) and SDS 1%. The obtained density and porosity were 1.08 g/cm^3 and 24.2%, respectively. In our case, the addition of 0.1% of Tween 60 or 0.2% of Triton X-100 together with SDS (0.2%) results in a material with obviously lower density (0.7 g/cm^3) and higher porosity (~69%). Another research [272] utilizing the same foaming agent (H_2O_2) and surfactant (CTAB) achieved a similar density of 0.6 g/cm^3, which, however, applied a much higher concentration of CTAB (0.05% vs. 0.005%) than in this study. Furthermore, Xu et al. [292] produced a comparable composite density using 2.5% H_2O_2, but the pore structure was optimized using 3.5% H_2O_2 and 2.85% SDS. Increasing the amount of foaming agent to 1% and using 3% SDS resulted in a similar density of 0.63 g/cm^3 [293], indicating that the mixed system contributes to reducing the amount of foaming agent and surfactant used while achieving similar values of density and volume of pores.

5.3.3 *Open porosity*

The influence of the co-surfactant mix on the formation of pore cavities is analysed in the following section based on the above-discussed total porosity value. The evaluation is carried out based on the μCT analysis. Firstly, image processing is performed by using an IPLFE v1.16 (Scanco Medical AG, Switzerland) to determine the open pores. The procedure is described in-depth in **Chapter 2**. The potential for fluid (e.g. water vapour) movement through the structure is evaluated to examine principally porosity using a μCT and measuring the gas permeability and mercury intrusion porosimetry for the volume of open pores and distribution of pore size respectively.

The pore separation demonstrates (**Fig. 5.5**) that in all of the pastes based on nonionic surfactant and cationic CTAB, the closed pores are more prominent, which is more prominent in T60CTAB, where the open pores account for 32.4 vol. %. It is evident that the samples with similar total porosity, namely

T100CTAB, T100SDS, and T60SDS (**Fig. 5.5**), are distinguished by a different value of open porosity, which is driven by the used surfactant.

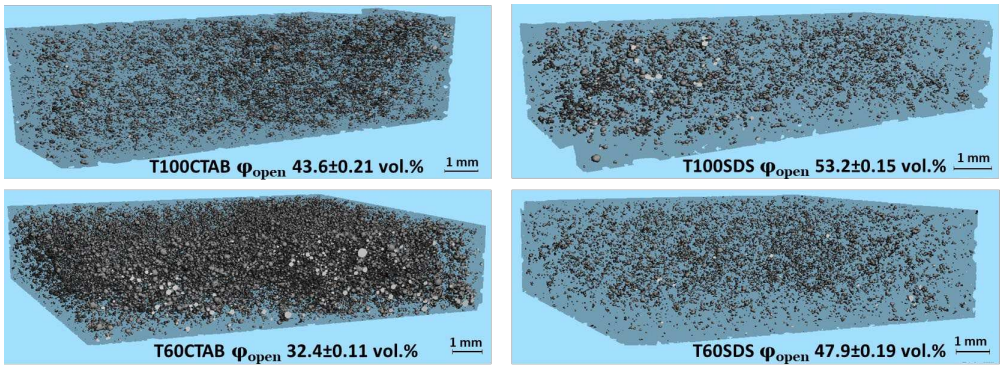

Fig. 5.5. Visualization of the specimens with marked closed pores.

Alteration is noted in the overall volume of the pores, their size, and distribution in the structure, i.e. the distances between the pores, depending on the mix of surfactants utilized. With a high porosity, a wide range of pore diameters, and dense packing of the bubbles, cavities between the pores might develop, defining the open porosity. **Section 5.4.1** is devoted to revealing the mechanism that promotes the development of two different types of pore structures under the premise that morphology is mostly driven by the type of used ionic surfactant in the mix. It is presumed that CTAB-containing mixtures have a higher paste viscosity [272], [294], which is due to substantial CTAB adsorption on fly ash particles. This strong interaction influences the gas-liquid interface, providing a rigid film that hinders the passage of gas between bubbles, resulting in an observable thicker wall between pores, and reducing the chances of the pores coming close enough to be able to create an opening in their wall and build a connection [272].

Lu and Qin [295] evaluated the porosity development of a fly ash-cement mix and discovered that, despite getting a similar value of total porosity (~70%), the volume of open pores was substantially lower (37%) than those in our study (48% for T60SDS and 53% T100SDS). Furthermore, Strozi Cilla et al. [267] reported similar open porosity, but with a greater quantity of single-surfactant added to the geopolymer slurry: with 2 wt.% of Triton X-100 or Tween 80 added, they achieved open porosities of 50% and 54%, respectively.

The findings of the μCT evaluation are supported by the measured gas permeability coefficient. The high material permeability implies good fluid movement through the pores. For high temperatures applications, as described above, it is desired to minimize the damage by cracking and spalling caused by the transport of water vapour through the structure. The highest value (8.1×10^{-13} m^2 = 0.83 D) was obtained for T100SDS, which has the greatest value of open pore volume. T100CTAB and T60SDS were distinguished by relatively lower permeability coefficient values (3.7×10^{-13} m^2 (0.38 D) and 4.1×10^{-13} m^2 (0.42 D), respectively). The results are in agreement with open porosity results, also for the mix based on T60CTAB the permeability was established as 2.8×10^{-13} m^2 (0.29 D). These values fall within the classified gel casting foams' permeability between 10^{-13} and 10^{-9} m^2 [296]. Airflow in porous materials is a volumetric phenomenon that is largely dependent on pore size, thus with decreasing solid volume fraction, as well as increasing pore size, Darcian permeability increases. The pore size distribution of T100SDS and T60SDS is shifted towards a bigger size than T100CTAB, thus causing a higher air permeability. Therefore, it is concluded that an improved permeability of the composite is resulted by applying non-ionic surfactants, both Triton X-100 or Tween 60, together in combination with SDS.

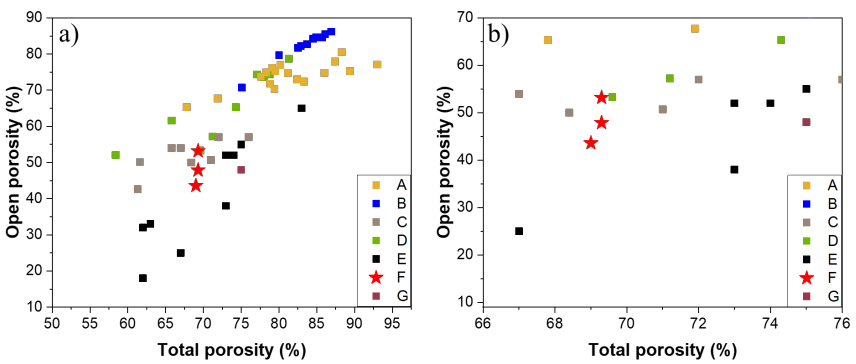

Fig. 5.6. Open porosity vs total porosity of designed composites and other foamed geopolymers. A[293]; B[31]; C[297]; D[30]; E[298]; F:this study; G[299].

In order to assess the efficiency of the proposed method, the obtained results were then compared with the literature, which also presents the method of obtaining foamed geopolymers with the use of surfactants such as SDS, oil, or proteins. **Fig. 5.6** depicts the relationship between the total and open porosity. Bai et al. [31] presented intriguing results in which the volume of open pores to total porosity ratio is close to 1: 1 as foaming agents, H_2O_2 (3%) and olive oil were used. Yan et al. [293] observed a high ratio of open porosity to total porosity (86.9 vol%) using SDS (3%) and H_2O_2 (3%) that can be compared to the present T100SDS result, which has a much lower fraction of foaming agent (0.5%), as well as total surfactant content. As can be seen in **Fig. 5.6a**, as porosity increases, the air bubbles are packed more closely together, thus increasing the probability of open cavities formation. For the total porosity range close to the composites T100SDS, T100CTAB, and T60SDS (see **Fig. 5.6b**), it can be seen that the obtained results are

promising in terms of the content of open porosity in total porosity as well as the amount of utilised surfactant. Noteworthy, the total porosity and open cavities of the material should be chosen based on its intended application. Further, it should be taken into account that as porosity increases, the compressive strength of the material decreases [300].

5.3.4 *Pore size distribution*

Aside from total and open porosity, the distribution of pore size in the structures determines the strength or hydrothermal properties of the composites, as well as the ability to generate pore cavities due to their way of packing in the matrix. Attention should be paid to air voids, macropores, and mesopores in order to track variations in the pore structure of the resulting composites. The μCT measurement covers the macropores, which are the main product of the chemical aeration of the structure, while the MIP was used to examine the pore nature between 5 nm and 5μm.

5.3.5 *μCT*

The pore characteristics are determined by using μCT on the samples (size 20 x 20 x 50 mm^3). This analysis helps to understand the composite microstructure, the pore size and their distribution in 3D. To focus on the details of the pores of geopolymers created as a result of the proposed chemical aeration, the observed values are presented in **Fig. 5.7**. The pore distribution is generated by combining total pores and pores determined by μCT, with a detection limit of 5 μm. Based on these graphs, it is clear that CTAB-based systems favour low-sized pores, whereas SDS provides the majority of pores above 200 μm. The pores above 200 μm overall for T100SDS and T60SDS comprise accordingly 56.1% and 50.6% in the normalized total porosity, while for T100CTAB and T60CTAB 23.2% and 14.3% respectively. In both CTAB-based systems, regardless of the type of nonionic surfactant, a majority of pores between 50-200 μm, as well as the higher contribution of pores between 5-50 μm is observed.

It can be observed that Tween 60 directs the formation of small-size pores (< 5μm) more effectively than Triton X-100 (23-25% in the total pore range). Moreover, when T60CTAB and T60SDS are compared, it is clear that Tween 60 creates small pore sizes, which is comparable to the effect derived by pure CTAB. Both Tween 60 and CTAB surfactants boost the formation of small pores, reducing the possibility of Ostwald ripening and merging air bubbles.

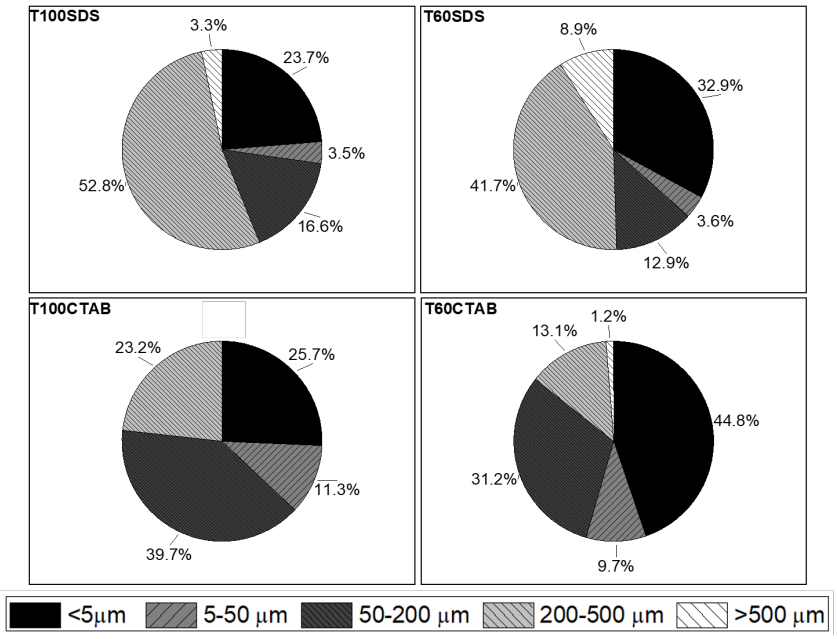

Fig. 5.7. Pore size distribution of the porous specimens in the range >5.0 μm.

The existence of pores in specific ranges has different impacts on performance such as heat conductivity and water suction. Small-diameter closed pores contribute to smaller thermal conductivity, simultaneously partially open small pores will increase water transport in the material's structure, whereas large pores increase the probability of open porosity and the contribution of pore radiation in the total heat transfer balance should not be omitted [301].

5.3.6 *MIP*

Further, to analyze the nature of the pores smaller than 5 μm, mercury intrusion porosimetry (MIP) analysis was performed. Despite the different nature of the measurement compared to μCT and the values obtained by the two methods, the trend among the four specimens is maintained. **Table 5.7.** also shows the calculated values obtained through the μCT route and the porosity obtained as bulk porosity. However, due to the variety of throat sizes and "ink bottle" effects, MIP measurements may misallocate the pore diameters, assigning them to sizes lower than the real ones [302].

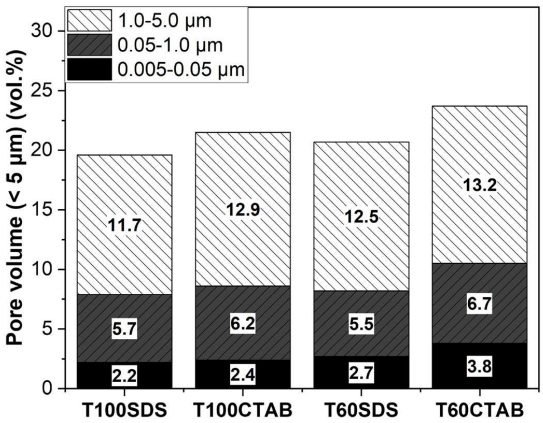

Fig. 5.8. Pore size distribution within the range 0.005-5 µm obtained via MIP method.

Pores between 0.005 and 1.0 µm present in the geopolymerization product can be classified as gel pores (< 0.01 µm) and capillary pores (0.01 – 1 µm) [303]. The four analysed samples constitute a similar contribution of pores (0.005- 1.0 µm) due to the geopolymeric gel structure of the composites. Furthermore, T60CTAB is characterized by a greater content of both 0.005-0.05 and 0.05-1.0 µm pores, which confirms the hypothesis of the formation of pores below 5 µm, determined by the presence of both Tween 60 and CTAB. The influence of CTAB on the formation of smaller size pores can be also observed in T100CTAB.

Table 5.7. Overview of porosity values (open/closed) by different methods.

		T100SDS	T100CTAB	T60SDS	T60CTAB
Total porosity	**(vol.%)**	69.3	69.0	69.3	57.4
µCT open pores >5 µm		53.2	43.6	47.9	32.4
MIP open pores <5 µm		19.6	23.5	20.5	23.7
µCT closed pores >5 µm		1.6	2.7	3.3	19.4

5.3.7 *Hygrothermal performance: Steady-state*

Several material parameters, such as bulk density, porosity, thermal conductivity, and vapour permeability play a significant role in hygrothermal performance evaluation [304], and the properties of the resulting composites differ from one another (**Figs. 5.4; 5.5**). As the humidity in the atmosphere rises, materials become partly saturated with water, negatively impacting thermal conductivity [305]. Noteworthy, the size, tortuosity, and type (closed/open) of pores are crucial in water transport through porous structures [306]. The permeability and diffusion coefficients rise as porosity and pore size increase. Therefore, the water vapour adsorption capacity is monitored for three out of four mixes due to their similar total porosity

(~69%), providing an insight into the influence of pore size and pore connectivity on the hygrothermal behaviour of foamed geopolymer (**Fig. 5.9**). It is well established that with the increased total porosity, the water adsorption increases. The sole transport mechanism at very low RH is vapour transfer. The number of layers of water molecules on the surface grows as air humidity rises and firstly small size pores are filled and then connected bigger pores are occupied with a single layer of H_2O. As demonstrated by Kato et al. [307], with an increase of open porosity water adsorption rise can be expected.

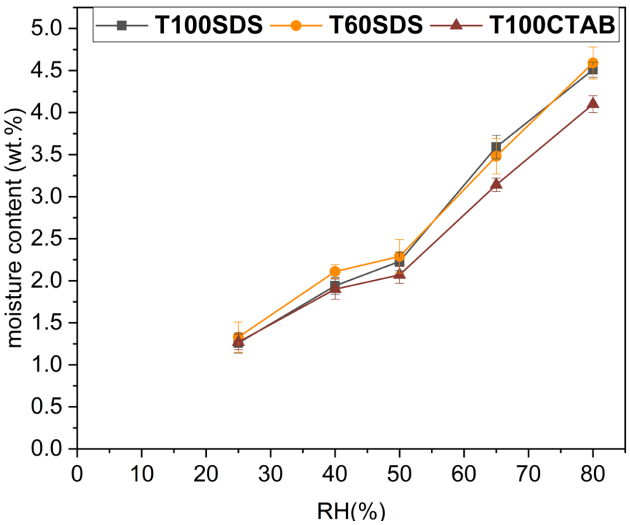

Fig. 5.9. Water uptake depends on the controlled relative humidity in the climate chamber.

It can be stated that among the three samples (T100SDS, T60SDS, and T100CTAB,) characterized by a total porosity of ~69 vol.%, the T60SDS sample has the highest proportion of small pores below 5 μm (**Fig. 5.7**), and up to 10% greater than the T100SDS sample, whose pores are firstly filled with water. When the relative humidity reaches 40%, water may be present in both small (5-50 nm) and big pores (> 50 nm) [308], and then the key role open porosity plays on permeability can be observed as a significant increase between RH 40% and 50% in T100SDS. It is in agreement with the observed results when combined with the open porosity, which rises in the sequence T100SDS> T60SDS> T100CTAB. T60SDS has the largest degree of water content at RH 40%, while at higher percentages of humidity, a stronger influence of permeability and open porosity on the passage of water vapour into the matrix is observed. This phenomenon can explain the minor difference between T100SDS and T60SDS at higher humidity.

High pore connectivity, and hence high gas permeability, is inversely proportional to tortuosity, which influences the fluid flow rate [309]. As a result, fluid (moisture) flow is more hindered in the sample characterized by low gas permeability, for example, T100CTAB compared to the SDS-based mixes. Additionally, the connection between pores above 5 μm in T100CTAB is limited, as illustrated in **Fig. 5.5**, and a considerable number of small-size isolated pores densely packed in the structure is observed.

Furthermore, more connectivity paths can be created by increasing the size of the pores [310]. When compared to composites with a predominance of small pores, the pore size increases the ability of media to pass more fluid through a porous matrix [311]. The sample T60SDS represents the material with a high proportion of pores smaller than 5 μm (**Fig. 5.7**), high pore volume connectivity and permeability, all of which play a crucial role in low humidity environments (RH=25%) (**Fig. 5.9**).

Thermal properties are critical for thermal insulating or fire-resistant materials. It is known that the heat conductivity of porous materials is affected by a variety of factors. In addition to overall pore volume, the pore size distribution, homogeneity, and opening level of pore cells also have an impact [301], [312], nevertheless, the thermal conductivity of the solid matrix and total porosity are the two dominant factors [313]. Porous materials with excellent thermal insulation properties are characterized by closed pores, which limit the heat flow of gases, and therefore T100CTAB sample, which, although having a similar total porosity as SDS-based samples (**Fig. 5.4**), has a smaller percentage of open porosity (**Fig. 5.5**). The lowest amount of overall porosity determines the maximum value of thermal conductivity for T60CTAB.

Total porosity and matrix conductivity show the largest influence on the effective thermal conductivity, which is the reason for the minor change between samples T60SDS >T100SDS >T100CTAB (Δλ: 0.009-0.02 W/m·K). However, the densely packed isolated pores above 5 μm define the better performance of T100CTAB than T60SDS. Chen et al. [314] stated that for the same porosity, the smaller the pore size, the greater the number of pores, and the lower the heat transfer efficiency. T60SDS has a larger content of pores above 500 μm (8.9 vol.%) than T100SDS (3.3 vol.%) and T100CTAB (0 vol.%), resulting in improved heat transmission and increased thermal conductivity.

Table 5.8. Thermal conductivity of the foamed geopolymers in the dry state 0% RH).

Groups	T100SDS	T100CTAB	T60SDS	T60CTAB
λ (W/(m·K))	0.116 ±0.002	0.104 ±0.003	0.125 ±0.001	0.146 ±0.001

Conditioning composites at varying humidity levels allowed us to assess not only their sorption capacity but also their steady-state thermal conductivity at a particular moisture content. **Fig. 5.10** depicts the obtained experimental values of effective thermal conductivity acquired after exposure to a controlled humidity chamber, where the values at 0% RH are taken from **Table 5.8** as in the dry state. By using the Memmert climate chamber, it was possible to digitally control active humidification and dehumidification and maintain a constant temperature. The selected sample set is first exposed to the lowest selected humidity range (25% RH) and then exposed until the highest value (80% RH) is reached. Consequently, materials' ability to adsorb moisture varies and their thermal characteristics in a saturated condition differ significantly (**Fig. 5.10).** T60SDS and T100SDS exhibit poorer thermal insulating capabilities (higher lambda) over the whole range of moisture content due to their greater volume of open pores (**Fig. 5.5**) and higher initial thermal conductivity value in a dry state (**Table 5.7**).

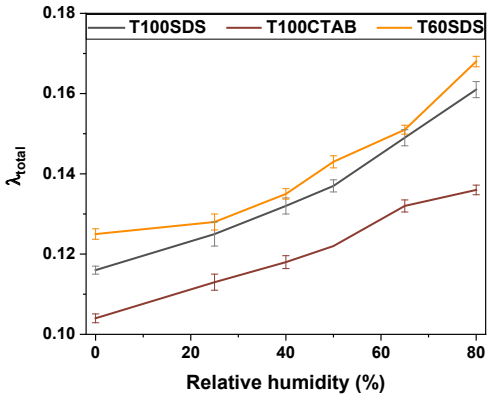

Fig. 5.10. Effective thermal conductivity as a function of relative humidity.

5.3.8 *Hygrothermal performance: Transient state*

Hygrothermal performance of each geopolymer composite is further investigated using validated software (WUFI® (Heat and Humidity transient)). The composite is modelled as a single-layer wall with a thickness of 4cm, and its material properties are extracted from the experimental data discussed in previous sections. Transient boundary conditions are imposed on the model; the exterior climate is set based on the climatic profile of Eindhoven (**Fig. 5.11**), and the interior climate is set as per EN 13788 with humidity class 3. The model is then simulated for a duration of five years. The temperature reading for each month is the arithmetic mean of all the days in a given month, while the error bar is the standard deviation from the mean value.

The transient heat and moisture transport processes are solved by coupled heat transport and moisture transport differential equations [315].

$$\frac{\partial H}{\partial T}\frac{\partial T}{\partial t} = \frac{\partial}{\partial x}\left[\lambda\frac{\partial T}{\partial x}\right] + h_v\frac{\partial}{\partial x}\left[\frac{\delta}{\mu}\frac{\partial p}{\partial x}\right] \tag{5.1}$$

and

$$\varrho_w\frac{\partial w}{\partial \varphi}\cdot\frac{\partial \varphi}{\partial t} = \frac{\partial}{\partial x}\left[\varrho_w D_w\frac{\partial w}{\partial \varphi}\frac{\partial \varphi}{\partial x}\right] + \frac{\partial}{\partial x}\left[\frac{\delta}{\mu}\frac{\partial p}{\partial x}\right] \tag{5.2}$$

respectively, where D_w is the liquid transport coefficient, H the enthalpy (J/kg), h_v the evaporation enthalpy of water (J/kg), p the water vapour partial pressure (Pa), w the water content (g), δ the water vapour diffusion coefficient in air (m^2/s), T the temperature (K), λ the thermal conductivity (W/mK), μ the vapour diffusion resistance factor, ϱ_w the density of water (kg/m^3) and ϕ the relative humidity RH. The input

parameters for material properties, boundary conditions and initial conditions used to solve the equation **5.1** and **5.2** are listed in Appendix B (Table B.1).

In the moisture transport model (**eq. (5.2)**), the moisture storage (left-hand term) is directly linked to the water vapour adsorption capabilities, and the moisture transport (right-hand term) contains both the liquid transport and vapour diffusion terms. The pore size and pore structure influence the moisture transport property of a porous material, which can be represented by its hygric properties, i.e. porosity and water vapour diffusion resistance factor. In addition, the variation of climate conditions, particularly exterior climate strongly affects its hygrothermal performance. By including a transient boundary condition, a more realistic simulation of the hygric processes of the geopolymer composites can be assessed, and the simulation results (transient moisture content and thermal transmission (U-value)) can be further evaluated against the pore structure.

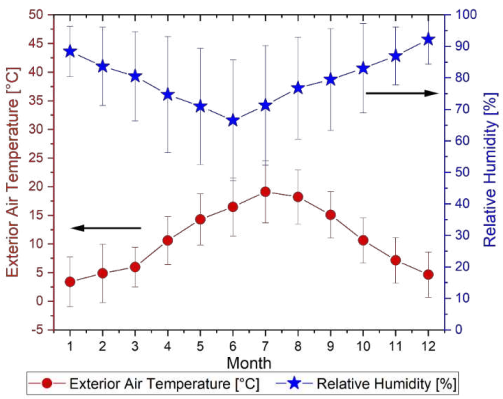

Fig. 5.11. Temperature and relative humidity profiles for simulated outdoor conditions.

Fig. 5.12 depicts the monthly averaged water content inside the geopolymer composites throughout a simulated year. Lower water content for the T100CTAB composite is observed in the range of 2.7% and 4.8%, in comparison to T60SDS and T100SDS where higher water contents are obtained. These simulated results have verified the proposition from the earlier experimental study, i.e. closed pores in a composite will reduce its water uptake capability, which coincides with T100CTAB which has a lower water content under ambient climatic conditions with its higher closed pores structure. Furthermore, all three developed geopolymers have a consistent course in their water content throughout the year, with only slight fluctuations represented in the form of deviation bars in **Fig. 5.12**. These stable trends show these three selected composites are effective in transporting water vapour, which further suggests that they can be potentially used to regulate the surrounding humidity fluctuations when used as wall assembly.

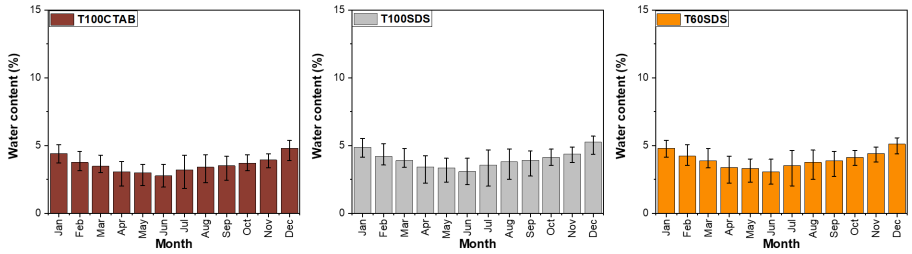

Fig. 5.12. The moisture content of geopolymers section in the 5th year under one climate condition. With marked min and max values of water content reported in each month.

The transient thermal transmittance (U) of the composites during the heating period (October to March) are summarized in **Fig. 5.13**. Additionally, the thermal transmittance at 80% relative humidity for each composite are included in the same plot, represented by dash lines for reference purpose. Due to their aforementioned ability to easily absorb and desorb water vapour from the surrounding air, all three geopolymers exhibit good thermal insulation performance and did not surpass their 80% humidity threshold. Their simulated transient thermal transmittance is also in agreement with the assumption derived from the thermal conductivity experimental study, with T100CTAB being the better insulating material, followed by T100SDS and T60SDS.

For comparison purposes, two commonly used commercial building materials are included in the simulation, namely gypsum plaster and cement lime plaster, both have similar applications as the developed geopolymers. A noticeable pattern can be straightaway observed from **Fig. 5.13**, where a larger range of thermal transmittance is gained by both commercial materials, with a major part of their heating period suffering thermal transmittance worse than their value at 80% humidity threshold. This is differing from the better and steadier thermal performance of the developed geopolymers. The main plausible cause is that the geopolymers have a better ability to regulate changes in relative humidity than the plasters (Appendix B, Figs. B.3, B.4). Another lesser element in play may be due to the water vapour diffusion resistance factor (μ) of investigated materials, where the geopolymers have a lower μ value in comparison to gypsum and cement lime plasters, i.e. the lower μ geopolymers have less resistance in preventing moisture transport throughout the material and consequently minimize the risk of accumulating higher water content inside the substrate.

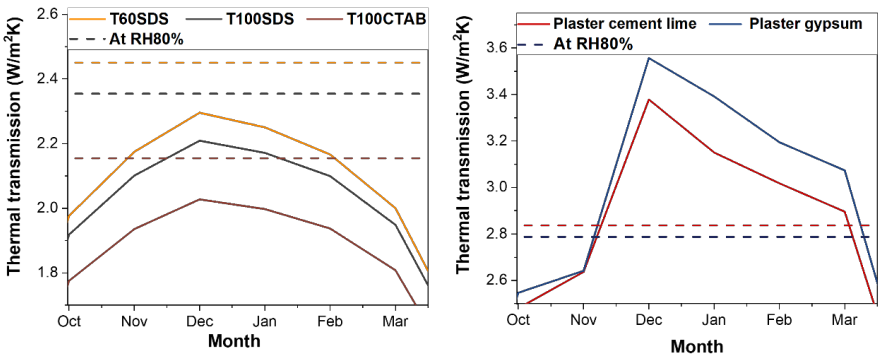

Fig. 5.13. Transient U-value of the designed porous materials compared to two commercially available products under one selected climate profile.

5.3.9 *Compressive strength*

In order to preserve their mechanical stability and integrity, alkali-activated foams need sufficient mechanical strength. However, as already noted, a flash setting has been observed in the investigation that has a detrimental impact on material strength growth over time and consequently low strength values are seen for all mixes. Overall, the obtained results suggest that the geopolymer matrix and pore shape determine the mechanical strength and the structural stability of the composites was influenced by pore size, distribution and cell-wall thicknesses.

It should also be noted that an increase in the median pore diameter has a detrimental impact on the composite's strength. The pore distribution plots of T100CTAB and T60CTAB demonstrate a shift towards lower values (< 200 μm) than the SDS-based systems, thus a higher fraction of pores with a diameter below 200 μm mitigates the porous structure's negative impact on compressive strength (**Table 5.8**). With the same pore volume, the sample with larger pores has lower strength, as observed in the T60SDS and T100SDS **(Table 5.9**). Regarding the pore connectivity, as stated by Ji et al. [310], pores smaller than 200 μm have a reduced possibility of collapsing due to their greater distance from one another when distributed in the same volume as pores of larger diameter provide a less fragile matrix backbone, contributing to the increased strength of composites.

Table 5.9. Collected data on porosity, pore size, and compressive strength.

	Pores < 200 μm (vol.%)	Pores >200 μm (vol.%)	Compressive strength (MPa)	Open porosity (vol.%)	Bulk density (kg/m³)
T60SDS	34.3	35.0	1.38	47.9	727
T100CTAB	53.0	16.0	2.51	43.6	733
T100SDS	30.4	38.9	1.16	53.2	726
T60CTAB	49.2	8.24	3.67	32.4	1007

Fig. 5.14 plots the compressive strength versus porosity of foam geopolymers made from various materials [316]. The fitting curve has been developed using the Ryshkevich model [317] based on Fiset et al. [298]. It demonstrates that the relationship between compressive strength and porosity may be predicted at the porosity above 75 vol.% (region II), and large variations are seen in the lower porosity region (55-75 vol.%- a region I). In region I, pore size distribution is more important than total porosity in the evolution of mechanical resistance. A narrow and small pore size distribution improves the mechanical performance of the composite, as emphasise Ji et al. [310]. Above this range (region II), total porosity increases due to increased volume occupation by air/gas phase, resulting in a decrease in total amount of solid matrix. As a result of the insufficient solid volume fraction, the overall mechanical strength in region II decreases.

According to Zhang and Wang [318], it is better to predict mechanical performance using pore volume above 100 μm rather than total porosity, since there are more substantial variations in mechanical performance. Comparing the obtained results with the literature it can be observed that the material is characterized by relatively low compressive strength, which is mainly due to the low raw material reactivity and high content of large air voids and relatively high open porosity (**Fig. 5.5**). Dhasindrakrishna et al. [15] proposed that curing at higher temperatures may be used to increase the early age strength, and the findings revealed that compressive strength of foamed geopolymer samples after high temperature can reach up to 3.5 times that of the equivalent unexposed geopolymer samples.

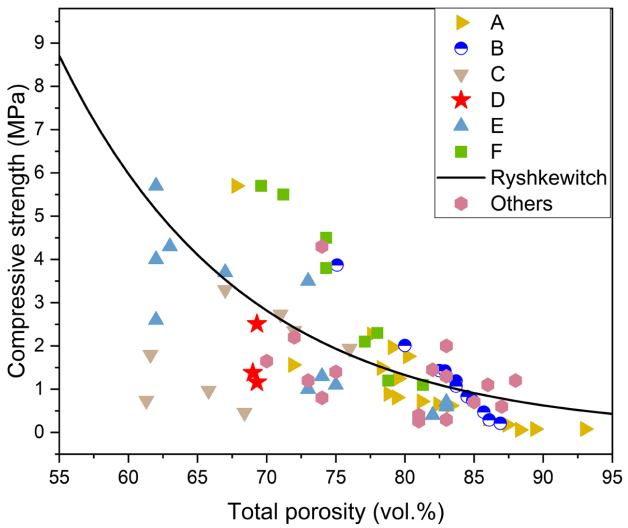

Fig. 5.14. Compressive strength vs porosity of various geopolymer foams. A[293]; B[31]; C[297]; D[30]; E[298]; F:this study; Others:[223], [300], [319]–[327].

5.4 Discussion

5.4.1 *Mechanism governing pore structure alteration*

Surfactant adsorption has been seen not only on the gas-liquid interface but also on the liquid-solid contact. Adsorption on the surface of solid particles happens as a result of electrostatic interaction for ionic surfactants [328] and through hydrogen bonds for non-ionic surfactants. The schematic diagram of the proposed mechanism is presented in **Fig. 5.15.** Geopolymer paste can be considered as a matrix loaded with solid particles, polyvalent ions, and negatively charged solid particles as a result of a very alkaline environment. The DLVO theory of colloid stability can be used to explain the stability of air bubbles in terms of the interaction between electrical forces between particle surfaces and attractive dispersion forces. The presence of charged colloidal particles in an electrolyte solution causes electrostatic interactions that affect the paste behavior. A particle's charge may come from surfactants, adsorbed ions, or dissociated charge groups. The negatively charged surface of the ash particles absorbs the cationic surfactant at a high pH (CTAB) [329]. The interaction between the surfactant molecule on the surface of the air bubble and the charged particle will result in high bubble surface stability, reducing the possibility of coalescence [330]–[332]. The scenario is different for anionic surfactants, as SDS is not as strongly attracted to negatively charged particles; nonetheless, the existence of multi-positive ions, such as calcium, can act as a bridge between the negatively charged solid and the surfactant molecule (**Fig. 5.15**). To conclude, SDS interactions are substantially weaker than cationic CTAB interactions, which impacts the ability to adhere bubbles or appear in extremely close contact, while maintaining greater stiffness at the liquid-vapour boundary than in non-enriched air bubbles, which promotes the formation of pore cavities.

The non-ionic surfactant is another component of a binary system (Tween 60 and Triton X-100). Because they are non-ionic, these surfactants do not adsorb strongly on charged surfaces. This reduces the unwanted loss of surfactant access at the solid-liquid interface while increasing surfactant availability at the liquid-vapour interface to saturate that surface [333]. Non-ionic surfactants exhibit the lack of characteristics required for appropriate air bubble stabilization, resulting in coarsening and coalescence. However, in a binary system with ionic surfactants, non-ionic Triton X-100 or Tween 60 can boost the solubility of ionic surfactants in the binary (cosurfactant) system and diminish the ionic surfactant's tendency to adsorb at the interface solid-liquid interface [333]. In the case of SDS-containing systems, a synergistic co-adsorption is proposed, in which a marginal co-adsorption occurs on negatively charged surfaces of mixed micelles even though SDS alone would not adsorb [334]. Moreover, the interaction between an anionic SDS and polyvalent cations increases at higher pH, thus a bridging effect between the negatively charged surface and SDS via cation can be observed (**Fig. 5.15**) [335], [336]. Although, as explained above for the CTAB scenario, this interaction may contribute to the improved stabilization of air bubbles in anionic-contained mixtures. However, interaction in a mixed system cationic-nonionic entails poorer interactions with negatively charged particles in a solution containing a cationic CTAB, as well as the potential of links between air bubbles close enough to form cavities.

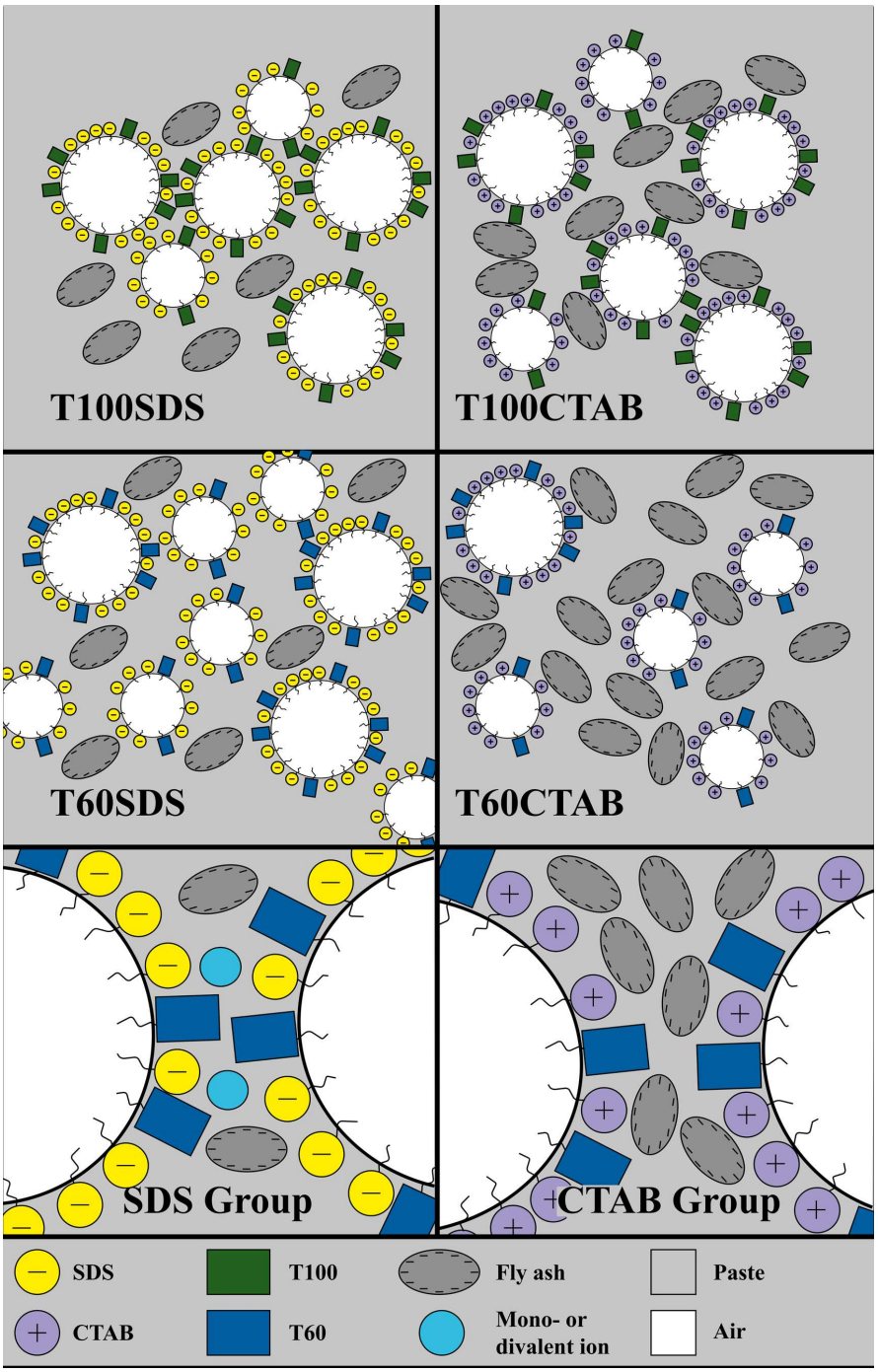

Fig. 5.15 Interaction mechanism between air bubbles stabilized by different binary surfactants mix and fly ash particles governing pore connectivity.

Moreover, because of the synergy between the surfactants used and the lower Critical Micelle Concentration (CMC_{mix}) value compared to pure ionic surfactant, the micelles formed in large quantities can be tightly packed in the structure, and the described properties of disjoining pressure prevent excessive aggregation and bubble rupture [337]. When the thin liquid film evaporates, connections between the pores, and small cavities in the thin walls separating the bubbles, may form in both systems based on CTAB and SDS. This phenomenon is owing to a decrease in surface tension caused by more migration of nonionic surfactant to the surface layer and a reduction in electrostatic self-repulsion between head groups in the ionic surfactant (**Fig. 5.15**). Additionally, the variation in the pore size can be expected, due to the different hydrophilic group structures [338]. Furthermore, the surfactant, which creates lower surface tension, is responsible for creating finer air bubbles [339]. This explains why Tween 60 results in lower pore sizes (a high fraction of pores less than 5 μm) in both T60CTAB and T60SDS (**Fig. 5.7)**.

5.4.2 *Potential application areas driven by pore size and connectivity*

Based on the present results, it is feasible to construct a list of morphological traits, and more specifically, the potential of various application areas. **Table 5.10** depicts the primary pore morphological traits that suggest the potential for usage in areas such as high temperature, fire protection, and thermal and acoustic insulators. Materials with a predominantly closed porosity are better thermal insulators than open structures attributed to the facilitated flow of heat through cavities [340]. Therefore, the T100CTAB with the lowest thermal conductivity coefficient value can be chosen as a thermal insulator.

The composites used in this work are made of a solid aluminosilicate skeleton which provides high-temperature stability [12]. In addition to the beneficial effects of the chemical and mineralogical composition, the role of open-pore structure in minimizing thermal shrinkage and cracks formation at high temperatures is significant, as indicated by Bell and Kriven [341] and Sarazin et al. [342]. The aforementioned fire resistance can be achieved by structures with low conductivity and well-connected pores, reducing the pore pressure both during heating and water release by evaporation, as well as during extinguishing / cooling the heated structure from high temperatures (e.g. 1100 ^{o}C). Assuming that the greater the open porosity and gas permeability, the lower the material's ability to degrade under the pore pressure caused by moisture migration and temperature difference, materials with the greatest open porosity and moisture absorption were proposed (T100SDS, T60SDS). When the water in the porous structure is heated to a high temperature, a highly endothermic process occurs, increasing the material's fire resistance [343]. As a result of this reaction, gaseous water (water vapour) is created, which is then transferred through the porous structure to colder regions where it condenses. The situation described above illustrates the combined influence of hygrothermal performance and pore structure on fire resistance.

Furthermore, geopolymer-based foams have the potential to be employed as acoustic barriers. Several studies were focused on the acoustic characteristics of direct-foamed alkali-activated materials [21], [22], [26], [344], [345]. Peceño et al. [346] stated that the materials with larger total porosity absorb sound better because the sound penetrates their matrixes and dissipates the sound energy. Moreover, open pores

generate continuous pathways between the interior and outside of the material matrix, resulting in enhanced permeability and good sound absorption capacity.

Table 5.10. Summary of pore morphology and possible application of geopolymer foams.

	T100SDS	T100CTAB	T60SDS	T60CTAB
Pore morphology	Highly-porous Majority of pores between 200-500 μm Open-pore structure	Highly-porous Pores above 500 μm not observed Low connectivity	Highly-porous High content of pores below 5μm Open-pore structure Open porosity-strength balance	Low total pore volume High content of pores below 5μm System of closed pores
Potential application	High-temperature Fire-protection Acoustic insulation	Thermal insulation	High-temperature Fire-protection Acoustic insulation	N/A

Hence, two composites with the highest total porosity and open-pore volume are additionally proposed for sound absorption application. Each of these solutions aims to demonstrate how we may direct porosity to the needs of the application by utilizing a well-determined mix of surfactants based on a similarly constituted geopolymer matrix. However, more research on the subject is required to ascertain the materials' viability for the suggested purposes. In the following chapter, the sounds absorption capacity of one of the selected mixed is examined and in C**hapter 7**, the high-temperature response of the three porous composites is evaluated.

5.5 Conclusions

This chapter aims to propose an economical method of developing porous geopolymers with a tailored pore structure. The synergetic effect between non-ionic and ionic surfactants is revealed and its influences on the porosity, pore size distribution, pore connectivity, compressive strength and potential thermal insulation are discussed. The amount of utilized surfactants in this research is greatly decreased in this research while maintaining a similar porosity compared to existing literature. This study demonstrates that a combination of non-ionic with ionic is an effective technique in the design of foamed materials. The following detailed conclusions have resulted from this study:

- The interactions of ionic surfactants with particles improve the stability of air bubbles. Because of the negative charge of the ash particle surface in the alkaline environment, stronger surfactant-solid particle attractions are seen for the cationic surfactant, as evidenced by a higher proportion of closed pores and a lack of air voids above 500 μm. These interactions are diminished by the incorporation of nonionic surfactants, and the electrostatic repulsion between head groups is reduced, increasing the potential of open porosity development and rising ionic surfactant molecules availability to stabilize air bubbles.

- In comparison to ionic surfactants, lowering the CMC of the combined solution results in more densely packed bubbles. It helps to create pore cavities by decreasing the distance between bubbles. In addition, lowering CMC causes composites to have a high porosity (70 vol.%), which enhances thermal insulation but diminishes mechanical performance.
- Cationic-contained systems favour small pores formation, whereas anionic systems supply the majority of pores larger than 200 μm. A majority of voids between 50-200 μm, as well as a larger proportion of pores between 5-50 μm, are found in both cationic-based systems, independent of the kind of nonionic surfactant used.
- The geopolymer is superior at controlling the moisture content inside the material compared to commercial reference gypsum plaster. Thanks to its greater moisture storage function at lower relative humidity, the geopolymer has a stronger humidity buffering ability to moderate changes in the relative humidity of surrounding air. The variation in its effective thermal transmittance throughout the year is reduced by regulating its moisture content. The composite with the largest proportion of closed porosity (nonionic+cationic) shows the best thermal insulating performance.
- The relationship between compressive strength and porosity may be predicted at a porosity above 75 vol.% using the Ryshkevich model. In the lower porosity region, pore size distribution is more important than total porosity in the evolution of mechanical resistance. The materials obtained in this investigation are characterized by relatively low compressive strength, which is mainly due to the low raw material reactivity and high content of large air voids and relatively high open porosity.
- Two SDS-based composites with the highest total porosity and open-pore volume are recommended for use in sound absorption, fire resistance, and high-temperature applications, while a CTAB-based composite with the highest closed-pore content and high total porosity is recommended as a thermal insulation material.

CHAPTER 6 EFFECT OF SILICA AEROGEL ON THERMAL INSULATION AND ACOUSTIC ABSORPTION OF GEOPOLYMER FOAM COMPOSITES

Silica aerogel features superthermal insulation and excellent sound absorption. The application of silica aerogel in building materials for energy saving has been investigated recently. However, the role of aerogel on geopolymer foam render is rarely studied although it can be crucial. In this research, two raw materials and two volume replacements of silica aerogel are applied to improve the thermal insulation and acoustic absorption performance. The microstructure is investigated in-depth with micro-CT and optical microscopy. The geopolymer foam based on biocoal fly ash and enriched with 10 vol.% silica is considered as an optimal mix design. The material reaches a thermal conductivity of 0.111 W/(m·K), an average acoustic absorption coefficient of 0.51 with a bulk density of 746.4 kg/m3. The result of this study is essential to enlighten the use of silica aerogel particles in geopolymer foam render, focusing on a low dosage of silica aerogel while utilising its full benefit.

The results presented in this chapter are partially shown in the following article:

Y.X. Chen, K. M. Klima, H.J.H. Brouwers, and Q.L. Yu, "Effect of silica aerogel on thermal insulation and acoustic absorption of geopolymer foam composites: The role of aerogel particle size" Compos. Part B Eng., vol. 242, p. 110048, (2022).

6.1 Introduction

Due to the overall growing awareness of sustainability and quality of life, the construction sector's energy efficiency and the comfort of the indoor living environment have gotten a lot of attention [347]–[349]. In wealthy nations, the construction industry accounts for over 40% of total energy and CO_2 emissions [350]. For the time being, several nations have implemented measures to reduce heat loss via building assemblies [5]. Furthermore, the functionalization of insulating materials is critical [351], [352], for example, enhancing acoustic absorption performance to improve the quietness of the interior environment and minimize noise pollution from daily life [353]–[355]. As a result, there is a pressing need to create novel high-performance insulating lightweight materials [356], [357].

Silica aerogel [358], [359] is a super-insulating inorganic material made out of a 3D network of crosslinking silica nanoparticles and 95% to 99% air. Because of its large porosity and low solid thermal conductivity, silica aerogel has a very low effective thermal conductivity, typically ranging from 0.012 to 0.018 W/(m·K) [360], [361]. Due to the brittleness and easy breakability of silica aerogels, commercial silica aerogels are always generated as powders or particles [362]. To enable its advantages, it is frequently mixed into other matrices, such as fibreglass mats or other lightweight materials [363]–[365]. As shown in **Table 6.1**, several studies on the inclusion of silica aerogel in construction materials have already been conducted. Ng et al. [366] produced high-performance aerogel concrete with a bulk density of 1300 kg/m^3 and a thermal conductivity of 0.4-0.5 W/(m·K), respectively. The concrete has a low water-to-binder ratio of 0.20 to 0.25 and a 50 % to 70 % silica aerogel replacement ratio with sand. Tao et al. [367] created a conventional cement mortar with a 60% aerogel replacement ratio that has a compressive strength of 8.3 MPa and thermal conductivity of 0.26 W/(m·K). Julio et al. [368] produced lightweight aerogel aggregate concrete with a 100 % silica aerogel to sand replacement ratio, yielding concrete with a low thermal conductivity of 0.085 W/(m·K) but a compressive strength of just 0.41 MPa. Seo et al. [369] studied the silica aerogel utilized in fly ash/slag geopolymer concrete at concentrations ranging from 25% to 75%. Thermal conductivity, on the other hand, is rather high, at 0.8 W/(m·K). Zhu et al. [370] looked at the inclusion of silica aerogel in cement-based mortars and coatings. With a compressive strength of 1.4 MPa, it has low thermal conductivity (0.17 W/(m·K)).

Specifically, silica aerogels are utilized to substitute normal-weight aggregate in order to minimize heat conductivity and increase insulating characteristics. However, the concentration of silica aerogel is rather high, implying that the resultant materials are expensive and difficult to use in the actual world. Finding a clever way to employ silica aerogel and selecting a cost-effective lightweight construction material for silica aerogel to permit its ultra-insulating capability is therefore critical.

An optimization may be made to alleviate the difficulties, either by lowering the quantity of silica aerogel utilized or by employing a low-conductive porous matrix. Furthermore, substituting the Portland cement-based matrix with a geopolymer with improved thermal characteristics can be used to optimize the composite mixture and retain adequate thermal and acoustic performance.

Table 6.1. Comparison of lightweight insulating concrete with the addition of silica aerogel.

Authors	Raw materials	w/b	AG RR/ PS	BD (g/cm^3)	CS (MPa)	λ (W/(m·K))	Literature
Ng, et al.	CEM, quartz fines, SF, AG, SP	0.2-0.25	0-80% 0.01~4 mm	0.8-2.3	5-150	0.3-2.3	[366]
Ng, et al.	CEM, quartz fines, SF, sand, AG, SP	0.2	60-70% 0.01~4 mm	~	5-19	0.12-0.53	[371]
Tao, et al.	CEM, SF, sand, SP and AG.	0.4	0-60% 2~4mm	1.00-198	8.3-60	0.26-1.86	[367]
Júlio, et al.	CEM, AG, surfactant	0.66-1.2	100%	0.218- 0.412	~	0.080-0.098	[368]
Seo, et al.	FA, slag, activator, AG	0.5	25/50/75%	1.28-1.53	13-28	0.9-1.8	[369]
Zhu, et al.	CEM, SF, SP, Sand, AG	0.4	33~67% 1.2–4 mm	0.74~1.55	1.4~13.0	0.17-0.40	[370]

Note: AG-aerogel, CEM-cement, SF-silica fume, SP-superplasticizer, RR-replacement ratio, PSD-particle size, BD-bulk density, CS-compressive strength, TC-thermal conductivity

Thermal insulating renders are one option, with thermal conductivities typically less than 0.2 W/(m·K) and densities comparable to ultralightweight concrete [372]. Despite its ability to insulate, cement used in the production of ultralightweight concrete, has a significant negative impact on the environment, particularly in terms of greenhouse gas emissions [373]. Geopolymer foam render is a potential solution in terms of decreasing CO_2 footprint and cost. Fly ash-based geopolymer [29,30] is a promising alternative construction material that is made by activating an aluminosilicate source, such as fly ash, with a strongly alkaline silicate solution (MOH and $(Na_2O)_x \cdot SiO_2$ M=Na, K) [258], [374]. Because of the bonds formed [375], it is possible to achieve good high-temperature resistance, which is improved further by using a potassium-based activator rather than a sodium-based activator [139]. Moreover, the use of industrial by-products in geopolymer features low energy consumption and is environmentally friendly, providing enhanced sustainability from material manufacture to construction operation [376], [377].

Apart from the environmental aspect, the geopolymer also is a promising binder for thermal insulation applications due to its relatively low heat conductivity [378]. However, various methods can be used to further reduce the thermal conductivity coefficient of a sole geopolymer-based matrix. Thus, to attain the required effects, the material must be enriched with a phase with a much lower thermal conductivity, such as silica aerogel. Huang et al. [379] demonstrated that combining geopolymer with silica aerogel may provide low thermal conductivity and sufficient sample mechanical properties, demonstrating the possibility of manufacturing an aerogel/geopolymer composite for insulation applications.

Another route for obtaining a material with a lower λ is to introduce air as the low thermal conductivity phase, resulting in a foam composite [15], [342], [380]. Chemical foaming agents or mechanical foaming techniques may be utilized to form the porous structure of geopolymer foam concrete, all of which provide a significant number of pores inside the geopolymer matrix [381]–[383]. However, depending on the desired pore structure, several approaches may be more suited. When it comes to chemical aeration, hydrogen peroxide (H_2O_2) is the most cost-effective and simple to use [264], [265], [384]. Surfactant specificities and mixing ability, on the other hand, can be employed to reduce total critical micelles concentration (CMC), resulting in a greater number of micelles formed and improved foam stability, as presented in **Chapter 5**.

An increase in H_2O_2 concentration alone may cause air bubbles to escape and clump together, promoting the formation of large air gaps that lower mechanical strength [263]. The number of bubbles reduces but their dimension grows as the quantity of the foaming agent is raised [268]. Although increasing the quantity of surfactants can assist to alleviate the negative consequences of this phenomenon, research has shown that too much surfactant has a negative influence on compressive strength [385]. Moreover, reduced surfactant concentrations reduce the overall volume of linked pores, lowering acoustic absorption.

Furthermore, the high water absorption of extremely porous concrete is a matter of concern [386]. Different heat transfer behaviour across the building envelope might be caused by soaking and drying porous building materials [387]. It is acknowledged that silica aerogel could increase the hygrothermal properties in insulation renderings [388], however, the effect of different raw material interactions with silica aerogel used for the same manufacturing route has not been studied yet. Also, the acoustic absorption of plain foam concrete is relatively low, due to the low pore interconnectivity with no multiscale pore size in the matrix. As a result, more thermal insulation and acoustic absorption are required, but moisture transport through the foam concrete is reduced. The use of silica aerogel is believed to improve the material's porosity while simultaneously maintaining a wide variety of pore diameters and reducing bubble coalescence.

The influence of raw material on the thermal insulating and acoustic absorption performance of a geopolymer foam aerogel composite with the addition of a low dosage silica aerogel (10 vol % and 20 vol %) is investigated in this work. Optical microscopy and a micro-CT test are used to analyze the microstructure of geopolymer foam aerogel composite. The thermal conductivity test and the acoustic impedance tube method are used to evaluate the porous composite performance.

6.2 Materials and methodology

6.2.1 *Starting materials*

Cabot provided four different types of silica aerogel: IC3100, IC3110, IC3120, and LA1000. The particle size and translucency of the silica aerogels varied. The particle sizes of IC3100, IC3110, IC3120, and LA1000, respectively, are 2-40 μm, 100-700 μm, 100-1200 μm, and 700-4000 μm. The particle size distribution of silica aerogel is displayed in **Fig. 6.1 (a),** as well as the curves of the mix employed in this investigation, which is estimated using sieving. A mixture of four different silica aerogel materials is used to achieve a broad particle size distribution of SA. The plotted distribution of SA+fly ash particles (**Fig.6.1 (b)** blue curve) was presented with the optimal curve using optimal packing calculated from a modified A&A model.

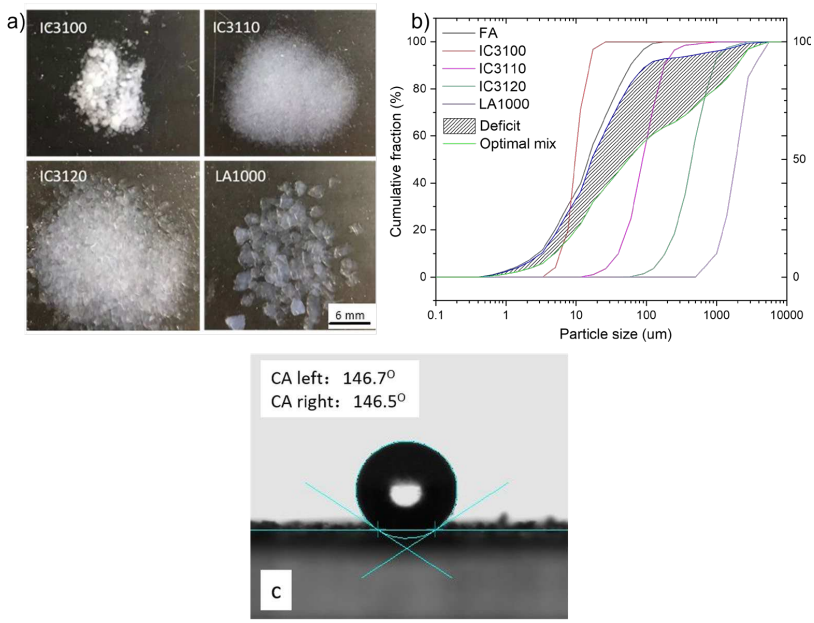

Fig. 6.1. (a) morphology of four types of silica aerogel (b) Particle size distribution of fly ash and silica aerogel (c)water contact angle of IC3100.

Table 6.2. Physical properties of the four types of silica aerogel.

Groups	Particle size* (μm)	SSA (m^2/g)	Pore size (nm)	BD (g/cm^3)*	λ* (W/(m·K))
IC3100	2~40	699	14.0	0.12-0.15	0.012
IC3110	100~700	688	12.5	0.12-0.15	0.012
IC3120	100~1200	694	13.1	0.12-0.15	0.012
LA1000	700~4000	683	12.4	0.12-0.15	0.018

*Data provided by Cabot. SSA-Specific surface area; BD: Bulk density; λ-Thermal conductivity

The silica modulus of molar SiO_2/K_2O 1.4 and 5.5 wt.% K_2O on dry fly ash were reached by mixing potassium hydroxide pellets (VWR life science, reagent grade) and potassium-silicate solutions for the manufacture of geopolymer matrix (WHC, K_2O 8 %, SiO_2 20.8 %, 72.8 H_2O by mass). Before applying for geopolymer preparation, the as-prepared activator solution was kept for 24 hours to establish equilibrium. As a chemical foaming agent, hydrogen peroxide (30 %, Sigma-Aldrich, Germany) was used in conjunction with the surfactant mix solution, non-ionic Triton X-100 (VWR chemicals), and anionic sodium dodecyl sulfates (SDS) (98 % purity, Sigma-Aldrich, Germany). The solid precursors for geopolymer production in this study were coal combustion fly ash (Vliegasunie) and biocoal fly ash (Vliegasunie). Their oxide and mineral compositions, as well as potential reactivity, are presented in **Chapter 4** and **5** [389].

6.2.2 *Methodology*

Preparation of the geopolymer foam aerogel concrete

The mix design of the paste is shown in **Table 6.3**. The detailed preparation description is as follows:

(1) Dry components homogenization

The dry components (fly ash and silica aerogel) were mixed in a 5-litre Hobart mixer until homogenized (60s) at a low mixing speed to avoid silica aerogel breakage. The indoor conditions are indoor temperature of 23 °C and relative humidity of 35%.

(2) Slurry preparation

Homogenized powder and the activator solution were stirred and mixed evenly at low speed (30s), To guarantee that there are no powdery remains on the bottom and sides of the mixer, mixing was stopped and the bowl was scraped manually. Furthermore, the slurry was mixed at high speed for 60 seconds.

(3) Foaming

A foaming ingredient, hydrogen peroxide (30%), was introduced while mixing at low speed, followed by two prepared surfactants, Sodium Dodecyl Sulphate and Triton X-100. After adding the surfactants, the rotation speed was raised, and the paste was stirred for 30 seconds. The same controlled indoor conditions 23 °C and relative humidity of 35% apply.

(4) Casting and hardening

The composites were cast into moulds of 40×40×160 mm^3, 100×100×100 mm^3 and cylindrical moulds H:50 mm r:40 mm. All samples were sealed with a plastic film and cured for 24 hours at 23 °C, RH 35%.

(5) Demoulding and curing

After 24 hours the samples were demolded, wrapped in a plastic film and cured for 24 hours at 60 °C in the oven.

(6) Ageing

After the elevated temperature curing, specimens were stored for a further 26 days at room temperature (23 °C) and relative humidity of 35% ± 5%

Table 6.3 Recipe of geopolymer foam aerogel composite (kg/m^3).

Groups	FA	BFA	Activator	HP	SDS	T100	IC3100	IC3110	IC3120	LA1000
AG-0	1172		421.9	7.9	3.5	2.6	-	-	-	-
AG-10	1055		379.7	7.1	3.1	2.3	0.67	1.67	2.87	3.67
AG-20	938		337.5	6.3	2.8	2.1	1.33	3.34	5.74	7.34
BG-0		1172	421.9	7.9	3.5	2.6	-	-	-	-
BG-10		1055	379.7	7.1	3.1	2.3	0.67	1.67	2.87	3.67
BG-20		938	337.5	6.3	2.8	2.1	1.33	3.34	5.74	7.34

Note: FA-siliceous fly ash; BFA biocoal fly ash; HP-Hydrogen peroxide; SDS-Sodium dodecyl sulphate; T100-Triton X 100; Aerogel volume percentage 10 means 10%, 20 group: 20 vol.% aerogel was added.

6.3 Results and discussions

6.3.1 *Physical and mechanical properties of composite*

The bulk density, skeleton density, porosity, and compressive strength are presented in **Table 6.4**. It can be observed that the dry bulk density is related to the dosage of aerogel. The more silica aerogel in the fresh paste, the lighter the paste will be. This is due to the silica aerogel particles occupying some of the solid parts in the fresh paste. Moreover, the key finding is that geopolymers made from biocoal fly ash have a larger pore volume than siliceous fly ash, resulting in a lower bulk density. It is noteworthy that the lowest density is achieved for the AG-20 and BG-20 samples, in which the aerogel content reaches 20% of the total volume of the paste. Therefore, it can be stated that the addition of silica aerogel could result in the formation of more voids that are provided by the aerogels.

The skeleton density is related to the inherent properties of the raw materials. The skeleton density measured by the pycnometer is almost the same for all specimens, which is due to the fact that all the raw materials used are fly ash and silica aerogel. Therefore, the skeleton density is in the range of 2279 kg/m^3 to 2330 kg/m^3, with very small deviations.

The porosity is calculated according to the dry bulk density and skeleton density. As presented in **Table 6.4.** The lowest porosity is 62.3 %, obtained from the plain AG-0 geopolymer foam concrete. An intriguing phenomenon is that the porosity of the material of 10 % and 20 % for both materials are comparable, although the starting porosity of the biocoal matrix was greater. As mentioned in **Chapter 5**, in the instance of biocoal, a flash setting was observed, which decreased the setting period and made buoyancy escape difficult.

In the presence of surfactants, the hydrophobic silica aerogel particles will tend to be in the non-aqueous phase, which in this case is the gas phase (air) in the pores, thus the hydrophobic solid particles (silica aerogel) remain attached to the air-water contact surface [390]. Furthermore, the hydrophobic attraction [391] due to the van der Waals forces in an air-water-air system [392] will enhance this activity. As a result, the molecules can cluster in the air-containing pores. According to Wang et al. [393], hydrophobic particles stay in contact with the air bubble for a long period. As a result, the silica aerogel particles are likely to remain in close contact with the air bubble, and once the paste reaches the initial setting time, the particles are entrapped in the structure, making the further movement of particles impossible. This mechanism could explain why big particles are found close to the pores, reinforcing their structure and playing the role of the skeleton of the gas phase (air) trapped in the liquid phase (paste). As shown by Chen et al. [344] the most porous structure can be achieved by the addition of large grain size silica aerogel solely. To be specific, the 700-4000 μm silica aerogel has the best pore generation.

It is also possible that the hydrophobic tail of a surfactant can become trapped on the surface of a silica aerogel, which could potentially reduce the surfactant's ability to stabilize air bubbles. This is because the hydrophobic tail of a surfactant is repelled by the hydrophobic surface of the aerogel, causing it to become trapped on the surface. The trapped surfactant molecules may not be able to interact with the air bubbles as effectively, leading to a reduction in the surfactant's ability to stabilize them. It is worth noting that the effectiveness of a surfactant in stabilizing air bubbles can also be influenced by a variety of other factors, such as the surface tension of the liquid, the size and shape of the air bubbles, and the nature of the surfactant itself. Although the hydrophobic surface of a silica aerogel and the hydrophobic tail of a surfactant may not be attracted to one another, the surfactant molecules can still become trapped on the surface of the aerogel due to van der Waals forces. In the case of a hydrophobic surfactant and a hydrophobic surface, the van der Waals forces may be the only attractive forces present between the two, and they may be sufficient to cause the surfactant molecule to become trapped on the surface.

The compressive strength at 28 days is presented in **Table 6.4**. The reference sample AG-0 has a compressive strength of 2.52 MPa, and the significantly lower strength of BG-0 is partially related to the flash setting and also higher total porosity than AG-0. With the addition of silica aerogel, the samples show lower strength as expected, which is attributed to the low strength of silica aerogel (10-100 kPa) [361]. This result can be explained by the total porosity as discussed above.

Table 6.4 Bulk density, skeleton density, total porosity and strength of the specimens.

Groups	Bulk density (kg/m³)	Skeleton density (kg/m³)	Total Porosity (%)	Compressive strength 28d (MPa)
AG-0	873.0±3.6	2312±0.9	62.25±0.20	2.52±0.10
AG-10	770.5±3.6	2330±7.1	66.94±0.26	1.60±0.07
AG-20	715.3±2.9	2315±1.0	69.10±0.14	1.45±0.03
BG-0	780.1±1.9	2318±5.2	67.19±0.31	1.82±0.20
BG-10	746.4±2.2	2306±1.3	67.63±0.12	1.54±0.23
BG-20	694.7±2.7	2279±2.9	69.52±0.09	1.40±0.14

As expected, the 20% dosage aerogel sample BG-20 has the lowest strength, however, due to the porous structure, it could have a better insulation performance. Another aspect is the weak bonding between the paste and the filler (silica aerogel particles) in the BG-10 sample which possesses similar pore volumes to BG-0, but lower mechanical performance.

6.3.2 *Microstructural analysis: Micro-CT*

The software IPLFE v1.16 (Scanco Medical AG, Switzerland) is used to analyze the pore distribution of the developed composites on a 3D slice view. The pixel intensity is related to the density of the object, making it possible to separate the surrounding air, air voids and aerogel particles from the denser matrix. However, the density difference between air and silica aerogel is small, making the distinction between air and aerogel rather difficult.

A distance transformation is applied [52] which enables the collection of the data in the 3D visualisation form in a 3D model of the sample. The empty region surrounding the geopolymer is turned into a solid by filling. Following the identification of all pores on the surface and inside the prescribed contour, the pores are coloured differently depending on the size of the examined pore/particle [53]. It can generate a 3D-pore shape visualization in all geopolymer renderings using the data gathered in this way on both the distribution and size of the pores (**Fig. 6.2**). Noteworthy, during this investigation, the μCT covers the pores above 10 μm which provides limitations related to small size pores. The pore size is divided into the groups related to the silica aerogel particles used in order to see the variations between samples (**Table 6.5**). The porosity below the detection threshold (10 μm) is calculated using the porosity estimated by the μCT and pycnometer technique.

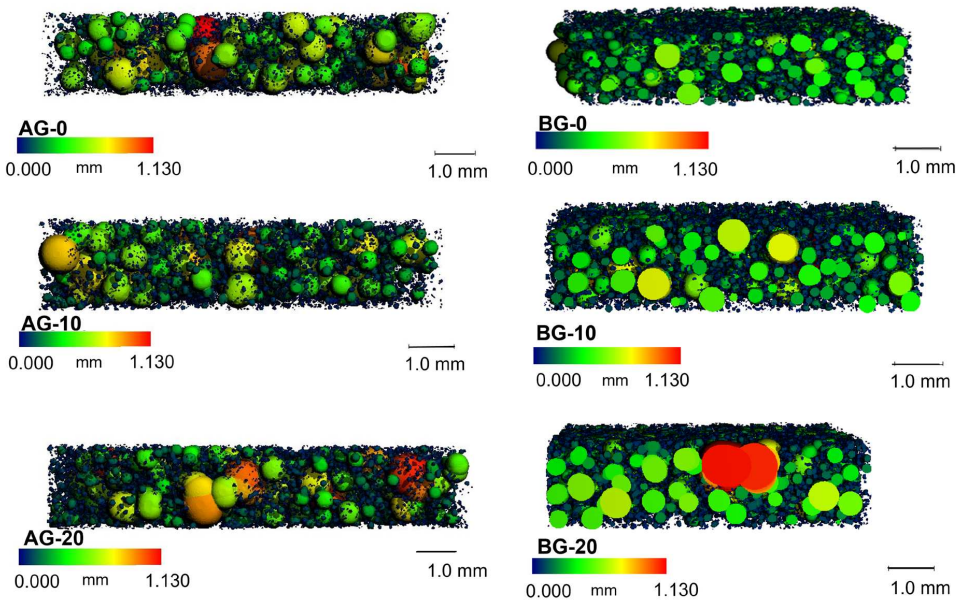

Fig. 6.2. Isolated air voids and silica aerogel particles system.

The goal of the porosity distribution analysis is to check how silica aerogel particles affect the pore size distribution of the porous composite. The size of the silica aerogel particles is used to establish the prescribed intervals to observe their possible impact on the pore size, which is also related to the presence of these particles in the matrix (**Table 6.5**). Empty gaps with a restricted range of sizes are undesirable because they influence the material's acoustic and strength characteristics. The size and distribution of pores in the materials are depicted in **Fig. 6.2**, where the order of magnitude has been standardized in the form of a colour scale, allowing for comparison of the matrices obtained.

The first observation concerns the considerably smaller pore diameter in BG samples compared to AG samples (**Table 6.5**), which may be related to the setting time, which is clearly shortened due to the observed flash setting, resulting in a significantly reduced amount of pores above 700 μm compared to AG samples. The introduction of particles with a size of up to 4000 μm into the system causes an increase in the proportion of pores exceeding 700 μm (IC3120, LA1000). In AG samples, there is a higher number of pores below 10 μm and above 700 μm, whereas BG has shifted toward the range of 10-700 μm. The porosity values obtained for all six samples are 60-70 %; however, the size distribution varies, which is mostly driven by the properties of fresh paste, which affects bubble coalesce and/or bubble splitting [331].

The open porosity calculated from μCT is presented in **Table 6.6**. Open porosity is important in determining acoustic absorption and hygrothermal performance. The open porosity increases with increasing particle size and concentration.

Table 6.5. Pore size distribution retrieved by μCT and total porosity measurement.

		Pore volume in the range (μm)				
	Overall porosity (%)	**<10**	**[10,50)**	**[50,100)**	**[100,700]**	**>700**
AG-0	62.3	24.5	1.1	0.5	23.0	13.1
AG-10	66.9	20.3	1.5	1.2	24.0	19.9
AG-20	69.1	23.0	1.7	1.6	25.9	16.9
BG-0	67.2	11.9	2.0	4.0	45.9	3.4
BG-10	67.6	8.1	2.4	4.4	52.4	6.9
BG-20	69.5	9.6	2.7	5.9	44.2	7.1

During the pore separation process, the resulting void spaces are examined for connection to identify individual objects, and their volume, as well as connectivity [52]. The entire group based on biocoal fly ash has a higher degree of open porosity, resulting in superior acoustic insulation properties. It is influenced by the pore size distribution which results in more bubble-packed structures which enable the formation of pore cavities. Furthermore, it can be shown that the rise in the volume of open pores increases with the increase in volumetric replacement by silica aerogel in each group, i.e. AG and BG. This implies the presence of silica aerogel particles near the bubbles, resulting in the formation of a bridge between the two bubbles, which during μCT analysis is considered as a pore connection.

Table 6.6. Open porosity of porous materials calculated from μCT.

Sample code	AG-0	AG-10	AG-20	BG-0	BG-10	BG-20
Open porosity vol.%	36.6	44.4	47.1	54.1	58.0	59.4

6.3.3 *Thermal conductivity of composites*

The thermal properties of the composites with different silica aerogel dosages are presented in **Table 6.7.** The reference sample shows the highest thermal conductivity of 0.173 W/(m·K). Noteworthy, the entire group of biocoal fly ash-based composites are characterized by lower conductivity value due to the higher total porosity and possibly, lower conductivity of the raw material, namely biocoal fly ash and siliceous fly ash.

On the other hand, the 20% silica aerogel AG-20 shows the best thermal insulation, reaching 0.135 W/(m·K) and 0.101 W/(m·K) for BG-20. This indicates the incorporation of more silica aerogel can decrease the thermal conductivity as expected. The silica aerogel plays a role as an insulating filler with ultra-low thermal conductivity in the geopolymer matrix, thus reducing the thermal conductivity of the samples.

Since silica aerogel particles are solid particles, they prevent the uninterrupted transfer of heat, which reduces the effective thermal conductivity of the designed composites, thus playing the role of closed pores in the system. It is important to note that the aerogel does not appear to have absorbed water or dissolved in the activator, both of which would have lessened this effect. Moreover, silica aerogel particles can create more inter-particle pores in the geopolymer matrix. The thermal insulation is closely related to the total porosity of the foam geopolymer. As can be referred to in **Table 6.4**, the total porosity for AG-0 is lower than BG-0, thus this factor can influence the thermal properties, as less heat was transported through the solid, i.e. less solid conductivity is contributed to the total effective thermal conductivity of the material.

Overall, the thermal conductivity is reduced with the increasing concentration of silica aerogel, thanks to the superior thermal insulation of silica aerogel. Therefore, the larger volume replacement (20 vol.%) particle size of aerogel in biocoal ash-based geopolymer can even function better as a thermal insulator, due to the creation of more interparticle pores, increased total porosity, and also the optimized distribution and stability of the pores in the matrix.

Table 6.7. Thermal conductivity of the composite.

Groups	AG-0	AG-10	AG-20	BG-0	BG-10	BG-20
λ (W/(m·K))	0.173	0.152	0.135	0.116	0.111	0.101

The thermal conductivity versus the density and compressive strength versus the thermal conductivity of building materials with the addition of silica aerogel particles are shown in **Fig. 6.3 (a)** and **(b),** respectively. Compared with the composites prepared in this study, other materials with silica aerogel have higher thermal conductivities. The UHPC aerogel concrete obtains similar thermal conductivity, but the silica aerogel loading is much higher, replacing 70% of the natural aggregate. Cement-based aerogel foam concrete has a lower density, showing a linear trend as the silica aerogel dosage increased from 20% to 70%. The thermal conductivity decreases from 0.164 to 0.07 W/(m·K). Cement aerogel render shows a higher thermal conductivity at the same density range as composite. Also, the AIC (aerogel-incorporated concrete) obtains higher density because coarse aggregate is used, showing a linear trend as well. Alkali-activated fly ash/slag concrete with silica aerogel has an even higher thermal conductivity than AIC, mainly because the used sand is much more conductive compared to the replaced aerogel. Cement aerogel mortar coating has a higher density and thermal conductivity. It is noteworthy that the composite has the lowest thermal conductivity in the specific density range compared to other aerogel-incorporated samples.

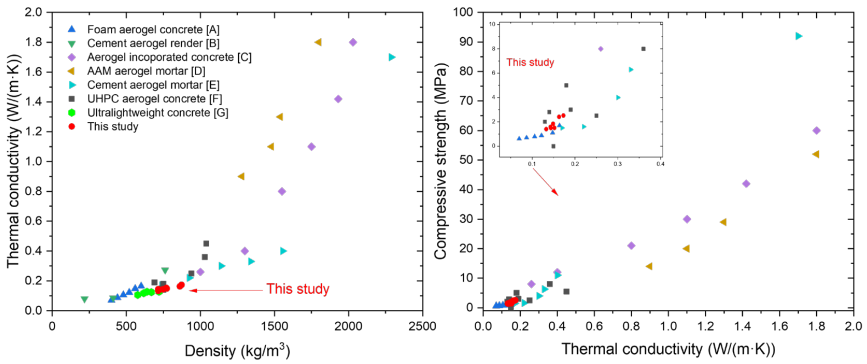

Fig. 6.3. (a) Thermal conductivity vs density (b) Compressive strength vs thermal conductivity of composites with other aerogel-incorporated building materials A: [394]; B: [368]; C: [367]; D:[369]; E: [395]; F: [371]; G:[357].

The comparison of compressive strength with other aerogel-incorporated materials is shown in **Fig. 6.3 (b)**. It is noteworthy that the compressive strength of specimens is only slightly lower than UHPC aerogel concrete. This is mainly because the UHPC recipe has a very low water-to-binder ratio of 0.20 to 0.25 and a better packing of the mixtures. For other materials with the addition of silica aerogel, the compressive strength is lower, which is attributed to the higher loading of silica aerogel to 50%, resulting in a lower strength. For the porous geopolymers, the aerogel loading is only 10%, while still reaching a lower thermal conductivity. Therefore, the optimized geopolymer foam matrix plays an important role. The less silica aerogel in the matrix, the fewer defects the interface of materials could have, thus leading to higher compressive strength.

6.3.4 *Water uptake and the effect on thermal conductivity*

The water uptake of the samples at 80% humidity environment chamber and its effect on thermal conductivity is shown in **Fig. 6.4**. The water uptake of the reference sample BG-0 is the highest, reaching 7.69%. This higher water uptake causes a significant rise in thermal conductivity, which shows a rise to 0.162 W/(m·K), increasing by 39.7% compared to the sample under 100% dry conditions. As can be observed, the silica aerogel incorporated samples show lower water uptake. Especially, the difference is visible for BG-0 and BG-10 samples, characterized by similar porosity, however, the water uptake was 7.7% and 6.0%, respectively (**Fig. 6.4**). This is attributed to the hydrophobic nature of silica aerogel, as shown in the water contact angle image in **Fig. 6.1 (c)**.

Different concentrations of silica aerogel show a different level of reduction in the water uptake of the composite. Despite its high total porosity, the samples containing 20 vol. % silica aerogel improve hygrothermal parameters significantly when conditioned at 80% relative humidity. The material has a low initial coefficient of heat conductivity. **Fig. 6.4 (a)** may be used to analyze the negative effect of water on

the degradation of thermal insulation qualities by taking into consideration as a starting value the effective thermal conductivity particular for a certain composite. The unfavourable effects of exposing the porous composite to high humidity conditions were decreased by enriching the geopolymer mix with 20 % of silica aerogel.

The biocoal-based samples show lower initial thermal conductivity, however, higher water uptake compared to siliceous fly ash-based. Noteworthy, regarding the thermal conductivity values after humidity conditioning, the BG samples do perform better even under very humid environment conditions. Noteworthy, for sample BG-20 an increase of thermal conductivity under 80% humidity is only 0.130 W/(m·K). Therefore, it is concluded that more silica aerogel dosage could have a significant positive effect on lowering the thermal conductivity in a high-humidity environment. Along with the higher water content and effective moisture transporting while maintaining good thermal insulation performance, biocoal-based porous geopolymers can act as moisture indoor regulators.

It can be observed the mixing particles could have a positive effect on the hygrothermal performance than the narrowed distribution particles. With a wide range of silica aerogel particles, the packing of the silica aerogel becomes better and thus more channels for water transport are blocked by aerogels. It is demonstrated the addition of randomly distributed graphene particles can enhance the tortuosity and decrease the chloride transport in both concrete and mortar [396], [397]. Therefore, a 10 vol% replacement by silica aerogel could improve the tortuosity, as can be reflected by the BG-10 where the wide particle size strategy also performs better in this case than in BG-0. In the case of RH80, it demonstrates the significance of silica aerogel particles in water transport retardation. The reference sample BG-0, which has a similar total porosity and lower open-pore volume, has a lower resistance to water sorption than BG-10.

When comparing materials with various pore size distributions (**Table 6.5**), the phenomena of enhanced moisture sorption through capillary suction is demonstrated. This implies that small pores are filled initially, and as the air humidity rises, larger pores are filled with several monolayers of water [398]. In the transfer a negligible role plays the pores above 700 μm, thus the higher content of pores above this size in AG samples does not cause the higher moisture content. Moreover, the increased permeability of the composite, which can be measured using the open porosity metric (**Table 6.6**), intensifies this effect, thus causing higher moisture matrix penetration for biocoal fly ash-based materials. The hygrothermal parameters are thus defined by the overlaying of three phenomena, namely the total porosity, pore structure and superior characteristics of silica aerogel.

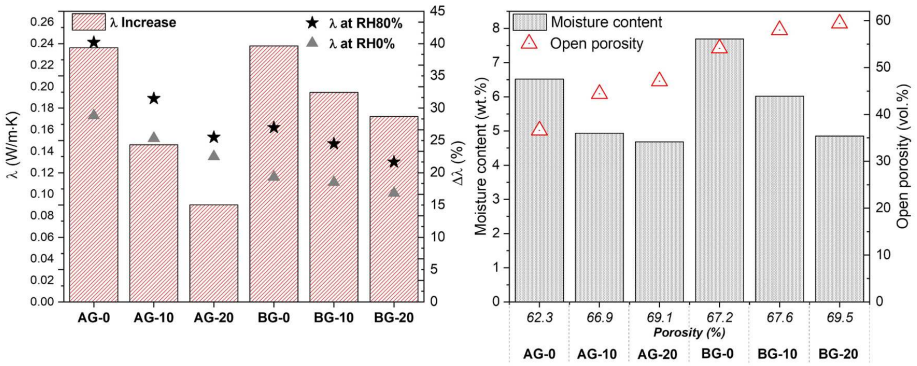

Fig. 6.4. Thermal conductivity in dry conditions and at 80% humidity and moisture content related to open porosity

6.3.5 *Acoustic absorption*

The acoustic absorption coefficient of the porous materials with different dosages of silica aerogel and average values of the coefficient of absorption (a_{med}) of the materials are presented in **Fig. 6.5**. The reference samples AG-0 and BG-0 present a relatively low acoustic absorption efficiency, namely 0.12 and 0.37. The maximum absorption for AG-0 occurs at 719 Hz with a coefficient of 0.37, and for BG-0 at 585 Hz reaching 0.54, which is typical for foamed concrete, whose efficiency is in the range of 0.13 to 0.50 over the frequency of 100-2000 Hz [399]. Noteworthy, samples enriched with silica aerogel, exceed the maximum value of sound absorption coefficient (α_{max}: 0.60 - 0.77). With a 10% aerogel dosage, both AG-10 and BG-10 present higher acoustic absorption performance than the plain geopolymers and the α increases to 0.41 (AG-10) and 0.50 (BG-10). For the fly ash-based system, the increase in silica aerogel dosage to 20% has a significant effect on the acoustic absorption efficiency of AG-20, achieving the highest α of 0.51. However, for biocoal-based composites, the increase is minor. Noteworthy, using biocoal fly ash can result in covering more range of sound frequency thus more sound can be effectively absorbed, both in plain material, as well as with 10% and 20% silica aerogel enrichment.

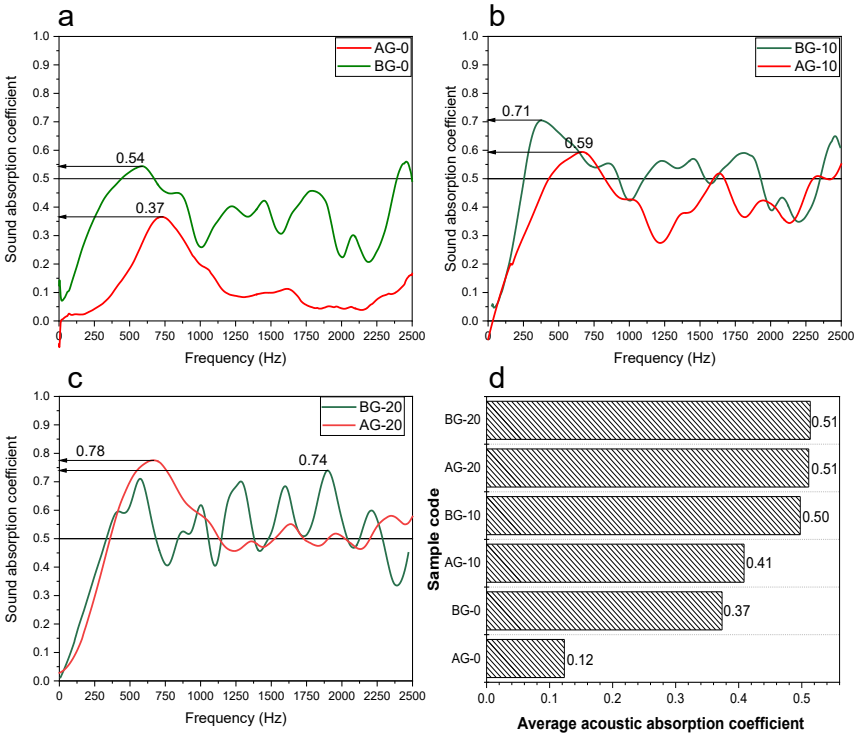

Fig. 6.5.(a,b,c): Acoustic absorption of geopolymers based on different raw materials and with different dosages. (d): Average values of the coefficient of absorption (a_{med}) of the samples.

Detailed studies on the acoustic absorption of foam concrete are relatively rare. Compared to other kinds of foam concrete, the sound absorption of the samples in this study is higher, and the range of coefficient above 0.5 is wider, from around 500 Hz to 2500 Hz. The rise in acoustic absorption could be attributed to the higher open porosity and the inherent acoustic absorption of silica aerogel. As shown in **Table 6.8**, the acoustic absorption of other foam concretes presents different values at different frequencies. The foam concrete can be prepared with different methods, for instance, pre-foamed concrete and aerated autoclaved concrete. Zhang et al. [21] investigated the acoustic absorption of fly ash/slag geopolymer pre-foam concrete, which has a maximum coefficient of 0.8, but with a very narrow absorption peak at 40-150 Hz. Neithalath et al. [400] prepared foamed concrete samples and presented absorption coefficients in the range of 0.20 to 0.30 with a bulk density of 400-700 kg/m^3. However, the foam concrete prepared had a closed pore network, mitigating the sound propagation and leading to reduced sound absorption. Therefore, it is also important to optimize the processing parameters, for instance, the optimal amount of foaming agent and surfactant, to make foam concrete with a much higher open porosity if the acoustic absorption property is desired.

Table 6.8. Acoustic absorption of different kinds of foam concrete.

Foam concretes	Maximum sound absorption coefficient	Peak frequency (Hz)	Density (kg/m³)	Literature
Foam geopolymer concrete with aerogel	0.79	450-700	700-800	This study
Geopolymer foam concrete	0.8	40-150	600-1200	[21]
Aerated autoclaved concrete	0.12-0.36	-	250-500	[401]
Foamed cellular concrete	0.2-0.3	-	400-700	[400]

6.3.6 *Potential applications*

Thanks to the interesting properties of silica aerogel mentioned above, geopolymer foam aerogel renders can be applied in certain kinds of field applications and for the reduction of carbon footprint in buildings, for instance, it can be applied for building refurbishment to save energy. Furthermore, because of the excellent sound absorption, hygrothermal properties and relatively low cost due to the use of low percentage aerogel, geopolymer foam aerogel render could be applied as a sound absorber in theatres or as an interlayer for house insulation in a humid area and become competitive in the market. Therefore, the geopolymer foam aerogel renders were investigated in terms of acoustic and thermal performance and were compared to those of plain aerogel-incorporated renders.

The developed material with optimal performance can reach a very high acoustic absorption performance compared to other materials as shown in **Section 6.3.5**. Previous studies showed that, concerning conventional aerogel plasters, the acoustic absorption of composite in this study increased 50 %–60 % (with only 10 % volume of aerogel), allowing a significant increase in sound absorption coefficient. The sound absorption coefficient at normal incidence was measured for a sample of 50 mm thickness and was compared to a conventional aerogel plaster. The composite shows better acoustic performance: the peak of absorption is 0.78 at about 505 Hz, compared to a value of about 0.37 for reference conventional plasters. Finally, the hygrothermal performance of the composite was investigated: it can be considered a multifunctional retrofit solution, especially for historic residential buildings in high-humidity areas.

6.4 Conclusions

The main objective of this study is to investigate the influence of the raw material and volumetric replacement by silica aerogel on the thermal and acoustic performance of foamed geopolymers. It is revealed that within a low dosage of aerogel (10 vol%), geopolymer can reach a very low thermal

conductivity while still possessing relatively excellent strength. Parameters such as thermal conductivity, acoustic absorption and hygrothermal performance of composite are the main focus of this study., and the following are its essential components:

- Both biocoal and siliceous fly ash provide high porosity of material (60-70 vol%), however, due to the difference in ash characteristics, fresh state properties are altered, thus affecting pore size distribution. The observed flash setting decreases the mechanical strength of biocoal-based composites, while the altered pore structure strongly affects hygrothermal and acoustic insulation properties.
- The total porosity of the geopolymer foam aerogel render is increased with the silica aerogel replacement. Moreover, the microstructure analysis indicates higher SA replacement introduces more medium-large particles of silica aerogel thus affecting calculated open porosity. The smaller silica aerogel can be spread in the solid network of the geopolymer matrix, while the large silica aerogel can be positioned between the pores, thus providing additional pore bridging.
- The hydrophobic tail of a surfactant may become trapped on the surface of a silica aerogel, potentially reducing the surfactant's ability to stabilise air bubbles, and hence the addition of 10 or 20 vol.% silica aerogel did not substantially improve the composites' characteristics.
- The acoustic absorption of geopolymer foam aerogel render is much higher than the plain foam geopolymer render, which is contributed by the more open porosity in composite, and the inherent sound absorption property of silica aerogel itself. Biocoal-based composite with 10 vol% is suggested as an optimal mix proportion for acoustic insulation.
- The thermal insulation property of composite is improved with the addition of silica aerogel. The thermal conductivity is firstly related to the total porosity. The silica aerogel act as a thermal barrier in the matrix. The interfacial thermal resistance related to aerogel particles is not facilitated. In the case of thermal insulation, improved performance for biocoal fly ash was observed, and better behaviour of the composite for 20 vol% was predicted, although this depends on the application requirements. 10% of the additive provides for a suitable thermal conductivity coefficient of λ_{dry}= 0.11 W/m·K and $\lambda_{RH80\%}$= 0.14 W/m·K, and it is selected due to the minor improvement when the enrichment is 20 vol.%.
- The hygrothermal behaviour is significantly improved compared to the plain geopolymer, demonstrated by the lower water uptake and thermal conductivity after exposure to an 80% humidity environment. A higher positive impact was observed at a replacement rate of 20%, which enriched the composite with a wide range of particle sizes of silica aerogel. A wide range of particles has a bigger influence, due to the more hydrophobic surface area and the tortuosity created that increase the moisture resistance of the composite.

CHAPTER 7 HIGH-TEMPERATURE EXPOSURE OF POROUS COMPOSITE: ROLE OF PORE CONNECTIVITY AND PORE SIZE DISTRIBUTION

This chapter presents a more in-depth examination of the indirect and direct influence of open pores and pore size distribution on the evolution of the material's microstructure and phase composition during high-temperature exposure, as well as the influence on the temperature profile within the material during one-side heating. The findings demonstrated the crucial role that moisture plays in the development and propagation of cracks and promoted the composite with a higher proportion of open pores by demonstrating much less degradation. Furthermore, a strong relationship was discovered between the generated fractures and the variance in mineralogical composition regardless of the same initial composition. Lastly, at high temperatures, the size and pore shape factor has a vital influence in regulating the temperature profile in the porous composite.

The results presented in this chapter are included in the following article:

K.M. Klima, C.H.A. Koh, J.C.O. Zepper, H.J.H. Brouwers, and Q.L. Yu, "High-temperature response of porous geopolymer – role of open porosity" (in preparation).)

7.1 Introduction

The fire-resistant materials must be able to withstand accidental rapid temperature raise for a certain period of time [402]. To reduce the risk of concrete spalling or steel deterioration, high-temperature-resistant coatings are used. Recent research [403]–[405] has shown that alkali-activated materials, an alternative to Portland cement and ceramics, have improved fire behaviour. Alkali-activated foams (AAFs) are one of the most promising materials, with various applications methods as adsorbents, catalysts, and thermal/acoustic insulators. The great thermal resistance of AAF has been reported recently. Inorganic foams [406] are suitable for application as fire-resistant materials because of their excellent mechanical properties and resistance to the thermally induced deterioration [12], and sufficient volume stability [407]. The inorganic structure based on the aluminosilicates structure contributes to enhanced fire resistance and durability under high-temperature conditions [130]. Instead of strength degradation like Portland cement, geopolymers can improve their mechanical characteristics up to 680 °C [125]. Hlavacek et al. [265] emphasised the advantages of employing foamed alkali-activated materials over aerated concrete since the temperature resistance is increased to 1100 °C, no autoclaving is required, and industrial by-products are used instead of Portland cement. In a recent investigation, a 2 cm thick fly ash-metakaolin-based geopolymer sample was heated to 1100 °C for three hours, during which the backside temperature was maintained below 250 °C, and the foam skeleton did not collapse but instead retained its integrity [218]. However, fewer experimental data were addressing the thermal performance and fire resistance of foamed alkali-activated materials. Moreover, several studies highlighted the importance of open-pore structures in limiting thermal shrinkage and fracture development [79], [341], [342], [408], [409]. According to these findings, a structure with high porosity and an open pore structure with a low thermal conductivity can provide a good thermal response. Open cavities reduce internal pressure and increase tolerance to temperature shock during fire initiation and extinguishment.

Closed porosity and small pores, on the other hand, determine better thermal insulation properties [314]. As a result, there is no definitive answer as to which structure is preferable for high-temperature applications. Moreover, it is unclear how much the material's response to high temperatures will change while maintaining the same total porosity and varying the volume of open pores. The stress associated with thermal exposure has already been demonstrated to be related to the transport properties (porosity, permeability), which determine the build-up of pore pressures [410], hence porous permeable materials are preferred to realize the aforementioned criteria. Mindeguia et al. [411] also highlighted that concrete transport quality (permeability, porosity, water content, and structural deterioration) appears to be particularly crucial among the basic variables that might explain the spalling phenomena.

Zhang et al. [412] emphasised the suitability of geopolymer porous composites in providing low-cost fire and thermal-resistant sealants due to their non-flammability, low thermal conductivity, and superior thermal resistance. Furthermore, a more in-depth study regarding the damage behaviour of geopolymer foams in high-temperature environments and thermal stress was proposed. Additionally, Perumal et al. [413]

emphasised the insufficiency of literature data on functional properties and their interactions with porous composites, and they advocated for more extensive research into these issues. Notably, three criteria influencing the usability of porous materials were identified, water content, heat conductivity, and fracture resistance. Dhasindrakrishna et al. [414] highlighted the advantage of open pore structure and its role as dehydration channels, which improve structural integrity when exposed to higher temperatures by releasing excess vapour pressure. However, the presence of water in well-connected pore networks can be favourable since the material can reach equilibrium temperature after the dehydration plateau, resulting in better thermal insulation performance and a longer time when serving fire protection. According to Gluth et al. [415], the comparably high permeability of geopolymer concretes prevented material spalling at high temperatures, resulting in less degradation and a lower depth impacted by temperature.

Our previous research (**Chapter 5**) has shown that the surfactant type in a cosurfactant mixture affects porosity, pore size distribution, and pore cavity formation [416]. It was revealed that cationic-contained systems encourage the production of small pores, whereas anionic systems provide the majority of pores greater than 200 μm. Furthermore, stronger surfactant-solid particle attractions are detected in the alkaline environment for the cationic surfactant, as shown by a higher proportion of closed pores than in SDS-contained composites. Assuming that the bigger the open porosity and gas permeability, the lesser the material's ability to degrade, materials based on anionic sodium dodecyl sulphate and nonionic Triton X-100 were proposed for high-temperature application. However, no experimental work has been done to confirm whether the composite structure with a higher proportion of closed pores and the same overall porosity would suffer more during high-temperature exposure. Therefore, this study aims to fill the above-discussed gap to provide an in-depth understanding of the fire-resistant behaviour of porous composites and discuss in detail the role of oper pores and permeability in ensuring the role of insulating and protective material at high temperatures. To determine whether higher gas permeability would indeed provide better thermal protection, two materials with the same total porosity and chemical composition but different open pore volumes were investigated.

The composites were subjected to high temperatures(up to 1100 ^{o}C) in one direction to study changes in overall porosity, the volume of open pores, crack formation, and phase composition. The test also provides data on the temperature profile within the material during the 1100 ^{o}C exposure. The results are then used to simulate the temperature profile for the examined composites to predict more material behaviour scenarios when different heating conditions are applied. The simulation demonstrates the material's potential thermal response under standardised conditions and allows for assessing the behaviour of the presented composite when compared to other investigated or commercial materials for high-temperature applications. The current study provides insights into the thermal response of composite exposed one-side heat source to evaluate pore structure alteration, cracks formation (μCT) and their interdependence with the thermally-induced mineralogical phase evolution (QXRD) at high temperatures. The investigation has shown that open porosity does play a critical role in serving as a protective material for high-temperature applications, with its pore architecture enabling to limit the negative impact of pore pressure.

7.2 Methodology

7.2.1 *Material characterization*

Biocoal fly ash, a by-product of coal-biomass co-combustion, was employed as the solid precursor for the geopolymers' design. **Table 7.1** shows the results of the elemental composition analysed by XRF of the new batch of biocoal fly ash. Silica is the dominant element within the ash composition, also the high amount of alumina can contribute to the good thermal performance of the composite [417]. The incorporation of biomass in the fuel causes a rise in calcium content, which, as earlier research has shown, impacts the setting time [416]. The molar ratio of reactive Si to Al is 2.91, calculated based on the extraction method with a concentrated base solution (10M NaOH) and HCl (32%).

Table 7.1. Oxide composition of fly ash obtained via XRF measurement.

SiO_2	Al_2O_3	CaO	Fe_2O_3	MgO	K_2O	SO_3	TiO_2	P_2O_5	MnO	Other	LOI
51.48	20.21	9.65	7.11	2.64	3.76	0.66	1.01	0.81	0.34	0.31	2.01

7.2.2 *Mix proportion and sample preparation*

Based on the prior research (**Chapter 5**), two mix designs have been chosen for high-temperature testing. The choice was led by very similar total porosity values based on the same non-ionic surfactant, but with varied pore size distribution and open porosity fractions. These variations are expected to have a major influence on high-temperature resistance.

7.2.3 *High-temperature exposure test*

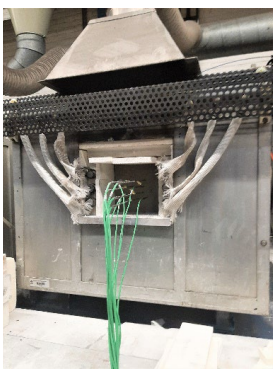

One-side high-temperature exposure test was performed on samples of 15 x 15 x 6 cm^3 at the age of 28 days. The thickness of the material was guided by EN 1992-1-2 in which the minimum wall thickness of a non-load-bearing wall is 60 mm for standard fire resistance EI30. The muffle furnace was preheated up to 800 ^oC and one side of the sample was placed in a muffle furnace and walls insulated to minimize the heat transfer to one direction. The sample was heated up to 1100 ^oC at a heating rate of 2 ^oC/min to mimic the temperature profile according to the Cellulose fire scenario (ISO 834). In total 10 thermocouples, type K were placed within the samples at the depths of 1 cm, 2.5 cm and 6 cm from the heated surface to monitor the temperature rise in the composite. The data were continuously monitored and logged every

1 second throughout the fire test. Afterwards, the sample was removed from the furnace and quenched in the air.

7.3 Results and discussion

7.3.1 *Thermal and physical properties of the material.*

Heat transport through a solid material is primarily governed by its bulk density, thermal conductivity and specific heat capacity. Since air has a lower thermal conductivity than a solid phase, incorporating pores into a material is en effective method to reduce its thermal conductivity. In addition, at ambient temperature, a porous material with a dominantly closed pores structure has a lower thermal conductivity in comparison to mainly opened pores [340]. In this study, both samples T100CTAB and T100SDS have a similar total porosity at around 69%, with Sample T100SDS having a higher open pores structure (**Table 7.2**).

Table 7.2. Basic parameters of the composites (**Chapter 5**).

		T100CTAB	T100SDS
Bulk density (kg/m^3)		733	726
Specific heat capacity (J/kg*K)		730	730
Thermal conductivity λ_{20} (W/m·K)		0.104	0.116
Gas permeability (m^2)		3.75 *10 $^{-13}$	8.19 ·10^{-13}
Φ_{open} (>5 μm) (vol.%)		43.6	53.2
$\Phi_{total-20}$ (vol.%)		69.0	69.3
Pore volume within the range (μm) at 20°C	**<5**	17.7	16.4
	5-50	7.8	2.4
	50-200	27.4	11.5
	200-500	16.0	36.6
	>500	0.0	2.3

This makes Sample T100CTAB a better heat-resistant material for ambient temperature application. However, as shown by Pelissari et al. [418], for the composites characterized by the same total porosity and thermal conductivity of the solid skeleton, the pore size distribution plays a critical role in defining the effective conductivity of the composite at high-temperature conditions. Moreover, Smith et al. [301] stated that the influence of pore size in heat radiation at high temperatures increases with the contribution of pores above 100 μm and can be established via Loeb's expression of equivalent thermal conductivity due to radiation across the pore.

$$\lambda_{rad}(T) = 4\varepsilon\gamma\sigma dT \tag{7.1}$$

where ε is the emissivity, σ is the Stefan-Boltzmann constant (1.380649×10^{-23} J/K), d is the pore size (m) in the heat flow direction and γ is the shape factor. Submicron and large pores both have a detrimental impact on high-temperature resistance because they are ineffective at dispersing radiant heat. **Table 7.4** reveals a comparable number of pores below 5 μm for both T100CTAB and T100SDS; however, the T100SDS composite has a higher fraction of pores above 200 μm in the total size distribution, hence it might be inefficient in dissipating radiant heat within the composite, and subsequently less effective in impeding heat transfer in comparison to Sample T100CTAB.

Another factor is the presence of water [411], [414] and its both positive and negative roles in the high-temperature performance of the material. On the one hand, since water is present, the heat energy consumed by evaporation and condensation of water slows down the temperature increase within the material structure. Pore channel constrictions and bottlenecks effect, on the other hand, can have a significant impact on transport behaviour. Water vapour collides with the pore walls during heating, and in the absence of open cavities, this movement is hindered. The analysed samples have moisture content in the range of 2.0 - 2.3 wt.% under normal ambient conditions (20°C, 50% relative humidity RH) [416]. It is therefore postulated that lower internal stress associated with water entrapment in closed pores in the T100SDS sample can be expected during the heating process, due to the much higher value of gas permeability and open pore volume above 5 μm.

7.3.2 *Deformation properties at high temperatures*

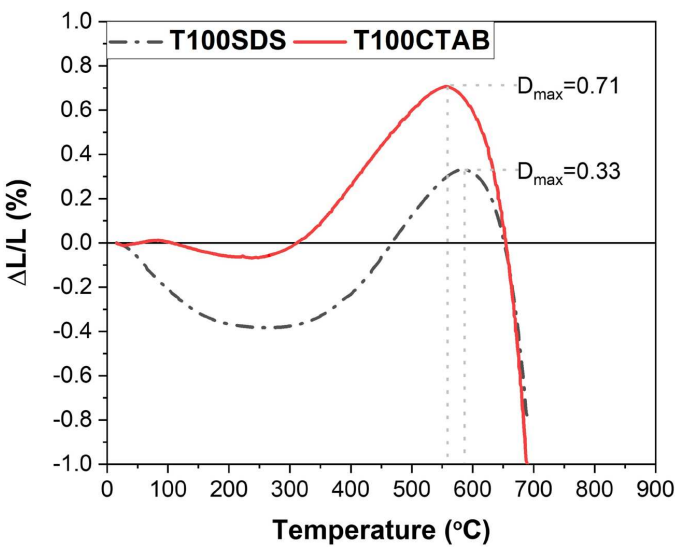

Fig 7.1 Refractoriness Under Load of the porous samples (load 0.5 MPa, cylidrical sample h= 50mm, r=50mm).

Refractoriness under load (RUL)(method described in **Chapter 2**) is a measure of the material resistance to deformation when heated to a high temperature under loading. The mechanical performance of a composite is closely related to its chemical composition and microstructure. Both samples shrank from 100 to 200 °C as free pore water is released and the T100SDS sample is characterized by a higher water content (**Table 7.4**). As a result, more shrinkage can be expected up to 200 °C, and the more pores of medium- and large-size T100SDS might be more prone to volume decrease during high-temperature exposure [419]. Further volume expansion can be attributed to a dehydroxylation process and the transition of quartz, formation of hematite and other thermally-induced crystalline phases. According to Fayyad et al. [420], porosity has a significant impact on refractoriness under load, as the deformation point occurs at a higher temperature in a denser matrix than in a less dense matrix., which could explain the stability loss at around 600 °C for both composites (**Fig. 7.1**). Excess activating solution or silica, as proposed by Provis et al. [99], can cause low mechanical strength, indicating that the extra solution did not result in the formation of a viable geopolymer binder, but rather in the formation of expanding silicate gel. The test results shown in Section 5.3.8 of **Chapter 5** confirm the significantly low compressive strength of both T100SDS and T100CTAB.

7.3.3 *One-side high-temperature exposure: temperature profile*

In order to evaluate the abovementioned thermal behaviour of the two composites and understand the effects of pore connectivity and gas permeability in maintaining structural integrity, a one-side elevated temperature exposure test (up to 1100 °C) was performed on two selected composites. The high-temperature test results are presented in **Fig. 7.2**. The temperature profile at the different depths of the specimens and in the furnace was monitored and recorded. The materials were pre-conditioned under ambient conditions (20°C and 50% RH) to reflect an actual built environment.

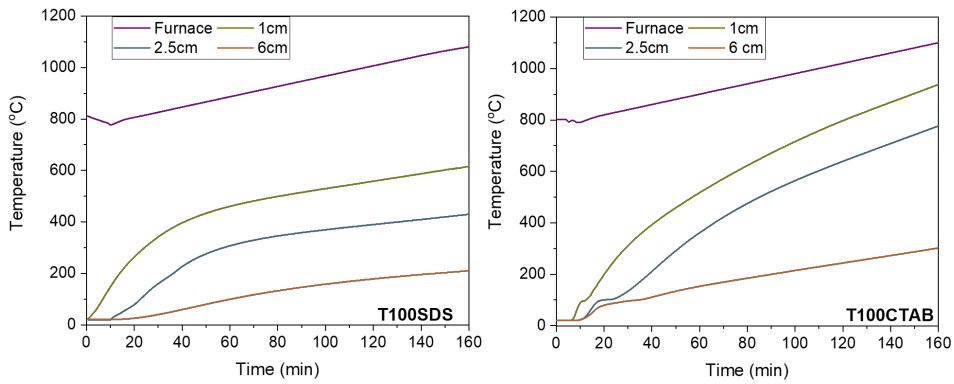

Fig. 7.2. Temperature profile recorded inside the furnace by thermocouple S and within the composite by thermocouple type K.

The results show a higher temperature rise in sample T100CTAB in comparison to sample T100SDS under the same heating boundary conditions. This is contradicting to the assumption that larger pore sizes provide a better medium for heat transfer in a material, in this case, Sample T100SDS with a higher fraction of pores above 200 μm. This implies that pore connectivity is playing a more significant role. Sample T100CTAB composite with a lower open porosity of 43.6 vol.% and gas permeability of $3.75 * 10^{-13}$ m^2, microcracks and cracks are formed due to internal stress associated with water entrapment in closed pores, which cause material degradation and accelerated heat transfer. Meanwhile, sample T100SDS, with an open porosity of 53.2 vol.% and gas permeability of $8.19 \cdot 10^{-13}$ m^2, can withstand rapid temperature rises while diminishing the pore pressure effect by allowing unhindered movement of water vapour. This formation of cracks was further validated by the X-ray tomography measurement (next section).

The Sample T100SDS has a higher initial thermal conductivity value, which causes a faster temperature increase within the composite in the first 10 minutes of the conducted test. However, for Sample T100CTAB, a distinct flat temperature plateau at 100°C can be observed within the first 10-18 minutes, which is coincided with the water vapourization process. The released latent heat increased the overall kinetic energy of the vapour trapped inside the closed pores in a short time frame, induced significant stress to the pore structures, and subsequently formed cracks and microcracks within the material. In contrast to Sample T100CTAB, the temperature curves for the T100SDS sample do not exhibit a similar flat plateau, indicating no signs of degradation or crack formation. This confirms the postulation that material with higher pores connectivity, i.e. Sample T100SDS, is more tenable in maintaining its pore structures during a heating process.

Once the water is released through evaporation, Sample T100CTAB experienced a steeper temperature increment compared to Sample T100SDS, suggesting those newly formed cracks have altered its thermal properties. Ba et al. [421] investigated the role of cracking on heat propagations and showed that the influence is significant. The air present in the cracks has several times higher thermal diffusivity than the solid skeleton material, thus increasing the temperature within the cracks. As a result, the temperature in the area of the fracture is higher than in the composite during heat transfer at the same depth. Notwithstanding, the heat transfer mechanism of these cracks is comparable to the pores, where the radiation increase with crack size. An equivalent thermal conductivity due to radiation across the cracks therefore can be applied using the same **eq. (7.1)**. The term d is modified to the crack size (or combination of crack and pore) in the heat flow direction. Another term shape factor γ is further adjusted, i.e. $\gamma=2/3$ assumes an average spherical pore [422]**.** The aeration method, namely direct foaming, supports the assumption of the spherical character of the pore within the composite. The introduced and stabilised pores are formed from spherical air bubbles. For cracks, the γ needs to be increased to the range of 2/3 and 1 to account for the more elongated shape of the cracks. Further, the validity of using **eq. (7.1)** to represent the heat transfer process of a porous material under a high-temperature heating process, together with treating cracks as pores, will be further confirmed in section 7.6 describing the modelling study.

7.3.4 *Cracks detection and pore size distribution*

After the high-temperature exposure, the composite was cut into 1-centimetre sections, where the fragment towards the heating source (oven) was labelled first. The scans were performed in the central part of each centimetre to reduce the influence of sample preparation on the microstructure evaluation. The first six segments were analyzed using microcomputed tomography (μCT) to observe possible cracks and their evolution. The first six segments were analyzed using microcomputed tomography (μCT) to observe possible cracks and their evolution in the macroscopic scale, namely above 6.6 μm.

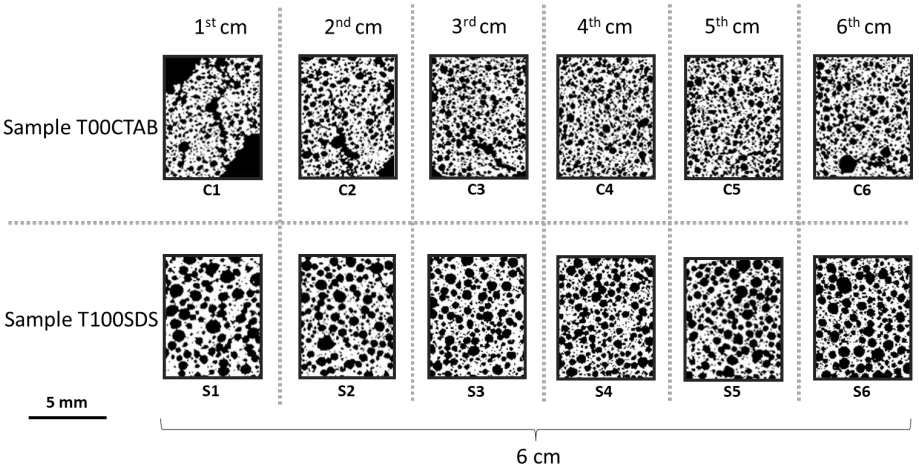

Fig. 7.3 Binary image of each section of the samples T100SDS and T100CTAB obtained via microCT.

Fig. 7.3 depicts the visual representation of the six analysed sections of both samples T100SDS and T100CTAB. For the μCT analysis, each section, from S1 to S6, consists of 705 slices. The first observation concerns the difference in pore size between samples T100CTAB and T100SDS, which results from the used binary cosurfactants. The cationic-nonionic system (T100CTAB) supports the formation and stabilization of smaller bubbles, while in the anionic-nonionic system, the bubbles are in the range of 200-500 μm and voids are above 500 μm (**Table 7.2**). The sample T100CTAB has a higher proportion of smaller and closed pores, together with numerous cracks, particularly in the first three centimetres (C1, C2, C3) (**Fig. 7.3**); there are also a few cracks connecting the pores in the following segments (C5, C6). The relatively thin wall between pores (pore wall) was damaged due to the pore pressure. For material T100SDS, particularly in the S1 segment, the formation of connections/cracks can be observed, but it was not as damaging to the material as in sample T100CTAB, and the analysis of subsequent sections revealed no significant cracks during the water's migration towards the cooler side.

It is critical to understand the defect formation as well as the involved mechanism. When the temperature is constant, the pressure formed by water evaporation in the pores of the composite is inversely proportional to the pore volume, according to the ideal gas law assuming the same volume of water [423].

The composite permeability is critical in determining pore pressure in the material subjected to fire. The more permeable the sample, the lower the peak vapour pressure. With extended fire exposure, the peak pressure in the pores rises and goes from the surface to the central part of the material [424]. Thus, it is possible to observe more cracks in C5 and C6. After the permeability is compensated for the effects of heat damage, such as (micro)cracks, the peak vapour pressure in the pores is reduced. The pressure zone moves towards the cooler side with the increased exposure time and the exposure duration for both samples was the same as the porosity of the composite volume. As a result, the sole influence is vapour permeability and initial water content. Assuming that the microcracks form first, and if the steam pressure is high enough, the microcracks expand quickly. When this damage develops, the vapour diffusion coefficient increases dramatically, causing the pressure to fall. Based on the path of the observed crack in the T100CTAB sample and negligible cracks in T100SDS, it is possible to state that for the porous composites (φ =69 vol.%), the gas permeability of 3.75 10 -13 m^2 is sufficient in minimizing the damaging effects of pore pressure during rapid heating of the composite.

In the next step, by applying the pore separation operation (regions of lower density) from the areas of larger density (skeleton), a graph of the pore size distribution of T100CTAB and T100SDS was generated, as shown respectively in **Figs. 7.4**. Sample T100CTAB revealed the presence of air gaps larger than 500 μm even up to a fifth centimetre within the structure. High temperature has a particularly strong impact in the area of two centimetres, where a rise in the contribution of bigger air voids was observed owing to the creation of cracks, the joining of pores, and the generation of new voids in the 500-1000 μm range. Compared to the non-exposed sample T100CTAB, the shift of pore size distribution (**Table 7.2**) towards big-size pores is significant. As discussed above the water vapour was moving towards the colder side, thus causing the formation of cracks, mostly within the first three sections of the T100CTAB sample. At the same time, the formed cracks lowered the pore pressure and thus the damages are less significant in further sections (C4 to C6). A distinctly different trend has been noted in sample T100SDS, where no significant presence of air gaps larger than 1 mm was noticed. Only in the S1 section, there was a shift in the distribution of the pores observed from the range of 100-300 μm to 400-700 μm, whereas the pore structure does not show any major deformations and is similar to the next segmental structure from the second centimetre, indicating better stability of the structure.

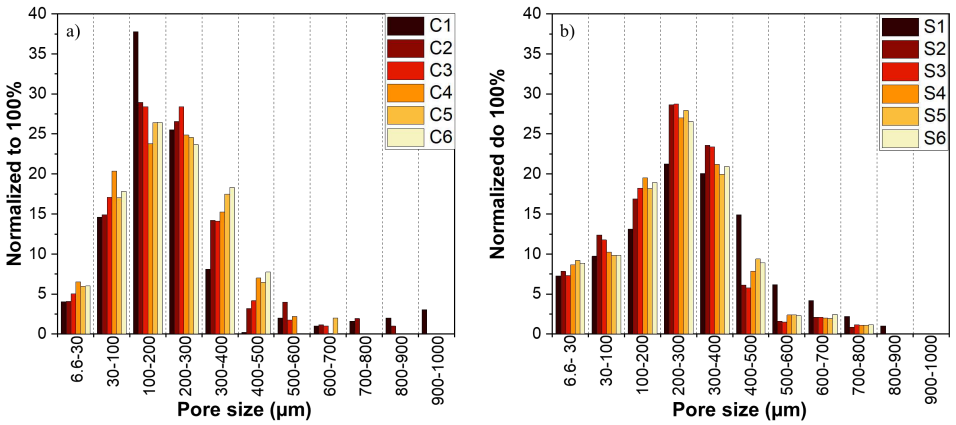

Fig. 7.4. Pore size distribution obtained via µCT (voxel size 6.6 µm) of samples a) T100CTAB and b) T100SDS.

According to Edouard et al. [425], the pressure drop reduces with the increased pore diameter for a given porosity. The obtained Darcy permeability shows that the permeability is inversely related to pressure drop and a lower pressure drop was indeed observed in sample T100SDS than in T100CTAB. From **Table 7.2** and **Fig. 7.4**, it is also clear that a wider distribution range of pores and higher content of bigger size pores are present in T100SDS. As a result, larger pore sizes are a superior solution for high-temperature applications, compared to the composite with the same total porosity. However, it should be kept in mind that a larger content of air voids causes a higher sensitivity of the system to mechanical damage than materials with smaller-size pores.

7.4 Open porosity and proposed mechanism

The open porosity was assessed using µCT. The detected pores and the connection between them were defined and their volume was quantified, as shown in **Fig. 7.5**. The results confirm the significant changes in the microstructure and the formation of cracks within the porous composite's front sections C1 (open pore volume increases from 43.8 to 52.9 vol %) and C2 (46.2 vol.%). For sample T100SDS, a minor increase within the first section is observed (52.5 to 54.1 vol.%), however, a rather consistent volume of open pores is noted. Noteworthy, fly ash particles can possibly be fused and densified at 400 °C. Because of the aforementioned densification, the open porosity is reduced, which for this composite oscillates between 48.8 and 52.9 vol. %.

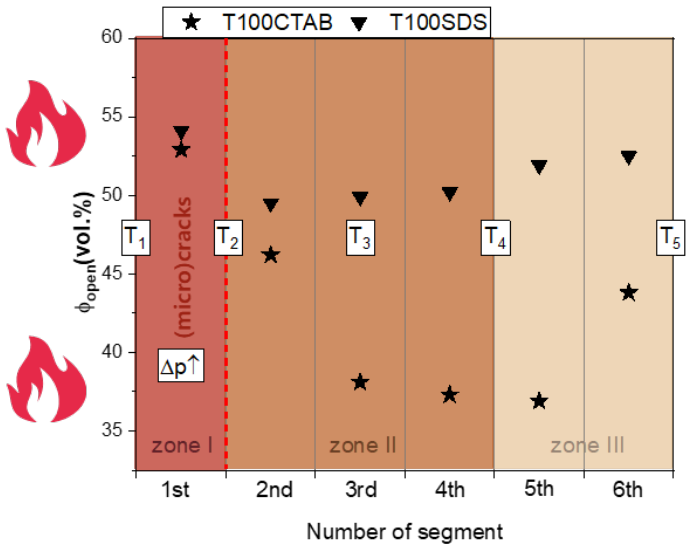

Fig. 7.5 Open porosity derived from μCT and schematic diagram of cracks formation within the composites. At the end of the test the temperature are as follow T_1=1100°C;$T_{2\text{-}T100CTAB}$=936°C, $T_{2\text{-}T100SDS}$=615°C;$T_{3\text{-}T100CTAB}$=773°C, $T_{3\text{-}T100SDS}$=430°C;$T_{5\text{-}T100CTAB}$=300°C, $T_{5\text{-}T100SDS}$=209°C.

The zones presented in **Fig. 7.5** represent three regions in which the general phenomena can be explained, as follows:

Zone I Heat transfer is slowed down for the first 18 minutes due to energy consumption during the evaporation process. Moreover, because $\Delta T=T_2-T_1$ is high, the quick temperature rise causes rapid moisture transport towards zone II. Cracks are highly likely to form.

Zone II: Phenomena in this zone are strongly related to the permeability of the material and the current water content. Further moisture movement and the formation of an accumulation zone in the T100CTAB cause crack propagation. The greater the number of cracks, the faster the heat transfer within the material. This effect in T100SDS is mitigated by the high permeability, and further undisrupted moisture flow towards colder sizes is observed. Additional moisture removal from the top porous surface of the material can take place. Due to the high temperature of T_2, and T_3, matrix densification, pore collapse, and the closing of open cavities may occur.

Zone III has a lower temperature gradient $\Delta T= T_5 - T_4$ than zones I and II. Permeability facilitates the transfer of air and moisture through the structure. The pores are filled with water, vapour, and air at room temperature. The pressure within the closed/poorly-connected pores differs from the atmospheric pressure during slow heating (provided by low λ) and has an additional impact on the pore structure, increasing the likelihood of further crack formation (sample T100CTAB 5th and 6th section) to reduce the pressure drop. Continuous moisture transfer and condensation occur.

7.5 Evolution of phase composition

Continuing the analysis from the previous section, the separated material sections were subjected to quantitative XRD analysis. The formation of thermally induced crystalline phases in the composite can be considered a factor in the formation of cracks and volumetric instability. As a result, the material's degraded surface structure allowed heat to penetrate deep into the material, causing further crystallisation. **Fig. 7.6** depicts the quantitative results of the phase composition. The five indicators of high temperature, namely mineralogical phases for evaluating high-temperature behaviour as a function of distance from the heat source have been presented and investigated. In both composites, two high-temperature phases were discovered, namely feldspar and augite.

Feldspars are likely formed from the amorphous phase and the amount of feldspars increases with the increased temperature. Sample T100SDS contains fewer feldspars than sample T100CTAB, due to the lower temperature reached within the composite T100SDS. Feldspars are only formed in the first four segments of T100SDS samples, as shown in **Fig. 7.6**, whereas they are also formed in the fifth segment of sample T100CTAB. It is assumed that feldspars are formed in low temperatures due to the presence of water and rapid heating conditions which was sufficient to provide felspars crystallization [426]–[428].

Within four centimetres from the exposed side, augite was also discovered, which is pyroxene with the formula of $Ca(Mg,Fe)Si_2O_6$. The presence of augite is observed in deeper layers of both T100SDS and T100CTAB materials; however, a reduction in the amount of augite in the first two sections of the T100CTAB sample is worth noting. This can be possibly explained by crystallization kinetics, namely the difficulty of pyroxene nucleation [1]. This difficulty may be related to the high cooling rate that may hinder the development of augite crystals, as shown by Kinzler and Grove [429]. The existence of cracks, particularly in the first two centimetres, expedited cooling after the material was removed from the furnace, resulting in a decrease in the amount of augite in these zones. Moreover, in the T100SDS sample already in the fifth centimetre, the augite is not detected, hence it is concluded that at this depth the temperature of T100SDS was lower than T100CTAB. The presence and content of hematite and maghemite are correlated with each other. The higher the temperature of the exposed section, the higher the hematite content and the lower the maghemite content. Even though both phases are seen as Fe_2O_3 polymorphs (i.e. hematite is α-Fe_2O_3 and maghemite is γ-Fe_2O_3), it is known that during the heat exposure, the loss of H+ ions in the maghemite crystal lattice caused it to transform to hematite [430].

After high-temperature exposure, the phase composition of the T100SDS sample changed slightly. Individual phase fluctuations are smaller than in T100CTAB, indicating less material degradation due to high temperature and lower temperature at individual depths of up to 6 centimetres. This demonstrates superior insulating characteristics at high temperatures. The quantitative variations between the samples were primarily induced by the altered pore structure and directly by the breakdown of the T100CTAB sample's top layer, which allowed more heat to penetrate the composite and initiate phase crystallization. Temperature-induced phase variation between the two samples is visible within the first five sections (5cm),

indicating that microstructure changes at temperatures up to 200 °C, namely (micro)crack formation resulted in higher temperatures in the material's deeper layers, causing thermally induced crystallisation. As a result, the changes in phase composition caused further degradation of the material. However, as shown in **Fig. 7.2**, thermal expansion is observed around 350 °C due to the nucleation phenomenon, which may cause the formation of microcracks. However, in low-strength and dense materials, the strain energy is insufficient to propagate the nucleated microcracks to the entire microstructure [431]. As a result, structural degradation caused by pore pressure caused the majority of the cracks to form, enhancing heat transfer in the composite T100CTAB and inducing the nucleation of the high-temperature phases. In terms of after-fire use of porous composites, the presence of newly formed crystalline phases, such as high-stability feldspars or pyroxene, might well reinforce the structure of the porous composite and improve its thermal performance of the T100SDS sample.

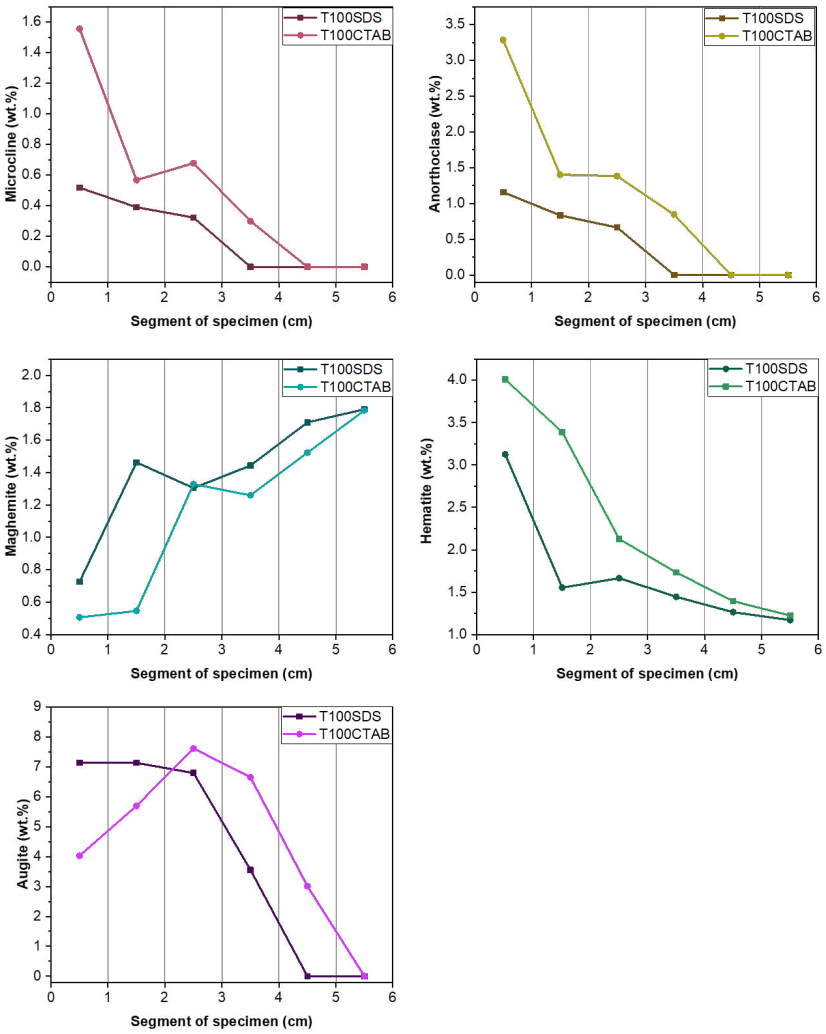

Fig. 7.6 Phase quantification in the function of distance from the heating source (furnace).

7.6 Heat transfer model validation

The temperature profile for both samples was modelled using the Comsol Multiphysics 5.6 software to validate the use of **eq. (7.1)** to represent the heat transfer process of a porous material under a high-temperature heating process. The model is further used to validate the hypothesis that cracks can be treated as equivalent to pores using the same equation for heat transfer study. The input parameters for material properties, boundary conditions and initial conditions used to solve equation **7.2** are listed in Appendix C (Table C.1). To model the heat transfer process, the following equation is used

$$\varrho C_p \left(\frac{\partial T}{\partial t} + u \cdot \nabla T\right) + \nabla \cdot (-\lambda_{eff} \nabla T) = Q \tag{7.2}$$

where T is the temperature of the sample (K), λ_{eff} is the effective thermal conductivity (W/m·K), ϱ is the bulk density (kg/m^3), C_p is the specific heat capacity (J/kg·K), Q is the heat source (W/m^2) and u is the velocity vector of translational motion (m/s). The sample is modelled as one-dimensional, with the heat transfer one directionally from the heat source to the ambient environment through the member. Heat is transferred from fire to the member by convection and radiation, which can be described by an equivalent heat transfer coefficient h, and the heat source can be described using the following equation

$$q_i = h(T_{ext} - T) \tag{7.3}$$

where T_{ext} is the temperature in the fire environment (furnace). The sample loses its heat to the ambient environment by convection at a lower temperature, which however is dominated by radiation at a higher temperature [432]. It is therefore only surface-to-ambient radiation is modelled using the following equation

$$q_o = \varepsilon\sigma(T_{amb}^4 - T^4) \tag{7.4}$$

where T_{amb} is the ambient temperature. For the overall heat transfer equation, **eq. (7.1)** representing an equivalent temperature-dependent thermal conductivity due to radiation $\lambda_{rad}(T)$ is applied on top of the measured thermal conductivity of the samples at room temperature λ_{cond}. Thus, the effective thermal conductivity λ_{eff} of the geopolymer can be expressed as

$$\lambda_{eff}(T) = \lambda_{cond} + \lambda_{rad}(T) \tag{7.5}$$

where $\lambda_{rad}(T)$ is calculated using **eq. (7.1).** Parameters γ=2/3 and d=0.5mm are applied to represent the average pores in both samples, and the measured pore emissivity is ε=0.72. For sample T100CTAB, the cracks are treated as pores as per early postulation, with pore size (including crack) up to 1.5 mm at 1 cm, up to 0.9 mm for the next 2-3cm based on μCT data (**Fig. 7.4**), and the rest of the mean pore size remains at 0.5 mm. To account for the more elongated shape of cracks in Sample T100CTAB, γ factor was modified from 2/3 to 3/4 and 4/5 at 2.5cm and 1cm respectively.

To focus on the high-temperature response of the samples, the sample is modelled as dry using λ_{cond} at the dry condition with an initial temperature of 100 °C, and will be used to validate the corresponding experimental data after 100 °C where vapour has been evaporated from the sample. By transforming the

initial condition, the model can now be solved using the heat transfer equation **eq. (7.2)** without bringing in the moisture transfer and phase change equations.

The results of the simulation together with the experimental data for validation purposes are presented in **Fig. 7.7.** The temperature results of this simulation based on the data set described above match the experimental data, with an average deviation of ±12.7, ±10.1, ±18.8 and ±7.9 °C for T100SDS-1cm, T100SDS-2.5cm, T100CTAB-1cm and T100CTAB-2.5cm respectively, validating the use of **eq. (7.1)** and **eq. (7.5)** to describe the heat transfer process of a porous material under high temperature, as well as treating cracks as pores in the heat transfer study.

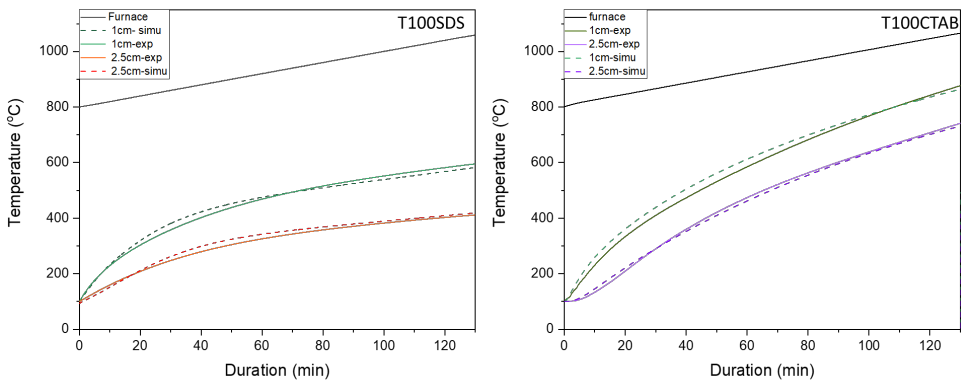

Fig. 7.7 Temperature curve obtain via simulation (dash line) and experimental data (solid line).

7.7 Example of application

The designed composite can be used as fire-resistant sheathing boards for a wall assembly such as a concrete wall. To show the advantage of applying such composite in a wall system, Sample T100SDS is selected and simulated using **eq.(7.2)** under the condition that one surface is exposed to fire as per Eurocode EN1991-1-2 requirement. To reflect the intended application, an assembly of 2.5 cm composite T100SDS board combined with an arbitrary 25 cm of a concrete wall is modelled. The concrete properties are based on requirements stated in EN1992-1-2, and the T100SDS properties are as per the validated model in the previous section.

The boundary conditions are modelled with a convective heat flux q_i as influx using **eq. (7.3)**, and surface-to-ambient radiation q_o as outflux as per **eq. (7.4)**, where T_{ext} (°C) is the gas temperature in the fire compartment based on the standard fire temperature-time curve [433], i.e.

$$T_{ext} = 20+345 \log(8t+1) \quad (7.6)$$

where t is the time in minutes. The coefficient of heat transfer by convection h is set as 25W/(m²·K) [433]. For outflux, T_{amb} is the ambient temperature, taken as 20 °C. The obtained results are shown in **Fig. 7.8.**

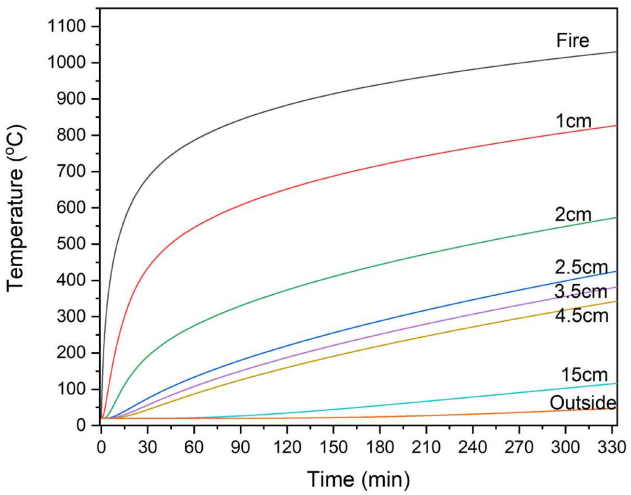

Fig. 7.8 Temperature profile within the assembly porous composite+concrete.

The temperature was calculated at various depths, with 2.5 cm being the temperature on the concrete surface at the composite T100SDS-concrete interface. The temperature curves obtained show that this material meets the fire insulation criteria of the European standard EN 1363-1, which determines the time during which the material performs a protective role without a sudden temperature change and for which the temperature of the unexposed wall to rise by 180°C at any point. The modelling results in 330 minutes reveal that the temperature on the unexposed side of the concrete reached 48.4 °C, which is significantly lower than 180 °C. Furthermore, the experimental section demonstrates that the material did not degrade within 130 minutes of the test and during the exposure from 800 to 1100 °C, demonstrating its excellent fire-insulating qualities under extreme temperature conditions (EI93) considering the time when the temperature at the interface between composite T100SDS and concrete surface reaches 180 °C based on EN 13501-2.

To compare the behaviour of sample T100SDS with other materials in similar applications, a single layer of 5 cm thick material was modelled using material parameters presented in the literature for an example of autoclaved concrete [434] and another geopolymer foam [435], and the temperature was calculated at a depth of 2.5 cm. The results are shown in **Fig. 7.9a** and the parameters of the materials can be found in Appendix C (Table C.2). Overall, the simulated 330-minute test showed that the sample T100SDS performed well, with the lowest temperature reached at 2.5cm comparable to aerated concrete with an 81% porosity. The shape of the curve above 400 ° C reflects the role of pore size in radiative heat transfer at

high temperatures. The rapid temperature rise above 400 °C is observed in geofoam samples (A1, A2, and A3), which may be due to the larger mean pore size value than in T100SDS and aerated concrete.

Fig. 7.9b shows the results after taking into account the isolation requirement as the time at which the reading at a given point will not exceed 180 °C. Among the three geopolymer foams (A1, A2, A3) studied, specimen A3 with the lowest porosity, the smallest mean pore diameter value, but similar thermal conductivity, exhibits the best performance, namely the longest protection time (33.4 min). Based on the insulation criterion, the sample T100SDS outperforms aerated concrete (16.3 min) and is comparable to other similar geopolymer foam from the literature (25.9 min).

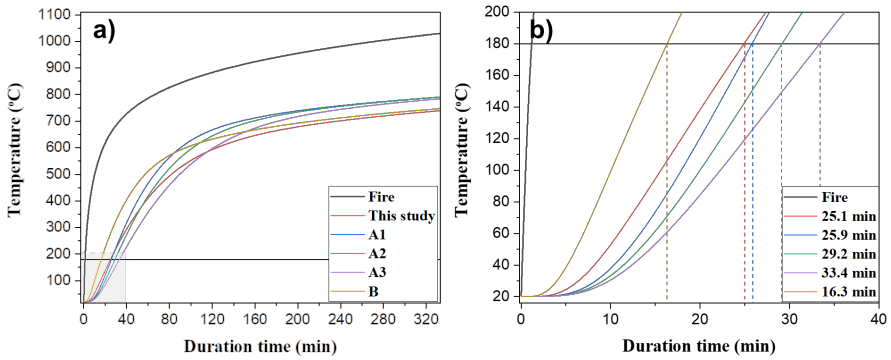

Fig. 7.9 a) Temperature curve of the single composite (thickness 2.5cm) T100SDS exposed to ISO 834 and compared with literature A1, A2, A3 [435]; B [434]; b) grey area from figure 9a with the marked time of reaching 180 °C.

7.8 Conclusions

The goal of this study is to examine the influence of open porosity, pore size distribution, and gas permeability on porous composite response to high-temperature exposure and the resulting structural damage. Overall, the study concluded that high permeability and open porosity provide better thermal stability under high temperatures, in terms of material deterioration and degree of thermal protection than a potentially better thermal insulator with a higher content of closed pores. The effect of one-sided high-temperature exposure on porosity and phase change, crack formation, and their role in heat transfer within composites is discussed. Finally, following the ISO 834 fire case scenario, a simulation of the wall assembly was performed in which the investigated material plays a protective role against high temperatures. The following are the key findings:

- The influence of open pores dominated the phenomena of increased heat transmission due to the integrity of the pore structure. Low pore connectivity induces pore structural deformation due to the detrimental effect of water vapour movement across the porous structure. A more permeable sample can

slow the rate of temperature rise and pore pressure increase, resulting in a slower temperature increase at a given depth.

- Even though two composites have the same initial chemical composition, high-temperature exposure reveals variances between them. These variations are caused primarily by changes in pore structure, but also indirectly by the disintegration of the top layer of the more disintegrated sample, which allowed more heat to penetrate the composite and trigger phase crystallisation. The newly formed crystalline phases ie feldspars (microcline, anorthoclase), augite and hematite. can be used to determine the temperature at a given depth.
- The presence of cracks above 100 μm has a significant impact on radiative heat flow at high temperatures, as evidenced by the higher achieved temperature at a depth of 2.5 cm for the more degraded sample (773 °C) than for the more permeable sample (430 °C).
- The effect of material deterioration on the heat transfer process can be described by approximating cracks as pores and employing Loeb's equation. Pore shape factors ranging from 2/3 to 1 can mimic the elongated shape of formed cracks. The formed cracks increased the number of open pores detected within the composite. Noteworthy, this model closely matches the experimental results.
- An example of an application was demonstrated. The 2.5 cm thick panel attached to the concrete wall meets the integrity and insulation condition for 93 cm during the simulated ISO 834 fire curve. When a single layer of porous material is compared to other geopolymer foam or autoclaved concrete, it provides very good insulation over a long period (330 min). At a depth of 2.5 cm, it reaches 180 ^{o}C after 25 minutes, which is comparable to the results of other foam geopolymers.

CHAPTER 8 AN ALTERNATIVE ROUTE TO UTILIZE MINERAL WOOL WASTE: ALKALI ACTIVATED-ARTIFICIAL AGGREGATES WITH IMPROVED HIGH-TEMPERATURE PROPERTIES

In this chapter, an alternative utilization route for Mineral Wool Waste (MWW) as a solid precursor for artificial aggregate manufacturing is proposed. The process parameters including alkali activation (Na or K) and curing regime, are investigated. Room and high-temperature (1000 °C) characterizations are performed, both on the sole aggregates and when incorporated in geopolymer composite. The results reveal that with an optimum pre-curing regime at room temperature for 3 days, artificial aggregates with particle density ranging from 1960 to 2090 kg/m³ and crushing strength of 7.0 to 7.9 MPa can be obtained. The behaviour of aggregates is strongly related to the alkali cation type. The Na-based activator with high viscosity resulted in a more irregular grain shape with lower particle density and lower crushing strength as compared to K-activated aggregates. High crystallinity is observed in K-activated aggregates, causing better thermal stability. The alkali-activated artificial aggregates show a geopolymer-like behaviour in geopolymer composites, which contributes to higher strength development over normal sand aggregate.

The results presented in this chapter are included in the following article:

K.M. Klima, Y. Luo, H.J.H. Brouwers, and Q.L. Yu, "An alternative route to utilize mineral wool waste: alkali activated-artificial aggregates with improved high-temperature properties" (in preparation)

8.1 Introduction

Nowadays, as the construction infrastructure develops rapidly (4300 Mt cement produced in 2021), the need for aggregate materials is significantly increasing since aggregates account for 60-70 % of the volume of concrete [436]. The increased demand for natural aggregates causes over-exploitation of natural resources, hence many countries have been forced to tighten their sourcing policies [437] to avoid irreversible topographic changes. With the high aggregate demand and limited supply, growing interests are raised in artificial aggregates (AA). This type of aggregate is often prepared by combining powdered material with water or alkaline activator solution, the particles are bonded together in a granulation process, following a hardening process with varied curing regimes, such as elevated temperature sintering, cold-bonding, accelerated carbonation and alkali activation [438]–[441]. In the last decades, the utilization of waste materials, such as recycled concrete, furnace bottom ash, GGBFS, or fly ash as raw material in making AA is a subject of growing interest, which not only equips the obtained AA with different characteristics but also helps to tackle the disposal problem with waste and industrial by-products [442], [443]. It is of great importance to investigate alternative waste streams to manufacture artificial aggregates from a sustainable development consideration.

As one of the most utilized insulation materials for building energy conservation, mineral wool is applied either as thermal insulation [444] or acoustic material [445] in the shape of slabs, mats, or loose material placed into wall cavities [446]. A large amount of mineral wool waste (MWW) is formed during the manufacturing, construction and demolition operations. The MWW production in Europe was estimated to be 3 million tons by 2020, which is expected to further grow[34]. Its low density, low stiffness and poor compressibility lead to severe disposal problems from the aspects of toxic concerns, transportation, costs, and its stability in landfills [447], [448]. There have been several attempts to recycle MWW to reproduce ceramic products [449], [450], fibre boards/panels [47], [451] or reutilize it as fibre reinforcement/supplementary cementitious material in cement-based composites [48], [452], [453]. Unfortunately, due to its fibrous nature and the inconsistency of the chemical/phase composition depending on the manufacturing process, the reutilization of MWW remains low [34]. Recently, Yliniemi et al. and Kinnunen et al. [45], [454]–[456] suggested reutilizing MWW as a precursor for alkali-activated materials due to its favourable chemical, and mineralogical composition and high surface area for alkali activation. In alkali-activated MWW, the reaction product assemblage is mainly dependent on the type of mineral wool and activating solution chemistry, with aluminosilicate hydrates as the dominating phase. Among those, a promising mechanical performance is achieved, showing a compressive strength of up to 30.0 MPa for sole MWW-based alkali-activated material and 12.8 MPa for MWW/fly ash geopolymer composites. Nevertheless, one of the main drawbacks in the MWW-based binder is that a huge amount of alkali-activator is needed, which leads to the environmental issue. In addition, the presence of organic resin in MWW such as phenolic resin, polyesters, and melamine-urea–formaldehyde may cause toxic volatile substances if the reuitilization includes heating or chemical treatment [34], [457]. The findings discussed above provide great potential to reutilize MWW as raw materials for artificial aggregate manufacturing.

Owing to its typical preparation technology, on the one hand, the pelletizing process can largely reduce the necessary moisture content thus lowering the alkali activator demand. On the other hand, the heating/curing process can not only burn off the resin [43] but also immobilized heavy metals [458]. Hence, this technology offers an alternative and more eco-friendly route for the valorization of MWW in large quantities. However, the design of artificial aggregate solely based on MWW has not been previously reported, and the possibility of reutilizing fibrous MWW in the process of making artificial aggregates via alkali activation is unclear yet.

In addition, as an eco-friendly alternative binder to ordinary Portland cement (OPC), the alkali-activated binder is known to exhibit promising high-temperature resistance over OPC-based materials [459]. Nevertheless, little information is available on making high-temperature resistant artificial aggregates based on alkali-activated materials. Up to now, lightweight aggregate (LWA) is the most commonly used for high-temperature resistance, such as pumice, perlite, vermiculite, expanded perlite and clay, etc. [460]–[462]. However, the intrinsically high cost of LWA's due to the specific fabrication process as well as their insufficient mechanical strength because of the porous structure largely restrict their large-scale application. Moreover, the inclusion of these aggregates in alkali-activated binders always results in a decline of mechanical strength due to the different thermal expansion behaviour between geopolymer and aggregates during high-temperature exposure [88], [112]. In this case, alkali-activated MWW aggregates could be a promising alternative to commercial lightweight aggregates, because on the one hand, given its mineral composition and manufacturing method, MWW equips itself with good thermal stability [463], on the other hand, the MWW-based binder after alkali activation has promising high-temperature resistance and exhibits similar thermal behaviour to other alkali-activated binders. Nevertheless, there is a lack of comprehensive understanding of the thermal behaviour of artificial aggregates when they are exposed to high temperatures, as well as the interreaction between alkali-activated artificial aggregates and either cement or geopolymer systems.

The goal of this work is to design alkali-activated aggregates based on MWW and determine their performance at both room and high temperatures (up to 1000 °C). To achieve this, the role of alkali cation (Na or K), and curing regime were reviewed and recommendations were established based on the material performance. A significantly lower curing temperature of 800 °C is applied as compared to that normally used in the manufacture (around 1200 °C) to remove organic resin and improve thermal stability. Basic room temperature properties including grain shape analysis, water absorption, particle density, and crushing strength of the obtain aggregate materials were determined. Thermogravimetric analysis, contour microscopy, and in-situ high-temperature XRD were used to establish the suitability of aggregates for high-temperature applications and predict their behaviour when applied in the composite. Lastly, the manufactured aggregates are further incorporated into the alkali-activated binder (geopolymer), and their performance at room temperature and after exposure to 1000 °C has been investigated and compared with commonly used sand aggregates. This study demonstrates the sufficient mechanical characteristics and bonding behaviour of the artificially fabricated aggregates, as well as the critical role of alkali in high-

temperature response. The findings propose a guideline for further research towards a potential reutilization strategy for MWW.

8.2 Experimental design

8.2.1 *Raw materials*

In this experiment, mineral wool waste (MWW) was employed as the raw material. The waste was provided by Rockwool, consisting of the waste material from the fine processing and crushed final products. It is a light material with a cured organic binder. The obtained MWW was processed using a disc mill (Retsch Vibratory Disc mill RS200) to reach the required particle size. The particle size distribution of raw materials was assessed using a laser particle size analyser (Mastersizer 2000, Malvern Instruments), as shown in **Fig. 8.1**.

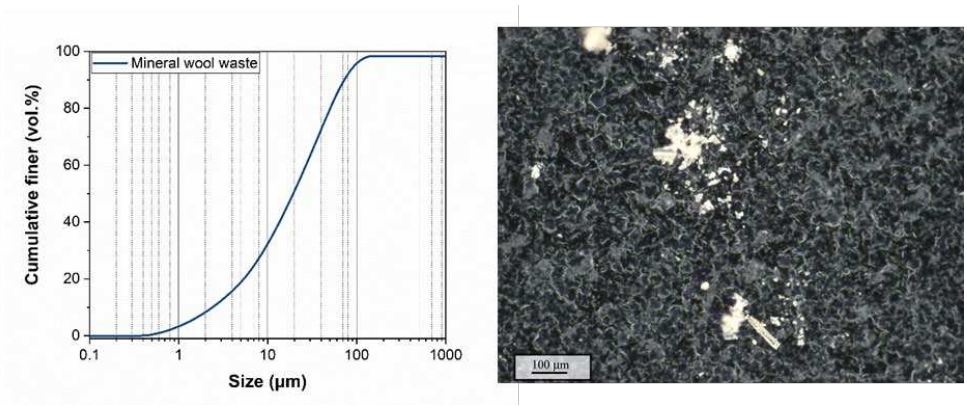

Fig. 8.1 Particle size distribution of waste material and the visual representation of MWW after milling.

The average particle size (d_{50}) of MWW was 20.2 µm. The chemical composition was measured using X-ray fluorescence spectrometry (XRF) (PANalytical Epsilon 3), and the loss on ignition was calculated using the mass difference after firing at 1000 °C.

Table 8.1. Chemical composition of mineral wool waste and siliceous fly ash (FA).

Content (%)	SiO_2	Al_2O_3	CaO	Fe_2O_3	MgO	K_2O	SO_3	TiO_2	V_2O_5	Cr_2O_3	MnO	Others	LOI	Si/Al (mol/mol)
MWW	37.6	17.5	19.6	9.9	7.8	1.3	0.3	1.9	0.1	0.1	0.4	0.2	3.5	1.82
FA	54.5	21.5	6.1	9.1	1.3	2.8	0.4	1.3	-	-	-	0.9	2.0	-

The chemical composition as well as the loss on ignition of MWW is shown in **Table 8.1**. TGA of raw material was carried out in an air environment between 30 and 1000 °C with a step of 20 °C/min, and **Fig.**

8.2 depicts the TG-DTG results with a brief description of temperature-induced events. The purpose of TGA was to clarify the thermal stability of MWW and establish the minimum sintering temperature required to remove the contained organic binder. Recent developments in artificial aggregate production have shown that sintering consumes energy at temperatures beyond 1000 °C. The TGA results supported by Ivanič et al. [464] confirmed that the combustion of the binder and other organic hydrophobic substances resulted in weight loss up to 800 °C. Thus, this study proposed an 800 °C alkali activation process that is cost-effective, practical, easy to use, and environmentally benign as compared to the traditional artificial aggregate production process.

Alkali activating solution was prepared using NaOH and KOH pellets (analytical level of 99 wt.%), commercial sodium silicate solution (8.4% Na_2O, 27.7% SiO_2, 63.9% H_2O), and potassium silicate (8% K_2O, 20.8% SiO_2, 72.8% H_2O). Activator solutions were tailored to provide the same silica modulus (1.5) and fixed oxide content of 6% M_2O (where M=Na, K) based on dry solid calculated as molar equivalent, and distilled water was employed in preparing the solution.

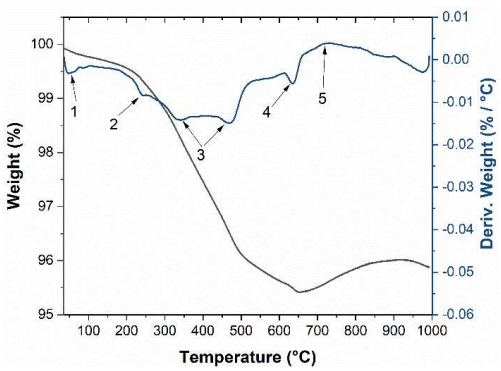

Fig. 8.2 TG-DTG results of raw MWW. 1) Water release present in the sizing agent and at the surface [464]; 2) 240 °C loss of volatiles from the organic binder and dust binding oil in the sample; 3) oxidation of the pyrolysis residues from binder [465]; 4) the binder evaporation at 650 °C [465]; 5) the oxidation of Fe^{2+} to Fe^{3+}[466].

The amorphous character of the initial material was disclosed through XRD phase analysis (**Fig. 8.3**). Trace amounts of crystalline phases were detected, such as quartz and calcite, in agreement with Pavlin et al. [467]. Furthermore, the presence of iron was confirmed, which occurs in a divalent state owing to the reducing conditions of material production. The presence of aluminosilicates (magnesium and potassium) is the consequence of the basic composition of stone wool fibre, which is manufactured from an aluminosilicate rock mixture (usually basalt). The fly ash characterization can be found in **Chapter 4** section 4.2.

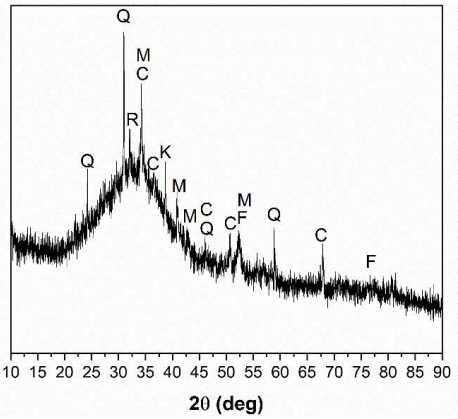

Fig. 8.3 XRD diffractograms of raw material. Legend: Q: Quartz; R: Rutile; C: Calcite; K: Potassium aluminium silicate ($K_{1.25}Al_{1.25}Si_{0.75}O_4$); F: Ferrite; M: Magnesium Aluminium Silicate (Pyrope $Mg_3Al_2(SiO_4)_3$).

8.2.2 *Motivation for the selected utilization method*

A partial life cycle assessment (A1-A3) is performed to motivate the choice of utilisation technique, namely the MWW-based paste (binder) and artificial aggregate design. When compared to binder design, sintered aggregates technology has reduced embodied energy. It should be mentioned that the global warming potential of aggregates in this study is evaluated at 0.23 kg CO_{2e}· kg^{-1} and geopolymer binder at 0.34 kg CO2e· kg-1 including the carbon in substracts and manufacturing energy (**Table 8.2**). The energy consumption for sintering/curing of geopolymer has been determined experimentally. The large difference between the two processes is mostly due to the potassium hydroxide and silicates, which account for only 1% of the total final product weight in geopolymer and 3% (KOH) and 18% in geopolymer (waterglass). Hence, the environmental aspect of the utilization of mineral wool waste to produce artificial aggregates regardless of the needs of the building industry is also more environmentally friendly.

Table 8.2. Comparison of the two utilization methods of MWW based on the embodied energy calculation for the production stage (A1-A3)

	Per unit*	**Per kg of the final product**	
	kg-CO2eq	**Aggregate**	**Geopolymer paste**
Potassium hydroxide	1.89917	0.0134	0.0600
Potassium silicate	1.49873	0.0187	0.2626
Water	0.00661	0.0002	0.0004
Production energy	0.50786	0.1981	0.0132
Total		**0.2304**	**0.3362**

*Open LCA database

8.2.3 *Sample preparation*

Aggregates manufacturing

Aggregates were produced by applying an agglomeration process using an Eirich-type GTE disc pelletizer. The settings were 150 rpm and a slope of 45°. First, the mineral wool waste powder was added to the pan, followed by alkali activator spraying until the surface was moist. Last, the dry powder of MWW was applied to promote aggregate formation. Finally, due to gravity and pan movement, the granules that had attained a stable shape dropped out of the pan, indicating the end of the production. Following that, moist granules were cured in the environment chamber at RH80% at varied temperatures and times (**Table 8.3**).

The cured aggregates were sieved (<125 μm) to remove small-size particles before being sintered at 800 °C for 2 hours. The sintering was introduced to remove residual organic resin and increase the reactivity of unreacted particles [436]. The aggregates were stored in sealed plastic bags until further testing.

Table 8.3. Mix details of manufactured aggregates.

Sample code	Alkali cation	Relative humidity (%)	Curing regime Temp (°C)	Time (day)
Na20-1	Sodium		20	1
Na20-2	Sodium	80	20	2
Na20-3	Sodium		20	3
K20-1	Potassium		20	1
K20-2	Potassium	80	20	2
K20-3	Potassium		20	3
Na50-1	Sodium		50	1
Na50-2	Sodium	80	50	2
Na50-3	Sodium		50	3
K50-1	Potassium		50	1
K50-2	Potassium	80	50	2
K50-3	Potassium		50	3

Geopolymer composite design

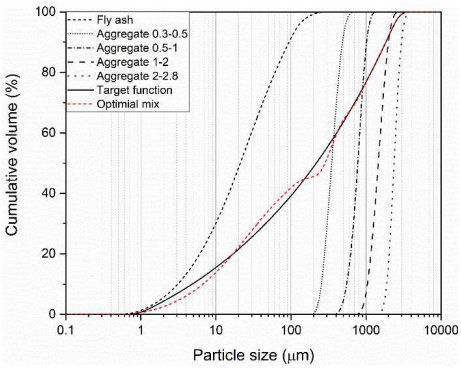

Fig. 8.4. Particle size distributions of the raw materials, the target curve and the resulting integral grading line of a sample mix.

In this work, the geopolymer-based composite was prepared by applying fly ash (FA) (Chemical composition in **Table 8.1**) as the binder material, and three size fractions of mineral wool waste-based aggregate were used. The particle size distribution of each fraction is shown in **Fig. 8.4**. The alkaline solution for the geopolymer was obtained by combining potassium hydroxide pellets (VWR Life Science, reagent grade) and potassium silicate solution (WHC, K_2O 8%, SiO_2 20%, 72.8 % H_2O by mass) to achieve a SiO_2/K_2O ratio of 1.4.

The geopolymer composite was designed based on the modified Andreasen & Andersen particle packing model [468]:

$$P(D) = \frac{D^q - D^q_{min}}{D^q_{max} - D^q_{min}} \tag{8.1}$$

In which P(D) is the cumulative fractions of particles smaller than D. D_{max} and D_{min} represent the maximum and minimum particle size, respectively. q is the distribution modulus. Brouwers [469], [470] suggested that a positive effect can be obtained with a q-value range of 0–0.37. Gao et al.[471], Borges et al.[472] and Ng et al.[473] recommended a q value in a range of 0.20-0.26 for a geopolymer-based binder. In this study, a q value of 0.2 was adopted to achieve good workability and packing without using any superplasticizers. Based on that, the calculated target function curve and the fitted grading curve are shown in **Fig. 8.4**, and the detailed mix proportions are listed in **Table 8.4**. In order to make the results comparable, in the mixtures with different aggregates (**Table 8.4**), the volume of each size fraction for different aggregates was kept constant. Moreover, as suggested by Yliniemi et al. [474], the aggregates used in geopolymer composites were not pre-wetted prior to mixing to establish a favourable ITZ between the fresh paste and the rough, porous grain surface. The amount of water was design to ensure good workability of the composites. It should be noted that due to the more irregular shape of Na-based aggregates, a slightly lower flowability is noticed in geopolymer with incorporated Na-based aggregates incorporated geopolymer. Two best performing aggregates material were used for this investigation and compared to commercially available sand (coarse industrial sand used in floor mortars). The detailed test methods used for aggregates characterization are presented in **Chapter 2** section 2.9.

Table 8.4. Mix proportions of geopolymer composites (kg/m^3).

Mix	Fly ash	Activator	Agg 0.3-0.5	Agg 0.5-1	Agg 1-2	Agg 2-2.8
K	790.8	404.2	173.5	164.6	221.4	121.5
Na	790.7	404.2	169.1	158.8	217.9	119.3
Sand	790.8	332.1	365.5	226.1	276.6	150.3

8.3 Results and discussion

8.3.1 *Shape analysis*

The aggregate morphology has a significant influence on the workability, mechanical properties and durability of concrete materials [475]. In this study, two categories of the obtained aggregates are investigated for the shape analysis, differing in activator used, i.e. sodium and potassium. Firstly, qualitative analysis is performed using an optical microscope. Furthermore, as one of the most important indicators of aggregate morphology, the circularity parameter of the aggregates is quantitatively determined by using ImageJ based on optical microscopy images. This parameter indicates the regularity of the shape and for which 1 is a perfect spherical shape whereas 0 is strongly irregular. The appearance of the exemplary grains as well as the circularity results for the three selected size ranges are summarized in **Fig. 8.5.**

The main observation concerning the grain shape is that the sodium-based aggregates are much more irregular than aggregates with potassium-based activator. More specifically, the most irregular fraction with the largest circularity variation is observed within the smallest analyzed range (0.5-2 mm), in particular for Na-based samples. It should be noted that in this particle size range, the dominant part is located between circularity factors 0.9 and 1.0. Further, it is clear to observe that the circularity is reduced in the larger size fraction. This confirms the relation between particle size and circularity, as reported by Wang et al. [65] that the regularity of their shape decreases with the increase in grain size. Moreover, K-based material grains in each range oscillate between 0.5-1.0 while Na-based material exhibits a larger circularity range between 0.2-1.0. It can therefore be confirmed that a greater irregularity in all size ranges is obtained for aggregates based on the sodium activator. This is mainly due to, despite maintaining the same activator parameters, the obtained Na-based activating solution (0.16 Pa·s) are much more viscous than K-based solution (0.05 Pa·s), leading to a faster agglomeration (growing) of the grains during the preparation, and hence a more irregular shape is obtained. The viscosity of two activator solutions was determined using the stress/strain-controlled rotational rheometer (Anton Paar MCR501) in a couette. Each solution was measured twice at 20 °C with a number of data points of 21 per measurement. The irregularly shaped aggregates have a higher surface-to-volume ratio and can provide better bond characteristics but impact the workability when applied in concrete [476]. Furthermore, the rough surface generates a stronger bond between the paste and the aggregate creating a higher paste-aggregate strength. As a result, the observed shape characteristic would determine their performance during application in the geopolymeric composite, which will be discussed later.

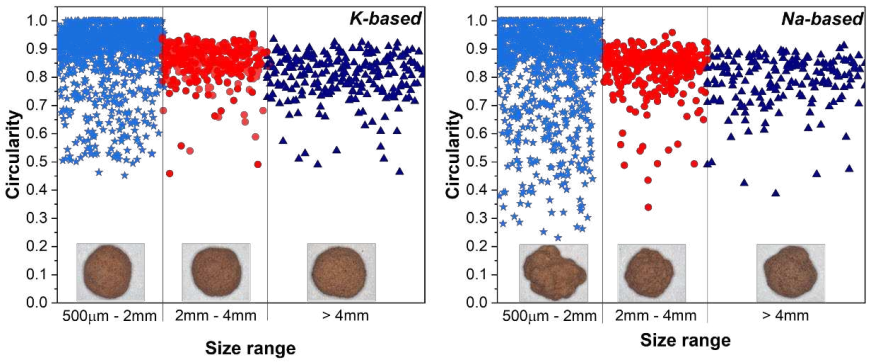

Fig. 8.5 Circularity of sodium (Na-based) and potassium (K-based) aggregated within each grain size range together with the average circularity value for each range and standard deviation.

8.3.2 *Particle density, water absorption and crushing strength*

Fig. 8.6a depicts particle density, whereas apparent density (**Fig. 8.6b)** represents impermeable grain density, as defined in ASTM C128-15. Overall, it can be concluded that changes within particle density are negligible, due to the use of sintering as a step following low temperature 20 or 50 °C pre-curing, oscillating in a narrow range of the limit value (2.0 g/cm^3) for lightweight and normal aggregates [442]. The pre-curing step is the only difference between aggregates based on the same type of activator (Na or K), so the analysis that follows is primarily concerned with determining the causes of variations in the sample parameters as a function of time (1 to 3 days) and temperature (20 or 50 °C). An increase in density is observed for samples pre-treated at 20 °C, along with an extension of conditioning time from one to three days, which may indicate a reduction in grain porosity without changing the binder gel structure, as evidenced by the similar value of the skeleton density. Regardless of temperature, sodium aggregates are less dense, which is related to the previously discussed phenomenon of the rapid growth of grains by agglomeration of smaller particles, resulting in reduced packing density with entrapped pores. Open porosity values can be calculated using the particle density and apparent density **(Table 8.5**). It is clear that as the curing time is increased at room temperature, the volume of open pores available for the penetrating medium (water) decreases, whereas at 50 °C, the increase in curing time results in the formation of cracks. when combined with the values of open porosity with the water absorption values (**Fig. 8.6c**), this might be the outcome of the early-age drying shrinkage of AAM observed and described by Češnovar et al. [477]. The research showed that at high relative humidity (90%) and temperature (60 °C) the volume shrinkage tends to be gradual, continuous and linear over 72 hours, while at the same humidity conditions, the shrinkage at room temperature is significantly smaller. This causes the formation of (micro)cracks, higher water absorption and low density and strength of the alkali-activated materials which could explain the better overall performance of room temperature conditioned aggregate. Noteworthy, the skeleton density

value of potassium-based aggregates is reduced when the pre-curing temperature changed from 20 °C to 50 °C, hence showing the higher sensitivity of the potassium-based system on the conditioning temperature.

Table 8.5. Open pore volume calculated from particle density and apparent density.

Curing time (day)	K20	Na20	K50	Na50
1	32.1	31.8	24.4	29.6
2	31.0	32.1	26.6	32.1
3	27.9	30.0	28.0	32.5

The crushing strength at different curing ages is shown in **Fig. 8.6d**. It can be seen that the crushing strength of the 20 °C cured samples developed fast at an early age and then gradually improved with time. However, for 50 °C cured samples, a minor improvement (Na50-3) or a decrease (K50-3) with increasing time is noticeable. Here, the strength evolution correlates well with water absorption. The drying shrinkage that might occur in 50 °C cured samples brings more microcracks and defects along with the curing duration, which largely offsets the strength gain effect during curing. Hence, it is stated that the defects and deformation after pre-curing have a direct impact on the performance of aggregates after 800 °C sintering. Conversely, the particle densification process under 20 °C from 1 to 3 days further contributes to the higher strength.

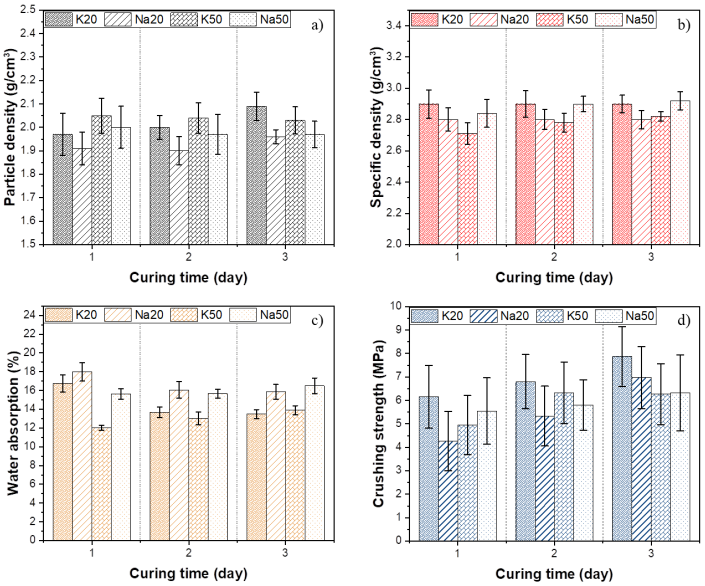

Fig. 8.6 Particle density, specific density, water absorption and crushing strength of the designed aggregates.

8.3.3 *Microstructure*

In order to study the microstructure of the aggregates, the SEM micrographs of the different aggregates are collected. The analysis aims to provide insight into the role of pre-curing temperature and alkali activation on microstructure development. Thus, the interior of the grain and the grains' surface of 3 days of curing samples are compared, and the micrographs after 1 and 2 days curing are presented in Appendix D (Fig. D.1). Note that these grains have been fired at 800 °C for 2 hours subsequently to curing. As shown in **Fig. 8.7**, a general examination of the aggregates' cross-section reveals a dense film, demonstrating the bonding development in the aggregate preparation process. Furthermore, it appears that K-activated samples have the most homogenous and dense structure with a visible smooth appearance, whereas sodium-based samples, particularly Na50-3, appear to be more granular and loosely packed (**Fig. 8.7d**).

It is known that the grain surface determines the adherence to the binder, and fresh-state properties of the mortar mix. Overall, all aggregates possess a significant surface roughness and irregularity. Unreacted particles in grains and voids are observed in all aggregates, which impacts their performance. Furthermore, within the compacted binder, the mineral wool fibres covered with the gel are observed, which reveals the nature of the raw material after milling, namely fine material containing short chopped fibres. In terms of the effect of pre-curing temperature, an intriguing observation concerning 50 °C cured samples (**Fig. 8.7 c,d**) indicates that, despite the sufficient binding within the core part, the surface appears to be more porous as compared to 20 °C cured samples, consisting of an insufficient amount of binder to produce a homogeneous structure. This is possibly due to the rapid water loss during pre-curing at 50 °C, which hinders the reaction product formation and good gel development at the surface. Moreover, from the inner structure of K-based samples shown in **Fig. 8.8**, increasing microcracks arise in samples cured at 50 °C (**Fig. 8.7c**) due to the drying shrinkage mentioned above. As a result, the present structural deterioration, namely the spaces between unreacted particles on the surface of aggregates as well as the microcracks and trapped air voids within the aggregates causes an increase in the amount of water absorption and deterioration of mechanical strength for high-temperature pre-cured samples.

When comparing the samples based on different types of activators, Na based sample (**Figs 8.7b, and d)** shows a greater amount of pores than K-based system. This phenomenon is suggested to arise from the varied viscosity between different activator types. As evidenced by the shape analysis in Section 8.3.1, the higher viscosity of the Na-based activator inevitably results in a more irregular particle shape, giving rise to a coarser inner microstructure with more pores and voids.

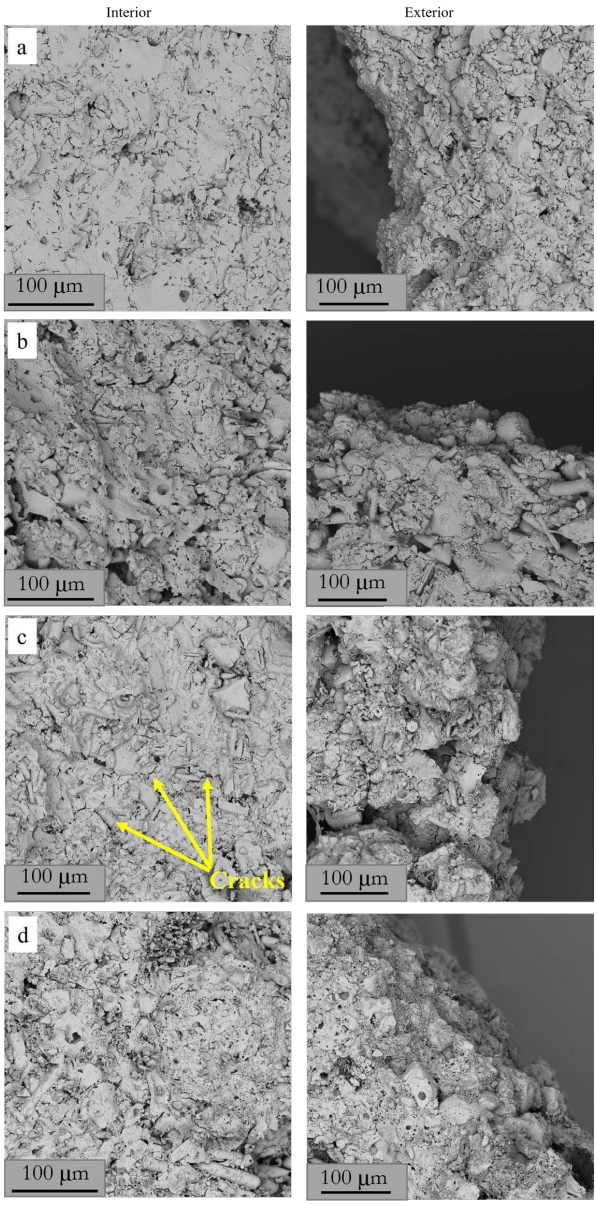

Fig. 8.7 SEM of four aggregates samples after 3 days curing a)K20-3; b)Na20-3; c)K50-3; d)Na50-3.

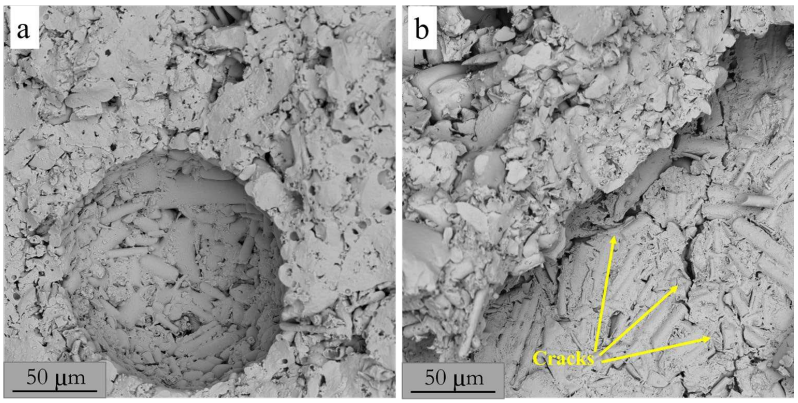

Fig. 8.8. Interior of potassium-based aggregates a) K20-3; b) K50-3.

8.3.4 *Thermal stability*

Based on the characteristics of aggregates at room temperature, such as water absorption and single crushing strength, K20-3 and Na20-3 samples are considered to be the optimal performing batches. Furthermore, from the energy consumption perspective, it is profitable to avoid an elevated pre-curing temperature and it is beneficial that a 20 °C pre-curing with controlled high humidity conditions turns out to limit the drying shrinkage and enables sufficient hydration reaction. Therefore, thermal analysis is performed on two selected types of aggregates, namely K20-3 and Na20-3.

Thermogravimetric analysis is performed under a nitrogen atmosphere to test the stability of the matrix from room temperature to 1000 °C (**Fig. 8.9a**). Overall, a relatively low-temperature treatment (800 °C 2h) provides the material with high stability up to a temperature of 1000 °C, achieving a mass loss of 0.18%, and 0.15% for Na and K-based samples respectively, which reflects the target temperature of the aggregate application. The DTG curve reflects the curing regime of conditioning of aggregates, where no significant changes are observed until 800 °C while a decrease in mass is noticed after 900 °C. This is related to the thermal treatment of industrial mineral-wool waste that results in the formation of a wide variety of pyrolysis products both in an inert atmosphere and in the air [478]. As the temperature increases, the surface of the solid sample gradually releases pyrolysis gas, noticing a loss of weight in DTG.

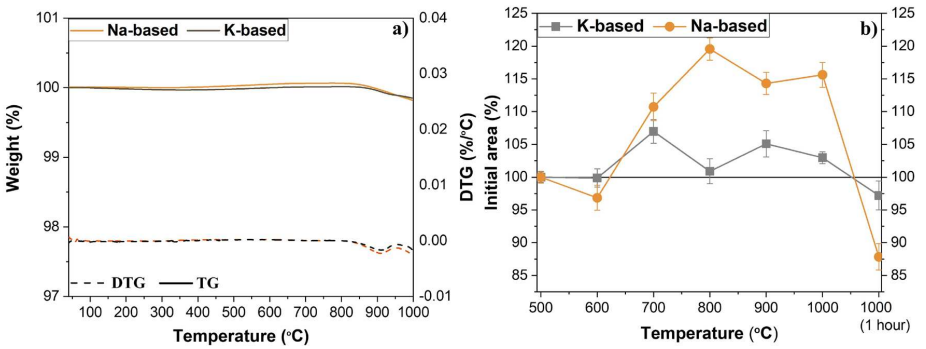

Fig. 8.9 a) Thermogravimetry analysis: TG and DTG curves of aggregates; b) grain area analysis via contour microscopy normalize to area at 500 °C.

The volumetric stability of aggregates at high temperatures is further analysed via in-situ grain size measurement (**Chapter 2** section 2.9) during heating to a temperature of 1000 °C. An important aspect is that different degree of thermal expansion is observed in both types of grains at or above the temperature of sintering (**Fig. 8.9b**). In Na-based aggregates, two significant expansion regions can be distinguished, with the maxima at 800 °C and 1000 °C, followed by an area decrease due to melting. While potassium-based materials are more thermally stable, with a less noticeable expansion above 800 °C and modest shrinkage at 800 and 1000 °C. The contraction event in K-based can be linked to the crystalization at 800 °C and melting at 1000 °C.

In order to explain the different thermal-induced volumetric change phenomena between Na and K-based samples, a quantitative in-situ XRD analysis was performed (**Fig. 8.10)** to reveal the phase transformation in the K_2O-Na_2O-CaO-MgO-Al_2O_3-SiO_2 system at high temperatures. The XRD diffractograms are attached in Appendix D (Fig.D.2). Considering that the material consists of pulverized mineral wool waste, with either potassium or sodium-based alkali activator, all others can be regarded as being the same. MWW is almost entirely glassy as a raw material, and only part of the glass reacts upon alkaline activation. The resulting product is a geopolymer gel with residual glass. It is noted in **Fig. 8.10** that in K-based aggregates no phase changes occur until 800 °C, when K-feldspar appears at the expense of the amorphous phase. At 1000 °C, pyroxene (augite) content increases. In the Na-based system, the pyroxene seems to increasingly form from 400 °C at the expense of amorphous. The higher proportion of the amorphous phase in Na-based systems additionally poses a negative influence on the grain volumetric stability, which is prone to melting and losing shape at elevated temperatures. The majority of the iron in the MWW raw material is divalent, with some being trivalent. Glass and geopolymer behave differently when heated for two hours at 800 °C. The amorphous compound in **Fig.8.10** may represent the remaining original MWW glass with negligible reactivity and amorphous alkali-activated gel which is expected to be reactive.

The equilibrium phase assemblages were calculated using FactSage for various proportions of MWW and activator with a silica modulus of 1.5. **Table 8.6** shows the phase proportions of melilite (akermanite

$Ca(Mg,Fe)_3Si_2O_7$) and clinopyroxene (augite $Ca(Fe,Mg)Si_2O_6$) in XRD that were best reproduced with the addition of 2 wt% SiO_2.via alkali activator solution. As previously mentioned, the amorphous phase is the remaining MWW-glass that was not alkali-activated at low temperatures during pre-curing, but it may also contain an alkali-rich residue from which the clinopyroxene and the melilite formed. During the production of the aggregate, no equilibrium phase assemblage was established. Since local equilibrium was already established at 800 °C during the earlier aggregate preparation stage, no changes in this composition will be noticed during reheating in the high-temperature XRD until it reaches that temperature.

Table 8.6. Factsage thermodynamic calculation of phase distribution at 800 °C for 2 wt% silica added (normalized to 100 wt.%).

	K-based	**Na-based**
	wt.%	**wt.%**
Clinopyroxene	45	58
Melilite	20	13
Spinel	13	11
Ilmenite	5	5
Leucite	16	5
Nepheline	0	18
Olivine	1	1

Above 800 °C, the systems begin to react once more, and more of the sample's mass is involved in reactions that lead to equilibrium. Amorphous decreases as more melilite and clinopyroxene are formed. K-tectosilicate is also formed, which is more difficult to crystallize because it requires an arrangement of the SiO_4 tetrahedra in a 3D structure (a tectosilicate structure). At 800 °C, it appears that all potassium-based phases remain in the amorphous state, whereas the resulting mineralogical composition in the sodium-based system is consistent with the Factsage calculation, i.e. the presence and predominance of pyroxene, nepheline, and akermanite. Spinel (hercynite $FeAl_2O_4$) formation was kinetically hindered in both cases and, contrary to Factsage calculations, was not observed in the system.

.

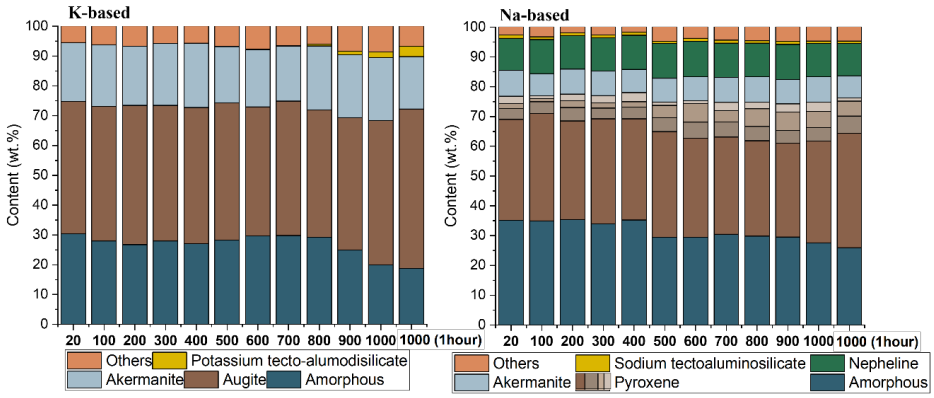

Fig. 8.10 In-situ high-temperature XRD quantification of potassium and sodium-based aggregates. Note: Sodium tectoaluminosilicate $NaAlSiO_4$; Potassium tectoaluminodisilicate $KalSi_2O_6$.

8.3.5 *Characterization of geopolymer with artificial aggregates*

Up to now, the study regarding composite properties with alkali-activated aggregates is still relatively limited and requires further investigation [442]. In this study, two selected groups of aggregates, NA20-3 and K20-3, are further incorporated into siliceous fly ash-based geopolymer as indicated in Section 8.2.2. The behaviour of reinforced composites under both room- and high-temperature conditions (1000 ^{o}C) is further compared to a reference sample with normal sand aggregate. The high-temperature exposure test conditions are set as the same as for the aggregates testing, thus from room temperature to 1000 ^{o}C at a heating rate of 10 ^{o}C/min, and then held at 1000 ^{o}C for the duration of 1 hour. Above all, the fundamental parameters such as flexural and compressive strength at room and high temperatures, density, thermal shrinkage, and interfacial transition zone (ITZ) after high-temperature exposure are investigated.

Appearance and ITZ evaluation of heated geopolymers

Fig. 8.11 depicts the cross-section of the matrix before and after high-temperature exposure. In **Figs.8.11a,b**, before being exposed to elevated temperature, the white and grey regions indicate binder gel, and yellow grains denote artificial aggregates. While the paste-aggregate interface is indistinct in colour for sand-contained geopolymer (**Fig. 8.12c**). It is widely reported that an alkali activation system can largely improve the ITZ between geopolymeric binder and artificial aggregates [442]. In this work, all mixtures show a dense ITZ, and the aggregates are uniformly distributed, with no evidence of separation or agglomeration, indicating a feasible mix design. After elevated temperature exposure, it is obvious that the colour of the paste binder changes from grey to brownish orange as a result of the iron oxidation from Fe^{2+} to Fe^{3+} [114]. Furthermore, the colour of the aggregates is lightened to a more yellowish, which was also

observed after the high-temperature contour microscopy examination as the result of the oxidation reactions mentioned above.

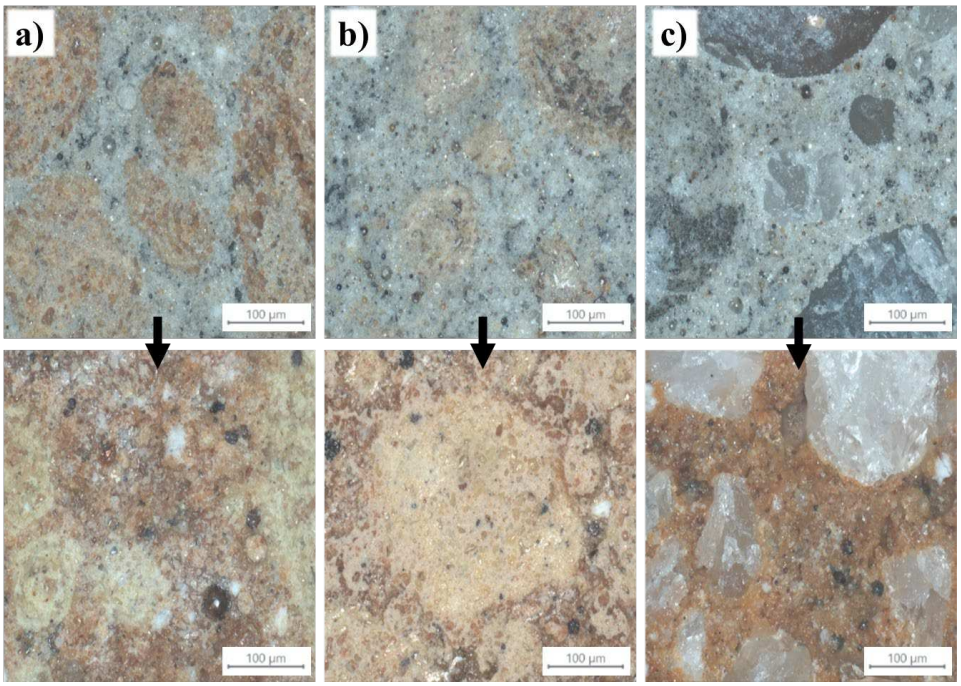

Fig. 8.11 Cross section of geopolymers before and after high-temperature exposure containing a) K-based; Na-based; c) sand aggregates. Top images at room temperature bottom after exposure to 1000 °C and cooled in air.

In order to learn the thermally induced deformation in ITZ in more detail, SEM analysis is carried out on samples after exposure to 1000 °C. As shown in **Fig. 8.12**, it is obvious that the ITZ of potassium and sodium-based aggregates is denser than that of sand after high-temperature exposure. In artificial aggregates reinforced geopolymer as seen in **Figs. 8.12a,b,** the ITZ after being subjected to high temperature is almost indistinguishable. This has resulted from a similar binding system, namely alkali activation, and the unreacted precursor on the aggregate surface tends to react with a binder, leading to the formation of mechanical interlocking on the porous, rough surface of aggregates [442]. Additionally, the sintering reaction among the fly ash-based binder and artificial aggregates above 600 °C further promotes the binding and strengthens the ITZ [12]. In terms of normal sand aggregates, a conversion takes place at a temperature of 573 °C when α-quartz undergoes a reversible change in its crystal structure to form β-quartz and causes a linear expansion, while during cooling the change is reversed from β- to α-quartz and shrinks [479]. Due to the reversible thermal expansion and shrinkage of sand aggregates at high temperatures, an obvious gap is observed between the grain and paste.

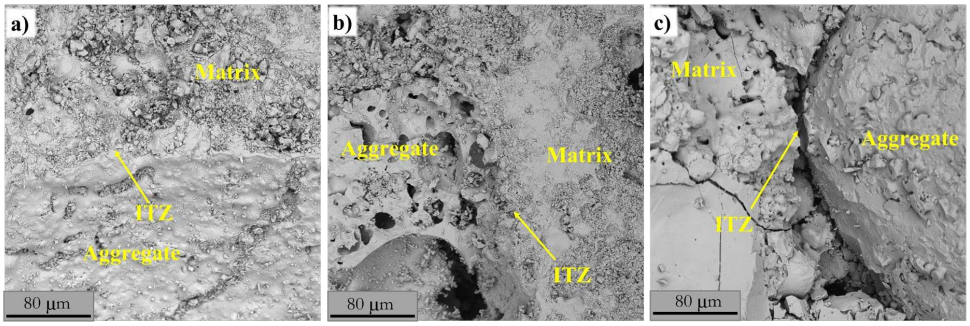

Fig. 8.12 SEM images of the ITZ after exposure to 1000 °C of a) K-based; b) Na-based and c) sand.

Volumetric stability and density evolution

Despite knowing their thermal response in an oxidizing environment and employing literature knowledge regarding paste behaviour during heating [12], aggregate performance within an alkaline matrix can be unpredictable. The processes that direct volume change are inextricably linked to reaching the glass transition and further melting temperature. As a transitional state between glass and liquid, the glassy phase becomes more plastic above the sintering temperature. These changes are observed as swelling in the air, but in geopolymer, the fly ash-based matrix also possesses its own response to high temperature, as shown in **Chapter 4**, namely shrinkage, densification and sintering at 1000 °C. As a result, the observed change in geometry is an indicator of the grain's stability and strength under high-temperature conditions, which explains the observed shrinkage caused by the aforementioned phenomena. As discussed above, the more vitreous phase presented in the Na-based aggregate has a more detrimental effect on the grain performance. In terms of the thermal behaviour of the binder, the applied geopolymeric binder contains a potassium activator, hence the softening temperature is expected to be around 800 °C [12], [125]. A lower temperature exposure may cause the formation of defect zones in the paste, as paste dehydration causes shrinkage. Furthermore, all samples begin to shrink significantly above the softening temperature due to the matrix sintering. For the thermal behaviour of aggregates, as learned above, the applied sodium and potassium aggregates expand at 700 °C and 900 °C (**Fig. 8.9b**), respectively, while sand expands at 573 °C.

Table 8.7: Bulk density of geopolymer at room and high temperature together with calculated volume change after thermal exposure.

Sample code	Density at 20 °C (g/cm^3)	Density after 1000 °C (g/cm^3)	Thermal volumetric change $\Delta v/v_0$ (%)
K-based	1.68	1.70	-3.0
Na-based	1.64	1.69	-4.35
Sand	1.90	1.90	-0.75

The paste melting and aggregate thermal expansion mechanisms overlap and pose a coupling effect on composite high-temperature stability. As can be observed in **Table 8.7**, all composites exhibit a much lower

thermal volumetric change than that of pure geopolymer paste at 1000 °C (~8%) [169]. However, the thermal shrinkage is significantly smaller when sand aggregate is employed. This is because the sand aggregates have high stiffness, which could act as a strong skeleton under high temperatures that largely offsets the matrix shrinkage. Nevertheless, owing to the drastic competition between the binder shrinkage and the thermal expansion of sand aggregates, severe structural deterioration such as gaps and cracks are obtained in the composite with sand as shown in **Fig. 8.12c.** The irreparable damage and gaps developed between the aggregate and the paste, causing problems with the material's use after high-temperature exposure.

Noteworthy, on the one hand, both artificial aggregates have an improved binding within the alkali-activated matrix due to the presence of unreacted precursor on the particle surface. On the other hand, as discussed above, the artificial aggregates show a geopolymer alike thermal behaviour due to the similar chemical composition, sintering and/or melting after 800 °C along with geopolymeric binder, which further weakens the competition mechanism between binder and aggregates. As a result, the matrix is largely preserved with less thermal deterioration after being subjected to elevated temperature as evidenced by SEM analysis in **Fig. 8.12a, and b**. In conclusion, selecting potassium aggregates with better thermal stability (lower thermal expansion value) further poses a positive impact on geopolymer performance at high temperatures than sodium aggregates.

Compressive and flexural strength before and after high temperature-exposure

Fig. 8.13 further compares the compressive and flexural strength before and after high-temperature exposure. At room temperature, the difference in mechanical strength of the three geopolymer samples is insignificant, indicating the suitability of replacing normal sand with the designed artificial aggregates. The geopolymer with sodium-based aggregates and sand aggregates shows slightly higher flexural and compressive strength than that of the geopolymer with potassium-based aggregates. This difference is mainly related to the shape variation of the aggregate grains, as investigated in *Section 8.3.1*. The sodium-based aggregate and sand are more irregular than the potassium-based aggregate, which contributes to a higher adherence force between binder and aggregates [480], [481]. In addition, the sodium-based aggregates are believed to further react with the geopolymer and adhere to the binder, hence providing a better bonding, resulting in the highest compressive and flexural strength at room temperature.

After exposure to a high temperature, artificial aggregates reinforced samples experience a significant gain in both compressive and flexural strength, while sand-incorporated geopolymer has an obviously lower compressive strength gain **(Table 8.8**) and the flexural strength is significantly reduced after high-temperature exposure.

Table 8.8. Mechanical performance of geopolymeric composite after exposure to high temperature.

Aggregate type	Binder	Exposure Temperature (°C)	Compressive strength gain (%)	Ref
River sand (1:2)	Fly ash	1000	36	[80]
River sand (1:1)	Fly ash	1000	33	
Copper slag (1:2)	Fly ash	1000	59	
Copper slag (1:1)	Fly ash	1000	38	
Silica sand	Metakaolin+Slag	800	-65	[482]
River sand	Metakaolin+Slag	800	-78	
Sandstone	Metakaolin+Slag	800	-97	
Waste concrete sand	Metakaolin+Slag	800	N/A failure	
Basalt sand	Metakaolin+Slag	800	-62	
Rilem sand	Metakaolin+Slag	800	-85	
Basalt	Fly ash	800	-71	[112]
K-based MWW	**Fly ash**	**1000**	**240**	**This study**
Na-based MWW	**Fly ash**	**1000**	**238**	
Sand	**Fly ash**	**1000**	**76**	

Lahoti et al. [88], [258] reported that the compressive strength of geopolymer-based materials after high-temperature exposure is mainly governed by competing mechanisms of crack formation, matrix densification and viscous sintering. In our case, the matrix densification and viscous sintering play a dominant role in determining the compressive strength, resulting in a strength gain for all samples. Meanwhile, the severe structural deterioration and cracking in the sample with sand aggregates described above weakens the strength gain effect, leading to the lowest compressive strength gain after high-temperature exposure. This negative effect of structural deterioration in sand-incorporated samples is more significant in flexural strength since the flexural property of materials is largely affected by crack formation. As a result, a halved flexural strength is obtained in the sand-involved sample after high-temperature exposure.

When comparing the sample with different types of artificial aggregates, the highest mechanical performance is obtained in the sample with sodium-based aggregates incorporated. An interesting phenomenon is related to the lower single-crushing strength of sodium-based aggregates (**Fig. 8.6d**) but higher geopolymer strength results. This resulting discrepancy is because of the compressive strength of composites not only depends on the aggregate crushing strength but also on other characteristics such as ITZ, which could positively contribute to paste-aggregate binding capabilities [474]. As discussed above, the more irregular shape and higher surface roughness of Na-based aggregates offer a larger contact surface for developing an ITZ, thus a higher mechanical strength is obtained. In addition, it is worth noting that this enhanced bonding in geopolymer with Na-based aggregates further poses a positive influence on thermal-mechanical performance, by strengthening the ITZ during viscous sintering and melting. As a result, the geopolymer with Na-based aggregates exhibits the highest mechanical strength after high-temperature exposure.

In conclusion, as compared to normal sand aggregate, the designed artificial aggregates show a geopolymer-alike thermal behaviour, such as re-crystallization, viscous sintering, and melting. The geopolymer-alike thermal behaviour provides artificial aggregates with the advantage over traditional aggregates at elevated temperatures **(Table 8.8**), by reducing the thermal mismatch between the geopolymer matrix and the aggregates, which contributes to better microstructural stability and mechanical performance subjected to high temperatures.

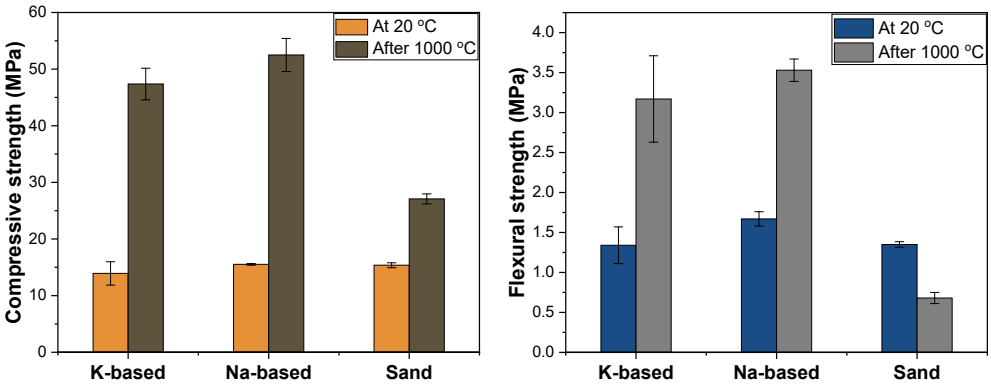

Fig. 8.13 Compressive and flexural strength of geopolymer samples before and after high-temperature exposure.

8.4 Conclusions

The objective of this study is to design a sustainable artificial aggregate solely based on mineral wool waste with a focus on high-temperature application. Overall, the proposed method shows that mineral wool waste can be a promising raw material for the alkali-activated artificial aggregate with excellent thermal performance. The initial properties, as well as the thermal behaviour of the designed artificial aggregate, are determined and the optimum preparation regime has been proposed. At last, the designed artificial aggregates are applied to prepare geopolymer-based composites, and their performances are further compared with that of normal sand-incorporated geopolymer. The following are the most noteworthy findings:

- To produce the artificial aggregate based on mineral wool waste, a room-temperature curing is proposed instead of elevated-temperature pre-curing in considering the energy costs and the structural deterioration with high-temperature curing. Regarding the curing time, it is beneficial for strength development to provide 3 days of curing prior to sintering at 800 °C. The obtained artificial aggregates (T=20°C, t=3 days), show particle density ranging from 1960 kg/m^3 to 2090 kg/m^3 and crushing strength of 7.0 to 7.9 MPa.

- The type of activator plays a dominant role in aggregate particle formation. The sodium-based activator with high viscosity leads to a more irregular shape of grains within the analyzed aggregates ranges (from 500 μm to above 4 mm) as well as a coarser microstructure with more pores and air voids. This consequently results in a lower particle density, higher water absorption and lower crushing strength as compared to potassium-based aggregate.
- High-temperature response of aggregates is strongly related to the alkali cation type. Both aggregate types show a certain degree of thermal expansion; however, in comparison, the expansion is reduced in the potassium-based system, which is mainly related to its high rate of crystallinity.
- As compared to normal sand, artificial aggregates exhibit better compatibility in the geopolymer composite given its comparable chemical composition to the geopolymer binder. Under the alkaline environment a better bonding between the binder and artificial aggregates is achieved, reflected by the development of mechanical interlocking on the porous and rough surface of the aggregates with an indistinguishable interfacial transition zone. As a result, superior mechanical performance is achieved in geopolymer composite with artificial aggregates.
- At high temperatures, the designed artificial aggregates show a geopolymer-alike thermal behaviour, namely re-crystallization, viscous sintering, and melting. It provides artificial aggregates with the advantage over traditional sand in high-temperature resistant geopolymer concrete, by reducing the thermal mismatch between the geopolymer matrix and the aggregates, thus contributing to better microstructural stability and mechanical performance when subjected to high temperatures.

CHAPTER 9 CONCLUSIONS AND RECOMMENDATIONS

This thesis is devoted to the development of a high-temperature stable geopolymer binder based on fly ash, as well as the investigation of improving the thermal behaviour of geopolymer-based materials. Several aspects were investigated in order to address this topic, including the thermal performance of siliceous fly ash-based geopolymers, foamed composites, and an innovative route to produce high-temperature resistant aggregates based on mineral wool waste. The outcome of this investment and its future prospects are shown below.

9.1 Conclusions

Siliceous fly ash-based geopolymer

The extensive literature review revealed the disparities between the existing literature findings. The reactive silica and alumina content cannot be straightforwardly determined via the XRF method due to the high crystalline content of raw fly ash. As a result, unless the reactive and/or amorphous content of alumina and silica has been determined, recommendations for an optimum silica modulus and Si/Al content are misleading. Furthermore, the melting temperature of the vitreous phase is strongly influenced by the type and content of alkali, and the analysis revealed that potassium can play a more important role in maintaining material stability than its sodium counterpart. In addition, a mechanism governing thermal performance up to 1000 ^{o}C was proposed in order to comprehend and predict the material response to high temperatures. Finally, because of the differences in thermal properties, the role of geopolymer-zeolite cannot be universally established. To investigate the possibility of enriching geopolymer with thermally stable zeolite, the sodalite was synthesised from siliceous fly ash and added in amounts of 2.5 and 5% to the geopolymer slurry. Ex-situ synthesised zeolites not only reduced volumetric shrinkage but also enriched the bulk composition with sodium ions, boosting the formation of different crystalline phases (wollastonite and anorthoclase) and changing the glass composition. The sodalite's mesoporous nature altered the pore size distribution at room temperature and influenced pore evolution up to 1000 ^{o}C. It has been determined that adding 5% sodalite to the geopolymer mix is considered a good practice to improve the high-temperature performance of geopolymers.

Foamed composites

The great room temperature properties and promising high-temperature resistance drove the design of porous composites. To design a porous matrix, a direct foaming method using hydrogen peroxide and surfactants was proposed. However, because the slurry is a complex system of solid particles and ions, interactions with ionic surfactants are unavoidable. Noteworthy, cationic-contained systems exhibited stronger surfactant-solid particle attraction, resulting in a system with smaller-size closed pores. Thus, the nonionic surfactant addition was proposed to reduce the aforementioned interaction and electrostatic

repulsion between head groups. Four different nonionic-ionic combinations of surfactants were tested to evaluate whether the pore structure could be tailored by choosing the right cosurfactant mix and the investigation revealed that it is possible to trigger the formation of pore cavities and increase the availability of ionic surfactant molecules to stabilise air bubbles by using this solution. According to the material properties investigation, the cationic CTAB (Cetyltrimethylammonium Bromide) stabilises the pores below 200 μm and the fraction of closed pores in total pore volume fraction is lower than that of Sodium Dodecyl Sulphate, providing better thermal insulation properties. Overall, the three investigated mixes are promising at transferring water vapour, which implies that when employed as wall assembly, they might be utilised to manage the surrounding humidity variations. Based on the contribution of open porosity, Sodium Dodecyl Sulphate with nonionic Triton X-100 is the best mix design. This mixture was also chosen for another study on the thermal and acoustic insulation properties at room temperature. The role of fly ash in defining the pore infrastructure was investigated, as well as the possibility of matrix enrichment with silica aerogel to improve the ambient temperature insulation characteristics. It was discovered that adding 10% silica aerogel significantly improves thermal and acoustic insulation properties, and due to the minor additional improvement when increased to 20% and satisfactory mechanical performance, it was selected as a compromise between performance and cost increase. Overall, increasing the amount of silica aerogel increased the total porosity of the composites. It has been stated that silica aerogel particles act as thermal barriers, and the wide range of particle size increased tortuosity, as evidenced by higher sound absorption coefficient value and better hygrothermal performance. Regarding the role of fly ash type, both provide sufficient total porosity (60-70%), but due to the rapid setting of the biocoal fly ash-based paste, the smaller size bubbles were stabilised, minimising the effect of bubble coalescence, thus the pore size distribution is shifted toward the lower size pores, which directly influences the insulation properties of the designed composites.

Two of the four investigated cosurfactant mixtures, based on the same nonionic surfactant, Triton X-100, were chosen for a further high-temperature related study. According to the literature, open porosity aids in the mitigation of fire-related damage by allowing moisture to move from the hot to the cold side of the wall. Pore size distribution on material degradation and thermal-induced crystalline phase formation has been investigated to evaluate the role of open porosity. Finally, the best-performing material was evaluated by simulating its performance in contact with fire up to 1100 °C. The results show that a 2.5 cm thick panel protects for 93 minutes until the surface of the concrete wall reaches 180 °C. The study emphasised the importance of maintaining material integrity during the first 20 minutes because possible cracks speed up the temperature rise within the material and accelerate crack propagation during high-temperature exposure (up to 1100 °C). Although the quantitative composition of both composites was initially the same, variations in the quantitative composition, such as feldspars, pyroxenes, or hematite, were observed as a result of an increased flow of heat into the structure of the material that had undergone thermal degradation on the surface.

Thermally stable artificial aggregates

Another approach for strengthening the geopolymer structure at high temperatures is to use thermally stable fillers and aggregates. To reduce thermal shrinkage, one approach presented in this thesis was to enrich the geopolymer matrix with synthesised crystalline sodalite. An alternative approach to designing aggregates from waste material was proposed and thoroughly investigated in this study. An alkali activation combined with a sintering route has been proposed using mineral wool waste as a solid precursor. As an optimal route for energy conservation, the room temperature (20 °C) and high relative humidity (RH80%) for three days prior to the low-temperature sintering (800 °C) were proposed to obtain aggregates with densities ranging from 1960 kg/m^3 to 2090 kg/m^3 and crushing strengths ranging from 7.0 to 7.9 MPa. Furthermore, when different alkali cations are used, the grain characteristics such as particle shape, water absorption, and crushing strength vary (sodium or potassium). Within the examined aggregate ranges (from 500 μm to 6 mm), the sodium-based aggregate has a more irregular grain shape, higher water absorption, and lower crushing strength. Also, the high-temperature response of sodium-based aggregates is unsatisfactory, with higher thermal expansion due to lower crystallinity rates and differences in vitreous phase composition. Since the bonding behaviour between the aggregates and the geopolymer, the generated two types of artificial aggregates perform better in the geopolymer matrix than sand in terms of strength development at room and after high-temperature exposure.

9.2 Recommendations

Alkali-activated materials show good thermal properties and provide an alternative solution for industrial by-products and waste materials utilization. As demonstrated in this thesis, a variety of techniques may be used to improve high-temperature material performance, including material aeration and incorporation of reinforcing materials as fillers or aggregates. As with any new technology, geopolymer manufacturing faces some challenges before it can be used efficiently in commercial applications. One of the challenges is the environmental impact assessment at an industrial scale also because the production process data are limited to the laboratory manufacturing procedure. Scaling effects result in energy efficiencies, economic benefits and environmental advantages. In this context, some specific recommendations for future studies that were identified while carrying out this work are provided.

(1) The flame resistance has not been evaluated due to testing facility constraints. Small-scale fire testing in the assembly with concrete is recommended to determine the extent to which geopolymer inhibits flame spread and reduced concrete damage during a fire. It is also essential to ensure material stability and safety before classifying the obtained fireboard as a fire-resistant material.

(2) The porous protective material which has been demonstrated in this thesis is in the form of the panel (fireboards). Given the lower adaptability to demanding building structures, more research into the use of the proposed porous geopolymer mix design as a sprayable material for complex

facades is suggested. The protective material's thickness can be further adjusted to meet the requirements of the protected material. This broad recommendation would pave the way for new sprayable material research, with a focus on tailoring the rheology of pumpable geopolymer.

(3) This thesis mainly examined the effects of heat and moisture on the performance of fireboards. The fireboards were conditioned without plastic foil wrapping for 26 days prior to testing to mimic normal conditions. Further research into the role of other external factors such as carbonation, atmospheric precipitation, freeze-thaw weathering, and other chemical attack cycles, as well as their impact on high-temperature properties, is of great need.

(4) The zeolite-geopolymer composites with small zeolite additions, namely 2.5% and 5%, exhibit intriguing properties; therefore, it is recommended to investigate higher enrichment with sodalite or to propose an alternative route for in-situ sodalite synthesis in geopolymer matrix to avoid excessive alkali anionic influencing the glass composition and thermal stability.

(5) The artificial aggregates research provides insight into the potential use of mineral wool waste from the construction and demolition waste stream. The results obtained are very promising, and there is plenty of room for further progress in determining aggregates' material suitability for other applications and binders, such as performance in OPC-based, alkali-activated calcium-rich binders. Furthermore, their environmental impact, including leaching behaviour and long-term durability, must be thoroughly examined.

(6) The alkaline activator used to produce the geopolymer accounts for approximately 74% to 97% of their total environmental impact. Although the silica modulus and alkali concentration employed in this experiment was limited, the alkali activator still has the potential to severely impact the view of geopolymer technology as green and sustainable. More research is therefore needed to determine how to lower the amount of alkali activators in the mix design. For instance, silica fume-based geopolymer appears to be a promising alternative for the production of concrete with reduced environmental impacts. Additional analysis could be performed by taking overall greenhouse gas (GHG) impact and energy consumption into account to enhance the sustainable decision-making process for high temperature resistant geopolymer production.

BIBLIOGRAPHY

[1] European Association, "Fire Safe Europe." https://firesafeeurope.eu/about-us/.

[2] Internal Association of Fire and Rescue Services, "Center for Fire Statistics World Fire Statistics" (2022). [Online]. Available: https://ctif.org/world-fire-statistics.

[3] The Business Research, "Fire Protection Materials For Construction Global Market Report 2022." [Online]. Available: https://www.reportlinker.com/p06233732/?utm_source=GNW.

[4] Q. Ma, R. Guo, Z. Zhao, Z. Lin, and K. He, "Mechanical properties of concrete at high temperature—A review" *Constr. Build. Mater.*, vol. 93, pp. 371–383, (2015).

[5] V. D. Glukhovsky, "Soil silicates: Their properties, technology and manufacturing and fields of application" *Doct. Tech. Sc. Degree Thesis, Civ. Eng. Institute, Kiev, Ukr.*, (1965).

[6] J. Davidovits, "Solid phase synthesis of mineral blockpolymer by low temperature polycondensation of alumino-silicate polymers." (1976).

[7] J. Davidovits, "Geopolymers and geopolymeric materials" *J. Therm. Anal.*, vol. 35, no. 2, pp. 429–441, (1989).

[8] S. Thokchom, P. Ghosh, and S. Ghosh, "Acid resistance of fly ash based geopolymer mortars" *Int. J. Recent Trends Eng.*, vol. 1, no. 6, p. 36, (2009).

[9] Z. Yunsheng, S. Wei, C. Qianli, and C. Lin, "Synthesis and heavy metal immobilization behaviors of slag based geopolymer" *J. Hazard. Mater.*, vol. 143, no. 1–2, pp. 206–213, (2007).

[10] J. Davidovits, "False values on CO_2 emission for geopolymer cement/concrete published in scientific papers" *Tech. Pap.*, vol. 24, pp. 1–9, (2015).

[11] J.L. Provis, and J.S.J. Van Deventer, Geopolymers: Structures, processing, properties and industrial applications. Elsevier Ltd, (2009).

[12] K.M. Klima, K. Schollbach, H.J.H. Brouwers, and Q.L. Yu, "Thermal and fire resistance of Class F fly ash based geopolymers–A review" *Constr. Build. Mater.*, vol. 323, p. 126529, (2022).

[13] D.L.Y. Kong, J.G. Sanjayan, and K. Sagoe-Crentsil, "Comparative performance of geopolymers made with metakaolin and fly ash after exposure to elevated temperatures" *Cem. Concr. Res.*, vol. 37, no. 12, pp. 1583–1589, (2007), doi: 10.1016/j.cemconres.2007.08.021.

[14] P. Rovnaník, and K. Šafránková, "Thermal behaviour of metakaolin/fly ash geopolymers with chamotte aggregate" *Materials (Basel)*, vol. 9, no. 7, p. 535, (2016).

[15] K. Dhasindrakrishna, K. Pasupathy, S. Ramakrishnan, and J. Sanjayan, "Progress, current thinking and challenges in geopolymer foam concrete technology" *Cem. Concr. Compos.*, vol. 116, p. 103886, (2021).

[16] E. Commission, "European Commission – Department: Energy – In focus. Energy efficiency in buildings" no. February, (2020).

[17] A.S. Tártaro, T.M. Mata, A.A. Martins, and J.C.G.E. da Silva, "Carbon footprint of the insulation cork board" *J. Clean. Prod.*, vol. 143, pp. 925–932, (2017).

[18] V. Kočí, and R. Černý, "Directly foamed geopolymers: A review of recent studies" *Cem. Concr. Compos.*, p. 104530, (2022).

[19] Z.N.M. Ngouloure, E. Kamseu, H.K. Tchakoute, L. Valentini, and C. Leonelli, "Design of porous Geopolymers for hygrothermal applications: role of nano and meso porosity" *Silicon*, pp. 1–15, (2022).

[20] P. Palmero, A. Formia, P. Antonaci, S. Brini, and J.-M. Tulliani, "Geopolymer technology for application-oriented dense and lightened materials. Elaboration and characterization" *Ceram. Int.*, vol. 41, no. 10, pp. 12967–12979, (2015).

[21] Z. Zhang, J. L. Provis, A. Reid, and H. Wang, "Mechanical, thermal insulation, thermal resistance and acoustic

absorption properties of geopolymer foam concrete" *Cem. Concr. Compos.*, vol. 62, pp. 97–105, (2015), doi: 10.1016/j.cemconcomp.2015.03.013.

[22] C. Leiva, Y. Luna-Galiano, C. Arenas, B. Alonso-Fariñas, and C. Fernández-Pereira, "A porous geopolymer based on aluminum-waste with acoustic properties" *Waste Manag.*, vol. 95, pp. 504–512, (2019).

[23] C. Bai, and P. Colombo, "Processing, properties and applications of highly porous geopolymers: A review" *Ceram. Int.*, vol. 44, no. 14, pp. 16103–16118, (2018), doi: 10.1016/j.ceramint.2018.05.219.

[24] J. G. Sanjayan, A. Nazari, L. Chen, and G. H. Nguyen, "Physical and mechanical properties of lightweight aerated geopolymer" *Constr. Build. Mater.*, vol. 79, pp. 236–244, (2015), doi: 10.1016/j.conbuildmat.2015.01.043.

[25] V. Medri, E. Papa, J. Dedecek, H. Jirglova, P. Benito, A. Vaccari, and E. Landi, "Effect of metallic Si addition on polymerization degree of in situ foamed alkali-aluminosilicates" *Ceram. Int.*, vol. 39, no. 7, pp. 7657–7668, (2013).

[26] X. Liu, C. Hu, and L. Chu, "Microstructure, compressive strength and sound insulation property of fly ash-based geopolymeric foams with silica fume as foaming agent" *Materials (Basel)*, vol. 13, no. 14, p. 3215, (2020).

[27] E. Prud'homme, E. Joussein, and S. Rossignol, "Use of silicon carbide sludge to form porous alkali-activated materials for insulating application" *Eur. Phys. J. Spec. Top.*, vol. 224, no. 9, pp. 1725–1735, (2015), doi: 10.1140/epjst/e2015-02494-7.

[28] S. Yan, F. Zhang, J. Kong, B. Wang, H. Li, Y. Yang, and P. Xing, "Mechanical properties of geopolymer composite foams reinforced with carbon nanofibers via modified hydrogen peroxide method" *Mater. Chem. Phys.*, vol. 253, p. 123258, (2020).

[29] B. Ren, J. Liu, J.-M. Wu, T. Wang, C. Liu, H. Chen, B. Li, and J. Chen, "Harnessing Ostwald ripening to fabricate hierarchically structured mullite-based cellular architecture via the gelation network-triggered morphology-regulation method" *J. Eur. Ceram. Soc.*, vol. 42, no. 1, pp. 238–244, (2022).

[30] C. Bai, and P. Colombo, "High-porosity geopolymer membrane supports by peroxide route with the addition of egg white as surfactant" *Ceram. Int.*, vol. 43, no. 2, pp. 2267–2273, (2017).

[31] C. Bai, J. Zheng, G. A. Rizzi, and P. Colombo, "Low-temperature fabrication of SiC/geopolymer cellular composites" *Compos. Part B Eng.*, vol. 137, pp. 23–30, (2018).

[32] V. Phavongkham, S. Wattanasiriwech, T.W. Cheng, and D. Wattanasiriwech, "Effects of surfactant on thermo-mechanical behavior of geopolymer foam paste made with sodium perborate foaming agent" *Constr. Build. Mater.*, vol. 243, p. 118282, (2020).

[33] S. Kaza, L. Yao, P. Bhada-Tata, and F. Van Woerden, "What a waste 2.0: a global snapshot of solid waste management to 2050" (2018).

[34] J. Yliniemi, R. Ramaswamy, T. Luukkonen, O. Laitinen, Á.N. de Sousa, M. Huuhtanen, and M. Illikainen, "Characterization of mineral wool waste chemical composition, organic resin content and fiber dimensions: Aspects for valorization" *Waste Manag.*, vol. 131, pp. 323–330, (2021).

[35] B. Łaźniewska-Piekarczyk, M. Czop, and D. Smyczek, "The Comparison of the Environmental Impact of Waste Mineral Wool and Mineral in Wool-Based Geopolymer" *Materials (Basel)*, vol. 15, no. 6, p. 2050, (2022).

[36] K. Harini, S. Karthiyaini, and M. Shanmugasundaram, "Reusable and Recyclable Industrial Waste in Geopolymer Concrete" *Proc. Int. Conf. Innov. Technol. Clean Sustain. Dev.*, pp. 157–171, (2022).

[37] P.O. Awoyera, A.D. Akinrinade, A.G. de Sousa Galdino, F. Althoey, M.S. Kirgiz, and B.A. Tayeh, "Thermal insulation and mechanical characteristics of cement mortar reinforced with mineral wool and rice straw fibers" *J. Build. Eng.*, vol. 53, p. 104568, (2022).

[38] R. Ji, Y. Zheng, Z. Zou, Z. Chen, S. Wei, X. Jin, and M. Zhang, "Utilization of mineral wool waste and waste glass for synthesis of foam glass at low temperature" *Constr. Build. Mater.*, vol. 215, pp. 623–632, (2019).

[39] R. Kubiliute, R. Kaminskas, and A. Kazlauskaite, "Mineral wool production waste as an additive for Portland cement"

Cem. Concr. Compos., vol. 88, pp. 130–138, (2018).

[40] O. Bergersen, and K. Haarstad, "Treating landfill gas hydrogen sulphide with mineral wool waste (MWW) and rod mill waste (RMW)" *Waste Manag.*, vol. 34, no. 1, pp. 141–147, (2014).

[41] S. Romaniega Piñeiro, M. del Río Merino, and C. Pérez García, "New plaster composite with mineral wool fibres from CDW recycling" *Adv. Mater. Sci. Eng.*, (2015).

[42] S. Islam, and G. Bhat, "Environmentally-friendly thermal and acoustic insulation materials from recycled textiles" *J. Environ. Manage.*, vol. 251, p. 109536, (2019).

[43] Z.S. Yap, N. H. A. Khalid, Z. Haron, A. Mohamed, M. M. Tahir, S. Hasyim, and A. Saggaff, "Waste Mineral Wool and Its Opportunities—A Review" *Materials (Basel)*, vol. 14, no. 19, p. 5777, (2021).

[44] M.S. Aslam, B. Huang, and L. Cui, "Review of construction and demolition waste management in China and USA" *J. Environ. Manage.*, vol. 264, p. 110445, (2020).

[45] J. Yliniemi, B. Walkley, J. L. Provis, P. Kinnunen, and M. Illikainen, "Nanostructural evolution of alkali-activated mineral wools" *Cem. Concr. Compos.*, vol. 106, p. 103472, (2020).

[46] O. Väntsi, and T. Kärki, "Utilization of recycled mineral wool as filler in wood–polypropylene composites" *Constr. Build. Mater.*, vol. 55, pp. 220–226, (2014).

[47] M.H. Ali, "Fire resistant gypsum board containing mineral wool fibers and method." Google Patents, Dec. 10, 1985.

[48] A. Cheng, W.-T. Lin, and R. Huang, "Application of rock wool waste in cement-based composites" *Mater. Des.*, vol. 32, no. 2, pp. 636–642, (2011).

[49] W. Hao, J. Xu, R. Li, X. Zhao, L. Qiu, and W. Yang, "Developing superhydrophobic rock wool for high-viscosity oil/water separation" *Chem. Eng. J.*, vol. 368, pp. 837–846, (2019).

[50] L. Zhou, R. Li, G. Zhang, D. Wang, D. Cai, and Z. Wu, "Zero-valent iron nanoparticles supported by functionalized waste rock wool for efficient removal of hexavalent chromium" *Chem. Eng. J.*, vol. 339, pp. 85–96, (2018).

[51] W. Hergert, and T. Wriedt, "The Mie theory: basics and applications" vol. 169, (2012).

[52] E.N. Landis, and D.J. Corr, "Three dimensional analysis of air void systems in concrete" in *Measuring, Monitoring and Modeling Concrete Properties*, Springer Dordrecht, (2006), pp. 517–524.

[53] L. Korat, V. Ducman, A. Legat, and B. Mirtič, "Characterisation of the pore-forming process in lightweight aggregate based on silica sludge by means of X-ray micro-tomography (micro-CT) and mercury intrusion porosimetry (MIP)" *Ceram. Int.*, vol. 39, no. 6, pp. 6997–7005, (2013).

[54] K. Scrivener, R. Snellings, and B. Lothenbach, "A practical guide to microstructural analysis of cementitious materials" (2018).

[55] X. Li, B. Liu, and Q. Wu, "Enhanced Low-Frequency Sound Absorption of a Porous Layer Mosaicked with Perforated Resonator" *Polymers (Basel).*, vol. 14, no. 2, p. 223, (2022).

[56] C. Buratti, F. Merli, and E. Moretti, "Aerogel-based materials for building applications: Influence of granule size on thermal and acoustic performance" *Energy Build.*, vol. 152, pp. 472–482, (2017).

[57] BS EN 196-1, "Methods of testing cement" *Part 1 Determ. strength*, (2005).

[58] EN 196-3, "Methods of testing cement - Part 3: Determination of setting times and soundness" (2009).

[59] ISO 12571: 2021, "Hygrothermal performance of building materials and products — Determination of hygroscopic sorption properties" (2021).

[60] ASTM C 128-01, "Standard Test Method for Density , Relative Density (Specific Gravity), and Absorption" *ASTM Int.*, pp. 1–6, (2001).

[61] F.J. Semel, and D.A. Lados, "Porosity analysis of PM materials by helium pycnometry" *Powder Metall.*, vol. 49, no. 2, pp. 173–182, Jun. (2006), doi: 10.1179/174329006X95347.

[62] P. Gomathi, and A. Sivakumar, "Characterization on the strength properties of pelletized fly ash aggregate" *ARPN J.*

Eng. Appl. Sci., vol. 7, no. 11, pp. 1523–1532, (2012).

[63] K.N. Shivaprasad, and B.B. Das, "Determination of optimized geopolymerization factors on the properties of pelletized fly ash aggregates" *Constr. Build. Mater.*, vol. 163, pp. 428–437, (2018).

[64] H. Hafid, G. Ovarlez, F. Toussaint, P.H. Jezequel, and N. Roussel, "Effect of particle morphological parameters on sand grains packing properties and rheology of model mortars" *Cem. Concr. Res.*, vol. 80, pp. 44–51, (2016).

[65] A. Wang, M. Huang, Y. Chu, Y. Zhu, K. Liu, L. Guo, P. Liu, and D. Sun, "Optimization of mix proportion of basic magnesium sulfate cement-based high-strength coral concrete" *Constr. Build. Mater.*, vol. 341, p. 127709, (2022).

[66] https://www.grandviewresearch.com/, "Fire protection Materials Market for Construction Inudstry Analysis Report." [Online]. Available: https://www.grandviewresearch.com/industry-analysis/fire-protection-materials-market/methodology.

[67] K.D. Hertz, "Limits of spalling of fire-exposed concrete" *Fire Saf. J.*, vol. 38, no. 2, pp. 103–116, (2003), doi: 10.1016/S0379-7112(02)00051-6.

[68] L. Alarcon-Ruiz, G. Platret, E. Massieu, and A. Ehrlacher, "The use of thermal analysis in assessing the effect of temperature on a cement paste" *Cem. Concr. Res.*, (2005), doi: 10.1016/j.cemconres.2004.06.015.

[69] P. Duxson, G.C. Lukey, and J.S.J. van Deventer, "Thermal evolution of metakaolin geopolymers: Part 1 - Physical evolution" *J. Non. Cryst. Solids*, vol. 352, no. 52–54, pp. 5541–5555, (2006), doi: 10.1016/j.jnoncrysol.2006.09.019.

[70] W.D.A. Rickard, C.D. Borstel, and A. Van Riessen, "The effect of pre-treatment on the thermal performance of fly ash geopolymers" *Thermochim. Acta*, vol. 573, pp. 130–137, (2013), doi: 10.1016/j.tca.2013.09.030.

[71] W.D.A. Rickard, G.J.G. Gluth, and K. Pistol, "In-situ thermo-mechanical testing of fly ash geopolymer concretes made with quartz and expanded clay aggregates" *Cem. Concr. Res.*, vol. 80, pp. 33–43, (2016), doi: 10.1016/j.cemconres.2015.11.006.

[72] P.J.Davidovits, "30 Years of Successes and Failures in Geopolymer Applications. Market Trends and Potential Breakthroughs" *Clim. Chang. 2013 - Phys. Sci. Basis*, pp. 1–30, (2002), doi: 10.1017/CBO9781107415324.004.

[73] Z. Tang, W. Li, Y. Hu, J. L. Zhou, and V.W.Y. Tam, "Review on designs and properties of multifunctional alkali-activated materials (AAMs)" *Constr. Build. Mater.*, vol. 200, pp. 474–489, (2019), doi: 10.1016/j.conbuildmat.2018.12.157.

[74] J. Davidovits, "Geopolymer cement" *A Rev. Geopolymer Institute, Tech. Pap.*, vol. 21, pp. 1–11, (2013).

[75] M. Ozawa, and F. U. A. Shaikh, "A study on spalling behaviour of geopolymer mortars using ring restraint test" *Constr. Build. Mater.*, vol. 279, p. 122494, (2021), doi: 10.1016/j.conbuildmat.2021.122494.

[76] V.S. Le, and P. Louda, "Research of Curing Time and Temperature-Dependent Strengths and Fire Resistance of Geopolymer Foam Coated on an Aluminum Plate" *Coatings*, vol. 11, no. 1, p. 87, (2021).

[77] J.C. Kuri, S. Majhi, P.K. Sarker, and A. Mukherjee, "Microstructural and non-destructive investigation of the effect of high temperature exposure on ground ferronickel slag blended fly ash geopolymer mortars" *J. Build. Eng.*, vol. 43, p. 103099, (2021).

[78] I. Hager, M. Sitarz, and K. Mróz, "Fly-ash based geopolymer mortar for high-temperature application–Effect of slag addition" *J. Clean. Prod.*, vol. 316, p. 128168, (2021).

[79] K. Traven, M. Češnovar, S.D. Škapin, and V. Ducman, "High temperature resistant fly-ash and metakaolin-based alkali-activated foams" *Ceram. Int.*, vol. 47, no. 17, pp. 25105–25120, (2021).

[80] M. Sivasakthi, R. Jeyalakshmi, and N.P. Rajamane, "Fly ash geopolymer mortar: Impact of the substitution of river sand by copper slag as a fine aggregate on its thermal resistance properties" *J. Clean. Prod.*, vol. 279, p. 123766, (2021).

[81] O.H. Li, L. Yun-Ming, H. Cheng-Yong, R. Bayuaji, M.M.A.B. Abdullah, F.K. Loong, T.S. Jin, N.H. Teng, "Evaluation of the effect of silica fume on amorphous fly ash geopolymers exposed to elevated temperature" *Magnetochemistry*, vol. 7, no. 1, pp. 1–14, (2021), doi: 10.3390/magnetochemistry7010009.

[82] M.E. Kalaw, J.M. Adiarte, R. dela Cruz, K.M. Martinez, C.A. Vega, and M.A. Promentilla, "Strength and fire resistance

characteristics of geopolymers synthesized from volcanic ash, red clay and waste pen shells" in *IOP Conference Series: Materials Science and Engineering*, (2021), vol. 1109, no. 1, p. 12068.

[83] M. Lahoti, K.K. Wong, K.H. Tan, and E.H. Yang, "Effect of alkali cation type on strength endurance of fly ash geopolymers subject to high temperature exposure" *Mater. Des.*, vol. 154, pp. 8–19, (2018).

[84] D. Yan, Y. Zhang, S. Chen, H. Fazli, Y. Liu, and Y. Ao, "Effect of Silica Moduli on the Thermal Degradation Mechanisms of Fly Ash–Based Geopolymer Mortars" *J. Mater. Civ. Eng.*, vol. 33, no. 5, p. 4021059, (2021).

[85] Y. Luna-Galiano, C. Fernández-Pereira, and M. Izquierdo, "Contributions to the study of porosity in fly ash-based geopolymers. Relationship between degree of reaction, porosity and compressive strength" *Mater. construcción*, vol. 66, no. 324, pp. e098–e098, (2016).

[86] W.D.A. Rickard, J. Temuujin, and A. Van Riessen, "Thermal analysis of geopolymer pastes synthesised from five fly ashes of variable composition" *J. Non. Cryst. Solids*, vol. 358, no. 15, pp. 1830–1839, (2012), doi: 10.1016/j.jnoncrysol.2012.05.032.

[87] L. Vickers, W.D.A. Rickard, and A. Van Riessen, "Strategies to control the high temperature shrinkage of fly ash based geopolymers" *Thermochim. Acta*, vol. 580, pp. 20–27, (2014), doi: 10.1016/j.tca.2014.01.020.

[88] M. Lahoti, K.H. Tan, and E.H. Yang, "A critical review of geopolymer properties for structural fire-resistance applications" *Constr. Build. Mater.*, vol. 221, pp. 514–526, (2019), doi: 10.1016/j.conbuildmat.2019.06.076.

[89] W.D.A. Rickard, R. Williams, J. Temuujin, and A. van Riessen, "Assessing the suitability of three Australian fly ashes as an aluminosilicate source for geopolymers in high temperature applications" *Mater. Sci. Eng. A*, vol. 528, no. 9, pp. 3390–3397, (2011), doi: 10.1016/j.msea.2011.01.005.

[90] R.T. Hemmings, and E. E. Berry, "On the Glass in Coal Fly Ashes: Recent Advances" *MRS Proc.*, (1987), doi: 10.1557/proc-113-3.

[91] D.M. Roy, K. Luke, and S. Diamond, "Characterization of fly ash and its reactions in concrete" *Materials Research Society Symposia Proceedings*. MRS Online Proceedings Library (OPL) 43, (1984), doi: 10.1557/proc-43-3.

[92] A. Bhatt, S. Priyadarshini, A.A. Mohanakrishnan, A. Abri, M. Sattler, and S. Techapaphawit, "Physical, chemical, and geotechnical properties of coal fly ash: A global review" *Case Stud. Constr. Mater.*, vol. 11, p. e00263, (2019).

[93] A. Fernández-Jiménez, and A. Palomo, "Characterisation of fly ashes. Potential reactivity as alkaline cements" *Fuel*, vol. 82, no. 18, pp. 2259–2265, (2003), doi: 10.1016/S0016-2361(03)00194-7.

[94] F.U.A. Shaikh, "23 - Fibre-reinforced geopolymer composites (FRGCs) for structural applications" in *Woodhead Publishing Series in Composites Science and Engineering*, Woodhead Publishing, 2014, pp. 569–593.

[95] D. Glosser, A. Choudhary, O.B. Isgor, and W.J. Weiss, "Investigation of Reactivity of Fly Ash and Its Effect on Mixture Properties" *ACI Mater. J.*, vol. 116, no. 4, pp. 193–200, (2019).

[96] H.S. Pietersen, A.L.A. Fraay, and J. M. Bijen, "Reactivity of fly ash at high pH" *MRS Online Proc. Libr. Arch.*, vol. 178, p. 139, (1989).

[97] A. Fernández-Jimenez, A.G. De La Torre, A. Palomo, G. López-Olmo, M. M. Alonso, and M. A. G. Aranda, "Quantitative determination of phases in the alkali activation of fly ash. Part I. Potential ash reactivity" *Fuel*, vol. 85, no. 5–6, pp. 625–634, (2006).

[98] K.U. Ambikakumari Sanalkumar, M. Lahoti, and E.H. Yang, "Investigating the potential reactivity of fly ash for geopolymerization" *Constr. Build. Mater.*, vol. 225, pp. 283–291, (2019), doi: https://doi.org/10.1016/j.conbuildmat.2019.07.140.

[99] J.L. Provis, C.Z. Yong, P. Duxson, and J.S.J. van Deventer, "Correlating mechanical and thermal properties of sodium silicate-fly ash geopolymers" *Colloids Surfaces A Physicochem. Eng. Asp.*, vol. 336, no. 1–3, pp. 57–63, (2009), doi: 10.1016/j.colsurfa.2008.11.019.

[100] L.P. Singh, S.R. Karade, S.K. Bhattacharyya, M.M. Yousuf, and S. Ahalawat, "Beneficial role of nanosilica in cement

based materials–A review" *Constr. Build. Mater.*, vol. 47, pp. 1069–1077, (2013).

[101] E.D. Rodríguez, S.A. Bernal, J.L. Provis, J. Paya, J.M. Monzo, and M.V. Borrachero, "Effect of nanosilica-based activators on the performance of an alkali-activated fly ash binder" *Cem. Concr. Compos.*, vol. 35, no. 1, pp. 1–11, (2013).

[102] S.K. Saxena, M. Kumar, and N.B. Singh, "Fire Resistant Properties of Alumino Silicate Geopolymer cement Mortars" *Mater. Today Proc.*, vol. 4, no. 4, pp. 5605–5612, (2017), doi: 10.1016/j.matpr.2017.06.018.

[103] F. Shaikh, and S. Haque, "Effect of nano silica and fine silica sand on compressive strength of sodium and potassium activators synthesised fly ash geopolymer at elevated temperatures" *Fire Mater.*, vol. 42, no. 3, pp. 324–335, (2018), doi: 10.1002/fam.2496.

[104] S. Wattanasiriwech, F.A. Nurgesang, D. Wattanasiriwech, and P. Timakul, "Characterisation and properties of geopolymer composites. Part 2: Role of cordierite-mullite reinforcement" *Ceram. Int.*, vol. 43, no. 18, pp. 16063–16069, (2017), doi: 10.1016/j.ceramint.2017.08.215.

[105] M.N.N. Khan, and P.K. Sarker, "Effect of waste glass fine aggregate on the strength, durability and high temperature resistance of alkali-activated fly ash and GGBFS blended mortar" *Constr. Build. Mater.*, vol. 263, p. 120177, (2020).

[106] X. Jiang, R. Xiao, Y. Ma, M. Zhang, Y. Bai, and B. Huang, "Influence of waste glass powder on the physico-mechanical properties and microstructures of fly ash-based geopolymer paste after exposure to high temperatures" *Constr. Build. Mater.*, vol. 262, p. 120579, (2020).

[107] S.A. Bernal, J. Bejarano, C. Garzón, R.M. De Gutiérrez, S. Delvasto, and E.D. Rodríguez, "Performance of refractory aluminosilicate particle / fiber-reinforced geopolymer composites" *Compos. Part B*, vol. 43, no. 4, pp. 1919–1928, (2012), doi: 10.1016/j.compositesb.2012.02.027.

[108] L. Carabba, R. Moricone, G.E. Scarponi, A. Tugnoli, and M.C. Bignozzi, "Alkali activated lightweight mortars for passive fire protection: A preliminary study" *Constr. Build. Mater.*, vol. 195, pp. 75–84, (2019), doi: https://doi.org/10.1016/j.conbuildmat.2018.11.005.

[109] I. Ozer, and S. Soyer-Uzun, "Relations between the structural characteristics and compressive strength in metakaolin based geopolymers with different molar Si/Al ratios" *Ceram. Int.*, vol. 41, no. 8, pp. 10192–10198, (2015), doi: 10.1016/j.ceramint.2015.04.125.

[110] P. Duxson, S.W. Mallicoat, G.C. Lukey, W.M. Kriven, and J.S.J. van Deventer, "The effect of alkali and Si/Al ratio on the development of mechanical properties of metakaolin-based geopolymers" *Colloids Surfaces A Physicochem. Eng. Asp.*, vol. 292, no. 1, pp. 8–20, (2007), doi: 10.1016/j.colsurfa.2006.05.044.

[111] P. Krivenko, and G. Kovalchuk, "Directed synthesis of alkaline aluminosilicate minerals in a geocement matrix" *J. Mater. Sci.*, vol. 42, no. 9, pp. 2944–2952, (2007), doi: 10.1007/s10853-006-0528-3.

[112] D.L.Y. Kong, and J.G. Sanjayan, "Effect of elevated temperatures on geopolymer paste, mortar and concrete" *Cem. Concr. Res.*, vol. 40, no. 2, pp. 334–339, (2010).

[113] K. Dombrowski, A. Buchwald, and M. Weil, "The influence of calcium content on the structure and thermal performance of fly ash based geopolymers" *J. Mater. Sci.*, vol. 42, no. 9, pp. 3033–3043, (2007), doi: 10.1007/s10853-006-0532-7.

[114] P.K. Sarker, S. Kelly, and Z. Yao, "Effect of fire exposure on cracking, spalling and residual strength of fly ash geopolymer concrete" *Mater. Des.*, vol. 63, pp. 584–592, (2014), doi: 10.1016/j.matdes.2014.06.059.

[115] A. Nazari, A. Bagheri, J.G. Sanjayan, M. Dao, C. Mallawa, P. Zannis, and S. Zumbo, "Thermal shock reactions of Ordinary Portland cement and geopolymer concrete: Microstructural and mechanical investigation" *Constr. Build. Mater.*, vol. 196, pp. 492–498, (2019), doi: 10.1016/j.conbuildmat.2018.11.098.

[116] N. Ranjbar, M. Mehrali, U.J. Alengaram, H.S.C. Metselaar, and M.Z. Jumaat, "Compressive strength and microstructural analysis of fly ash/palm oil fuel ash based geopolymer mortar under elevated temperatures" *Constr. Build. Mater.*, vol. 65, pp. 114–121, (2014), doi: 10.1016/j.conbuildmat.2014.04.064.

[117] W.D.A. Rickard, C.S. Kealley, and A. Van Riessen, "Thermally induced microstructural changes in fly ash geopolymers:

Experimental results and proposed model" *J. Am. Ceram. Soc.*, vol. 98, no. 2, pp. 929–939, (2015), doi: 10.1111/jace.13370.

[118] F.U.A. Shaikh, and V. Vimonsatit, "Compressive strength of fly-ash-based geopolymer concrete at elevated temperatures" *Fire Mater.*, vol. 39, no. 2, pp. 174–188, (2015), doi: 10.1002/fam.2240.

[119] S. Wattanasiriwech, F.A. Nurgesang, D. Wattanasiriwech, and P. Timakul, "Characterisation and properties of geopolymer composite part 1: Role of mullite reinforcement" *Ceram. Int.*, vol. 43, no. 18, pp. 16055–16062, (2017).

[120] H. Zhang, L. Li, C. Yuan, Q. Wang, P.K. Sarker, and X. Shi, "Deterioration of ambient-cured and heat-cured fly ash geopolymer concrete by high temperature exposure and prediction of its residual compressive strength" *Constr. Build. Mater.*, vol. 262, p. 120924, (2020).

[121] T.W. Cheng, and J.P. Chiu, "Fire-resistant geopolymer produce by granulated blast furnace slag" *Miner. Eng.*, vol. 16, no. 3, pp. 205–210, (2003), doi: 10.1016/S0892-6875(03)00008-6.

[122] J. Cai, X. Li, J. Tan, and B. Vandevyvere, "Thermal and compressive behaviors of fly ash and metakaolin-based geopolymer" *J. Build. Eng.*, vol. 30, p. 101307, (2020), doi: https://doi.org/10.1016/j.jobe.2020.101307.

[123] Sindhunata, J.S.J. Van Deventer, G. C. Lukey, and H. Xu, "Effect of curing temperature and silicate concentration on fly-ash-based geopolymerization" *Ind. Eng. Chem. Res.*, vol. 45, no. 10, pp. 3559–3568, (2006), doi: 10.1021/ie051251p.

[124] F. Uddin Ahmed Shaikh, S. Haque, and J. Sanjayan, "Behavior of fly ash geopolymer as fire resistant coating for timber" *J. Sustain. Cem. Mater.*, vol. 8, no. 5, pp. 259–274, (2018), doi: 10.1080/21650373.2018.1537015.

[125] Z. Pan, and J.G. Sanjayan, "Factors influencing softening temperature and hot-strength of geopolymers" *Cem. Concr. Compos.*, vol. 34, no. 2, pp. 261–264, (2012), doi: 10.1016/j.cemconcomp.2011.09.019.

[126] H.Y. Zhang, V. Kodur, B. Wu, J. Yan, and Z.S. Yuan, "Effect of temperature on bond characteristics of geopolymer concrete" *Constr. Build. Mater.*, vol. 163, pp. 277–285, (2018), doi: 10.1016/j.conbuildmat.2017.12.043.

[127] S. Luhar, S. Chaudhary, and I. Luhar, "Thermal resistance of fly ash based rubberized geopolymer concrete" *J. Build. Eng.*, vol. 19, pp. 420–428, (2018), doi: 10.1016/j.jobe.2018.05.025.

[128] Z. Pan, J.G. Sanjayan, and B.V. Rangan, "An investigation of the mechanisms for strength gain or loss of geopolymer mortar after exposure to elevated temperature" *J. Mater. Sci.*, vol. 44, no. 7, pp. 1873–1880, (2009), doi: 10.1007/s10853-009-3243-z.

[129] D.L.Y. Kong, and J.G. Sanjayan, "Damage behavior of geopolymer composites exposed to elevated temperatures" *Cem. Concr. Compos.*, vol. 30, no. 10, pp. 986–991, (2008), doi: 10.1016/j.cemconcomp.2008.08.001.

[130] A. Hosan, S. Haque, and F. Shaikh, "Compressive behaviour of sodium and potassium activators synthetized fly ash geopolymer at elevated temperatures: A comparative study" *J. Build. Eng.*, (2016), doi: 10.1016/j.jobe.2016.10.005.

[131] S.M. Park, J.G. Jang, N.K. Lee, and H.K. Lee, "Physicochemical properties of binder gel in alkali-activated fly ash/slag exposed to high temperatures" *Cem. Concr. Res.*, vol. 89, pp. 72–79, (2016), doi: 10.1016/j.cemconres.2016.08.004.

[132] P.W.J.G. Wijnen, T.P.M. Beelen, J.W. De Haan, L.J.M. Van De Ven, and R.A. Van Santen, "The structure directing effect of cations in aqueous silicate solutions. A ^{29}Si-NMR study" *Colloids and Surfaces*, vol. 45, pp. 255–268, (1990), doi: 10.1016/0166-6622(90)80029-4.

[133] P. Duxson, G.C. Lukey, F. Separovic, and J.S.J. Van Deventer, "Effect of alkali cations on aluminum incorporation in geopolymeric gels" *Ind. Eng. Chem. Res.*, vol. 44, no. 4, pp. 832–839, (2005), doi: 10.1021/ie0494216.

[134] A. Fernández-Jiménez, A. Palomo, and M. Criado, "Alkali activated fly ash binders. A comparative study between sodium and potassium activators [Activación alcalina de cenizas volantes. Estudio comparativo entre activadores sódicos y potásicos]" *Mater. Construcción*, vol. 56, no. 281, pp. 51–65, (2006), doi: 10.3989/mc.2006.v56.i281.92.

[135] K. Sakkas, D. Panias, P. Nomikos, and A. Sofianos, "Comparison of Fire Resistant Geopolymers for Passive Fire Protection of Concrete Tunnel Linings" *Open Access Libr. J.*, vol. 4, no. 1, pp. 1–15, (2017).

[136] M. Carrillo-Tripp, H. Saint-Martin, and I. Ortega-Blake, "A comparative study of the hydration of Na^+ and K^+ with

refined polarizable model potentials" *J. Chem. Phys.*, vol. 118, no. 15, pp. 7062–7073, (2003), doi: 10.1063/1.1559673.

[137] I. Barin, "Thermochemical Data of Pure Substances" *Thermochem. Data Pure Subst.*, vol. 303, p. 1117, Oct. (1995), doi: 10.1002/9783527619825.

[138] T. Doan, P. Louda, D. Kroisova, O. Bortnovsky, and N. Thang, "New Generation of Geopolymer Composite for Fire-Resistance" *Adv. Compos. Mater. - Anal. Nat. Man-Made Mater.*, no. InTech, (2011), doi: 10.5772/17933.

[139] T. Bakharev, "Thermal behaviour of geopolymers prepared using class F fly ash and elevated temperature curing" *Cem. Concr. Res.*, vol. 36, no. 6, pp. 1134–1147, (2006), doi: 10.1016/j.cemconres.2006.03.022.

[140] H. Van Vlack, "Physical Ceramics for Engineers, Addison" *Wesley, London*, pp. 94–102, (1964).

[141] M. Taylor, and G.E. Brown, "Structure of mineral glasses-I. The feldspar glasses $NaAlSi_3O_8$, $KAlSi_3O_8$, $CaAl_2Si_2O_8$" *Geochim. Cosmochim. Acta*, vol. 43, no. 1, pp. 61–75, (1979), doi: 10.1016/0016-7037(79)90047-4.

[142] V.F.F. Barbosa, and K.J.D. MacKenzie, "Synthesis and thermal behaviour of potassium sialate geopolymers" *Mater. Lett.*, vol. 57, no. 9–10, pp. 1477–1482, (2003), doi: 10.1016/S0167-577X(02)01009-1.

[143] M. Lizcano, A. Gonzalez, S. Basu, K. Lozano, and M. Radovic, "Effects of water content and chemical composition on structural properties of alkaline activated metakaolin-based geopolymers" *J. Am. Ceram. Soc.*, vol. 95, no. 7, pp. 2169–2177, (2012), doi: 10.1111/j.1551-2916.2012.05184.x.

[144] M. Lizcano, H.S. Kim, S. Basu, and M. Radovic, "Mechanical properties of sodium and potassium activated metakaolin-based geopolymers" *J. Mater. Sci.*, vol. 47, no. 6, pp. 2606–2616, (2012), doi: 10.1007/s10853-011-6085-4.

[145] P. Duxson, J.L. Provis, G.C. Lukey, S.W. Mallicoat, W.M. Kriven, and J.S.J. Van Deventer, "Understanding the relationship between geopolymer composition, microstructure and mechanical properties" *Colloids Surfaces A Physicochem. Eng. Asp.*, vol. 269, no. 1–3, pp. 47–58, (2005), doi: 10.1016/j.colsurfa.2005.06.060.

[146] H. Xu, and J.S.J. Van Deventer, "The effect of alkali metals on the formation of geopolymeric gels from alkali-feldspars" *Colloids Surfaces A Physicochem. Eng. Asp.*, vol. 216, no. 1–3, pp. 27–44, (2003), doi: 10.1016/S0927-7757(02)00499-5.

[147] K. Okada, A. Ooyama, T. Isobe, Y. Kameshima, A. Nakajima, and K. J. D. MacKenzie, "Water retention properties of porous geopolymers for use in cooling applications" *J. Eur. Ceram. Soc.*, vol. 29, no. 10, pp. 1917–1923, (2009), doi: 10.1016/j.jeurceramsoc.2008.11.006.

[148] L. Vitola, I. Pundiene, J. Pranckeviciene, and D. Bajare, "The Impact of the Amount of Water Used in Activation Solution and the Initial Temperature of Paste on the Rheological Behaviour and Structural Evolution of Metakaolin-Based Geopolymer Pastes" *Sustainability*, vol. 12, no. 19, p. 8216, (2020).

[149] Z. Zhang, Y. Xiao, Z. Huajun, and C. Yue, "Role of water in the synthesis of calcined kaolin-based geopolymer" *Appl. Clay Sci.*, vol. 43, no. 2, pp. 218–223, (2009), doi: 10.1016/j.clay.2008.09.003.

[150] V.F.F. Barbosa, and K.J.D. Mackenzie, "Thermal behaviour of inorganic geopolymers and composites derived from sodium polysialate" vol. 38, pp. 319–331, (2003).

[151] J.C. Swanepoel, and C. a. Strydom, "Utilisation of fly ash in a geopolymeric material" *Appl. Geochemistry*, vol. 17, no. 8, pp. 1143–1148, (2002), doi: 10.1016/S0883-2927(02)00005-7.

[152] S. Kumar, and R. Kumar, "Mechanical activation of fly ash: Effect on reaction, structure and properties of resulting geopolymer" *Ceram. Int.*, vol. 37, no. 2, pp. 533–541, (2011), doi: https://doi.org/10.1016/j.ceramint.2010.09.038.

[153] M.M.A.B. Abdullah, H. Kamarudin, M. Bnhussain, I. Khairul Nizar, A.R. Rafiza, and Y. Zarina, "The relationship of NaOH molarity, Na2SiO3/NaOH ratio, fly ash/alkaline activator ratio, and curing temperature to the strength of fly ash-based geopolymer" *Adv. Mater. Res.*, vol. 328, pp. 1475–1482, (2011).

[154] G.S. Ryu, Y.B. Lee, K.T. Koh, and Y.S. Chung, "The mechanical properties of fly ash-based geopolymer concrete with alkaline activators" *Constr. Build. Mater.*, vol. 47, pp. 409–418, (2013), doi: https://doi.org/10.1016/j.conbuildmat.2013.05.069.

[155] D. Hardjito, and B.V. Rangan, "Development and properties of low-calcium fly ash-based geopolymer concrete" Perth, (2005). Accessed: Jun. 13, 2012. [Online]. Available: http://www.geopolymer.org/fichiers_pdf/curtin-flyash-GP-concrete-report.pdf.

[156] F. Canpolat, and T.R. Naik, "Effect Of Curing Conditions On Strength And Durability Of High-Performance Concrete" *Sci. Iran.*, vol. 24, no. 2, pp. 576–583, (2017), doi: 10.24200/sci.2017.2419.

[157] R.T. Chancey, P. Stutzman, M.C.G. Juenger, and D.W. Fowler, "Comprehensive phase characterization of crystalline and amorphous phases of a Class F fly ash" *Cem. Concr. Res.*, vol. 40, no. 1, pp. 146–156, (2010), doi: 10.1016/j.cemconres.2009.08.029.

[158] P. Nath, and P.K. Sarker, "Effect of GGBFS on setting, workability and early strength properties of fly ash geopolymer concrete cured in ambient condition" *Constr. Build. Mater.*, vol. 66, pp. 163–171, (2014), doi: 10.1016/j.conbuildmat.2014.05.080.

[159] P.S. Deb, P. Nath, and P.K. Sarker, "The effects of ground granulated blast-furnace slag blending with fly ash and activator content on the workability and strength properties of geopolymer concrete cured at ambient temperature" *Mater. Des.*, vol. 62, pp. 32–39, (2014), doi: 10.1016/j.matdes.2014.05.001.

[160] B. Udvardi, K. Róman, E. Kurovics, R. Géber, and I. Kocserha, "Preparation and investigation of geopolymers generated from construction, demolition and industrial wastes" *WIT Trans. Eng. Sci.*, vol. 124, pp. 49–59, (2019).

[161] A.M. Kaja, A. Lazaro, and Q.L. Yu, "Effects of Portland cement on activation mechanism of class F fly ash geopolymer cured under ambient conditions" *Constr. Build. Mater.*, (2018), doi: 10.1016/j.conbuildmat.2018.09.065.

[162] E. Tajuelo Rodriguez, K. Garbev, D. Merz, L. Black, and I. G. Richardson, "Thermal stability of C-S-H phases and applicability of Richardson and Groves' and Richardson C-(A)-S-H(I) models to synthetic C-S-H" *Cem. Concr. Res.*, vol. 93, pp. 45–56, (2017), doi: 10.1016/j.cemconres.2016.12.005.

[163] W. K. W. Lee, and J. S. J. Van Deventer, "The effect of ionic contaminants on the early-age properties of alkali-activated fly ash-based cements" *Cem. Concr. Res.*, vol. 32, no. 4, pp. 577–584, (2002), doi: 10.1016/S0008-8846(01)00724-4.

[164] J. Temuujin, A. van Riessen, and R. Williams, "Influence of calcium compounds on the mechanical properties of fly ash geopolymer pastes" *J. Hazard. Mater.*, vol. 167, no. 1–3, pp. 82–88, (2009), doi: 10.1016/j.jhazmat.2008.12.121.

[165] R. Świetlik, M. Trojanowska, and M.A. Jóźwiak, "Evaluation of the distribution of heavy metals and their chemical forms in ESP-fractions of fly ash" *Fuel Process. Technol.*, vol. 95, pp. 109–118, (2012).

[166] T.A. Vereshchagina, N.N. Anshits, N.G. Maksimov, S.N. Vereshchagin, O.A. Bayukov, and A.G. Anshits, "The nature and properties of iron-containing nanoparticles dispersed in an aluminosilicate matrix of cenospheres" *Glas. Phys. Chem.*, vol. 30, no. 3, pp. 247–256, (2004).

[167] W.D.A. Rickard, A. Van Riessen, and P. Walls, "Thermal character of geopolymers synthesized from class F Fly ash containing high concentrations of iron and α-quartz" *Int. J. Appl. Ceram. Technol.*, vol. 7, no. 1, pp. 81–88, (2010), doi: 10.1111/j.1744-7402.2008.02328.x.

[168] R. Williams, "Characterisation of Fly Ash for production of Geopolymer" *Honours Diss. Curtin Univ. Technol. Perth, Aust.*, (2006).

[169] K.M. Klima, K. Schollbach, H.J.H. Brouwers, and Q.L. Yu, "Enhancing the thermal performance of Class F fly ash-based geopolymer by sodalite" *Constr. Build. Mater.*, vol. 314, p. 125574, (2022).

[170] M.W. McElhinny, and P. L. B. T.-I. G. McFadden, Eds., "Chapter Two - Rock Magnetism" *Paleomagnetism*, vol. 73, pp. 31–77, (2000), doi: https://doi.org/10.1016/S0074-6142(00)80095-9.

[171] T. Yang, Q. Wu, H. Zhu, and Z. Zhang, "Geopolymer with improved thermal stability by incorporating high-magnesium nickel slag" *Constr. Build. Mater.*, vol. 155, pp. 475–484, (2017), doi: 10.1016/j.conbuildmat.2017.08.081.

[172] F. Jin, K. Gu, and A. Al-Tabbaa, "Strength and hydration properties of reactive MgO-activated ground granulated blastfurnace slag paste" *Cem. Concr. Compos.*, vol. 57, pp. 8–16, (2015), doi: 10.1016/j.cemconcomp.2014.10.007.

[173] A.M. Rashad, and S.R. Zeedan, "The effect of activator concentration on the residual strength of alkali-activated fly ash pastes subjected to thermal load" *Constr. Build. Mater.*, vol. 25, no. 7, pp. 3098–3107, (2011), doi: 10.1016/j.conbuildmat.2010.12.044.

[174] I. Ismail, S.A. Bernal, J.L. Provis, R. San Nicolas, S. Hamdan, and J.S.J. Van Deventer, "Modification of phase evolution in alkali-activated blast furnace slag by the incorporation of fly ash" *Cem. Concr. Compos.*, vol. 45, pp. 125–135, (2014), doi: 10.1016/j.cemconcomp.2013.09.006.

[175] T. Bakharev, "Durability of geopolymer materials in sodium and magnesium sulfate solutions" *Cem. Concr. Res.*, vol. 35, no. 6, pp. 1`233-1246, (2005), doi: 10.1016/j.cemconres.2004.09.002.

[176] A. Fernández-Jiménez, N. Cristelo, T. Miranda, and Á. Palomo, "Sustainable alkali activated materials: Precursor and activator derived from industrial wastes" *J. Clean. Prod.*, vol. 162, pp. 1200–1209, (2017), doi: 10.1016/j.jclepro.2017.06.151.

[177] P. Rożek, M. Król, and W. Mozgawa, "Geopolymer-zeolite composites: A review" *J. Clean. Prod.*, vol. 230, pp. 557–579, (2019), doi: 10.1016/j.jclepro.2019.05.152.

[178] M. Xu, Y. He, Y. Wang, and C. Xue-min, "Preparation of a non-hydrothermal NaA zeolite membrane and defect elimination by vacuum-inhalation repair method" *Chem. Eng. Sci.*, vol. 158, (2016), doi: 10.1016/j.ces.2016.10.001.

[179] E. Álvarez-Ayuso, X. Querol, F. Plana, A. Alastuey, N. Moreno, M. Izquierdo, O. Font, T. Moreno., "Environmental, physical and structural characterisation of geopolymer matrixes synthesised from coal (co-)combustion fly ashes" *J. Hazard. Mater.*, vol. 154, no. 1–3, pp. 175–183, (2008), doi: 10.1016/j.jhazmat.2007.10.008.

[180] W.M.K. Manuel E. Brito, Eldon Case, "Developments in Porous, Biological and Geopolymer Ceramics" *Dev. Porous, Biol. Geopolymer Ceram.*, (2007), doi: 10.1002/9780470339749.

[181] B. Jha, and D.N. Singh, "Fly Ash Zeolites: Innovations, applications and directions" vol. 78, p. 211, (2016), doi: 10.1007/978-981-10-1404-8.

[182] C. Kosanovic, B. Subotic, and I. Smit, "Thermally induced phase transformations in cation-exchanged zeolites 4A, 13X and synthetic mordenite and their amorphous derivatives obtained by mechanochemical treatment" *Thermochim. Acta*, vol. 317, no. 1, pp. 25–37, (1998), doi: 10.1016/S0040-6031(98)00353-0.

[183] T. Carey, "Chemical Control of Thermal Expansion in Zeolites with the LTA Topology" no. April, (2013), [Online]. Available: http://etheses.bham.ac.uk/4258/1/Carey13PhD.pdf.

[184] T. Kihara, A. Mikuni, Y. Nakamura, R. Komatsu, and K. Ikeda, "Consolidation of Pressurised Fluidised Bed Combustion Ash (PF-Ash) by the geopolymer technique at ambient temperature" *Adv. Sci. Technol. 34*, pp. 163–168, (2002).

[185] H. Takeda, S. Hashimoto, H. Yokoyama, S. Honda, and Y. Iwamoto, "Characterization of zeolite in zeolite-geopolymer hybrid bulk materials derived from kaolinitic clays" *Materials (Basel)*, vol. 6, no. 5, pp. 1767–1778, (2013), doi: 10.3390/ma6051767.

[186] P. Sturm, G.J.G. Gluth, S. Simon, H.J.H. Brouwers, and H.C. Kühne, "The effect of heat treatment on the mechanical and structural properties of one-part geopolymer-zeolite composites" *Thermochim. Acta*, vol. 635, pp. 41–58, (2016), doi: 10.1016/j.tca.2016.04.015.

[187] L.P. van Reeuwijk, "The thermal dehydration of natural zeolites" (1974).

[188] Z. Pan, and J. G. Sanjayan, "Stress-strain behaviour and abrupt loss of stiffness of geopolymer at elevated temperatures" *Cem. Concr. Compos.*, vol. 32, no. 9, pp. 657–664, (2010), doi: 10.1016/j.cemconcomp.2010.07.010.

[189] D. Kong, J. Sanjayan, and K. Sagoe-Crentsil, "The behaviour of geopolymer paste and concrete at elevated temperatures" *Int. Conf. Pozzolan, Concr. Geopolymer, Khon Kaen Univ. Khon Kaen, Thail. (2006), pp. 105-119*, (2006).

[190] Z. Pan, J. G. Sanjayan, and F. Collins, "Effect of transient creep on compressive strength of geopolymer concrete for elevated temperature exposure" *Cem. Concr. Res.*, vol. 56, pp. 182–189, (2014), doi: 10.1016/j.cemconres.2013.11.014.

[191] P. Duxson, G.C. Lukey, and J. S. J. Van Deventer, "Physical evolution of Na-geopolymer derived from metakaolin up to 1000 °c" *J. Mater. Sci.*, vol. 42, no. 9, pp. 3044–3054, (2007), doi: 10.1007/s10853-006-0535-4.

[192] P. Ptáček, F. Šoukal, T. Opravil, E. Bartoníčková, and J. Wasserbauer, "The formation of feldspar strontian ($SrAl_2Si_2O_8$) via ceramic route: Reaction mechanism, kinetics and thermodynamics of the process" *Ceram. Int.*, vol. 42, no. 7, pp. 8170–8178, (2016).

[193] J.M. Branlund, and A. M. Hofmeister, "Heat transfer in plagioclase feldspars" *Am. Mineral.*, vol. 97, no. 7, pp. 1145–1154, (2012).

[194] J.H. Perry, "Chemical engineers' handbook" *J. Chem. Educ.*, (1950), doi: 10.1021/ed027p533.1.

[195] S. Alehyen, M. Zerzouri, M. El Alouani, M. El Achouri, and M. Taibi, "Porosity and fire resistance of fly ash based geopolymer" *J. Mater. Environ. Sci.*, vol. 8, no. 10, pp. 3676–3689, (2017).

[196] R. Kumar, and S.S. Mayengbam, "Enhancement of the Thermal Durability of Fly Ash-Based Geopolymer Paste by Incorporating Potassium Feldspar" *J. Inst. Eng. Ser. A*, vol. 102, no. 1, pp. 175–183, (2021).

[197] R.N. Thakur, and S. Ghosh, "Effect of mix composition on compressive strength and microstructure of fly ash based geopolymer composites" *J. Eng. Appl. Sci.*, vol. 4, no. 4, pp. 68–74, (2009), doi: 10.1016/j.actamat.2006.08.032.

[198] M.W. Hussin, M.A.R. Bhutta, M. Azreen, P.J. Ramadhansyah, and J. Mirza, "Performance of blended ash geopolymer concrete at elevated temperatures" *Mater. Struct. Constr.*, (2015), doi: 10.1617/s11527-014-0251-5.

[199] C.W.Bale, E. Bélisle, P. Chartrand, S.A. Decterov, G. Eriksson, A.E. Gheribi, K. Hack, I.H. Jung, "FactSage thermochemical software and databases" *Calphad Comput. Coupling Phase Diagrams Thermochem.*, vol. 26, no. 2, pp. 189–228, (2002), doi: 10.1016/j.calphad.2016.05.002.

[200] J.L. Provis, P.Duxson, G.C. Lukey, and J.S.J. van Deventer, "Statistical thermodynamic model for Si/Al ordering in amorphous aluminosilicates" *Chem. Mater.*, vol. 17, no. 11, pp. 2976–2986, (2005).

[201] V.D. Cao, S. Pilehvar, C. Salas-Bringas, A.M. Szczotok, J.F. Rodriguez, M. Carmona, N. Al-Manasir, and A.L. Kjøniksen, "Microencapsulated phase change materials for enhancing the thermal performance of Portland cement concrete and geopolymer concrete for passive building applications" *Energy Convers. Manag.*, vol. 133, pp. 56–66, (2017).

[202] A. Hassan, M. Arif, and M. Shariq, "Influence of microstructure of geopolymer concrete on its mechanical properties—a review" *Adv. Sustain. Constr. Mater. Geotech. Eng.*, pp. 119–129, (2020).

[203] M.Z.N. Khan, Y. Hao, and H. Hao, "Synthesis of high strength ambient cured geopolymer composite by using low calcium fly ash" *Constr. Build. Mater.*, vol. 125, pp. 809–820, (2016).

[204] A.Z.M. Ali, and J. Sanjayan, "The spalling of geopolymer high strength concrete wall panels and cylinders under hydrocarbon fire" *MATEC Web Conf.*, vol. 47, p. 02005, (2016).

[205] P.K. Sarker, and S. McBeath, "Fire endurance of steel reinforced fly ash geopolymer concrete elements" *Constr. Build. Mater.*, vol. 90, pp. 91–98, (2015), doi: 10.1016/j.conbuildmat.2015.04.054.

[206] F. Colangelo, R. Cioffi, G. Roviello, I. Capasso, D. Caputo, P. Aprea, B. Liguori, and C. Ferone, "Thermal cycling stability of fly ash based geopolymer mortars" *Compos. part b Eng.*, vol. 129, pp. 11–17, (2017).

[207] H.Y. Zhang, G.H. Qiu, V. Kodur, and Z.S. Yuan, "Spalling behavior of metakaolin-fly ash based geopolymer concrete under elevated temperature exposure" *Cem. Concr. Compos.*, vol. 106, p. 103483, (2020).

[208] Y. Luo, S. Li, K.M. Klima, H.J.H. Brouwers, Q.L. Yu, "Degradation mechanism of hybrid fly ash/slag based geopolymers exposed to elevated temperatures" *Cem. Concr. Res.*, vol. 151, no. 106649, (2021).

[209] J.L.Bell, P. E. Driemeyer, and W. M. Kriven, "Formation of Ceramics from Metakaolin-Based Geopolymers. Part II: K-Based Geopolymer" *J. Am. Ceram. Soc.*, vol. 92, no. 3, pp. 607–615, (2009), doi: 10.1111/j.1551-2916.2008.02922.x.

[210] D.D. Burduhos Nergis, M.M.A.B. Abdullah, A. V. Sandu, and P. Vizureanu, "XRD and TG-DTA Study of New Alkali Activated Materials Based on Fly Ash with Sand and Glass Powder" *Materials (Basel)*, vol. 13, p. 343, (2020), doi: 10.3390/ma13020343.

[211] T. Kovářík, D. Rieger, J. Kadlec, T. Křenek, L. Kullová, M. Pola, P. Bělský, P. Franče, "Thermomechanical properties of particle-reinforced geopolymer composite with various aggregate gradation of fine ceramic filler" *Constr. Build. Mater.*, vol. 143, pp. 599–606, (2017), doi: 10.1016/j.conbuildmat.2017.03.134.

[212] P. He, D. Jia, M. Wang, and Y. Zhou, "Thermal evolution and crystallization kinetics of potassium-based geopolymer" *Ceram. Int.*, vol. 37, no. 1, pp. 59–63, (2011), doi: 10.1016/j.ceramint.2010.08.008.

[213] H. Ma, S. Zhang, and J. Feng, "Physicochemical properties of MgO-silica fume cementitious materials exposed to high temperatures" *J. Build. Eng.*, vol. 50, p. 104124, (2022).

[214] A.S. Rahman, and D.W. Radford, "Evaluation of the geopolymer/nanofiber interfacial bond strength and their effects on Mode-I fracture toughness of geopolymer matrix at high temperature" *Compos. Interfaces*, vol. 24, no. 8, pp. 817–831, (2017), doi: 10.1080/09276440.2017.1279479.

[215] M. Sivasakthi, R. Jeyalakshmi, and N. P. Rajamane, "Investigation of Microstructure and Thermomechanical Properties of Nano-TiO2 Admixed Geopolymer for Thermal Resistance Applications" *J. Mater. Eng. Perform.*, vol. 30, no. 5, pp. 3642–3653, (2021), doi: 10.1007/s11665-021-05708-1.

[216] S.K. Shill, S. Al-Deen, M. Ashraf, and W. Hutchison, "Resistance of fly ash based geopolymer mortar to both chemicals and high thermal cycles simultaneously" *Constr. Build. Mater.*, vol. 239, p. 117886, (2020).

[217] E.A. Azimi, M.M.A.B. Abdullah, P. Vizureanu, M. A. A. M. Salleh, A. V. Sandu, J. Chaiprapa, S. Yoriya, K. Hussin, "Strength development and elemental distribution of dolomite/fly ash geopolymer composite under elevated temperature" *Materials (Basel)*, vol. 13, no. 4, p. 1015, (2020).

[218] X. Peng, Q. Shuai, H. Li, Q. Ding, Y. Gu, C. Cheng, and Z. Xu, "Fabrication and fireproofing performance of the coal fly ash-metakaolin-based geopolymer foams" *Materials (Basel)*, vol. 13, no. 7, p. 1750, (2020).

[219] S. Yan, F. Zhang, X. Feng, J. Kong, B. Wang, and J. Yang, "Effect of high temperature on the mechanical properties of hierarchical porous cenosphere/geopolymer composite foams" *Int. J. Appl. Ceram. Technol.*, vol. 18, no. 3, pp. 817–829, (2021).

[220] R. Jacob, N. Trout, A. Solé, S. Clarke, A.I. Fernández, L.F. Cabeza, W. Saman, and F. Bruno, "Novel geopolymer for use as a sensible storage option in high temperature thermal energy storage systems" *AIP Conf. Proc.*, vol. 2303, no. 1, p. 190019, (2020).

[221] P. Duxson, G. C. Lukey, and J. S. J. van Deventer, "The thermal evolution of metakaolin geopolymers: Part 2 - Phase stability and structural development" *J. Non. Cryst. Solids*, vol. 353, no. 22–23, pp. 2186–2200, (2007), doi: 10.1016/j.jnoncrysol.2007.02.050.

[222] S. Yan, X. Feng, Y. Yang, and P. Xing, "Effects of high-temperature exposure on properties of lightweight geopolymer foams incorporating diatomite powders" *Int. J. Appl. Ceram. Technol.*, vol. 18, no. 6, pp. 2158–2168, (2021).

[223] V. Vaou, and D. Panias, "Thermal insulating foamy geopolymers from perlite" *Miner. Eng.*, vol. 23, no. 14, pp. 1146–1151, (2010), doi: 10.1016/j.mineng.2010.07.015.

[224] G. Franchin, and P. Colombo, "Porous geopolymer components through inverse replica of 3D printed sacrificial templates" *J. Ceram. Sci. Technol.*, vol. 6, no. 2, pp. 105–111, (2015), doi: 10.4416/JCST2014-00057.

[225] E. Papa, V. Medri, P. Benito, A. Vaccari, S. Bugani, J. Jaroszewicz, W. Swieszkowski, and E. Landi, "Synthesis of porous hierarchical geopolymer monoliths by ice-templating" *Microporous Mesoporous Mater.*, vol. 215, pp. 206–214, (2015), doi: 10.1016/j.micromeso.2015.05.043.

[226] G. Roviello, C. Menna, O. Tarallo, L. Ricciotti, C. Ferone, F. Colangelo, D. Asprone, R. Di Maggio, "Preparation, structure and properties of hybrid materials based on geopolymers and polysiloxanes" *Mater. Des.*, vol. 87, pp. 82–94, (2015).

[227] A. Pfenninger, "Manufacture and Use of Zeolites for Adsorption Processes" *Springer Berlin*, pp. 163–198, (1999), doi: 10.1007/3-540-69749-7_6.

[228] A. Nikolov, I. Rostovsky, and H. Nugteren, "Geopolymer materials based on natural zeolite" *Case Stud. Constr. Mater.*, vol. 6, pp. 198–205, (2017).

[229] C. Villa, E.T. Pecina, R. Torres, and L. Gómez, "Geopolymer synthesis using alkaline activation of natural zeolite" *Constr. Build. Mater.*, vol. 24, no. 11, pp. 2084–2090, (2010).

[230] A.A. Shahmansouri, M. Nematzadeh, and A. Behnood, "Mechanical properties of GGBFS-based geopolymer concrete incorporating natural zeolite and silica fume with an optimum design using response surface method" *J. Build. Eng.*, vol. 36, p. 102138, (2021).

[231] D.W. Breck, "Zeolite Molecular Sieves: Structure, Chemistry and Use" *John Wiley Sons*, (1973), doi: 10.1016/s0003-2670(01)85391-5.

[232] S. Chong, "Characterization of Sodalite Based Waste Forms for Immobilization of 129I" (2017), [Online]. Available: https://books.google.nl/books?id=o3PtvQEACAAJ.

[233] J. Luo, H. Zhang, and J. Yang, "Hydrothermal Synthesis of Sodalite on Alkali-Activated Coal Fly Ash for Removal of Lead Ions" *Procedia Environ. Sci.*, vol. 31, p. `605-614, (2016), doi: 10.1016/j.proenv.2016.02.105.

[234] W. Franus, M. Wdowin, and M. Franus, "Synthesis and characterization of zeolites prepared from industrial fly ash" *Environ. Monit. Assess.*, vol. 186, no. 9, pp. 5721–5729, (2014), doi: 10.1007/s10661-014-3815-5.

[235] H. Beyer, "Dealumination Techniques for Zeolites" *Mol. Sieves*, vol. 3, pp. 203–255, (2002), doi: 10.1007/3-540-69750-0_3.

[236] S. Khajavi, S. Sartipi, J. Gascon, J. C. Jansen, and F. Kapteijn, "Thermostability of hydroxy sodalite in view of membrane applications" *Microporous Mesoporous Mater.*, vol. 132, no. 3, pp. 510–517, (2010), doi: https://doi.org/10.1016/j.micromeso.2010.03.035.

[237] S. Golbad, P. Khoshnoud, and N. Abu-Zahra, "Hydrothermal synthesis of hydroxy sodalite from fly ash for the removal of lead ions from water" *Int. J. Environ. Sci. Technol.*, vol. 14, no. 1, pp. 135–142, (2017).

[238] J. Li, X. Zeng, X. Yang, C. Wang, and X. Luo, "Synthesis of pure sodalite with wool ball morphology from alkali fusion kaolin" *Mater. Lett.*, vol. 161, pp. 157–159, (2015), doi: 10.1016/j.matlet.2015.08.058.

[239] J. Yang, T. Li, X. Bao, Y. Yue, and H. Liu, "Mesoporogen-free synthesis of hierarchical sodalite as a solid base catalyst from sub-molten salt-activated aluminosilicate" *Particuology*, vol. 48, pp. 48–54, (2020), doi: 10.1016/j.partic.2018.07.005.

[240] A.V Borhade, and S.R. Kankrej, "An efficient cost-effective removal of Ca^{2+}, Mg^{2+}, and Cu^{2+} ions from aqueous medium using chlorosodalite synthesized from coal fly ash" *J. Chem. Eng. Data*, vol. 62, no. 2, pp. 596–607, (2017).

[241] E. Papa, V. Medri, S. Amari, J. Manaud, P. Benito, A. Vaccari, and E. Landi, "Zeolite-geopolymer composite materials: Production and characterization" *J. Clean. Prod.*, vol. 171, pp. 76–84, (2018), doi: 10.1016/j.jclepro.2017.09.270.

[242] T. Bakharev, "Geopolymeric materials prepared using Class F fly ash and elevated temperature curing" *Cem. Concr. Res.*, vol. 35, no. 6, pp. 1224–1232, (2005), doi: 10.1016/j.cemconres.2004.06.031.

[243] H. Baykara, M.H. Cornejo, R. Murillo, A. Gavilanes, C. Paredes, and J. Elsen, "Preparation, characterization and reaction kinetics of green cement: Ecuadorian natural mordenite-based geopolymers" *Mater. Struct.*, vol. 50, no. 3, p. 188, (2017).

[244] I. Bardez, L. Campayo, D. Rigaud, M. Chartier, A. Calvet, M. Céramiques, and S. De Marcoule, "Investigation of sodalites for conditioning halide salts (NaCl and NaI):" *Nucl. fuel cycle a Sustain. Futur.*, (2008).

[245] J.L. Provis, V. Rose, S.A. Bernal, and J.S.J. van Deventer, "High-resolution nanoprobe X-ray fluorescence characterization of heterogeneous calcium and heavy metal distributions in alkali-activated fly ash" *Langmuir*, vol. 25, no. 19, pp. 11897–11904, (2009).

[246] R.G. Ribas, T.M. B. Campos, V.M. Schatkoski, B.R.C. de Menezes, T.L. do Amaral Montanheiro, and G.P. Thim, "α-wollastonite crystallization at low temperature" *Ceram. Int.*, vol. 46, no. 5, pp. 6575–6580, (2020).

[247] S.V Vassilev, R. Menendez, D. Alvarez, M. Diaz-Somoano, and M.R. Martinez-Tarazona, "Phase-mineral and chemical

composition of coal fly ashes as a basis for their multicomponent utilization. 1. Characterization of feed coals and fly ashes☆" *Fuel*, vol. 82, no. 14, pp. 1793–1811, (2003).

[248] X. Chen, N. Karpukhina, D. S. Brauer, and R. G. Hill, "High chloride content calcium silicate glasses" *Phys. Chem. Chem. Phys.*, vol. 19, no. 10, pp. 7078–7085, (2017).

[249] M. Mouiya, A. Bouazizi, A. Abourriche, A. Benhammou, Y. El Hafiane, M. Ouammou, Y. Abouliatim, S. A. Younssi, "Fabrication and characterization of a ceramic membrane from clay and banana peel powder: Application to industrial wastewater treatment" *Mater. Chem. Phys.*, vol. 227, pp. 291–301, (2019), doi: 10.1016/j.matchemphys.2019.02.011.

[250] L.A.M. Scudeller, E. Longo, and J.A. Varela, "Potassium vapor attack in refractories of the alumina–silica system" *J. Am. Ceram. Soc.*, vol. 73, no. 5, pp. 1413–1416, (1990).

[251] D. Novembre, D. Gimeno, A. Pasculli, and B. Di Sabatino, "Synthesis and characterization of sodalite using natural kaolinite: An analytical and mathematical approach to simulate the loss in weight of chlorine during the synthesis process" *Fresenius Environ. Bull.*, vol. 19, no. 6, pp. 1109–1117, (2010).

[252] B.J. Riley, J. D. Vienna, S.M. Frank, J.O. Kroll, J.A. Peterson, N.L. Canfield, Z. Zhu, J. Zhang, "Glass binder development for a glass-bonded sodalite ceramic waste form" *J. Nucl. Mater.*, vol. 489, pp. 42–63, (2017), doi: 10.1016/j.jnucmat.2017.03.041.

[253] J. Stjernberg, B. Lindblom, J. Wikström, M.L. Antti, and M. Odén, "Microstructural characterization of alkali metal mediated high temperature reactions in mullite based refractories" *Ceram. Int.*, vol. 36, no. 2, pp. 733–740, (2010).

[254] J. Stjernberg, M. Antti, L. Nordin, and M. Odén, "Degradation of refractory bricks used as thermal insulation in rotary kilns for iron ore pellet production" *Int. J. Appl. Ceram. Technol.*, vol. 6, no. 6, pp. 717–726, (2009).

[255] A.M.El Nagar, and H. M. Khater, "Development of High Thermal Stability Geopolymer Composites Enhanced by Nano Metakaolin" *J. Build. Mater. Struct.*, vol. 6, no. 1, pp. 10–19, (2019).

[256] Q. Li, H. Xu, F. Li, P. Li, L. Shen, and J. Zhai, "Synthesis of geopolymer composites from blends of CFBC fly and bottom ashes" *Fuel*, vol. 97, pp. 366–372, (2012).

[257] S. Khajavi, S. Sartipi, J. Gascon, J. C. Jansen, and F. Kapteijn, "Thermostability of hydroxy sodalite in view of membrane applications" *Microporous Mesoporous Mater.*, vol. 132, no. 3, pp. 510–517, (2010), doi: 10.1016/j.micromeso.2010.03.035.

[258] M. Lahoti, S. F. Wijaya, K.H. Tan, and E.H. Yang, "Tailoring sodium-based fly ash geopolymers with variegated thermal performance" *Cem. Concr. Compos.*, vol. 107, p. 103507, (2020), doi: 10.1016/j.cemconcomp.2019.103507.

[259] L. Vickers, A. van Riessen, and W. Rickard, "Fire-resistant Geopolymers: Role of Fibres and Fillers to Enhance Thermal Properties" *Springer Singapore*, (2015).

[260] M. Mouiya, A. Bouazizi, A. Abourriche, Y. El Khessaimi, A. Benhammou, Y. El hafiane, Y. Taha, M. Oumam, "Effect of sintering temperature on the microstructure and mechanical behavior of porous ceramics made from clay and banana peel powder" *Results Mater.*, vol. 4, p. 100028, (2019), doi: 10.1016/j.rinma.2019.100028.

[261] T.S. Lin, D.C. Jia, P.G. He, and M.R. Wang, "Thermo-mechanical and microstructural characterization of geopolymers with α-Al 2 O 3 particle filler" *Int. J. Thermophys.*, vol. 30, no. 5, p. 1568, (2009).

[262] L. Cao, Q. Fu, Y. Si, B. Ding, and J. Yu, "Porous materials for sound absorption" *Compos. Commun.*, vol. 10, pp. 25–35, (2018).

[263] C. Bai, G. Franchin, H. Elsayed, A. Zaggia, L. Conte, H. Li, and P. Colombo, "High-porosity geopolymer foams with tailored porosity for thermal insulation and wastewater treatment" *J. Mater. Res.*, vol. 32, no. 17, pp. 3251–3259, (2017), doi: 10.1557/jmr.2017.127.

[264] G. Masi, W.D.A. Rickard, L. Vickers, M.C. Bignozzi, and A. Van Riessen, "A comparison between different foaming methods for the synthesis of light weight geopolymers" *Ceram. Int.*, vol. 40, no. 9 part A, pp. 13891–13902, (2014), doi: 10.1016/j.ceramint.2014.05.108.

[265] P. Hlaváček, V. Šmilauer, F. Škvára, L. Kopecký, and R. Šulc, "Inorganic foams made from alkali-activated fly ash: Mechanical, chemical and physical properties" *J. Eur. Ceram. Soc.*, vol. 35, no. 2, pp. 703–709, (2015), doi: 10.1016/j.jeurceramsoc.2014.08.024.

[266] A. Hajimohammadi, T. Ngo, P. Mendis, A. Kashani, and J. S. J. van Deventer, "Alkali activated slag foams: the effect of the alkali reaction on foam characteristics" *J. Clean. Prod.*, vol. 147, pp. 330–339, (2017).

[267] M. Strozi Cilla, M. Raymundo Morelli, and P. Colombo, "Effect of process parameters on the physical properties of porous geopolymers obtained by gelcasting" *Ceram. Int.*, vol. 40, no. 8 PART B, pp. 13585–13590, (2014), doi: 10.1016/j.ceramint.2014.05.074.

[268] A. Tarameshloo, E. N. Kani, and A. Allahverdi, "Performance evaluation of foaming agents in cellular concrete based on foamed alkali-activated slag" *Can. J. Civ. Eng.*, vol. 44, no. 11, pp. 893–898, (2017).

[269] L. Verdolotti, B. Liguori, I. Capasso, A. Errico, D. Caputo, M. Lavorgna, and S. Iannace, "Synergistic effect of vegetable protein and silicon addition on geopolymeric foams properties" *J. Mater. Sci.*, vol. 50, no. 6, pp. 2459–2466, (2015).

[270] N.A. Jaya, L. Yun-Ming, H. Cheng-Yong, M.M.A.B. Abdullah, and K. Hussin, "Correlation between pore structure, compressive strength and thermal conductivity of porous metakaolin geopolymer" *Constr. Build. Mater.*, vol. 247, (2020), doi: 10.1016/j.conbuildmat.2020.118641.

[271] L. Korat, and V. Ducman, "The influence of the stabilizing agent SDS on porosity development in alkali-activated fly-ash based foams" *Cem. Concr. Compos.*, vol. 80, pp. 168–174, (2017), doi: 10.1016/j.cemconcomp.2017.03.010.

[272] S. Petlitckaia, and A. Poulesquen, "Design of lightweight metakaolin based geopolymer foamed with hydrogen peroxide" *Ceram. Int.*, no. October, pp. 1–9, (2018), doi: 10.1016/j.ceramint.2018.10.021.

[273] A. Bera, K. Ojha, and A. Mandal, "Synergistic effect of mixed surfactant systems on foam behavior and surface tension" *J. Surfactants Deterg.*, vol. 16, no. 4, pp. 621–630, (2013), doi: 10.1007/s11743-012-1422-4.

[274] K. Osei-Bonsu, N. Shokri, and P. Grassia, "Foam stability in the presence and absence of hydrocarbons: From bubble- to bulk-scale" *Colloids Surfaces A Physicochem. Eng. Asp.*, vol. 481, pp. 514–526, (2015).

[275] B. Qin, Y. Lu, F. Li, Y. Jia, C. Zhu, and Q. Shi, "Preparation and stability of inorganic solidified foam for preventing coal fires" *Adv. Mater. Sci. Eng. 2014*, (2014), doi: 10.1155/2014/347386.

[276] M. Wang, H. Du, A. Guo, R. Hao, and Z. Hou, "Microstructure control in ceramic foams via mixed cationic/anionic surfactant" *Mater. Lett.*, vol. 88, pp. 97–100, (2012), doi: 10.1016/j.matlet.2012.08.028.

[277] O. Owoyomi, I. Jide, M. S. Akanni, O. O. Soriyan, and M. K. Morakinyo, "Interactions between sodium dodecylsulphate and Triton X-100: Molecular properties and kinetics investigation" *J Appl Sci*, vol. 5, pp. 729–734, (2005).

[278] T. Sidim, and M. Arda, "Some surface properties of polysorbates and cetyl trimethyl ammonium bromine mixed systems" *J. Surfactants Deterg.*, vol. 14, no. 3, pp. 409–414, (2011).

[279] H. Kesarwani, A. Saxena, A. Mandal, and S. Sharma, "Anionic/Nonionic Surfactant Mixture for Enhanced Oil Recovery through the Investigation of Adsorption, Interfacial, Rheological, and Rock Wetting Characteristics" *Energy & Fuels*, vol. 35, no. 4, pp. 3065–3078, (2021).

[280] H. Huang, Q. Yuan, D. Deng, J. Peng, and Y. Huang, "Effects of chemical and mineral admixtures on the foam indexes of cement-based materials" *Case Stud. Constr. Mater.*, vol. 11, p. e00232, (2019), doi: 10.1016/j.cscm.2019.e00232.

[281] K.H. Pedersen, S.I. Andersen, A.D. Jensen, and K. Dam-Johansen, "Replacement of the foam index test with surface tension measurements" *Cem. Concr. Res.*, vol. 37, no. 6, pp. 996–1004, (2007), doi: 10.1016/j.cemconres.2007.02.007.

[282] J.G. Parra, P. Iza, H. Dominguez, E. Schott, and X. Zarate, "Effect of Triton X-100 surfactant on the interfacial activity of ionic surfactants SDS, CTAB and SDBS at the air/water interface: A study using molecular dynamic simulations" *Colloids Surfaces A Physicochem. Eng. Asp.*, vol. 603, p. 125284, (2020).

[283] D.M. Ćirin, M.M. Poša, V.S. Krstonošić, and M.L. Milanović, "Conductometric study of sodium dodecyl sulfate-

nonionic surfactant (Triton X-100, Tween 20, Tween 60, Tween 80 or Tween 85) mixed micelles in aqueous solution" *Hem. Ind.*, vol. 66, no. 1, pp. 21–28, (2012).

[284] J. Saien, and S. Asadabadi, "Synergistic adsorption of Triton X-100 and CTAB surfactants at the toluene+ water interface" *Fluid Phase Equilib.*, vol. 307, no. 1, pp. 16–23, (2011).

[285] H.J.Y. El-Aila, "Interaction of nonionic surfactant Triton-X-100 with ionic surfactants" *J. Dispers. Sci. Technol.*, vol. 30, no. 9, pp. 1277–1280, (2009).

[286] A.H. Saiyad, A. K. Rakshit, and S.G.T. Bhat, "Solution and foaming properties of mixed aqueous solution of CTAB-Triton X-100" (1995).

[287] K.R. Lange, "Surfactants: a practical handbook" p. 237, (1999).

[288] S.K. Nath, S. Mukherjee, S. Maitra, and S. Kumar, "Kinetics study of geopolymerization of fly ash using isothermal conduction calorimetry" *J. Therm. Anal. Calorim.*, vol. 127, no. 3, pp. 1953–1961, (2017).

[289] M. Mazur, T. Janda, and W. Żukowski, "Chemical and thermal methods for removing ammonia from fly ashes" *Czas. Tech.*, vol. 2017, no. Volume 6, pp. 31–50, (2017).

[290] S.C. Kothekar, A. M. Ware, J. T. Waghmare, and S. A. Momin, "Comparative analysis of the properties of Tween-20, Tween-60, Tween-80, Arlacel-60, and Arlacel-80" *J. Dispers. Sci. Technol.*, vol. 28, no. 3, pp. 477–484, (2007), doi: 10.1080/01932690601108045.

[291] M.H. Amaral, J. das Neves, Â.Z. Oliveira, and M.F. Bahia, "Foamability of detergent solutions prepared with different types of surfactants and waters" *J. Surfactants Deterg.*, vol. 11, no. 4, pp. 275–278, (2008).

[292] F. Xu, G. Gu, W. Zhang, H. Wang, X. Huang, and J. Zhu, "Pore structure analysis and properties evaluations of fly ash-based geopolymer foams by chemical foaming method" *Ceram. Int.*, vol. 44, no. 16, pp. 19989–19997, (2018).

[293] S. Yan, F. Zhang, J. Liu, B. Ren, P. He, D. Jia, and J. Yang, "Green synthesis of high porosity waste gangue microsphere/geopolymer composite foams via hydrogen peroxide modification" *J. Clean. Prod.*, vol. 227, pp. 483–494, (2019).

[294] V. Cantarel, D. Lambertin, A. Poulesquen, F. Leroux, G. Renaudin, and F. Frizon, "Geopolymer assembly by emulsion templating: emulsion stability and hardening mechanisms" *Ceram. Int.*, vol. 44, no. 9, pp. 10558–10568, (2018).

[295] Y. Lu, and B. Qin, "Experimental Investigation of Closed Porosity of Inorganic Solidified Foam Designed to Prevent Coal Fires" *Adv. Mater. Sci. Eng.*, vol. 2015, p. 724548, (2015), doi: 10.1155/2015/724548.

[296] J. Seuba, S. Deville, C. Guizard, and A. J. Stevenson, "Gas permeability of ice-templated, unidirectional porous ceramics" *Sci. Technol. Adv. Mater.*, vol. 17, no. 1, pp. 313–323, (2016).

[297] M.S. Cilla, P. Colombo, and M. R. Morelli, "Geopolymer foams by gelcasting" *Ceram. Int.*, vol. 40, no. 4, pp. 5723–5730, (2014).

[298] J. Fiset, M. Cellier, and P. Y. Vuillaume, "Macroporous geopolymers designed for facile polymers post-infusion" *Cem. Concr. Compos.*, vol. 110, p. 103591, (2020).

[299] R. Li, G. Wu, L. Jiang, and D. Sun, "Characterization of multi-scale porous structure of fly ash/phosphate geopolymer hollow sphere structures: From submillimeter to nano-scale" *Micron*, vol. 68, pp. 54–58, (2015).

[300] C. Bai, T. Ni, Q. Wang, H. Li, and P. Colombo, "Porosity, mechanical and insulating properties of geopolymer foams using vegetable oil as the stabilizing agent" *J. Eur. Ceram. Soc.*, vol. 38, no. 2, pp. 799–805, (2018).

[301] D.S. Smith, A. Alzina, J. Bourret, B. Nait-Ali, F. Pennec, N. Tessier-Doyen, K. Otsu, H. Matsubara, "Thermal conductivity of porous materials" *J. Mater. Res.*, vol. 28, no. 17, pp. 2260–2272, (2013).

[302] S. Diamond, "Mercury porosimetry: an inappropriate method for the measurement of pore size distributions in cement-based materials" *Cem. Concr. Res.*, vol. 30, no. 10, pp. 1517–1525, (2000).

[303] S. Mindess, and J. F. Young, "Concrete" (2002).

[304] J. Delgado, N. M. M. Ramos, E. Barreira, and V. P. De Freitas, "A critical review of hygrothermal models used in

porous building materials" *J. Porous Media*, vol. 13, no. 3, (2010).

[305] D. Benavente, and C. Pla, "Effect of pore structure and moisture content on gas diffusion and permeability in porous building stones" *Mater. Struct.*, vol. 51, no. 1, pp. 1–14, (2018).

[306] H. Schmidt, D. Marcinkowska, and M. Cieślak, "Testing water vapour permeability through porous membranes" *Fibres Text. East. Eur.*, no. 2 (50), pp. 66–68, (2005).

[307] T. Kato, K. Ohashi, M. Fuji, and M. Takahashi, "Water absorption and retention of porous ceramics fabricated by waste resources" *J. Ceram. Soc. Japan*, vol. 116, no. 1350, pp. 212–215, (2008).

[308] Z. Jiang, Y. Xi, X. Gu, Q. Huang, and W. Zhang, "Modelling of water vapour sorption hysteresis of cement-based materials based on pore size distribution" *Cem. Concr. Res.*, vol. 115, pp. 8–19, (2019).

[309] A. Koponen, M. Kataja, and J. Timonen, "Permeability and effective porosity of porous media" *Phys. Rev. E*, vol. 56, no. 3, p. 3319, (1997).

[310] Z. Ji, M. Li, L. Su, and Y. Pei, "Porosity, mechanical strength and structure of waste-based geopolymer foams by different stabilizing agents" *Constr. Build. Mater.*, vol. 258, p. 119555, (2020).

[311] M. Masihi, R. Shams, and P. R. King, "Pore level characterization of Micro-CT images using percolation theory" *J. Pet. Sci. Eng.*, vol. 211, p. 110113, (2022).

[312] J. Skibinski, K. Cwieka, S. H. Ibrahim, and T. Wejrzanowski, "Influence of pore size variation on thermal conductivity of open-porous foams" *Materials (Basel)*, vol. 12, no. 12, (2019), doi: 10.3390/ma12122017.

[313] H. Janssen, and W. Van De Walle, "The impact of pore structure parameters on the thermal conductivity of porous building blocks" *Constr. Build. Mater.*, vol. 324, p. 126681, (2022).

[314] G. Chen, F. Li, P. Jing, J. Geng, and Z. Si, "Effect of pore structure on thermal conductivity and mechanical properties of autoclaved aerated concrete" *Materials (Basel)*, vol. 14, no. 2, p. 339, (2021).

[315] B. Nusser, and M. Teibinger, "Coupled Heat and Moisture Transfer in Building Components-Implementing WUFI Approaches in COMSOL Multiphysics" *Proc. COMSOL Users Conf. 2012 Milan*, (2012).

[316] R.M. Novais, R.C. Pullar, and J.A. Labrincha, "Geopolymer foams: An overview of recent advancements" *Prog. Mater. Sci.*, vol. 109, p. 100621, (2020).

[317] E. Ryshkewitch, "Compression Strength of Porous Sintered Alumina and Zirconia." *J. Am. Ceram. Soc.*, vol. 36, no. 2, pp. 65–68, (1953), doi: 10.1111/j.1151-2916.1953.tb12837.x.

[318] Z. Zhang, and H. Wang, "The pore characteristics of geopolymer foam concrete and their impact on the compressive strength and modulus" *Front. Mater.*, vol. 3, p. 38, (2016).

[319] L. Dembovska, D. Bajare, V. Ducman, L. Korat, and G. Bumanis, "The use of different by-products in the production of lightweight alkali activated building materials" *Constr. Build. Mater.*, vol. 135, pp. 315–322, (2017).

[320] H.S. Hassan, H.A. Abdel-Gawwad, S.R.V. García, and I. Israde-Alcántara, "Fabrication and characterization of thermally-insulating coconut ash-based geopolymer foam" *Waste Manag.*, vol. 80, pp. 235–240, (2018).

[321] J. Wu, Z. Zhang, Y. Zhang, and D. Li, "Preparation and characterization of ultra-lightweight foamed geopolymer (UFG) based on fly ash-metakaolin blends" *Constr. Build. Mater.*, vol. 168, pp. 771–779, (2018).

[322] J. Feng, R. Zhang, L. Gong, Y. Li, W. Cao, and X. Cheng, "Development of porous fly ash-based geopolymer with low thermal conductivity" *Mater. Des.*, vol. 65, pp. 529–533, (2015), doi: 10.1016/j.matdes.2014.09.024.

[323] R.M. Novais, G. Ascensão, N. Ferreira, M.P. Seabra, and J.A. Labrincha, "Influence of water and aluminium powder content on the properties of waste-containing geopolymer foams" *Ceram. Int.*, vol. 44, no. 6, pp. 6242–6249, (2018).

[324] R.M. Novais, G. Ascensão, L.H. Buruberri, L. Senff, and J.A. Labrincha, "Influence of blowing agent on the fresh-and hardened-state properties of lightweight geopolymers" *Mater. Des.*, vol. 108, pp. 551–559, (2016).

[325] Y. Cui, D. Wang, J. Zhao, D. Li, S. Ng, and Y. Rui, "Effect of calcium stearate based foam stabilizer on pore characteristics and thermal conductivity of geopolymer foam material" *J. Build. Eng.*, vol. 20, pp. 21–29, (2018).

[326] R.M. Novais, L.H. Buruberri, G. Ascensão, M.P. Seabra, and J.A. Labrincha, "Porous biomass fly ash-based geopolymers with tailored thermal conductivity" *J. Clean. Prod.*, vol. 119, pp. 99–107, (2016), doi: 10.1016/j.jclepro.2016.01.083.

[327] C. Bai, H. Li, E. Bernardo, and P. Colombo, "Waste-to-resource preparation of glass-containing foams from geopolymers" *Ceram. Int.*, vol. 45, no. 6, pp. 7196–7202, (2019).

[328] T. F. Tadros, "Applied surfactants: principles and applications" (2006).

[329] D. Yan, S. Ruan, S. Chen, Y. Liu, Y. Tian, H. Wang, and T. Ye, "Effects and mechanisms of surfactants on physical properties and microstructures of metakaolin-based geopolymer" *J. Zhejiang Univ. A*, vol. 22, no. 2, pp. 130–146, (2021).

[330] M.T. Ley, K.J. Folliard, and K.C. Hover, "Observations of air-bubbles escaped from fresh cement paste" *Cem. Concr. Res.*, vol. 39, no. 5, pp. 409–416, (2009).

[331] Q. Liu, Z. Chen, and Y. Yang, "Study of the air-entraining behavior based on the interactions between cement particles and selected cationic, anionic and nonionic surfactants" *Materials (Basel)*, vol. 13, no. 16, p. 3514, (2020).

[332] J.C. Mendes, T.K. Moro, A.S. Figueiredo, K.D. do Carmo Silva, G. C. Silva, G. J. B. Silva, and R. A. F. Peixoto, "Mechanical, rheological and morphological analysis of cement-based composites with a new LAS-based air entraining agent" *Constr. Build. Mater.*, vol. 145, pp. 648–661, (2017).

[333] G. Gelardi, S. Mantellato, D. Marchon, M. Palacios, A. B. Eberhardt, and R. J. Flatt, "Chemistry of chemical admixtures" *Sci. Technol. Concr. Admixtures*, pp. 149–218, (2016), doi: 10.1016/B978-0-08-100693-1.00009-6.

[334] J. Penfold, E. Staples, I. Tucker, and R. K. Thomas, "Adsorption of mixed anionic and nonionic surfactants at the hydrophilic silicon surface" *Langmuir*, vol. 18, no. 15, pp. 5755–5760, (2002).

[335] Z. Liu, M. K. Ghatkesar, E. J. R. Sudhölter, B. Singh, and N. Kumar, "Understanding the cation-dependent surfactant adsorption on clay minerals in oil recovery" *Energy & Fuels*, vol. 33, no. 12, pp. 12319–12329, (2019).

[336] Z. Liu, G. Zhao, M. Brewer, Q. Lv, and E.J.R. Sudhölter, "Comprehensive review on surfactant adsorption on mineral surfaces in chemical enhanced oil recovery" *Adv. Colloid Interface Sci.*, vol. 294, p. 102467, (2021).

[337] N. Buchavzov, and C. Stubenrauch, "A disjoining pressure study of foam films stabilized by mixtures of nonionic and ionic surfactants" *Langmuir*, vol. 23, no. 10, pp. 5315–5323, (2007).

[338] M. Parhizkar, M. Edirisinghe, and E. Stride, "The effect of surfactant type and concentration on the size and stability of microbubbles produced in a capillary embedded T-junction device" *Rsc Adv.*, vol. 5, no. 14, pp. 10751–10762, (2015).

[339] Q. Liu, Z. Chen, and Y. Yang, "Effect of fly ash on the air void size distribution entrained by selected anionic, cationic and nonionic surfactants in hardened cement mortars" *Cem. Concr. Compos.*, vol. 124, p. 104253, (2021).

[340] X. Zhao, A.H. Brozena, and L. Hu, "Critical roles of pores and moisture in sustainable nanocellulose-based super-thermal insulators" *Matter*, vol. 4, no. 3, pp. 769–772, (2021).

[341] J.L. Bell, and W.M. Kriven, "Preparation of ceramic foams from metakaolin-based geopolymer gels" *Ceram Eng Sci Proc*, vol. 29, no. 10, pp. 97–112, (2009).

[342] J. Sarazin, C.A. Davy, S. Bourbigot, G. Tricot, J. Hosdez, D. Lambertin, and G. Fontaine, "Flame resistance of geopolymer foam coatings for the fire protection of steel" *Compos. Part B Eng.*, vol. 222, p. 109045, (2021).

[343] C.N. Ang, and Y.C. Wang, "The effect of water movement on specific heat of gypsum plasterboard in heat transfer analysis under natural fire exposure" *Constr. Build. Mater.*, vol. 18, no. 7, pp. 505–515, (2004).

[344] Y.X. Chen, K.M. Klima, H.J.H. Brouwers, and Q.L. Yu, "Effect of silica aerogel on thermal insulation and acoustic absorption of geopolymer foam composites: The role of aerogel particle size" *Compos. Part B Eng.*, vol. 242, p. 110048, (2022), doi: https://doi.org/10.1016/j.compositesb.2022.110048.

[345] E. Papa, V. Medri, D. Kpogbemabou, V. Morinière, J. Laumonier, A. Vaccari, and S. Rossignol, "Porosity and insulating properties of silica-fume based foams" *Energy Build.*, vol. 131, pp. 223–232, (2016).

[346] B. Peceño, E.M. Perez-Soriano, J.D. Ríos, Y. Luna-Galiano, H. Cifuentes, and C. Leiva Fernández, "Morphological

analysis of porosity and sound absorption in sustainable materials from rice husk" *Build. Acoust.*, vol. 29, no. 3, pp. 387–399, (2022).

[347] B.P. Jelle, "Traditional, state-of-the-art and future thermal building insulation materials and solutions – Properties, requirements and possibilities" *Energy Build.*, vol. 43, no. 10, pp. 2549–2563, Oct. (2011), doi: 10.1016/J.enbuild.2011.05.015.

[348] R. Baetens, B.P. Jelle, and A. Gustavsen, "Aerogel insulation for building applications: A state-of-the-art review" *Energy Build.*, vol. 43, no. 4, pp. 761–769, Apr. (2011), doi: 10.1016/J.enbuild.2010.12.012.

[349] O.A. Madyan, M. Fan, L. Feo, and D. Hui, "Physical properties of clay aerogel composites: An overview" *Compos. Part B Eng.*, vol. 102, pp. 29–37, Oct. (2016), doi: 10.1016/j.compositesb.2016.06.057.

[350] P. Nejat, F. Jomehzadeh, M.M. Taheri, M. Gohari, and M.Z. Muhd, "A global review of energy consumption, CO_2 emissions and policy in the residential sector (with an overview of the top ten CO_2 emitting countries)" *Renew. Sustain. Energy Rev.*, vol. 43, pp. 843–862, Mar. (2015), doi: 10.1016/j.rser.2014.11.066.

[351] X. Gao, and Q.L. Yu, "Effects of an eco-silica source based activator on functional alkali activated lightweight composites" *Constr. Build. Mater.*, vol. 215, pp. 686–695, Aug. (2019), doi: 10.1016/j.conbuildmat.2019.04.251.

[352] C. Giosuè, Q.L. Yu, M.L. Ruello, F. Tittarelli, and H.J.H. Brouwers, "Effect of pore structure on the performance of photocatalytic lightweight lime-based finishing mortar" *Constr. Build. Mater.*, vol. 171, pp. 232–242, May (2018), doi: 10.1016/j.conbuildmat.2018.03.106.

[353] Q.L. Yu, D. J. Glas, and H.J.H. Brouwers, "Effects of hydrophobic expanded silicate aggregates on properties of structural lightweight aggregate concrete" *J. Mater. Civ. Eng.*, vol. 32, no. 6, p. 6020006, (2020).

[354] Y.X. Chen, F. Wu, Q.L. Yu, and H.J.H. Brouwers, "Bio-based ultra-lightweight concrete applying miscanthus fibers: Acoustic absorption and thermal insulation" *Cem. Concr. Compos.*, vol. 114, (2020), doi: 10.1016/j.cemconcomp.2020.103829.

[355] Y. Chen, Q.L. Yu, and H.J.H. Brouwers, "Acoustic performance and microstructural analysis of bio-based lightweight concrete containing miscanthus" *Constr. Build. Mater.*, vol. 157, pp. 839–851, (2017), doi: 10.1016/j.conbuildmat.2017.09.161.

[356] Q.L. Yu, P. Spiesz, and H.J.H. Brouwers, "Ultra-lightweight concrete: Conceptual design and performance evaluation" *Cem. Concr. Compos.*, vol. 61, pp. 18–28, Aug. (2015), doi: 10.1016/j.cemconcomp.2015.04.012.

[357] Q.L. Yu, P.Spiesz, and H.J.H. Brouwers, "Development of cement-based lightweight composites – Part 1: Mix design methodology and hardened properties" *Cem. Concr. Compos.*, vol. 44, pp. 17–29, Nov. (2013), doi: 10.1016/j.cemconcomp.2013.03.030.

[358] S.S. Kistler, "Coherent Expanded Aerogels and Jellies" *Nature*, vol. 127, p. 741, (1931), doi: 10.1038/127741a0.

[359] Y.X. Chen, Y. Hendrix, K. Schollbach, and H.J.H. Brouwers, "A silica aerogel synthesized from olivine and its application as a photocatalytic support" *Constr. Build. Mater.*, vol. 248, p. 118709, (2020), doi: https://doi.org/10.1016/j.conbuildmat.2020.118709.

[360] G. Wei, Y. Liu, X. Zhang, F. Yu, and X. Du, "Thermal conductivities study on silica aerogel and its composite insulation materials" *Int. J. Heat Mass Transf.*, vol. 54, no. 11–12, pp. 2355–2366, May (2011), doi: 10.1016/j.Ijheatmasstransfer.2011.02.026.

[361] Y.X. Chen, S. Sepahvand, F. Gauvin, K. Schollbach, H.J.H. Brouwers, and Q.L. Yu, "One-pot synthesis of monolithic silica-cellulose aerogel applying a sustainable sodium silicate precursor" *Constr. Build. Mater.*, vol. 293, p. 123289, Jul. (2021), doi: 10.1016/j.conbuildmat.2021.123289.

[362] O.A. Madyan, M. Fan, L. Feo, and D. Hui, "Enhancing mechanical properties of clay aerogel composites: An overview" *Composites Part B: Engineering*, vol. 98. Elsevier, pp. 314–329, Aug. 2016, doi: 10.1016/j.compositesb.2016.04.059.

[363] A. Lamy-Mendes, A. D. R. Pontinha, P. Alves, P. Santos, and L. Durães, "Progress in silica aerogel-containing materials for buildings' thermal insulation" *Constr. Build. Mater.*, vol. 286, p. 122815, Jun. (2021), doi:

10.1016/j.conbuildmat.2021.122815.

[364] P. Liu, H. Gao, X. Chen, D. Chen, J. Lv, M. Han, P. Cheng, and G. Wang, "In situ one-step construction of monolithic silica aerogel-based composite phase change materials for thermal protection" *Compos. Part B Eng.*, vol. 195, p. 108072, Aug. (2020), doi: 10.1016/j.compositesb.2020.108072.

[365] Y. Wang, X. Gao, Y. Fu, X. Wu, Q. Wang, W. Zhang, and C. Luo, "Enhanced microwave absorption performances of polyaniline/graphene aerogel by covalent bonding" *Compos. Part B Eng.*, vol. 169, pp. 221–228, Jul. (2019), doi: 10.1016/j.compositesb.2019.04.008.

[366] S. Ng, B.P. Jelle, L.I.C. Sandberg, T. Gao, and Ó.H. Wallevik, "Experimental investigations of aerogel-incorporated ultra-high performance concrete" *Constr. Build. Mater.*, vol. 77, pp. 307–316, Feb. (2015), doi: 10.1016/j.conbuildmat.2014.12.064.

[367] T. Gao, B.P. Jelle, A. Gustavsen, and S. Jacobsen, "Aerogel-incorporated concrete: An experimental study" *Constr. Build. Mater.*, vol. 52, pp. 130–136, Feb. (2014), doi: 10.1016/j.conbuildmat.2013.10.100.

[368] M. de Fátima Júlio, L.M. Ilharco, A. Soares, I. Flores-Colen, and J. de Brito, "Silica-based aerogels as aggregates for cement-based thermal renders" *Cem. Concr. Compos.*, vol. 72, pp. 309–318, Sep. (2016), doi: 10.1016/j.cemconcomp.2016.06.013.

[369] J. Seo, S. J. Bae, D. I. Jang, S. Park, B. Yang, and H. K. Lee, "Thermal behavior of alkali-activated fly ash/slag with the addition of an aerogel as an aggregate replacement" *Cem. Concr. Compos.*, vol. 106, p. 103462, Feb. (2020), doi: 10.1016/j.cemconcomp.2019.103462.

[370] P. Zhu, X. Xu, H. Liu, S. Liu, C. Chen, and Z. Jia, "Tunnel fire resistance of self-compacting concrete coated with SiO_2 aerogel cement paste under 2.5 h HC fire loading" *Constr. Build. Mater.*, vol. 239, p. 117857, Apr. (2020), doi: 10.1016/j.conbuildmat.2019.117857.

[371] S. Ng, B.P. Jelle, Y. Zhen, and Ó.H. Wallevik, "Effect of storage and curing conditions at elevated temperatures on aerogel-incorporated mortar samples based on UHPC recipe" *Constr. Build. Mater.*, vol. 106, pp. 640–649, Mar. (2016), doi: 10.1016/j.conbuildmat.2015.12.162.

[372] M. Pedroso, I. Flores-Colen, J.D. Silvestre, M.G. Gomes, L. Silva, and L. Ilharco, "Physical, mechanical, and microstructural characterisation of an innovative thermal insulating render incorporating silica aerogel" *Energy Build.*, vol. 211, p. 109793, Mar. (2020), doi: 10.1016/j.enbuild.2020.109793.

[373] C.Y. Zhang, R. Han, B. Yu, and Y.M. Wei, "Accounting process-related CO_2 emissions from global cement production under Shared Socioeconomic Pathways" *J. Clean. Prod.*, vol. 184, pp. 451–465, May (2018), doi: 10.1016/j.jclepro.2018.02.284.

[374] P. Duxson, J.L. Provis, G.C. Lukey, and J.S.J. Van Deventer, "The role of inorganic polymer technology in the development of 'green concrete,'" *Cem. Concr. Res.*, vol. 37, no. 12, pp. 1590–1597, (2007).

[375] M.T. Marvila, A.R.G. Azevedo, G.C.G. Delaqua, B.C. Mendes, L.G. Pedroti, and C.M.F. Vieira, "Performance of geopolymer tiles in high temperature and saturation conditions" *Constr. Build. Mater.*, vol. 286, p. 122994, (2021), doi: 10.1016/j.conbuildmat.2021.122994.

[376] J. Zhao, L. Tong, B. Li, T. Chen, C. Wang, G. Yang, and Y. Zheng, "Eco-friendly geopolymer materials: a review of performance improvement, potential application and sustainability assessment" *J. Clean. Prod.*, p. 127085, (2021).

[377] D.M.A. Huiskes, A. Keulen, Q.L. Yu, and H.J.H. Brouwers, "Design and performance evaluation of ultra-lightweight geopolymer concrete" *Mater. Des.*, vol. 89, pp. 516–526, Jan. (2016), doi: 10.1016/j.matdes.2015.09.167.

[378] O. Krotov, P. Gromyko, M. Gravit, and S. Sultanov, "Thermal conductivity of geopolymer concrete with different types of aggregate" *Int. Sci. Conf. Energy, Environ. Constr. Eng.*, pp. 296–303, (2020).

[379] Y. Huang, L. Gong, Y. Pan, C. Li, T. Zhou, and X. Cheng, "Facile construction of the aerogel/geopolymer composite with ultra-low thermal conductivity and high mechanical performance" *RSC Adv.*, vol. 8, no. 5, pp. 2350–2356, (2018).

[380] Y. Huang, L. Gong, L. Shi, W. Cao, Y. Pan, and X. Cheng, "Experimental investigation on the influencing factors of

preparing porous fly ash-based geopolymer for insulation material" *Energy Build.*, vol. 168, pp. 9–18, Jun. (2018), doi: 10.1016/j.enbuild.2018.02.043.

[381] C. Liu, J. Luo, Q. Li, S. Gao, D. Su, J. Zhang, and S. Chen, "Calcination of green high-belite sulphoaluminate cement (GHSC) and performance optimizations of GHSC-based foamed concrete" *Mater. Des.*, vol. 182, p. 107986, (2019), doi: 10.1016/j.matdes.2019.107986.

[382] X. Wang, L. Liu, H. Zhou, T. Song, Q. Qiao, and H. Zhang, "Improving the compressive performance of foam concrete with ceramsite: Experimental and meso-scale numerical investigation" *Mater. Des.*, vol. 208, p. 109938, (2021), doi: 10.1016/j.matdes.2021.109938.

[383] G. Samson, M. Cyr, and X.X. Gao, "Thermomechanical performance of blended metakaolin-GGBS alkali-activated foam concrete" *Constr. Build. Mater.*, vol. 157, pp. 982–993, (2017), doi: 10.1016/j.conbuildmat.2017.09.146.

[384] J.G. Sanjayan, A. Nazari, L. Chen, and G.H. Nguyen, "Physical and mechanical properties of lightweight aerated geopolymer" *Constr. Build. Mater.*, vol. 79, pp. 236–244, Mar. (2015), doi: 10.1016/j.conbuildmat.2015.01.043.

[385] G. Samson, and M. Cyr, "Porous structure optimisation of flash-calcined metakaolin/fly ash geopolymer foam concrete" *Eur. J. Environ. Civ. Eng.*, vol. 22, no. 12, pp. 1482–1498, (2018).

[386] J. Maia, M. Pedroso, N.M.M. Ramos, P.F. Pereira, I. Flores-Colen, M.G. Gomes, and L. Silva, "Hygrothermal performance of a new thermal aerogel-based render under distinct climatic conditions" *Energy Build.*, vol. 243, p. 111001, (2021), doi: 10.1016/j.enbuild.2021.111001.

[387] T. Alioua, B. Agoudjil, A. Boudenne, and K. Benzarti, "Sensitivity analysis of transient heat and moisture transfer in a bio-based date palm concrete wall" *Build. Environ.*, vol. 202, no. May, p. 108019, (2021), doi: 10.1016/j.buildenv.2021.108019.

[388] T. Stahl, S. Brunner, M. Zimmermann, and K. Ghazi Wakili, "Thermo-hygric properties of a newly developed aerogel based insulation rendering for both exterior and interior applications" *Energy Build.*, vol. 44, no. 1, pp. 114–117, (2012), doi: 10.1016/j.enbuild.2011.09.041.

[389] W.D.A. Rickard, R. Williams, J. Temuujin, and A. Van Riessen, "Assessing the suitability of three Australian fly ashes as an aluminosilicate source for geopolymers in high temperature applications" *Mater. Sci. Eng. A*, vol. 528, no. 9, pp. 3390–3397, (2011).

[390] B. Tansel, and D. Boglaienko, "Characterization of aggregation and declustering tendency of hydrophobic fine particles in water" *Granul. Matter*, vol. 21, no. 2, pp. 1–12, (2019).

[391] A. Maestro, and E. Guzmán, "Colloids at Fluid Interfaces" *Processes*, vol. 7, no. 12, (2019), doi: 10.3390/pr7120942.

[392] R.F. Tabor, F. Grieser, R.R. Dagastine, and D.Y.C. Chan, "The hydrophobic force: measurements and methods" *Phys. Chem. Chem. Phys.*, vol. 16, no. 34, pp. 18065–18075, (2014).

[393] C. Wang, Y. Liu, L. Xu, M. Qiu, H. Jiang, and R. Chen, "Rebound behaviors of hydrophilic particle on gas bubble: effect of particle size and liquid properties" *J. Chem. Technol. Biotechnol.*, vol. 96, no. 8, pp. 2400–2413, (2021).

[394] P. Li, H. Wu, Y. Liu, J. Yang, Z. Fang, and B. Lin, "Preparation and optimization of ultra-light and thermal insulative aerogel foam concrete" *Constr. Build. Mater.*, vol. 205, pp. 529–542, Apr. (2019), doi: 10.1016/j.conbuildmat.2019.01.212.

[395] P. Zhu, S. Brunner, S. Zhao, M. Griffa, A. Leemann, N. Toropovs, A. Malekos, M.M. Koebel, "Study of physical properties and microstructure of aerogel-cement mortars for improving the fire safety of high-performance concrete linings in tunnels" *Cem. Concr. Compos.*, vol. 104, p. 103414, Nov. (2019), doi: 10.1016/j.cemconcomp.2019.103414.

[396] H. Du, and S.D. Pang, "Enhancement of barrier properties of cement mortar with graphene nanoplatelet" *Cem. Concr. Res.*, vol. 76, pp. 10–19, Oct. (2015), doi: 10.1016/j.cemconres.2015.05.007.

[397] H. Du, H.J. Gao, and S.D. Pang, "Improvement in concrete resistance against water and chloride ingress by adding graphene nanoplatelet" *Cem. Concr. Res.*, vol. 83, pp. 114–123, May (2016), doi: 10.1016/j.cemconres.2016.02.005.

[398] A.V Neimark, P.I. Ravikovitch, and A.Vishnyakov, "Bridging scales from molecular simulations to classical

thermodynamics: density functional theory of capillary condensation in nanopores" *J. Phys. Condens. Matter*, vol. 15, no. 3, p. 347, (2003).

[399] R. Fediuk, M. Amran, N. Vatin, Y. Vasilev, V. Lesovik, and T. Ozbakkaloglu, "Acoustic Properties of Innovative Concretes: A Review" *Materials (Basel)*, vol. 14, no. 2, p. 398, (2021).

[400] J.W.N. Neithalath and J. Olek, "Acoustically Efficient Concretes Through Engineered Pore Structure" *ACI Symp. Publ.*, pp. 135–148, (2003), doi: 10.14359/14395.

[401] A. Laukaitis, and B. Fiks, "Acoustical properties of aerated autoclaved concrete" *Appl. Acoust.*, vol. 67, no. 3, pp. 284–296, (2006), doi: 10.1016/j.apacoust.2005.07.003.

[402] W.D.A. Rickard, L. Vickers, and A. van Riessen, "Performance of fibre reinforced, low density metakaolin geopolymers under simulated fire conditions" *Appl. Clay Sci.*, vol. 73, no. 1, pp. 71–77, (2013), doi: 10.1016/j.clay.2012.10.006.

[403] H. Li, X. Peng, J.Li, L.Li, D.Hu, Y. Xiang, L. Han, and Z. Xu, "Preparation and fireproofing performance of the wollastonite-metakaolin-based geopolymer foams" *Mater. Lett.*, vol. 307, p. 131020, (2022).

[404] M.F. Zawrah, H.E.H. Sadek, R.E.A. Ngida, S.E.A. Sawan, and A. A. El-Kheshen, "Effect of low-rate firing on physico-mechanical properties of unfoamed and foamed geopolymers prepared from waste clays" *Ceram. Int.*, vol. 48, no. 8, pp. 11330–11337, (2022).

[405] W. Chen, A.C. Garofalo, H. Geng, Y. Liu, D. Wang, and Q. Li, "Effect of high temperature heating on the microstructure and performance of cesium-based geopolymer reinforced by cordierite" *Cem. Concr. Compos.*, vol. 129, p. 104474, (2022).

[406] Y.C. Ding, Y.S. Fang, and T.W. Cheng, "Preparation and characterization of vitrified slag/geopolymers for construction and fire-resistance applications" *Mater. Struct.*, vol. 49, no. 5, pp. 1883–1891, (2016).

[407] M. Lahoti, K.K. Wong, E.H. Yang, and K.H. Tan, "Effects of Si/Al molar ratio on strength endurance and volume stability of metakaolin geopolymers subject to elevated temperature" *Ceram. Int.*, vol. 44, no. 5, pp. 5726–5734, (2018).

[408] T. Pantongsuk, P. Kittisayarm, N. Muenglue, S. Benjawan, P. Thavorniti, C. Tippayasam, S. Nilpairach, G. Heness, "Effect of hydrogen peroxide and bagasse ash additions on thermal conductivity and thermal resistance of geopolymer foams" *Mater. Today Commun.*, vol. 26, p. 102149, (2021).

[409] B. Kozub, P. Bazan, R. Gailitis, K. Korniejenko, and D. Mierzwiński, "Foamed geopolymer composites with the addition of glass wool waste" *Materials (Basel)*, vol. 14, no. 17, p. 4978, (2021).

[410] D. Gawin, F. Pesavento, and B.A. Schrefler, "Towards prediction of the thermal spalling risk through a multi-phase porous media model of concrete" *Comput. Methods Appl. Mech. Eng.*, vol. 195, no. 41–43, pp. 5707–5729, (2006).

[411] J.C. Mindeguia, P. Pimienta, A. Noumowé, and M. Kanema, "Temperature, pore pressure and mass variation of concrete subjected to high temperature—Experimental and numerical discussion on spalling risk" *Cem. Concr. Res.*, vol. 40, no. 3, pp. 477–487, (2010).

[412] X. Zhang, C. Bai, Y. Qiao, X. Wang, D. Jia, H. Li, and P. Colombo, "Porous geopolymer composites: A review" *Compos. Part A Appl. Sci. Manuf.*, vol. 150, p. 106629, (2021).

[413] P. Perumal, T. Luukkonen, H. Sreenivasan, P. Kinnunen, and M. Illikainen, "15 - Porous alkali-activated materials" pp. 529–563, (2020), doi: https://doi.org/10.1016/B978-0-12-818961-0.00015-6.

[414] K. Dhasindrakrishna, S. Ramakrishnan, K. Pasupathy, and J. Sanjayan, "Synthesis and performance of intumescent alkali-activated rice husk ash for fire-resistant applications" *J. Build. Eng.*, vol. 51, p. 104281, (2022).

[415] G.J.G. Gluth, W.D.A. Rickard, S. Werner, and S. Pirskawetz, "Acoustic emission and microstructural changes in fly ash geopolymer concretes exposed to simulated fire" *Mater. Struct.*, vol. 49, no. 12, pp. 5243–5254, (2016).

[416] K.M.Klima, C.H.A. Koh, H.J.H. Brouwers, and Q.L. Yu, "Synergistic effect of surfactants in porous geopolymer: Tailoring pore size and pore connectivity" *Cem. Concr. Compos.*, vol. 134, p. 104774, (2022).

[417] P.De Silva, K. Sagoe-Crenstil, and V. Sirivivatnanon, "Kinetics of geopolymerization: Role of Al_2O_3 and SiO_2" *Cem.*

Concr. Res., vol. 37, no. 4, pp. 512–518, (2007), doi: https://doi.org/10.1016/j.cemconres.2007.01.003.

[418] P.I. Pelissari, R.A. Angélico, V.R. Salvini, D.O. Vivaldini, and V.C. Pandolfelli, "Analysis and modeling of the pore size effect on the thermal conductivity of alumina foams for high temperature applications" *Ceram. Int.*, vol. 43, no. 16, pp. 13356–13363, (2017).

[419] F. Wang, L. Kong, and Z. Zhou, "Study on Pore Structure and Mechanical Property of Expansive Soil under Different Dehydration Conditions" *Appl. Sci.*, vol. 12, no. 12, p. 5981, (2022).

[420] S.M. Fayyad, G.S. Al-Marahleh, and S.Q. Abu-Ein, "Improvement of the refractoriness under load of fire-clay refractory bricks" *Adv. Theor. Appl. Mech*, vol. 5, no. 4, pp. 161–172, (2012).

[421] G. Ba, J. Miao, W. Zhang, and C. Liu, "Influence of cracking on heat propagation in reinforced concrete structures" *J. Struct. Eng.*, vol. 142, no. 7, p. 4016035, (2016).

[422] Z. Živcová, E. Gregorová, W. Pabst, D.S. Smith, A. Michot, and C. Poulier, "Thermal conductivity of porous alumina ceramics prepared using starch as a pore-forming agent" *J. Eur. Ceram. Soc.*, vol. 29, no. 3, pp. 347–353, (2009).

[423] L. Min, W. Zhishen, K. Hongtao, Q. Chunxiang, and S. Wei, "Calculation and analysis of pore vapor pressure of concrete exposed to fire" *Int. J. Phys. Sci.*, vol. 5, no. 8, pp. 1315–1323, (2010).

[424] G.H.A. Van der Heijden, L. Pel, and O.C.G. Adan, "Fire spalling of concrete, as studied by NMR" *Cem. Concr. Res.*, vol. 42, no. 2, pp. 265–271, (2012).

[425] D. Edouard, M. Lacroix, C. P. Huu, and F. Luck, "Pressure drop modeling on SOLID foam: State-of-the art correlation" *Chem. Eng. J.*, vol. 144, no. 2, pp. 299–311, (2008).

[426] J. Du, J. Cai, Z. Chen, T. Lei, S. Zhang, and Z. Xie, "A contrastive study of effects of different organic matter on the smectite illitization in hydrothermal experiments" *Appl. Clay Sci.*, vol. 168, pp. 249–259, (2019).

[427] D.A. Sverjensky, J.J. Hemley, and W.M. d'Angelo, "Thermodynamic assessment of hydrothermal alkali feldspar-mica-aluminosilicate equilibria" *Geochim. Cosmochim. Acta*, vol. 55, no. 4, pp. 989–1004, (1991).

[428] G.W. Morey, and P. Niggli, "The hydrothermal formation of silicates, a review" *J. Am. Chem. Soc.*, vol. 35, no. 9, pp. 1086–1130, (1913).

[429] R.J. Kinzler, and T.L. Grove, "Crystallization and differentiation of Archean komatiite lavas from northeast Ontario: phase equilibrium and kinetic studies" *Am. Mineral.*, vol. 70, no. 1–2, pp. 40–51, (1985).

[430] T.W. Swaddle, and P. Oltmann, "Kinetics of the magnetite–maghemite–hematite transformation, with special reference to hydrothermal systems" *Can. J. Chem.*, vol. 58, no. 17, pp. 1763–1772, (1980).

[431] A. Abaza, J. Laurencin, A. Nakajo, S. Meille, J. Debayle, and D. Leguillon, "Prediction of crack nucleation and propagation in porous ceramics using the phase-field approach" *Theor. Appl. Fract. Mech.*, vol. 119, p. 103349, (2022).

[432] K.S. Suslick, "Encyclopedia of physical science and technology" *Sonoluminescence sonochemistry, 3rd edn. Elsevier Sci. Ltd, Massachusetts*, pp. 1–20, (2001).

[433] E. 1991-1-2. 200. E, "Eurocode 1: Actions on structure - Part 1-2: General actions - Actions on structures exposed to fire" no. 2002, (2002).

[434] K.G. Wakili, E. Hugi, L. Karvonen, P. Schnewlin, and F. Winnefeld, "Thermal behaviour of autoclaved aerated concrete exposed to fire" *Cem. Concr. Compos.*, vol. 62, pp. 52–58, (2015).

[435] G.-M. Tsaousi, K.-M. Sakkas, and D. Panias, "Development of advanced materials from industrial waste, with high thermal performance" *Constr. Build. Mater.*, vol. 315, p. 125779, (2022).

[436] L.P. Qian, L.Y. Xu, Y. Alrefaei, T. Wang, T. Ishida, and J.G. Dai, "Artificial alkali-activated aggregates developed from wastes and by-products: A state-of-the-art review" *Resour. Conserv. Recycl.*, vol. 177, no. July 2021, p. 105971, (2022), doi: 10.1016/j.resconrec.2021.105971.

[437] U.S. Agrawal, S.P. Wanjari, and D.N. Naresh, "Impact of replacement of natural river sand with geopolymer fly ash sand on hardened properties of concrete" *Constr. Build. Mater.*, vol. 209, pp. 499–507, (2019).

[438] M.S. Nadesan, and P. Dinakar, "Structural concrete using sintered flyash lightweight aggregate: A review" *Constr. Build. Mater.*, vol. 154, pp. 928–944, (2017).

[439] P. Nielsen, R. Baciocchi, G. Costa, M. Quaghebeur, and R. Snellings, "Carbonate-bonded construction materials from alkaline residues" *RILEM Tech. Lett.*, vol. 2, pp. 53–58, (2017).

[440] F. Tajra, M. Abd Elrahman, and D. Stephan, "The production and properties of cold-bonded aggregate and its applications in concrete: A review" *Constr. Build. Mater.*, vol. 225, pp. 29–43, (2019).

[441] P. Risdanareni, K. Schollbach, J. Wang, and N.De Belie, "The effect of NaOH concentration on the mechanical and physical properties of alkali activated fly ash-based artificial lightweight aggregate" *Constr. Build. Mater.*, vol. 259, p. 119832, (2020).

[442] P. Ren, T. Ling, and K. Hung, "Recent advances in artificial aggregate production" vol. 291, (2021), doi: 10.1016/j.jclepro.2020.125215.

[443] F. Tajra, M. Abd Elrahman, C. Lehmann, and D. Stephan, "Properties of lightweight concrete made with core-shell structured lightweight aggregate" *Constr. Build. Mater.*, vol. 205, pp. 39–51, (2019).

[444] B. Nagy, T.K. Simon, and R. Nemes, "Effect of built-in mineral wool insulations durability on its thermal and mechanical performance" *J. Therm. Anal. Calorim.*, vol. 139, no. 1, pp. 169–181, (2020).

[445] N. Voronina, "Acoustic properties of fibrous materials" *Appl. Acoust.*, vol. 42, no. 2, pp. 165–174, (1994), doi: https://doi.org/10.1016/0003-682X(94)90005-1.

[446] O. Väntsi, and T. Kärki, "Mineral wool waste in Europe: a review of mineral wool waste quantity, quality, and current recycling methods" *J. Mater. Cycles Waste Manag.*, vol. 16, no. 1, pp. 62–72, (2014).

[447] T. Sattler, M. Sartori, R. Galler, R. Pomberger, J. Krainz, J. Schimek, and D. Vollprecht, "Effects of cement addition and briquetting of rock wool on its geomechanical stability in landfills" *Waste Manag. Res.*, vol. 38, no. 4, pp. 408–414, (2020).

[448] T. Sattler, R. Pomberger, J. Schimek, and D. Vollprecht, "Mineral wool waste in austria, associated health aspects and recycling options" *Detritus*, vol. 9, no. March, pp. 174–180, (2020).

[449] J. Pranckevičienė, "Impact of mineral wool production waste on properties of sintered ceramics" (2011).

[450] O. Kizinievič, V. Balkevičius, J. Pranckevičienė, and V. Kizinievič, "Investigation of the usage of centrifuging waste of mineral wool melt (CMWW), contaminated with phenol and formaldehyde, in manufacturing of ceramic products" *Waste Manag.*, vol. 34, no. 8, pp. 1488–1494, (2014).

[451] J. Felegi Jr, and K.P. Kehrer, "Composite fiberboard and process of manufacture" Oct. (1990).

[452] W.T. Lin, A. Cheng, R. Huang, Y.C. Wu, and T.Y. Han, "Rock wool wastes as a supplementary cementitious material replacement in cement-based composites" *Comput. Concr*, vol. 11, no. 2, pp. 93–104, (2013).

[453] W.T. Lin, T.Y. Han, C.C. Huang, A. Cheng, and R. Huang, "Using rock wool wastes as partial replacement of cement in cement-based composites" *Adv. Sci. Lett.*, vol. 8, no. 1, pp. 489–494, (2012).

[454] J. Yliniemi, B. Walkley, J.L. Provis, P. Kinnunen, and M. Illikainen, "Influence of activator type on reaction kinetics, setting time, and compressive strength of alkali-activated mineral wools" *J. Therm. Anal. Calorim.*, vol. 144, no. 4, pp. 1129–1138, (2021).

[455] J. Yliniemi, P. Kinnunen, P. Karinkanta, and M. Illikainen, "Utilization of mineral wools as alkali-activated material precursor" *Materials (Basel)*, vol. 9, no. 5, p. 312, (2016), doi: 10.3390/ma9050312.

[456] P. Kinnunen, J. Yliniemi, B. Talling, and M. Illikainen, "Rockwool waste in fly ash geopolymer composites" *J. Mater. Cycles Waste Manag.*, vol. 19, no. 3, pp. 1220–1227, (2017), doi: 10.1007/s10163-016-0514-z.

[457] L. Pilato, "Phenolic resins: a century of progress" vol. 11, (2010).

[458] X. Wang, Y. Jin, Z. Wang, R.B. Mahar, and Y. Nie, "A research on sintering characteristics and mechanisms of dried sewage sludge" *J. Hazard. Mater.*, vol. 160, no. 2–3, pp. 489–494, (2008).

[459] J.L. Provis, "Alkali-activated materials" *Cem. Concr. Res.*, vol. 114, pp. 40–48, (2018).

[460] C.G. Go, J.R. Tang, J.H. Chi, C.T. Chen, and Y.L. Huang, "Fire-resistance property of reinforced lightweight aggregate concrete wall" *Constr. Build. Mater.*, vol. 30, pp. 725–733, (2012).

[461] M. Dener, M. Karatas, and M. Mohabbi, "High temperature resistance of self compacting alkali activated slag/portland cement composite using lightweight aggregate" *Constr. Build. Mater.*, vol. 290, p. 123250, (2021).

[462] M.B. Karakoç, "Effect of cooling regimes on compressive strength of concrete with lightweight aggregate exposed to high temperature" *Constr. Build. Mater.*, vol. 41, pp. 21–25, (2013).

[463] P. Krivenko, "Alkali-activated cements and concretes" *CRC Press*, (2003).

[464] A. Ivanič, G. Kravanja, W. Kidess, R. Rudolf, and S. Lubej, "The influences of moisture on the mechanical, morphological and thermogravimetric properties of mineral wool made from basalt glass fibers" *Materials (Basel)*, vol. 13, no. 10, p. 2392, (2020).

[465] J. Sjostrom, and R.J. Mcnamee, "Measuring thermal material properties for structural fire engineering" *Proc. 15th Int. Conf. Exp. Mech. ICEM 15, Porto, Port.*, pp. 22–27, (2020).

[466] M.M. Smedskjaer, M. Solvang, and Y. Yue, "Crystallisation behaviour and high-temperature stability of stone wool fibres" *J. Eur. Ceram. Soc.*, vol. 30, no. 6, pp. 1287–1295, (2010).

[467] M. Pavlin, B. Horvat, A. Frankovič, and V. Ducman, "Mechanical, microstructural and mineralogical evaluation of alkali-activated waste glass and stone wool" *Ceram. Int.*, vol. 47, no. 11, pp. 15102–15113, (2021).

[468] R. Yu, P. Spiesz, and H.J.H. Brouwers, "Mix design and properties assessment of ultra-high performance fibre reinforced concrete (UHPFRC)" *Cem. Concr. Res.*, vol. 56, pp. 29–39, (2014).

[469] H.J.H. Brouwers, "Particle-size distribution and packing fraction of geometric random packings" *Phys. Rev. E*, vol. 74, no. 3, p. 31309, (2006).

[470] H.J.H. Brouwers, and H.J. Radix, "Self-compacting concrete: theoretical and experimental study" *Cem. Concr. Res.*, vol. 35, no. 11, pp. 2116–2136, (2005).

[471] X. Gao, Q.L. Yu, and H.J.H. Brouwers, "Assessing the porosity and shrinkage of alkali activated slag-fly ash composites designed applying a packing model" *Constr. Build. Mater.*, vol. 119, pp. 175–184, (2016).

[472] P.H.R. Borges, L.F. Fonseca, V.A. Nunes, T.H. Panzera, and C.C. Martuscelli, "Andreasen particle packing method on the development of geopolymer concrete for civil engineering" *J. Mater. Civ. Eng.*, vol. 26, no. 4, pp. 692–697, (2014).

[473] T.S. Ng, and S.J. Foster, "Development of a mix design methodology for high-performance geopolymer mortars" *Struct. Concr.*, vol. 14, no. 2, pp. 148–156, (2013).

[474] Yliniemi, Paiva, Ferreira, Tiainen, and Illikainen, "Development and incorporation of lightweight waste-based geopolymer aggregates in mortar and concrete" *Constr. Build. Mater.*, vol. 131, pp. 784–792, (2017).

[475] P.K. Mehta, and P.J.M. Monteiro, "Concrete: microstructure, properties, and materials" (2014).

[476] B.M. Aïssoun, S.D. Hwang, and K.H. Khayat, "Influence of aggregate characteristics on workability of superworkable concrete" *Mater. Struct.*, vol. 49, no. 1, pp. 597–609, (2016).

[477] M. Češnovar, K. Traven, and V. Ducman, "Deformation of alkali-activated materials at an early age under different curing conditions" *Front. Chem.*, p. 378, (2021).

[478] M.P. Krasnovskih, N.G. Maksimovich, Y.I. Vaisman, and A. A. Ketov, "Thermal stability of mineral-wool heat-insulating materials" *Russ. J. Appl. Chem.*, vol. 87, no. 10, pp. 1430–1434, (2014).

[479] J.D. Axe, and G. Shirane, "Study of the Alpha-Beta Quartz phase transformation by inelastic neutron scattering" *Phys. Rev. B*, vol. 1, no. 1, pp. 342–348, (1970), doi: 10.1103/PhysRevB.1.342.

[480] H.Z. Cui, T.Y. Lo, S.A. Memon, and W. Xu, "Effect of lightweight aggregates on the mechanical properties and brittleness of lightweight aggregate concrete" *Constr. Build. Mater.*, vol. 35, pp. 149–158, (2012).

[481] O. Kayali, "Fly ash lightweight aggregates in high performance concrete" *Constr. Build. Mater.*, vol. 22, no. 12, pp. 2393–

2399, (2008).

[482] F. Şahin, M. Uysal, and O. Canpolat, "Systematic evaluation of the aggregate types and properties on metakaolin based geopolymer composites" *Constr. Build. Mater.*, vol. 278, p. 122414, (2021), doi: https://doi.org/10.1016/j.conbuildmat.2021.122414.

APPENDIX A

Table A.1. Qualitative and quantitative analysis of raw materials and pastes at ambient temperature (errors show in the brackets).

Phase	Fly Ash	Sodalite-[illegible]	G-FA	G-S1	G-S2
Amorphous	78.1 (0.66)	45.1(0.61)	82.2 (0.43)	77.4 (0.60)	76.7 (0.50)
Mullite	11.3 (0.25)	10.8 (0.17)	9.0 (0.17)	9.7 (0.20)	9.0 (0.17)
Quartz	7.09 (0.16)	4.0 (0.08)	5.1 (0.10)	6.1 (0.12)	6.6 (0.14)
Hematite	1.4 (0.13)	1.1 (0.08)	1.0 (0.1)	1.3 (0.13)	1.3 (0.09)
Magnetite	0.6 (0.10)	0.2 (0.06)	0.7 (0.08)	0.5 (0.09)	0.2 (0.06)
Anatase	0.2 (0.05)	0.1 (0.03)	0.2 (0.04)	0.1 (0.04)	0.11 (0.03)
Periclase	0.2 (0.10)	0.5 (0.11)	0.3 (0.08)	0.7 (0.09)	0.5 (0.08)
Wollastonite	0.6 (0.46)	0.7 (0.28)	0.9 (0.32)	1.0 (0.44)	1.0 (0.33)
Pyrrhotite	0.3 (0.08)	0.4 (0.06)	0.2 (0.06)		
Calcite	0.3 (0.09)	0.8 (0.11)	0.4 (0.08)	0.7 (0.09)	0.5 (0.07)
Sodalite group		36.3 (0.24)		2.6 (0.14)	**3.9 (0.15)**

Table A.2. Qualitative and quantitative analysis of sample G-FA at elevated temperature.

	400°C	**600°C**	**800°C**	**1000°C**
Amorphous	80.1 (0.39)	78.3 (0.48)	77.6 (0.56)	80.4 (0.43)
Mullite	10.2 (0.17)	10.5 (0.19)	9.9 (0.22)	5.9 (0.20)
Quartz	5.7 (0.11)	6.7 (0.12)	7.3 (0.13)	5.7 (0.11)
Hematite	1.2 (0.11)	1.8 (0.11)	2.3 (0.13)	2.6 (0.12)
Magnetite	0.8 (0.08)	0.3 (0.06)	0.4 (0.09)	0.2 (0.07)
Anatase	0.1 (0.03)	0.1 (0.03)	0.2 (0.05)	0.2 (0.05)
Periclase	0.3 (0.08)	0.3 (0.09)	0.3 (0.09)	
Wollastonite	1.0 (0.23)	1.1 (0.35)	1.1 (0.4)	1.1 (0.18)
Pyrrhotite	0.2 (0.07)	0.3 (0.07)	0.3 (0.08)	0.9 (0.09)
Calcite	0.4 (0.08)	0.6 (0.08)	0.3 (0.08)	0.2 (0.07)
Nepheline			0.4 (0.13)	0.7 (0.13)
Anorthoclase				2.1 (0.13)

Table A.3. Qualitative and quantitative analysis of sample G-S1 at elevated temperature.

	400°C	600°C	800°C	1000°C
Amorphous	79.2 (0.32)	74.6 (0.54)	74.0 (0.43)	72.5 (0.62)
Sodalite	2.0 (0.09)	2.3 (0.11)	1.3 (0.09)	
Mullite	9.0 (0.15)	10.7 (0.20)	9.3 (0.17)	6.9 (0.22)
Quartz	6.2 (0.08)	7.0 (0.12)	6.9 (0.1)	7.1 (0.13)
Hematite	1.3 (0.12)	2.1 (0.11)	2.7 (0.13)	3.6 (0.13)
Magnetite	0.6 (0.08)	0.1 (0.07)	0.5 (0.09)	0.6 (0.08)
Anatase	0.2 (0.04)	0.1 (0.04)	0.1 (0.04)	0.2 (0.06)
Calcite	0.6 (0.08)	0.5 (0.09)	0.5 (0.09)	0.1 (0.07)
Periclase	0.5 (0.09)	0.8(0.1)	0.6 (0.09)	0.6 (0.11)
Wollastonite	0.4 (0.24)	1.5 (0.40)	2.3 (0.18)	2.3 (0.23)
Halite potassian		0.3 (0.03)	0.3 (0.03)	0.4 (0.04)
Anorthoclase			1.0 (0.12)	4.1 (0.19)
Nepheline			0.4 (0.13)	0.4 (0.16)
Leucite				1.1 (0.13)

Table A.4. Qualitative and quantitative analysis of sample G-S2 at elevated temperature.

	400°C	600°C	800°C	1000°C
Amorphous	75.4 (0.48)	74.0 (0.50)	71.3 (0.44)	70.3 (0.47)
Sodalite	3.8 (0.10)	3.7 (0.10)	2.9 (0.09)	
Mullite	10.3 (0.19)	10.7 (0.19)	10.1 (0.18)	6.5 (0.19)
Quartz	6.4 (0.11)	6.8 (0.11)	6.8 (0.09)	7.2 (0.11)
Hematite	1.3 (0.12)	1.7 (0.12)	2.7 (0.13)	3.2 (0.12)
Magnetite	0.5 (0.09)	0.5 (0.09)	0.6 (0.09)	0.6 (0.07)
Anatase	0.1 (0.03)	0.1 (0.03)	0.1 (0.04)	0.1 (0.05)
Calcite	0.5 (0.08)	0.5 (0.08)	0.5 (0.09)	0.2 (0.06)
Periclase	0.7 (0.10)	0.7 (0.09)	0.6 (0.09)	0.3 (0.07)
Wollastonite	1.0 (0.37)	1.1 (0.37)	2.8 (0.18)	2.8 (0.23)
Halite potassian		0.2 (0.03)	0.3 (0.04)	0.3 (0.04)
Anorthoclase			1.0 (0.13)	6.6 (0.14)
Nepheline			0.3 (0.13)	0.1 (0.07)
Leucite				1.8 (0.12)

APPENDIX B

Table B.1. Input parameters: material properties, boundary conditions and initial conditions.

Material properties	**T100CTAB**	**T100SDS**	**T60SDS**
Bulk density ϱ (kg/m³)	733	726	727
Porosity (-)	0.690	0.693	0.693
Heat capacity C_p (J/kg·K)	730	730	730
Thermal conductivity λ (W/m·K)	0.104	0.116	0.125
Vapour diffusion resistance factor μ (-)	4	4	4
Sorption isotherm	Refer Figure 5.9		
Thermal conductivity, moisture-dep	Refer Figure 5.10		
Exterior boundary condition			
Climate	Refer Figure 5.11 following Eindhoven, facing south-west		
Heat resistance (m²·K/W)	0.0588		
Short wave radiation absorptivity (-)	0.68		
Long wave radiation emissivity (-)	-		
Adhering fraction of rain (-)	0.7		
Interior boundary condition			
Climate	EN13788 humidity class 3, temperature 20°C		
Heat resistance (m²·K /W)	0.125		
Initial condition			
Initial RH (-)	0.8		
Initial temperature in component (°C)	20		

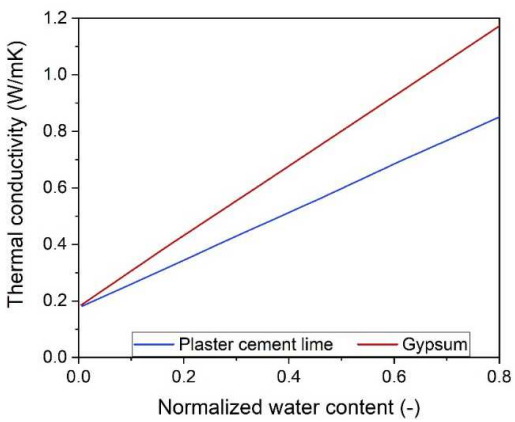

Fig. B.1. Moisture dependent thermal conductivity – input data for calculation.

Table B.2. Material properties used in time-dependent calculations (source: WUFI database).

	Plaster cement lime	Gypsum
Bulk density (kg/m³)	1024	850
Porosity (%)	61	65
Specific heat capacity (J/kgK)	850	850
Thermal conductivity (W/m·K)	0.179	0.2
Water Vapour Diffusion Resistance Factor (-)	6.1	8.3

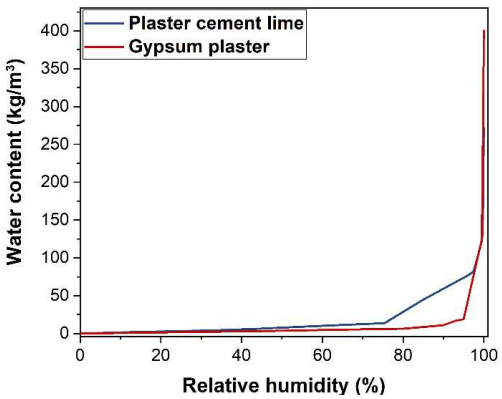

Fig. B.2. Moisture storage function of two commercially-available materials.

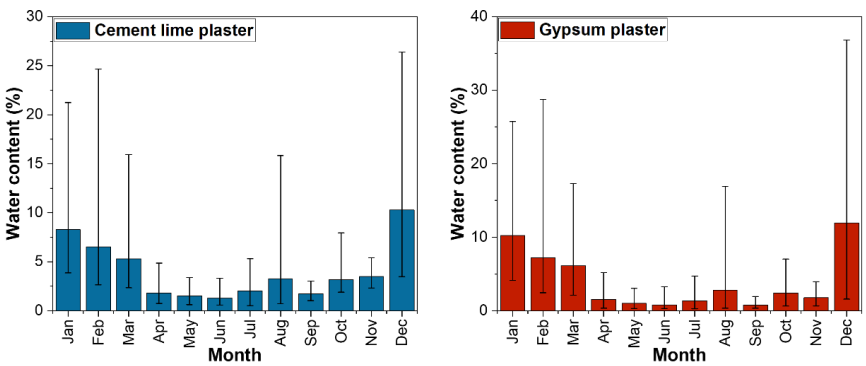

Fig. B.3. Moisture content of two commercial materials in the 5th year under one climate condition. With marked min and max values of water content reported in each month.

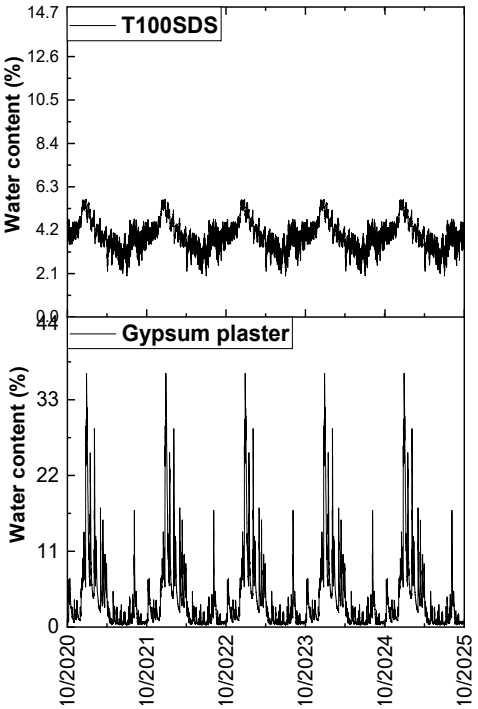

Fig. B.4. An example of water content in geopolymer and gypsum plaster 4 cm layers within 5 years.

APPENDIX C

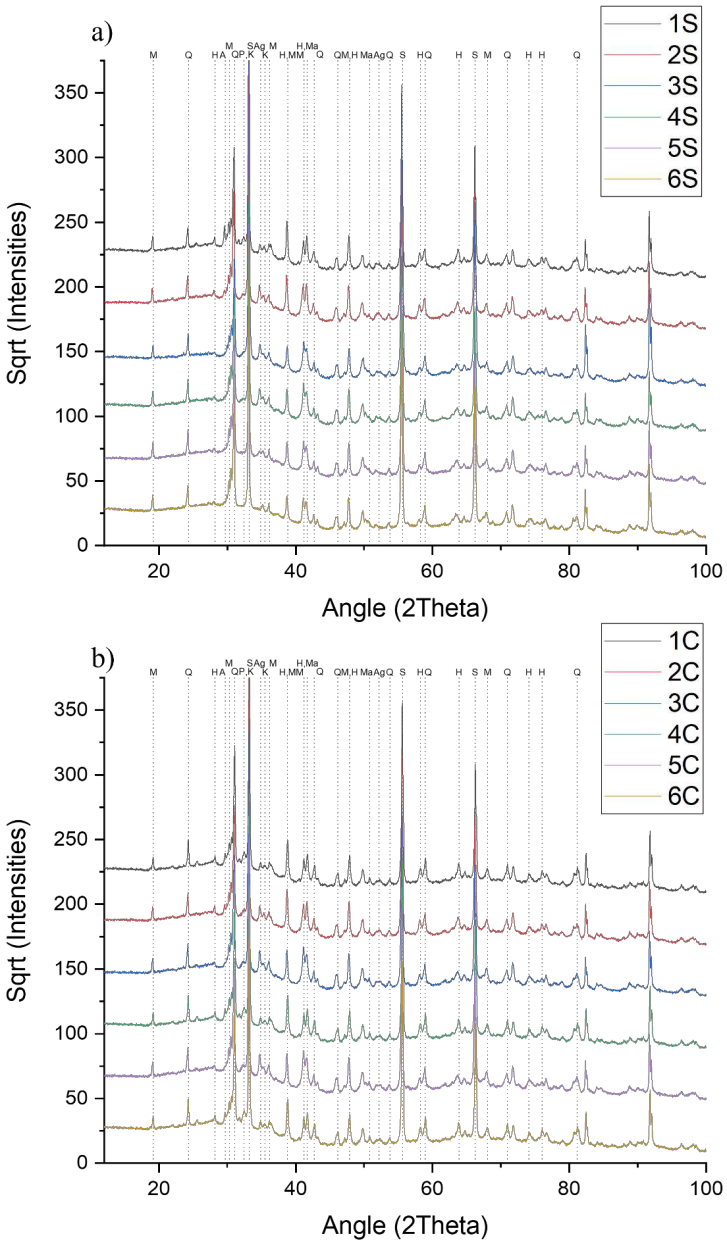

Fig. C.1. XRD of sample a) T100SDS and b) T100CTAB. Legend: M:Mullite; Q: Quartz; H: Hematite; A: Anorthoclase;P: Anhydrite; S: Silicone; Ag: Augite; K: Microcline; Ma: Maghemite.

Table C.1. Input parameters: material properties, boundary conditions and initial conditions.

Material properties	T100CTAB	T100SDS
Bulk density ϱ (kg/m³)	733	726
Porosity (-)	0.690	0.693
Heat capacity C_p (J/kg·K)	730	730
Thermal conductivity λ (W/m·K)	0.104	0.116
Thermal conductivity, temp-dep	Refer eq. (7.5)	
Surface emissivity ε (-)	0.72	
Pore diameter d (mm)	0.5; 0.9, 1.5	0.5
Shape factor sf (-)	2/3; 3/4, 4/5	2/3
Boundary condition, left		
Heat source	Refer eq. (7.3)	
Heat transfer coefficient h (W/m²·K)	10	
Temperature, furnace (°C)	Refer Fig.7.2), 'Furnace' temperature from 100°C onward	
Boundary condition, right		
Heat sink	Refer eq. (7.4)	
Surface emissivity ε (-)	0.72	
Temperature, ambient (°C)	20	
Initial condition		
Initial temperature in component (°C)	100	

Table C.2. Data extracted from the literature used to simulate ISO 834 fire scenario.

	Sample code	Porosity (-)	Thermal conductivity (W/m·K)	Density (kg/m³)	Mean pore size (m)	Ref
Geofoam	A1	0.823	0.085	805.0	0.00222	[435]
GeoCem-Foam	A2	0.754	0.089	917.0	0.00188	[435]
GeoSiCem-Foam	A3	0.721	0.092	997.6	0.00116	[435]
Aerated concrete	B	0.81	0.133	480.0	0.00080	[434]

APPENDIX D

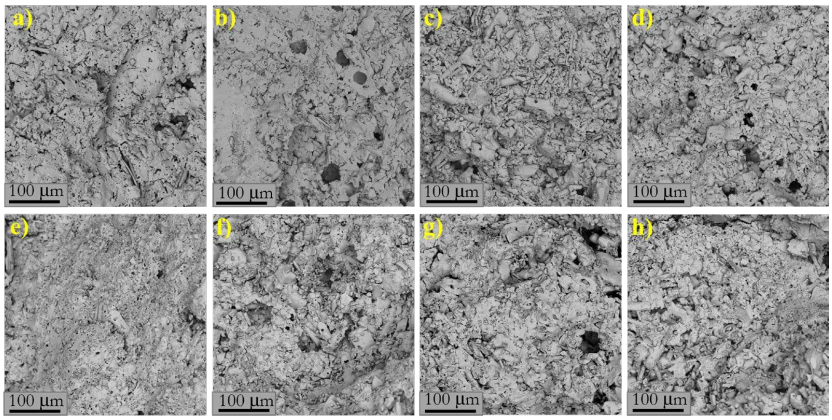

Fig. D.1 SEM pictures of aggregates core part. a) K20-1; b) K20-2; c) Na20-1; d) Na20-2; e) K50-1; f) K50-2; g) Na50-1; h) Na50-2.

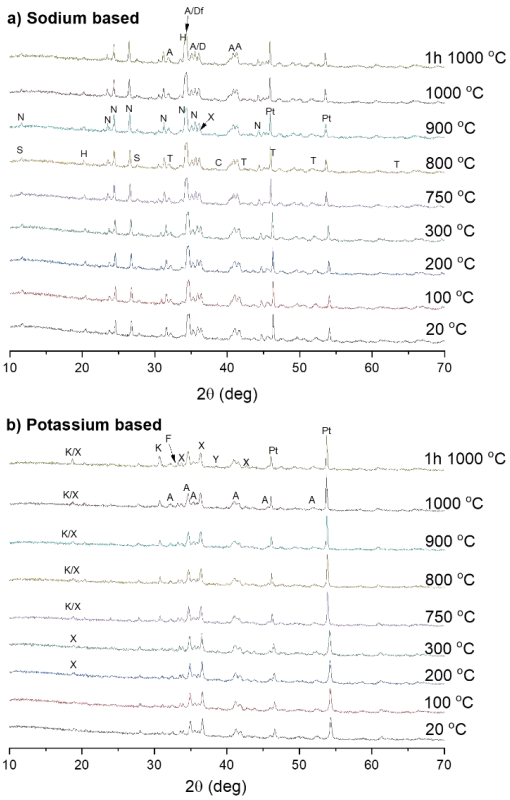

Fig. D.2. XRD diffractograms of in-situ high-temperature XRD (selected sample data) a) sodium-based b) potassium-basedLegend: **N**-Nepheline; **X**-Akermanite; **S**-Sodium-tectoaluminosilicate; **K**-Potassium aluminosilicate; **A**-Augite; **Pt**-Platinum; **D**-Diopside; **Df**-Diopside ferran; **T**-Rutile; **H**-Ammonium sulphate; **C**-Calcium magnesium nitrate; **F**-Potaassium iron phosphate; **Y**-Perovskite.

SUMMARY

The construction industry has worked hard in recent years to promote environmentally friendly materials, and a growing body of literature has identified aluminosilicate-based materials as a promising alternative to Portland Cement. Simultaneously, in recent years, there has been a growing emphasis on fire safety and passive fire protection of buildings. It is expected that investments in the sector of fireproof and safe materials will increase in the coming years. This dissertation focuses on geopolymers and their parameters that have a direct and indirect impact on behaviour under high-temperature conditions, combining the aforementioned environmental aspects and material functionality.

As a result, the first section reviews the literature and examines recent advances in fly ash fire-resistant geopolymers. The emphasis was on several parameters such as solid precursor reactivity, composition, the role of an activator, curing regime, and the investigation of the mechanism underlying high-temperature behaviour, the evolution of the microstructure, and the potential for performance improvement through the use of fibres or aggregates. The review demonstrates that potassium-based activators are better suited for high-temperature applications and emphasises the importance of pore interconnectivity in minimising material damage such as cracking and spalling.

The recommendations from the literature review are applied in the fourth chapter, and the effect of the addition of synthetic sodalite on the behaviour of the geopolymer based on fly ash and potassium activator is investigated. The morphological and compositional changes, porosity evolution, high-temperature gel behaviour, and influence of sodalite on material performance after heat exposure up to 1000 °C are investigated using a multiple-analytical method. The results show that introducing 5% of the sodalite phase significantly improves high-temperature performance by triggering phase development. The development of a mixed K-Na glass phase by the sodium-bearing sodalite phases, on the other hand, lowers the glass transition temperature. Furthermore, the presence of sodalite reduces thermal shrinkage at high temperatures, implying its role as the high-temperature backbone of the composite.

The third section (Chapter 5,6,7) discusses porous composites and their properties at room and elevated temperatures. The emphasis is on creating a more sustainable and optimized foaming process for geopolymers by utilising the synergistic properties of surfactants and the possibility of reducing the amount used while improving system stability. For low-temperature applications, studies show that a material based on cationic Cetyltrimethylammonium Bromide and nonionic Triton X-100 shows good hygrothermal properties, whereas anionic Sodium Dodecyl Sulphate forms a structure with strongly interconnected pores. The SDS-based mix is selected for further thermal and acoustic insulation tests and the mix is enriched with silica aerogel (SA). The influence of the starting material, siliceous fly ash and biocoal fly ash used, as well as the SA volume replacement of 10% and 20%, are tested to select the best-performing mixture in terms of hygrothermal and acoustic properties. A geopolymer foam based on biocoal fly ash enriched with 10% silica is regarded as an optimal mix design. Furthermore, two samples with different microstructures

but similar bulk porosities are subjected to one-side high-temperature exposure up to 1100 ^{o}C. The change in total and open porosity with depth, the cracks formation at various depths, and the mineralogical composition based solely on the temperature obtained at a specific distance from the heat source have all been investigated. As presumed, the material with a higher proportion of open porosity performs better at high temperatures. Due to the material's integrity being preserved during the test duration (180 minutes), its behaviour is further simulated under standardized conditions following Eurocode EN1991-1-2 recommendations, and it has been demonstrated that the 2.5 cm sheet protects the concrete ($T_{surface}$=180 ^{o}C) for 93 minutes.

The final section focuses on the role of aggregates in the high-temperature behaviour of a fly ash-based geopolymer, in accordance with the recommendations from the literature review. As a result, the use of mineral wool waste in the process of manufacturing artificial aggregates through the alkali-activation and sintering route is investigated. The role of alkali cation and curing regime on the aggregates' performance consists of the core part of this investigation. The basic room temperature characteristics and in-situ high-temperature performance of the resulting aggregates are established. Finally, at room temperature and after 1000 ^{o}C exposure, the performance of aggregates in fly ash-based geopolymer is evaluated and compared to sand, a commonly used aggregate. The study reveals that manufactured aggregates have appropriate mechanical properties and bonding behaviour and during mix design, the alkali cation plays a vital role in the high-temperature responsiveness of aggregates.

LIST OF PUBLICATIONS

1. **K.M. Klima**, K. Schollbach, H.J.H. Brouwers, and Q.L. Yu, "Thermal and fire resistance of Class F fly ash based geopolymers–A review" Constr. Build. Mater., vol. 323, p. 126529, (2022).
2. **K.M. Klima**, K. Schollbach, H.J.H. Brouwers, and Q.L. Yu, "Enhancing the thermal performance of Class F fly ash-based geopolymer by sodalite" Constr. Build. Mater., vol. 314, p. 125574, (2022).
3. Y. Luo, S.H. Li, **K.M. Klima**, H.J.H. Brouwers, and Q.L. Yu, "Degradation mechanism of hybrid fly ash/slag based geopolymers exposed to elevated temperatures" Cem. Concr. Res., vol. 151, no. 106649, (2021).
4. Y. Luo, **K.M. Klima**, H.J.H. Brouwers, and Q.L. Yu, "Effects of ladle slag on Class F fly ash geopolymer: Reaction mechanism and high temperature behavior" *Cem. Concr. Compos.*, vol. 129, p. 104468, (2022)
5. **K.M. Klima**, C.H.A. Koh, H.J.H. Brouwers, and Q.L. Yu, "Synergistic effect of surfactants in porous geopolymer: Tailoring pore size and pore connectivity" Cem. Concr. Compos., vol. 134, p. 104774, (2022).
6. Y.X. Chen, **K.M. Klima**, H.J.H. Brouwers, and Q.L. Yu, "Effect of silica aerogel on thermal insulation and acoustic absorption of geopolymer foam composites: The role of aerogel particle size" Compos. Part B Eng., vol. 242, p. 110048, (2022).
7. **K.M. Klima**, C.H.A. Koh, J.C.O Zepper, H.J.H. Brouwers, and Q.L. Yu, "High-temperature response of porous geopolymer – role of open porosity" (in preparation).
8. **K.M. Klima**, Y. Luo, H.J.H. Brouwers, and Q.L. Yu, "An alternative route to utilize mineral wool waste: alkali activated-artificial aggregates with improved high-temperature properties" (in preparation).

Conference Proceedings

1. **K.M. Klima**, H.J.H. Brouwers, and Q.L. Yu, "Eco-synthesis of zeolite from coal fly ash", The 2nd International Conference of Sustainable Building Materials, 12-15 August 2019, Eindhoven, The Netherlands.
2. **K.M. Klima**, H.J.H. Brouwers, and Q.L. Yu, "Geopolymer-based fireboard", 4th International Conference on the Chemistry of Construction Materials - ICCCM 2022 Karlsruhe, September 26 - 28, 2022.

CURRICULUM VITAE

Kinga Klima was born on June 8, 1994, in Limanowa, Poland. In 2017, she graduated from the department of Drilling Oil and Gas at the AGH University of Science and Technology in Krakow with a Bachelor's degree in Mining and Geology. During her Bachelor's degree, she worked on the development of a sustainable method for purifying flowback water from hydrocarbon deposits using fly ash-derived zeolites. She then pursued a master's degree at the Faculty of Energy and Fuels, graduating with honours (cum laude) in the field of Chemical Technology with a major in Industrial and Environmental Analytics in 2018. Her graduation project, "Synthesis of geopolymers from natural and waste materials" introduced her to the world of sustainable building materials. She moved to the Netherlands in October 2018 to pursue her PhD in the Building Materials group at Eindhoven University of Technology. She worked on the M2i/NWO project "Fire safety of innovative geopolymer-based building materials" with Profs. H.J.H. Brouwers and Q.L. Yu. The project's findings are presented in this dissertation.

Bouwstenen is een publicatiereeks
van de Faculteit Bouwkunde,
Technische Universiteit Eindhoven.
Zij presenteert resultaten van
onderzoek en andere activiteiten op
het vakgebied der Bouwkunde,
uitgevoerd in het kader van deze
Faculteit.

Bouwstenen en andere proefschriften van de
TU/e zijn online beschikbaar via:
https://research.tue.nl/

Reeds verschenen in de serie
Bouwstenen

nr 1
Elan: A Computer Model for Building Energy Design: Theory and Validation
Martin H. de Wit
H.H. Driessen
R.M.M. van der Velden

nr 2
Kwaliteit, Keuzevrijheid en Kosten: Evaluatie van Experiment Klarendal, Arnhem
J. Smeets
C. le Nobel
M. Broos
J. Frenken
A. v.d. Sanden

nr 3
Crooswijk: Van 'Bijzonder' naar 'Gewoon'
Vincent Smit
Kees Noort

nr 4
Staal in de Woningbouw
Edwin J.F. Delsing

nr 5
Mathematical Theory of Stressed Skin Action in Profiled Sheeting with Various Edge Conditions
Andre W.A.M.J. van den Bogaard

nr 6
Hoe Berekenbaar en Betrouwbaar is de Coëfficiënt k in x-ksigma en x-ks?
K.B. Lub
A.J. Bosch

nr 7
Het Typologisch Gereedschap: Een Verkennende Studie Omtrent Typologie en Omtrent de Aanpak van Typologisch Onderzoek
J.H. Luiten

nr 8
Informatievoorziening en Beheerprocessen
A. Nauta
Jos Smeets (red.)
Helga Fassbinder (projectleider)
Adrie Proveniers
J. v.d. Moosdijk

nr 9
Strukturering en Verwerking van Tijdgegevens voor de Uitvoering van Bouwwerken
ir. W.F. Schaefer
P.A. Erkelens

nr 10
Stedebouw en de Vorming van een Speciale Wetenschap
K. Doevendans

nr 11
Informatica en Ondersteuning van Ruimtelijke Besluitvorming
G.G. van der Meulen

nr 12
Staal in de Woningbouw, Korrosie-Bescherming van de Begane Grondvloer
Edwin J.F. Delsing

nr 13
Een Thermisch Model voor de Berekening van Staalplaatbetonvloeren onder Brandomstandigheden
A.F. Hamerlinck

nr 14
De Wijkgedachte in Nederland: Gemeenschapsstreven in een Stedebouwkundige Context
K. Doevendans
R. Stolzenburg

nr 15
Diaphragm Effect of Trapezoidally Profiled Steel Sheets: Experimental Research into the Influence of Force Application
Andre W.A.M.J. van den Bogaard

nr 16
Versterken met Spuit-Ferrocement: Het Mechanische Gedrag van met Spuit-Ferrocement Versterkte Gewapend Betonbalken
K.B. Lubir
M.C.G. van Wanroy

nr 17
De Tractaten van Jean Nicolas Louis Durand
G. van Zeyl

nr 18
Wonen onder een Plat Dak: Drie Opstellen over Enkele Vooronderstellingen van de Stedebouw
K. Doevendans

nr 19
Supporting Decision Making Processes: A Graphical and Interactive Analysis of Multivariate Data
W. Adams

nr 20
Self-Help Building Productivity: A Method for Improving House Building by Low-Income Groups Applied to Kenya 1990-2000
P. A. Erkelens

nr 21
De Verdeling van Woningen: Een Kwestie van Onderhandelen
Vincent Smit

nr 22
Flexibiliteit en Kosten in het Ontwerpproces: Een Besluitvormingondersteunend Model
M. Prins

nr 23
Spontane Nederzettingen Begeleid: Voorwaarden en Criteria in Sri Lanka
Po Hin Thung

nr 24
Fundamentals of the Design of Bamboo Structures
Oscar Arce-Villalobos

nr 25
Concepten van de Bouwkunde
M.F.Th. Bax (red.)
H.M.G.J. Trum (red.)

nr 26
Meaning of the Site
Xiaodong Li

nr 27
Het Woonmilieu op Begrip Gebracht: Een Speurtocht naar de Betekenis van het Begrip 'Woonmilieu'
Jaap Ketelaar

nr 28
Urban Environment in Developing Countries
editors: Peter A. Erkelens
George G. van der Meulen (red.)

nr 29
Stategische Plannen voor de Stad: Onderzoek en Planning in Drie Steden
prof.dr. H. Fassbinder (red.)
H. Rikhof (red.)

nr 30
Stedebouwkunde en Stadsbestuur
Piet Beekman

nr 31
De Architectuur van Djenné: Een Onderzoek naar de Historische Stad
P.C.M. Maas

nr 32
Conjoint Experiments and Retail Planning
Harmen Oppewal

nr 33
Strukturformen Indonesischer Bautechnik: Entwicklung Methodischer Grundlagen für eine 'Konstruktive Pattern Language' in Indonesien
Heinz Frick arch. SIA

nr 34
Styles of Architectural Designing: Empirical Research on Working Styles and Personality Dispositions
Anton P.M. van Bakel

nr 35
Conjoint Choice Models for Urban Tourism Planning and Marketing
Benedict Dellaert

nr 36
Stedelijke Planvorming als Co-Produktie
Helga Fassbinder (red.)

nr 37
Design Research in the Netherlands
editors: R.M. Oxman
M.F.Th. Bax
H.H. Achten

nr 38
Communication in the Building Industry
Bauke de Vries

nr 39
Optimaal Dimensioneren van Gelaste Plaatliggers
J.B.W. Stark
F. van Pelt
L.F.M. van Gorp
B.W.E.M. van Hove

nr 40
Huisvesting en Overwinning van Armoede
P.H. Thung
P. Beekman (red.)

nr 41
Urban Habitat: The Environment of Tomorrow
George G. van der Meulen
Peter A. Erkelens

nr 42
A Typology of Joints
John C.M. Olie

nr 43
Modeling Constraints-Based Choices for Leisure Mobility Planning
Marcus P. Stemerding

nr 44
Activity-Based Travel Demand Modeling
Dick Ettema

nr 45
Wind-Induced Pressure Fluctuations on Building Facades
Chris Geurts

nr 46
Generic Representations
Henri Achten

nr 47
Johann Santini Aichel: Architectuur en Ambiguiteit
Dirk De Meyer

nr 48
Concrete Behaviour in Multiaxial Compression
Erik van Geel

nr 49
Modelling Site Selection
Frank Witlox

nr 50
Ecolemma Model
Ferdinand Beetstra

nr 51
Conjoint Approaches to Developing Activity-Based Models
Donggen Wang

nr 52
On the Effectiveness of Ventilation
Ad Roos

nr 53
Conjoint Modeling Approaches for Residential Group preferences
Eric Molin

nr 54
Modelling Architectural Design Information by Features
Jos van Leeuwen

nr 55
A Spatial Decision Support System for the Planning of Retail and Service Facilities
Theo Arentze

nr 56
Integrated Lighting System Assistant
Ellie de Groot

nr 57
Ontwerpend Leren, Leren Ontwerpen
J.T. Boekholt

nr 58
Temporal Aspects of Theme Park Choice Behavior
Astrid Kemperman

nr 59
Ontwerp van een Geïndustrialiseerde Funderingswijze
Faas Moonen

nr 60
Merlin: A Decision Support System for Outdoor Leisure Planning
Manon van Middelkoop

nr 61
The Aura of Modernity
Jos Bosman

nr 62
Urban Form and Activity-Travel Patterns
Daniëlle Snellen

nr 63
Design Research in the Netherlands 2000
Henri Achten

nr 64
Computer Aided Dimensional Control in Building Construction
Rui Wu

nr 65
Beyond Sustainable Building
editors: Peter A. Erkelens
Sander de Jonge
August A.M. van Vliet
co-editor: Ruth J.G. Verhagen

nr 66
Das Globalrecyclingfähige Haus
Hans Löfflad

nr 67
Cool Schools for Hot Suburbs
René J. Dierkx

nr 68
A Bamboo Building Design Decision Support Tool
Fitri Mardjono

nr 69
Driving Rain on Building Envelopes
Fabien van Mook

nr 70
Heating Monumental Churches
Henk Schellen

nr 71
Van Woningverhuurder naar Aanbieder van Woongenot
Patrick Dogge

nr 72
Moisture Transfer Properties of Coated Gypsum
Emile Goossens

nr 73
Plybamboo Wall-Panels for Housing
Guillermo E. González-Beltrán

nr 74
The Future Site-Proceedings
Ger Maas
Frans van Gassel

nr 75
Radon transport in Autoclaved Aerated Concrete
Michel van der Pal

nr 76
The Reliability and Validity of Interactive Virtual Reality Computer Experiments
Amy Tan

nr 77
Measuring Housing Preferences Using Virtual Reality and Belief Networks
Maciej A. Orzechowski

nr 78
Computational Representations of Words and Associations in Architectural Design
Nicole Segers

nr 79
Measuring and Predicting Adaptation in Multidimensional Activity-Travel Patterns
Chang-Hyeon Joh

nr 80
Strategic Briefing
Fayez Al Hassan

nr 81
Well Being in Hospitals
Simona Di Cicco

nr 82
Solares Bauen: Implementierungs- und Umsetzungs-Aspekte in der Hochschulausbildung in Österreich
Gerhard Schuster

nr 83
Supporting Strategic Design of Workplace Environments with Case-Based Reasoning
Shauna Mallory-Hill

nr 84
ACCEL: A Tool for Supporting Concept Generation in the Early Design Phase
Maxim Ivashkov

nr 85
Brick-Mortar Interaction in Masonry under Compression
Ad Vermeltfoort

nr 86
Zelfredzaam Wonen
Guus van Vliet

nr 87
Een Ensemble met Grootstedelijke Allure
Jos Bosman
Hans Schippers

nr 88
On the Computation of Well-Structured Graphic Representations in Architectural Design
Henri Achten

nr 89
De Evolutie van een West-Afrikaanse Vernaculaire Architectuur
Wolf Schijns

nr 90
ROMBO Tactiek
Christoph Maria Ravesloot

nr 91
External Coupling between Building Energy Simulation and Computational Fluid Dynamics
Ery Djunaedy

nr 92
Design Research in the Netherlands 2005
editors: Henri Achten
Kees Dorst
Pieter Jan Stappers
Bauke de Vries

nr 93
Ein Modell zur Baulichen Transformation
Jalil H. Saber Zaimian

nr 94
Human Lighting Demands: Healthy Lighting in an Office Environment
Myriam Aries

nr 95
A Spatial Decision Support System for the Provision and Monitoring of Urban Greenspace
Claudia Pelizaro

nr 96
Leren Creëren
Adri Proveniers

nr 97
Simlandscape
Rob de Waard

nr 98
Design Team Communication
Ad den Otter

nr 99
Humaan-Ecologisch Georiënteerde Woningbouw
Juri Czabanowski

nr 100
Hambase
Martin de Wit

nr 101
Sound Transmission through Pipe Systems and into Building Structures
Susanne Bron-van der Jagt

nr 102
Het Bouwkundig Contrapunt
Jan Francis Boelen

nr 103
A Framework for a Multi-Agent Planning Support System
Dick Saarloos

nr 104
Bracing Steel Frames with Calcium Silicate Element Walls
Bright Mweene Ng'andu

nr 105
Naar een Nieuwe Houtskeletbouw
F.N.G. De Medts

nr 106 and 107
Niet gepubliceerd

nr 108
Geborgenheid
T.E.L. van Pinxteren

nr 109
Modelling Strategic Behaviour in Anticipation of Congestion
Qi Han

nr 110
Reflecties op het Woondomein
Fred Sanders

nr 111
On Assessment of Wind Comfort by Sand Erosion
Gábor Dezsö

nr 112
Bench Heating in Monumental Churches
Dionne Limpens-Neilen

nr 113
RE. Architecture
Ana Pereira Roders

nr 114
Toward Applicable Green Architecture
Usama El Fiky

nr 115
Knowledge Representation under Inherent Uncertainty in a Multi-Agent System for Land Use Planning
Liying Ma

nr 116
Integrated Heat Air and Moisture Modeling and Simulation
Jos van Schijndel

nr 117
Concrete Behaviour in Multiaxial Compression
J.P.W. Bongers

nr 118
The Image of the Urban Landscape
Ana Moya Pellitero

nr 119
The Self-Organizing City in Vietnam
Stephanie Geertman

nr 120
A Multi-Agent Planning Support System for Assessing Externalities of Urban Form Scenarios
Rachel Katoshevski-Cavari

nr 121
Den Schulbau Neu Denken, Fühlen und Wollen
Urs Christian Maurer-Dietrich

nr 122
Peter Eisenman Theories and Practices
Bernhard Kormoss

nr 123
User Simulation of Space Utilisation
Vincent Tabak

nr 125
In Search of a Complex System Model
Oswald Devisch

nr 126
Lighting at Work: Environmental Study of Direct Effects of Lighting Level and Spectrum on Psycho-Physiological Variables
Grazyna Górnicka

nr 127
Flanking Sound Transmission through Lightweight Framed Double Leaf Walls
Stefan Schoenwald

nr 128
Bounded Rationality and Spatio-Temporal Pedestrian Shopping Behavior
Wei Zhu

nr 129
Travel Information: Impact on Activity Travel Pattern
Zhongwei Sun

nr 130
Co-Simulation for Performance Prediction of Innovative Integrated Mechanical Energy Systems in Buildings
Marija Trčka

nr 131
Niet gepubliceerd

nr 132
Architectural Cue Model in Evacuation Simulation for Underground Space Design
Chengyu Sun

nr 133
Uncertainty and Sensitivity Analysis in Building Performance Simulation for Decision Support and Design Optimization
Christina Hopfe

nr 134
Facilitating Distributed Collaboration in the AEC/FM Sector Using Semantic Web Technologies
Jacob Beetz

nr 135
Circumferentially Adhesive Bonded Glass Panes for Bracing Steel Frame in Façades
Edwin Huveners

nr 136
Influence of Temperature on Concrete Beams Strengthened in Flexure with CFRP
Ernst-Lucas Klamer

nr 137
Sturen op Klantwaarde
Jos Smeets

nr 139
Lateral Behavior of Steel Frames with Discretely Connected Precast Concrete Infill Panels
Paul Teewen

nr 140
Integral Design Method in the Context of Sustainable Building Design
Perica Savanović

nr 141
Household Activity-Travel Behavior: Implementation of Within-Household Interactions
Renni Anggraini

nr 142
Design Research in the Netherlands 2010
Henri Achten

nr 143
Modelling Life Trajectories and Transport Mode Choice Using Bayesian Belief Networks
Marloes Verhoeven

nr 144
Assessing Construction Project Performance in Ghana
William Gyadu-Asiedu

nr 145
Empowering Seniors through Domotic Homes
Masi Mohammadi

nr 146
An Integral Design Concept for Ecological Self-Compacting Concrete
Martin Hunger

nr 147
Governing Multi-Actor Decision Processes in Dutch Industrial Area Redevelopment
Erik Blokhuis

nr 148
A Multifunctional Design Approach for Sustainable Concrete
Götz Hüsken

nr 149
Quality Monitoring in Infrastructural Design-Build Projects
Ruben Favié

nr 150
Assessment Matrix for Conservation of Valuable Timber Structures
Michael Abels

nr 151
Co-simulation of Building Energy Simulation and Computational Fluid Dynamics for Whole-Building Heat, Air and Moisture Engineering
Mohammad Mirsadeghi

nr 152
External Coupling of Building Energy Simulation and Building Element Heat, Air and Moisture Simulation
Daniel Cóstola

nr 153
Adaptive Decision Making In Multi-Stakeholder Retail Planning
Ingrid Janssen

nr 154
Landscape Generator
Kymo Slager

nr 155
Constraint Specification in Architecture
Remco Niemeijer

nr 156
A Need-Based Approach to Dynamic Activity Generation
Linda Nijland

nr 157
Modeling Office Firm Dynamics in an Agent-Based Micro Simulation Framework
Gustavo Garcia Manzato

nr 158
Lightweight Floor System for Vibration Comfort
Sander Zegers

nr 159
Aanpasbaarheid van de Draagstructuur
Roel Gijsbers

nr 160
'Village in the City' in Guangzhou, China
Yanliu Lin

nr 161
Climate Risk Assessment in Museums
Marco Martens

nr 162
Social Activity-Travel Patterns
Pauline van den Berg

nr 163
Sound Concentration Caused by Curved Surfaces
Martijn Vercammen

nr 164
Design of Environmentally Friendly Calcium Sulfate-Based Building Materials: Towards an Improved Indoor Air Quality
Qingliang Yu

nr 165
Beyond Uniform Thermal Comfort on the Effects of Non-Uniformity and Individual Physiology
Lisje Schellen

nr 166
Sustainable Residential Districts
Gaby Abdalla

nr 167
Towards a Performance Assessment Methodology using Computational Simulation for Air Distribution System Designs in Operating Rooms
Mônica do Amaral Melhado

nr 168
Strategic Decision Modeling in Brownfield Redevelopment
Brano Glumac

nr 169
Pamela: A Parking Analysis Model for Predicting Effects in Local Areas
Peter van der Waerden

nr 170
A Vision Driven Wayfinding Simulation-System Based on the Architectural Features Perceived in the Office Environment
Qunli Chen

nr 171
Measuring Mental Representations Underlying Activity-Travel Choices
Oliver Horeni

nr 172
Modelling the Effects of Social Networks on Activity and Travel Behaviour
Nicole Ronald

nr 173
Uncertainty Propagation and Sensitivity Analysis Techniques in Building Performance Simulation to Support Conceptual Building and System Design
Christian Struck

nr 174
Numerical Modeling of Micro-Scale Wind-Induced Pollutant Dispersion in the Built Environment
Pierre Gousseau

nr 175
Modeling Recreation Choices over the Family Lifecycle
Anna Beatriz Grigolon

nr 176
Experimental and Numerical Analysis of Mixing Ventilation at Laminar, Transitional and Turbulent Slot Reynolds Numbers
Twan van Hooff

nr 177
Collaborative Design Support: Workshops to Stimulate Interaction and Knowledge Exchange Between Practitioners
Emile M.C.J. Quanjel

nr 178
Future-Proof Platforms for Aging-in-Place
Michiel Brink

nr 179
Motivate: A Context-Aware Mobile Application for Physical Activity Promotion
Yuzhong Lin

nr 180
Experience the City: Analysis of Space-Time Behaviour and Spatial Learning
Anastasia Moiseeva

nr 181
Unbonded Post-Tensioned Shear Walls of Calcium Silicate Element Masonry
Lex van der Meer

nr 182
Construction and Demolition Waste Recycling into Innovative Building Materials for Sustainable Construction in Tanzania
Mwita M. Sabai

nr 183
Durability of Concrete with Emphasis on Chloride Migration
Przemysław Spiesz

nr 184
Computational Modeling of Urban Wind Flow and Natural Ventilation Potential of Buildings
Rubina Ramponi

nr 185
A Distributed Dynamic Simulation Mechanism for Buildings Automation and Control Systems
Azzedine Yahiaoui

nr 186
Modeling Cognitive Learning of Urban Networks in Daily Activity-Travel Behavior
Şehnaz Cenani Durmazoğlu

nr 187
Functionality and Adaptability of Design Solutions for Public Apartment Buildings in Ghana
Stephen Agyefi-Mensah

nr 188
A Construction Waste Generation Model for Developing Countries
Lilliana Abarca-Guerrero

nr 189
Synchronizing Networks: The Modeling of Supernetworks for Activity-Travel Behavior
Feixiong Liao

nr 190
Time and Money Allocation Decisions in Out-of-Home Leisure Activity Choices
Gamze Zeynep Dane

nr 191
How to Measure Added Value of CRE and Building Design
Rianne Appel-Meulenbroek

nr 192
Secondary Materials in Cement-Based Products: Treatment, Modeling and Environmental Interaction
Miruna Florea

nr 193
Concepts for the Robustness Improvement of Self-Compacting Concrete: Effects of Admixtures and Mixture Components on the Rheology and Early Hydration at Varying Temperatures
Wolfram Schmidt

nr 194
Modelling and Simulation of Virtual Natural Lighting Solutions in Buildings
Rizki A. Mangkuto

nr 195
Nano-Silica Production at Low Temperatures from the Dissolution of Olivine - Synthesis, Tailoring and Modelling
Alberto Lazaro Garcia

nr 196
Building Energy Simulation Based Assessment of Industrial Halls for Design Support
Bruno Lee

nr 197
Computational Performance Prediction of the Potential of Hybrid Adaptable Thermal Storage Concepts for Lightweight Low-Energy Houses
Pieter-Jan Hoes

nr 198
Application of Nano-Silica in Concrete
George Quercia Bianchi

nr 199
Dynamics of Social Networks and Activity Travel Behaviour
Fariya Sharmeen

nr 200
Building Structural Design Generation and Optimisation including Spatial Modification
Juan Manuel Davila Delgado

nr 201
Hydration and Thermal Decomposition of Cement/Calcium-Sulphate Based Materials
Ariën de Korte

nr 202
Republiek van Beelden:
De Politieke Werkingen van het Ontwerp in Regionale Planvorming
Bart de Zwart

nr 203
Effects of Energy Price Increases on Individual Activity-Travel Repertoires and Energy Consumption
Dujuan Yang

nr 204
Geometry and Ventilation:
Evaluation of the Leeward Sawtooth Roof Potential in the Natural Ventilation of Buildings
Jorge Isaac Perén Montero

nr 205
Computational Modelling of Evaporative Cooling as a Climate Change Adaptation Measure at the Spatial Scale of Buildings and Streets
Hamid Montazeri

nr 206
Local Buckling of Aluminium Beams in Fire Conditions
Ronald van der Meulen

nr 207
Historic Urban Landscapes:
Framing the Integration of Urban and Heritage Planning in Multilevel Governance
Loes Veldpaus

nr 208
Sustainable Transformation of the Cities:
Urban Design Pragmatics to Achieve a Sustainable City
Ernesto Antonio Zumelzu Scheel

nr 209
Development of Sustainable Protective Ultra-High Performance Fibre Reinforced Concrete (UHPFRC):
Design, Assessment and Modeling
Rui Yu

nr 210
Uncertainty in Modeling Activity-Travel Demand in Complex Uban Systems
Soora Rasouli

nr 211
Simulation-based Performance Assessment of Climate Adaptive Greenhouse Shells
Chul-sung Lee

nr 212
Green Cities:
Modelling the Spatial Transformation of the Urban Environment using Renewable Energy Technologies
Saleh Mohammadi

nr 213
A Bounded Rationality Model of Short and Long-Term Dynamics of Activity-Travel Behavior
Ifigeneia Psarra

nr 214
Effects of Pricing Strategies on Dynamic Repertoires of Activity-Travel Behaviour
Elaheh Khademi

nr 215
Handstorm Principles for Creative and Collaborative Working
Frans van Gassel

nr 216
Light Conditions in Nursing Homes: Visual Comfort and Visual Functioning of Residents
Marianne M. Sinoo

nr 217
Woonsporen: De Sociale en Ruimtelijke Biografie van een Stedelijk Bouwblok in de Amsterdamse Transvaalbuurt
Hüseyin Hüsnü Yegenoglu

nr 218
Studies on User Control in Ambient Intelligent Systems
Berent Willem Meerbeek

nr 219
Daily Livings in a Smart Home: Users' Living Preference Modeling of Smart Homes
Erfaneh Allameh

nr 220
Smart Home Design: Spatial Preference Modeling of Smart Homes
Mohammadali Heidari Jozam

nr 221
Wonen: Discoursen, Praktijken, Perspectieven
Jos Smeets

nr 222
Personal Control over Indoor Climate in Offices: Impact on Comfort, Health and Productivity
Atze Christiaan Boerstra

nr 223
Personalized Route Finding in Multimodal Transportation Networks
Jianwe Zhang

nr 224
The Design of an Adaptive Healing Room for Stroke Patients
Elke Daemen

nr 225
Experimental and Numerical Analysis of Climate Change Induced Risks to Historic Buildings and Collections
Zara Huijbregts

nr 226
Wind Flow Modeling in Urban Areas Through Experimental and Numerical Techniques
Alessio Ricci

nr 227
Clever Climate Control for Culture: Energy Efficient Indoor Climate Control Strategies for Museums Respecting Collection Preservation and Thermal Comfort of Visitors
Rick Kramer

nr 228
Fatigue Life Estimation of Metal Structures Based on Damage Modeling
Sarmediran Silitonga

nr 229
A multi-agents and occupancy based strategy for energy management and process control on the room-level
Timilehin Moses Labeodan

nr 230
Environmental assessment of Building Integrated Photovoltaics: Numerical and Experimental Carrying Capacity Based Approach
Michiel Ritzen

nr 231
Performance of Admixture and Secondary Minerals in Alkali Activated Concrete: Sustaining a Concrete Future
Arno Keulen

nr 232
World Heritage Cities and Sustainable Urban Development:
Bridging Global and Local Levels in Monitoring the Sustainable Urban Development of World Heritage Cities
Paloma C. Guzman Molina

nr 233
Stage Acoustics and Sound Exposure in Performance and Rehearsal Spaces for Orchestras:
Methods for Physical Measurements
Remy Wenmaekers

nr 234
Municipal Solid Waste Incineration (MSWI) Bottom Ash:
From Waste to Value Characterization, Treatments and Application
Pei Tang

nr 235
Large Eddy Simulations Applied to Wind Loading and Pollutant Dispersion
Mattia Ricci

nr 236
Alkali Activated Slag-Fly Ash Binders: Design, Modeling and Application
Xu Gao

nr 237
Sodium Carbonate Activated Slag: Reaction Analysis, Microstructural Modification & Engineering Application
Bo Yuan

nr 238
Shopping Behavior in Malls
Widiyani

nr 239
Smart Grid-Building Energy Interactions: Demand Side Power Flexibility in Office Buildings
Kennedy Otieno Aduda

nr 240
Modeling Taxis Dynamic Behavior in Uncertain Urban Environments
Zheng Zhong

nr 241
Gap-Theoretical Analyses of Residential Satisfaction and Intention to Move
Wen Jiang

nr 242
Travel Satisfaction and Subjective Well-Being: A Behavioral Modeling Perspective
Yanan Gao

nr 243
Building Energy Modelling to Support the Commissioning of Holistic Data Centre Operation
Vojtech Zavrel

nr 244
Regret-Based Travel Behavior Modeling: An Extended Framework
Sunghoon Jang

nr 245
Towards Robust Low-Energy Houses: A Computational Approach for Performance Robustness Assessment using Scenario Analysis
Rajesh Reddy Kotireddy

nr 246
Development of sustainable and functionalized inorganic binder-biofiber composites
Guillaume Doudart de la Grée

nr 247
A Multiscale Analysis of the Urban Heat Island Effect: From City Averaged Temperatures to the Energy Demand of Individual Buildings
Yasin Toparlar

nr 248
Design Method for Adaptive Daylight Systems for buildings covered by large (span) roofs
Florian Heinzelmann

nr 249
Hardening, high-temperature resistance and acid resistance of one-part geopolymers
Patrick Sturm

nr 250
Effects of the built environment on dynamic repertoires of activity-travel behaviour
Aida Pontes de Aquino

nr 251
Modeling for auralization of urban environments: Incorporation of directivity in sound propagation and analysis of a framework for auralizing a car pass-by
Fotis Georgiou

nr 252
Wind Loads on Heliostats and Photovoltaic Trackers
Andreas Pfahl

nr 253
Approaches for computational performance optimization of innovative adaptive façade concepts
Roel Loonen

nr 254
Multi-scale FEM-DEM Model for Granular Materials: Micro-scale boundary conditions, Statics, and Dynamics
Jiadun Liu

nr 255
Bending Moment - Shear Force Interaction of Rolled I-Shaped Steel Sections
Rianne Willie Adriana Dekker

nr 256
Paralympic tandem cycling and handcycling: Computational and wind tunnel analysis of aerodynamic performance
Paul Fionn Mannion

nr 257
Experimental characterization and numerical modelling of 3D printed concrete: Controlling structural behaviour in the fresh and hardened state
Robert Johannes Maria Wolfs

nr 258
Requirement checking in the building industry: Enabling modularized and extensible requirement checking systems based on semantic web technologies
Chi Zhang

nr 259
A Sustainable Industrial Site Redevelopment Planning Support System
Tong Wang

nr 260
Efficient storage and retrieval of detailed building models: Multi-disciplinary and long-term use of geometric and semantic construction information
Thomas Ferdinand Krijnen

nr 261
The users' value of business center concepts for knowledge sharing and networking behavior within and between organizations
Minou Weijs-Perrée

nr 262
Characterization and improvement of aerodynamic performance of vertical axis wind turbines using computational fluid dynamics (CFD)
Abdolrahim Rezaeiha

nr 263
In-situ characterization of the acoustic impedance of vegetated roofs
Chang Liu

nr 264
Occupancy-based lighting control: Developing an energy saving strategy that ensures office workers' comfort
Christel de Bakker

nr 265
Stakeholders-Oriented Spatial Decision Support System
Cahyono Susetyo

nr 266
Climate-induced damage in oak museum objects
Rianne Aleida Luimes

nr 267
Towards individual thermal comfort: Model predictive personalized control of heating systems
Katarina Katic

nr 268
Modelling and Measuring Quality of Urban Life: Housing, Neighborhood, Transport and Job
Lida Aminian

nr 269
Optimization of an aquifer thermal energy storage system through integrated modelling of aquifer, HVAC systems and building
Basar Bozkaya

nr 270
Numerical modeling for urban sound propagation: developments in wave-based and energy-based methods
Raúl Pagán Muñoz

nr 271
Lighting in multi-user office environments: improving employee wellbeing through personal control
Sanae van der Vleuten-Chraibi

nr 272
A strategy for fit-for-purpose occupant behavior modelling in building energy and comfort performance simulation
Isabella I. Gaetani dell'Aquila d'Aragona

nr 273
Een architectuurhistorische waardestelling van naoorlogse woonwijken in Nederland: Het voorbeeld van de Westelijke Tuinsteden in Amsterdam
Eleonore Henriette Marie Mens

nr 274
Job-Housing Co-Dependent Mobility Decisions in Life Trajectories
Jia Guo

nr 275
A user-oriented focus to create healthcare facilities: decision making on strategic values
Emilia Rosalia Catharina Maria Huisman

nr 276
Dynamics of plane impinging jets at moderate Reynolds numbers – with applications to air curtains
Adelya Khayrullina

nr 277
Valorization of Municipal Solid Waste Incineration Bottom Ash - Chemical Nature, Leachability and Treatments of Hazardous Elements
Qadeer Alam

nr 278
Treatments and valorization of MSWI bottom ash - application in cement-based materials
Veronica Caprai

nr 279
Personal lighting conditions of office workers - input for intelligent systems to optimize subjective alertness
Juliëtte van Duijnhoven

nr 280
Social influence effects in tourism travel: air trip itinerary and destination choices
Xiaofeng Pan

nr 281
Advancing Post-War Housing: Integrating Heritage Impact, Environmental Impact, Hygrothermal Risk and Costs in Renovation Design Decisions
Lisanne Claartje Havinga

nr 282
Impact resistant ultra-high performance fibre reinforced concrete: materials, components and properties
Peipeng Li

nr 283
Demand-driven Science Parks: The Perceived Benefits and Trade-offs of Tenant Firms with regard to Science Park Attributes
Wei Keat Benny Ng

nr 284
Raise the lantern; how light can help to maintain a healthy and safe hospital environment focusing on nurses
Maria Petronella Johanna Aarts

nr 285
Modelling Learning and Dynamic Route and Parking Choice Behaviour under Uncertainty
Elaine Cristina Schneider de Carvalho

nr 286
Identifying indoor local microclimates for safekeeping of cultural heritage
Karin Kompatscher

nr 287
Probabilistic modeling of fatigue resistance for welded and riveted bridge details. Resistance models and estimation of uncertainty.
Davide Leonetti

nr 288
Performance of Layered UHPFRC under Static and Dynamic Loads: Effects of steel fibers, coarse aggregates and layered structures
Yangyueye Cao

nr 289
Photocatalytic abatement of the nitrogen oxide pollution: synthesis, application and long-term evaluation of titania-silica composites
Yuri Hendrix

nr 290
Assessing knowledge adoption in post-disaster reconstruction: Understanding the impact of hazard-resistant construction knowledge on reconstruction processes of self-recovering communities in Nepal and the Philippines
Eefje Hendriks

nr 291
Locating electric vehicle charging stations: A multi-agent based dynamic simulation
Seheon Kim

nr 292
De invloed van Lean Management op de beheersing van het bouwproces
Wim van den Bouwhuijsen

nr 293
Neighborhood Environment and Physical Activity of Older Adults
Zhengying Liu

nr 294
Practical and continuous luminance distribution measurements for lighting quality
Thijs Willem Kruisselbrink

nr 295
Auditory Distraction in Open-Plan Study Environments in Higher Education
Pieternella Elizabeth Braat-Eggen

nr 296
Exploring the effect of the sound environment on nurses' task performance: an applied approach focusing on prospective memory
Jikke Reinten

nr 297
Design and performance of water resistant cementitious materials– Mechanisms, evaluation and applications
Zhengyao Qu

nr 298
Design Optimization of Seasonal Thermal Energy Storage Integrated District Heating and Cooling System: A Modeling and Simulation Approach
Luyi Xu

nr 299
Land use and transport: Integrated approaches for planning and management
Zhongqi Wang

nr 300
Multi-disciplinary optimization of building spatial designs: co-evolutionary design process simulations, evolutionary algorithms, hybrid approaches
Sjonnie Boonstra

nr 301
Modeling the spatial and temporal relation between urban land use, temperature, and energy demand
Hung-Chu Chen

nr 302
Seismic retrofitting of masonry walls with flexible deep mounted CFRP strips
Ömer Serhat Türkmen

nr 303
Coupled Aerostructural Shape and Topology Optimization of Horizontal-Axis Wind Turbine Rotor Blades
Zhijun Wang

nr 304
Valorization of Recycled Waste Glass and Converter Steel Slag as Ingredients for Building Materials: Hydration and Carbonation Studies
Gang Liu

nr 305
Low-Carbon City Development based on Land Use Planning
Gengzhe Wang

nr 306
Sustainable energy transition scenario analysis for buildings and neighborhoods - Data driven optimization
Shalika Saubhagya Wickramarachchi Walker

nr 307
In-between living and manufactured: an exploratory study on biobuilding components for building design
Berrak Kirbas Akyurek

nr 308
Development of alternative cementitious binders and functionalized materials: design, performance and durability
Anna Monika Kaja

nr 309
Development a morphological approach for interactive kinetic façade design: Improving multiple occupants' visual comfort
Seyed Morteza Hosseini

nr 310
PV in urban context: modeling and simulation strategies for analyzing the performance of shaded PV systems
Ádám Bognár

nr 311
Life Trajectory, Household Car Ownership Dynamics and Home Renewable Energy Equipment Adoption
Gaofeng Gu

nr 312
Impact of Street-Scale Built Environment on Walking/Cycling around Metro Stations
Yanan Liu

nr 313
Advances in Urban Traffic Network Equilibrium Models and Algorithms
Dong Wang

nr 314
Development of an uncertainty analysis framework for model-based consequential life cycle assessment: application to activity-based modelling and life cycle assessment of multimodal mobility
Paul Martin Baustert

nr 315
Variable stiffness and damping structural joints for semi-active vibration control
Qinyu Wang

nr 316
Understanding Carsharing-Facilitating Neighborhood Preferences
Juan Wang

nr 317
Dynamic alignment of Corporate Real Estate to business strategies: An empirical analysis using historical data and in-depth modelling of decision making
Howard Cooke

nr 318
Local People Matter: Towards participatory governance of cultural heritage in China
Ji Li

nr 319
Walkability and Walkable Healthy Neighborhoods
Bojing Liao

nr 320
Light directionality in design of healthy offices: exploration of two methods
Parisa Khademagha

nr 321
Room acoustic modeling with the time-domain discontinuous Galerkin method
Huiqing Wang

nr 322
Sustainable insulating lightweight materials for enhancing indoor building performance: miscanthus, aerogel and nano-silica
Yuxuan Chen

nr 323
Computational analysis of the impact of façade geometrical details on wind flow and pollutant dispersion
Xing Zheng

nr 324
Analysis of urban wind energy potential around high-rise buildings in close proximity using computational fluid dynamics
Yu-Hsuan Jang

nr 325
A new approach to automated energy performance and fault detection and diagnosis of HVAC systems: Development of the 4S3F method
Arie Taal

nr 326
Innovative Admixtures for Modifying Viscosity and Volume Change of Cement Composites
Hossein Karimi

nr 327
Towards houses with low grid dependency: A simulation-based design optimization approach
Zahra Mohammadi

nr 328
Activation of demand flexibility for heating systems in buildings: Real-life demonstration of optimal control for power-to-heat and thermal energy storage
Christian Finck

nr 329
A computational framework for analysis and optimisation of automated solar shading systems
Samuel B. de Vries

nr 330
Challenges and potential solutions for cultural heritage adaptive reuse: a comparative study employing the Historic Urban Landscape approach
Nadia Pintossi

nr 331
Shared control in office lighting systems
Tatiana Aleksandrovna Lashina

nr 332
Comfort in Urban Public Spaces
You Peng

nr 333
Numerical modelling of metal soap formation in historical oil paintings
Gerardus Johannes Anna Maria Eumelen

nr 334
A transdisciplinary decision-making approach to food-water-energy nexus: A guide towards sustainable development
Maryam Ghodsvali

nr 335
Numerical modelling of transient low-frequency sound propagation and vibration in buildings
Indra Sihar

nr 336
Characterization of impact sound from lightweight joist floors
Yi Qin

nr 337
Cities for Children: Supporting Children and Caregivers in Participatory Urban Planning
Özlemnur Ataol

nr 338
Engaging the unengaged: Exploring citizen participation in nature-based solutions in China
Li Dai

nr 339
Municipal Solid Waste Incineration Residues: analysis, treatments, and applications
Ekaterina Loginova

nr 340
Enhancing the Uptake of Nature-Based Solutions in Urban Settings: An Information Systems Approach
Shahryar Ershad Sarabi

nr 341
Work Schedule Arrangements in Two-Adult Households with Children
Bilin Han

nr 342
Increasing awareness of urban cultural heritage using digital technologies: empirical design and analysis of a new multi-media web platform
Benshuo Wang

nr 343
Mechanical and physical properties of fibre-cement composites using alternative natural fibres
Katerina Kochova

nr 344
Numerical and experimental investigation of urban microclimate in a real compact heterogeneous urban area
Nestoras Antoniou

nr 345
Higher education classrooms' indoor environmental conditions: Input for the development of guidelines for higher education
Henk W. Brink

This thesis examines the utilization potential of alternative raw materials, such as biocoal fly ash or mineral wool waste, and offers improvements for currently used eco-efficient geopolymer technologies, with a general strategy to provide environmentally friendly solutions in the building industry. Novel high-temperature resistant materials are of great interest to enhance passive fire protection in the building sector. Research on multifunctional materials is gaining popularity as a result of the growing demand for improved material functionality, such as resistance to high temperatures, indoor humidity regulation, and thermal insulation. In order to provide sustainable solutions, industrial by-products are utilized, and specific material characteristics like pore size distribution, pore interconnectivity, and gas permeability are tailored. In addition to considering the various industrial by-products, it is advantageous to promote alternative methods of use for specific applications, such as protection against high temperatures. Besides the use of by-products as raw materials for the manufacture of high-temperature stable binders, it is crucial to encourage other forms of reuse, such as the formation of granular materials (aggregates). The proposed artificial equivalent offers an alternative to the current depletion of aggregates from natural resources.

DEPARTMENT OF THE BUILT ENVIRONMENT

TU/e EINDHOVEN UNIVERSITY OF TECHNOLOGY